Heat Transfer Modeling for the Quench Hardening of Aeronautical Steel

by

Gamaliel SALAZAR JIMENEZ

MANUSCRIPT-BASED THESIS PRESENTED TO ÉCOLE DE TECHNOLOGIE SUPÉRIEURE IN PARTIAL FULFILLEMENT FOR THE DEGREE OF DOCTOR OF PHILOSOPHY
Ph.D.

MONTREAL, APRIL 24TH 2026

ÉCOLE DE TECHNOLOGIE SUPÉRIEURE
UNIVERSITÉ DU QUÉBEC

BOARD OF EXAMINERS

THIS THESIS HAS BEEN EVALUATED

BY THE FOLLOWING BOARD OF EXAMINERS

Prof. Henri Champliaud, Thesis Supervisor
Department of Mechanical Engineering at École de technologie supérieure

Prof. Mohammad Jahazi, Thesis Co-supervisor
Department of Mechanical Engineering at École de technologie supérieure

Prof. Antoine Tahan, Thesis Co-supervisor
Department of Mechanical Engineering at École de technologie supérieure

Prof. Simon Joncas, President of the Board of Examiners
Department of Systems Engineering at École de technologie supérieure

Prof. Louis Lamarche, Member of the jury
Department of Mechanical Engineering at École de technologie supérieure

Prof. Moussa Tembely, External Evaluator
Department of Mechanical, Industrial and Aerospace Engineering at Concordia University

THIS THESIS WAS PRENSENTED AND DEFENDED

IN THE PRESENCE OF A BOARD OF EXAMINERS AND PUBLIC

APRIL 21^{TH} 2026

AT ÉCOLE DE TECHNOLOGIE SUPÉRIEURE

ACKNOWLEDGMENT

This accomplishment is the fruit of unmeasurable support from people around me, few words of gratitude will never be enough to express it nor list everyone involved, thank you all!

Gratitude without limits to the board of academic advisors, whose direction, guidance, and observations were always encouraging to explore the boundaries of the domain of interest during my research project. Their impact extends beyond that; it has forged me to become a better professional. That is exactly what the education and mentoring is for, thus my time at École de technologie supérieure would have not been as fruitful and relevant without them. Thank you, professors Mohammad Jahazi, Henri Champliaud, and Antoine Tahan.

Heartfelt gratitude to the board of industrial advisors from SAFRAN, heat-treatment engineer expert Mr. Jean-Sebastien Lemyre-Baron, located at SLS Mirabel, and retired professor and group level expert Mr. René Billardon. The endless discussions and industrial expertise truly led me to execute this project with the real-life application in mind, making this project an outstanding melting pot between academy and industry. Your comradery, generosity, and relentless support will be forever engraved in my heart.

Younger me had no clue of the fantastic people I would encounter along this journey: Anastasiia, Ana, Adriel, Azcari, Eduard, Edmundo, Grace, Lety, Pablo, Stephan, Thibault, and many other brothers and sisters, thank you from the bottom of my heart. To my bestie, the extraordinary memories, laughs, sorrows, patience, support, and words of encouragement are now engraved in my heart, so blessed to have you!

Gratitud total para ustedes: mama, papa, y hermana, su apoyo incondicional ha estado ahí. Gracias por todo ¡los llevo en mi corazón!

Gracias a todos!
Gama

MODÉLISATION DU TRANSFERT DE CHALEUR POUR LA TREMPE DE L'ACIER AÉRONAUTIQUE

Gamaliel SALAZAR JIMENEZ

RÉSUMÉ

La trempe est une étape essentielle de la fabrication des caissons principaux des trains d'atterrissage d'aéronefs. Ce procédé confère aux caissons les propriétés mécaniques nécessaires pour résister aux charges élevées et aux environnements corrosifs. Malheureusement, la trempe engendre des effets non désirés, notamment la déformation induite par la trempe, susceptibles d'affecter la productivité des fabricants. Le contrôle et la prédiction de cette déformation constituent un domaine d'application important en ingénierie. Notamment, les outils numériques capables de traiter les interactions complexes entre les différents domaines thermique, métallurgique et mécanique lors de la trempe reposent encore sur la définition des conditions frontières thermiques. Il est donc essentiel de caractériser et de modéliser avec précision les conditions frontières thermiques du procédé considéré, c'est-à-dire celles des installations industrielles dédiées où les grands caissons principaux de trains d'atterrissage sont traités.

Les conditions rencontrées dans les environnements industriels, très différentes des environnements de laboratoire hautement contrôlés, augmentent la difficulté de caractériser et de modéliser avec précision les conditions frontières thermiques. La configuration des fours à fosse exige que la charge traitée thermiquement soit extraite puis transférée par air vers le bain de trempe, ce qui modifie les conditions initiales avant l'immersion. De plus, un refroidissement hétérogène peut être causé par l'outillage de traitement thermique, une mauvaise circulation du fluide, ou par les conditions locales dans l'espace de travail du bain de trempe. Ces différences ont conduit de nombreux chercheurs à s'interroger sur l'applicabilité des essais normalisés en laboratoire dans les conditions réelles des pièces industrielles.

Par conséquent, ce projet utilise des sondes de trempe dans les conditions industrielles, de type plaque et cylindre, afin de caractériser le processus de trempe du partenaire industriel. Les travaux expérimentaux ont permis d'explorer l'hétérogénéité de procédé, l'influence de

l'orientation de la sonde, de sa position dans l'outillage. Ainsi que l'influence de la sonde de trempe, de sa géométrie et de ses dimensions, a été analysée en comparant les données obtenues avec différentes sondes.

Les conditions frontières thermiques sont estimées en résolvant le problème inverse de transfert de chaleur pour les deux étapes: le transfert aérien du four au bain de trempe et l'immersion. La stratégie adoptée consiste en reconstruire la température sur la surface, et ensuite à déterminer les flux de chaleur transitoires par simulation directe en utilisant l'évolution de la température identifiée comme condition frontière. Les méthodes produisent des résultats précis, avec une erreur relative inférieure à 5% par rapport aux courbes de refroidissement acquises expérimentalement. La base de données développée, qui prend en compte les mêmes facteurs que les travaux expérimentaux décrits précédemment, représente une source unique de coefficients représentatifs d'un procédé industriel réel, actuellement non-disponible dans la littérature.

À partir de ces résultats, des modèles mathématiques des conditions frontières thermiques sont proposés pour les deux étapes (le transfert aérien et l'immersion), prenant en compte l'influence de la taille de la sonde de trempe. Ces modèles sont basés sur des points caractéristiques qui définissent l'évolution des différents régimes de refroidissement. Lors de l'immersion, les points caractéristiques sont liés aux phénomènes physiques associés à la transition entre les régimes d'ébullition (chambre de vapeur, ébullition transitoire et ébullition nucléée). Par conséquent, chaque régime de refroidissement d'une courbe d'ébullition typique est modélisé séparément. La validation des modèles mathématiques par un test indépendant a donné une erreur relative inférieure à 8%, une augmentation par rapport aux résultats de la solution inverse, mais acceptable dans les conditions de l'étude, et même comparable aux résultats de problèmes inverses disponibles dans la littérature.

Mots-clés: trempe, sonde de trempe, coefficient d'échange thermique, identification inverse, courbe d'ébullition

HEAT TRANSFER MODELING FOR THE QUENCH HARDENING OF AERONAUTICAL STEEL

Gamaliel SALAZAR JIMENEZ

ABSTRACT

The quenching process is an essential part of the manufacturing process of aircraft landing gear main fittings. It provides the required material properties to achieve the desired strength to withstand high loads and corrosive environments. Unfortunately, quenching comes with undesired effects such as quenched induced distortion, which might impact the productivity of the manufacturers. Control and prediction of distortion remain an important field of engineering application. Notably, the numerical tools capable of dealing with the complex interactions between the thermal, metallurgical, and mechanical fields during quenching still rely on the definition of the thermal boundary conditions. Therefore, it is essential to accurately characterize and model the thermal boundary conditions of the process of interest, i.e., the facilities where large landing gear main fittings are processed.

The conditions encountered under industrial environments, often distant from the highly controlled laboratory setups, increase the challenge of accurately characterizing and modeling the thermal boundary conditions. For instance, pit furnace layouts require the heat-treated load to be extracted and then transferred by air to the quench bath which alters the starting condition before immersion even occurs. Moreover, uneven cooling might be caused by the heat treatment rig itself, poor circulation of the fluid, or even local conditions in the working space of the bath itself. Such differences encountered in the daily practice have led multiple researchers to question the applicability of standard testing on real workpieces.

This project implements industry-oriented quench probes, plate-like and hollow cylinder like, to characterize the quenching process of the industrial partner. The experimental means in this study successfully assessed the bath heterogeneity, the influence of probe orientation, and the position on the tooling. Likewise, the influence of the quench probe, in terms of geometry and size, was analyzed by comparing data from different test specimens.

The thermal boundary conditions were estimated by solving the inverse heat transfer problem for both the air transfer step and immersion step. The surface temperature is reconstructed first before retrieving the surface heat fluxes from a direct simulation using the identified temperature as a boundary condition. The chosen methodology produces accurate results in the form of a relative error below 5% with regards to the experimentally acquired cooling curves. The resulting database, which accounts for the same factors as the experimental work outlined above, represents a unique source of representative coefficients of an industrial scale process, currently unavailable in the literature.

Furthermore, mathematical models of the thermal boundary conditions are proposed for both steps (air transfer and immersion) accounting for the influence of the quench probe size. The models are based on characteristic points delimiting the evolution of the different cooling stages. During immersion, the characteristic points are linked to the physical phenomena associated with the transition between the boiling regimes (film, transition, and nucleate boiling). Therefore, each cooling regime of a typical boiling curve is modeled separately. The validation of the proposed models against the cooling curves of an independent test produced a relative error below 8%, a slight increase when compared with the inverse results, yet comparable with data in the literature and therefore deemed acceptable for the conditions of study.

Keywords: quenching, quench probes, HTC, inverse heat transfer, boiling curve

TABLE OF CONTENTS

Page

LIST OF TABLES

LIST OF FIGURES

Page

LIST OF ABREVIATIONS

ANN	Artificial Neural Networks
BC	Boundary Condition
Bi	Biot number
CGM	Conjugate Gradient Method
CHF	Critical Heat Flux
C.I.	Confidence Interval
CP	Control Point
CR	Cooling Rate
FB	Film Boiling
FD	Finite Difference
FE	Finite Element
FEM	Finite Element Model
FSM	Function Specification Method
GA	Genetic Algorithms
HC	Hollow Cylinder probe
HT	Heat Treatment
HTC	Heat Transfer Coefficient
INBD	Inbound (surface or direction)
IHCP	Inverse Heat Conduction Problem
IHTP	Inverse Heat Transfer Problem
KM	Koistinen-Marburger model
MAD	Mean Absolute Difference

MF	Main Fitting
MHF	Minimum Heat Flux
MID	Mid thickness (location)
MRD	Mean relative difference
MSSE	minimum sum squared error
Nu	Nusselt number
NB	Nucleate boiling
ONB	Onset of nucleate boiling
OTBD	Outbound (surface or direction)
PP	Plate probe (A, B or C)
PPS	Probe Positioning System
RMSE	Root Mean Square Error
SE	Standard Error
SFSM	Sequential Function Specification Method
SLS	SAFRAN Landing Systems
SS	Stainless Steel
TB	Transition Boiling
TC	Thermocouple
TFR	Temperature Field Reconstruction method
TGM	Temperature Gradient Method

LIST OF SYMBOLS

a_i, b_i, c_i, d_i	Coefficients of Hermite polynomials
α	thermal diffusivity
α_0	regularization parameter
Bi	Biot number
β	thermal coefficient of expansion
β_l	specific heat capacity of liquid
β_{tr}	transformation rate parameter
β_w	specific heat capacity of wall
C	model constants
CR	cooling rate
CR_{max}	maximum cooling rate
C_p	specific heat
c_{pv}	specific heat at constant pressure of vapor
$E_{max,min}$	Error between test and simulation results
ϵ	surface emissivity
ε	total strain
ε^e	elastic strain
ε^p	plastic strain
ε^{pt}	phase transformation strain
ε^{th}	thermal strain
ε^{tr}	transformation induced plasticity strain

η	direction normal to the surface Ψ
°C	degree Celsius
D	diameter
ΔT_{CHF}	excess temperature at critical heat flux
ΔT_e	excess temperature above saturation temperature
ΔT_{MHF}	excess temperature at minimum heat flux
ΔT_{sat}	overheat temperature
ΔT_{sub}	subcooled temperature
ΔT_{wf}	temperature difference between wall and fluid
δ	specimen thickness
g	gravitational constant
γ	subsurface distance from sensor to nearest surface
h	heat transfer coefficient
h_{Amax}	peak air transfer HTC as function of Bi number
h_{Arat}	ratio of model peak HTC and linearized radiative HTC
$h_{C,conv}$	heat transfer coefficient during convection
h_{FB}	heat transfer coefficient during film boiling
h_{fg}	latent heat of vaporization
h_n	non-dimensional HTC
h_r	linearized radiative HTC
$\overline{h_{c,n}}$	mean heat transfer coefficient during natural convection
Ja	Jacob number

K	constant or parameter
K	degree Kelvin
k	thermal conductivity
k_v	thermal conductivity of vapor
L	characteristic length
λ	time step
λ_c	critical wavelength
M_s	martensitic start temperature
m_{TB}	parameter during transition boiling
μ_v	vapor viscosity
n	iterations, steps
Nu_v	Nusselt number of vapor
$\overline{Nu_l}$	local Nusselt number of liquid
Ø	diameter of specimen
Ω	symbol of domain
P	ambient pressure
P_c	reduced pressure
Pe	Peclet number
Pr	Prandtl number
Φ	contact angle
Ψ	boundary of domain Ω
Ψ_{TB}	weighting parameter during transition boiling
φ	test data acquisition frequency

ψ_{tb}	vapor collapse probability
Q'	internal heat source
Q_{CHF}	characteristic point at CHF
Q_{conv}	characteristic point at convection
Q_{MHF}	characteristic point at MHF
q'	surface heat flux
q_{CHF}	critical heat flux
q_{MHF}	minimum heat flux
q_{TB}	transition boiling heat flux
q_{cr1}	first critical heat flux density
q_{cr2}	second critical heat flux density
q_{end}	surface heat flux at end of cooling
q_{in}	initial heat flux density
q_{sub}	subcooled surface heat flux
q_0	non-dimensional surface heat flux
Ra	Rayleigh number
R_a	surface roughness
r_{bore}	inner bore radius
R^2	coefficient of determination
S	objective or penalty function
S_m	mean spacing between roughness peaks
s_i	segments width

σ	surface tension
σ_r	Stefan Boltzmann constant
ρ	density of solid
ρ_l	density of liquid phase
ρ_v	density of vapor phase
T	temperature
T_{CHF}	surface temperature at critical heat flux
T_{MHF}	surface temperature at minimum heat flux
$T_{RelDiff}$	temperature relative difference
T_{conv}	surface temperature at convection
$T_{n,0}$	non-dimensional temperature
T_s, T_{surf}	surface temperature
T_{sat}	saturation temperature
T_{start}	start temperature
T_{surr}	surrounding temperature
$T_{t_{120}}, T_{imm}$	surface temperature at immersion
$T_{\infty,bulk}$	infinite or bulk temperature
t	time
ϑ	flow velocity during quenching
ν	kinematic viscosity
x, y, z	special coordinates
Y	experimentally measured temperatures

ξ_a	volume fraction of austenite
ξ_m	fraction of martensite

INTRODUCTION

Aircraft landing gear operates during the two most critical stages of flight: take off and landing. High-strength materials are required on structural components of the gear to withstand the design loads during such critical stages. However, the gear is an unproductive weight for most of the flight cycle, thus high specific strength materials (ratio between strength and density) are required to aid the designers to reduce the weight and volume of the gear (Schmidt, 2020). Thereby, steel remains one of the preferred materials even nowadays, as it provides the smallest volume solution and good manufacturability (Schmidt, 2020).

Structural components of the landing gear, such as the main fitting (MF), come with complex shapes and geometries (see Figure 0.1). According to one of the major single aisle manufacturers, a production cadence of 75 aircraft per month is expected for 2025 (Hepher, 2022), meaning that leading landing gear manufacturers, such as the industrial partner SAFRAN Landing Systems, are expected to maintain a cadence of 150 MFs per month. Moreover, during the manufacturing process, around 85% of the material is removed from the original forging. Therefore, material cost and availability must be considered, which fits perfectly with martensitic 300M steel.

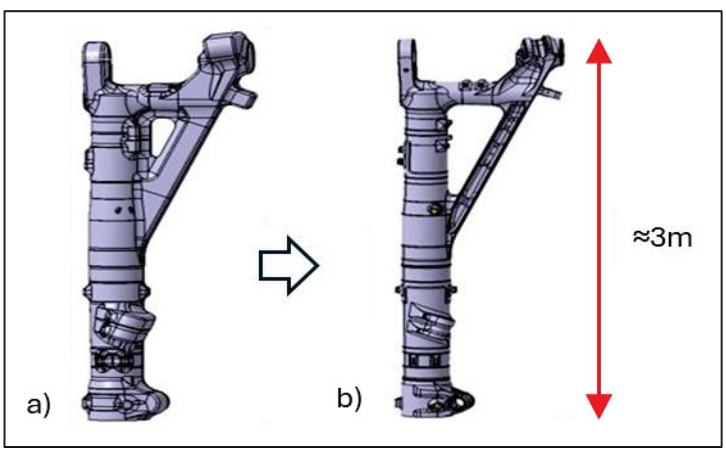

Figure 0.1 Geometry evolution of a typical main fitting
a) forging, and b) condition after machining
Reproduced with the authorization of SAFRAN

In order to fulfill the design requirements, the MFs undergo several machining steps and special processes, including a quenching process, to improve the mechanical properties of the material. Quenching is arguably one of the most complex processes, as it is a combination of the thermal-metallurgical-mechanical fields. It is an essential process that modifies the microstructure of the material, evolving from austenite to the harder martensitic phase. However, quenching is carried out once the component has reached almost its final shape, meaning that any geometrical change is likely to lead to undesired non-conformities on the component, and in a worst-case scenario, lead to scrapping the part, which can have a strong impact on production costs.

The geometrical changes during quenching are often referred to as distortion, a phenomenon that is always expected, hardly understood and often challenging to predict. Quench induced distortion occurs by a combination of factors, mainly changes in volume due to temperature gradient and phase transformation (Narazaki & Totten, 2007). First, a thermal gradient appears due to the rapid cooling at the surface, which is well over 800°C, considerably higher temperatures than an oil bath (≈40°C). Thus, thermal stresses develop as the surface cools and shrinks rapidly before the core does. Once the martensitic transformation temperature is reached, volume changes start to occur at the surface and then the core. Note that large components like the MF (see Figure 0.1) take several seconds to fully immerse, while the variable ruling section and non-symmetry lead to uneven cooling, thus, the phenomena above occur unevenly in different instances along the component.

Quenching under industrial conditions adds up to the complexity of understanding and predicting distortion. Heterogeneities in the quench bath contribute to the non-uniform cooling of the component. Similarly, the influence of the heat treatment rig requires to be accounted as it might influence the local conditions. Moreover, industrial layouts for pit furnaces, like in the case of the industrial partner (see Figure 0.2), influence the starting condition of the component due to the required transfer of the load from the furnace to quench bath. Consequently, predicting distortion under industrial environments remains a true challenge.

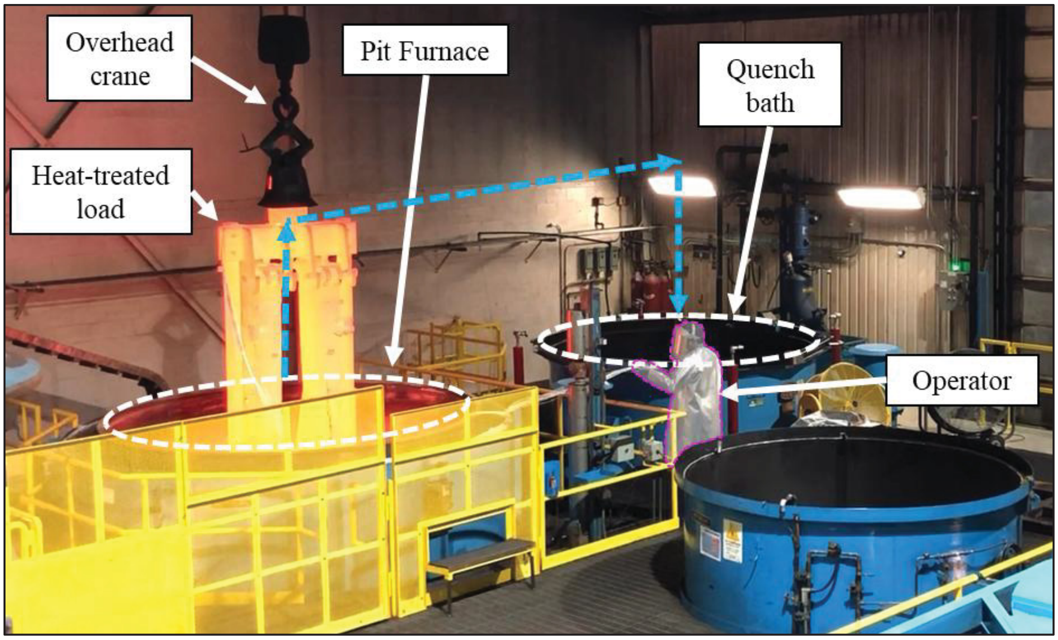

Figure 0.2 Layout of heat treatment and quenching operations
Reproduced with the authorization of SAFRAN

Multiple researches have successfully predicted quenched induced distortion of steel (DANTE, 2019; Narazaki, Kogawara, Shirayori, Kim & Kubota, 2012; Simsir, 2008) using numerical simulation tools incorporating constitutive laws with varying degrees of thermal-metallurgical-mechanical coupling or linkage (i.e., DANTE, DEFORM-HT, SYSWELD, etc.). These tools still rely on the adequate definition of a boundary condition (BC), often found in the form of surface heat flux or heat transfer coefficients (HTC). As the thermal field is considered the fundamental driving factor of the metallurgical-mechanical fields (Simsir, 2014), the accuracy of the whole simulation can be compromised by inaccuracies in the thermal BC which must be known for the complete quenching process. Therefore, accurate characterization of the thermal BC is necessary to enable proper simulation of the thermal field, and consequently, decreasing the uncertainties in the prediction of distortion.

Previous works by the industrial partner include the thermal field characterization using surface mounted thermocouples. Due to the installation strategy, highly perturbated data was obtained, thus raising concerns about the reliability of the experimental results. Clearly, characterization of the thermal BC is difficult due to the hazardous environment and limited accessibility of measuring instruments during both heating (furnace) and cooling (quench bath). Nevertheless, the most conclusive work with regards to the identification of the thermal BC under an industrial environment similar to the industrial partner was carried out by (Lemyre-Baron, 2025). The author confirmed the need to utilize specially designed quench probes with in-body sensors to measure the thermal history through the complete process and then solve the inverse heat transfer problem to estimate the thermal BC.

Quench probes are often used under laboratory conditions as per standard procedures (i.e., ASTM D6200-21, 2021). However, the procedures and standard specimens are distant from real life operations. Standard testing requires instantaneous quenching, thus preventing heterogeneities before immersion, which is great for analysis and comparison of the cooling performance of multiple quenchant but distant from the case under consideration (see Figure 0.2). Similarly, the size of the standard specimen (Ø12.5 x 60mm as per ASTM D6200-21) is considerably smaller than actual workpieces, thus cooling faster and leading to higher cooling rates (Kobasko & Liscic, 2017; Prasanna Kumar, Hernandez-Morales & Totten, 2014). Moreover, using standard specimens could be misleading as they lead to assume a lump condition, neglecting the thermal gradients inside the probe due to its size. Thereby, studies that have characterized industrial processes inevitably require custom-made quench probes (Ferguson, Freborg & Li, 2012; Lemyre-Baron, 2025; Liscic, 2016; Wallis, 2010). Nonetheless, the geometry and size of the probe, its material, and the instrumentation strategy vary among authors. Therefore, industry-oriented quench probes must be developed first to obtain characteristic cooling curves while considering the particularities of the process and geometries representative of the workpiece.

The experimentally acquired data from the quench probes can be used to solve the inverse heat transfer problem (IHTP) to estimate the thermal BC at the surface of the probes. Multiple methods are available in the literature, including the sequential function specification method (Beck, 1968), deterministic and stochastic methods (Colaço & Dulikravich, 2011; Ozisik & Orlande, 2000), temperature gradient method (Liscic & Singer, 2013), etc. The postulates and considerations for a given method should be carefully considered; often the methods are developed for one-dimensional or axisymmetric cases, constant material properties, homogeneous starting conditions that might work perfectly when identifying a single unknown boundary condition. Likewise, the computational power required to implement a given method should be considered, especially for iterative methods, but also depending on the selected time domain (i.e., future time steps, or complete time domain). Moreover, accuracy levels on the identification of thermal BCs during the process vary in the literature. Error values, as low as 1.5%, have been reported for a small cylindrical specimen (Ø20 mm x 50 mm) using the function specification method (Babu & Prasanna, 2010). The thermal BCs for larger specimens (Ø25, 50, up to 75 mm) have been estimated with a relative error below 5% using an optimization algorithm (Behrem & Hrnjica, 2018). Thereby, the numerical tools to estimate the thermal BCs for the case herein shall be developed. The assumptions and postulates implemented in the numerical tools must consider the industry-oriented probes geometry and instrumentation strategy, as well as the particularities of the process of interest: the air transfer step, and the immersion into oil (see Figure 0.2). The numerical tools must provide accurate results, comparable to the accuracy levels as per the literature, for its later use on the numerical simulation of quenching.

The thermal BCs are often given in the form of temperature dependent HTCs (see Figure 0.3), which, as mentioned before, are critical to carry out accurate numerical simulations of the quenching process. Even if a reference BC is available or suggested by the industrial partner (see Figure 0.3), multiple questions remain open. One of the biggest needs is the mapping of the BCs at different locations in the working space (Ebner, Lubben & Surm, 2025). This would account for flow perturbations caused by the tooling and proximity to the agitation systems (Ebner, Lubben & Surm, 2025; MacKenzie & Banka, 2009). Similarly, the influence of the orientation of the probe, with regards to the oil flow, is likely to impact the local BCs (MacKenzie & Banka, 2009; Thibault, 1978). Moreover, the size and orientation of the probe need to be studied as the cooling performance and cooling regimes are affected (Behrem & Hrnjica, 2021; Kobasko & Liscic, 2017; Ramesh & Prabhu, 2012, 2014). Likewise, the variation of the BC, due to the geometry of the quench probe, needs to be accounted, as plate-like geometries may produce different results than tube-like specimens, which might better represent the actual workpiece (Liscic & Singer, 2013). Thereby, a database of cooling curves and thermal BCs must be developed to address the influence of such variables.

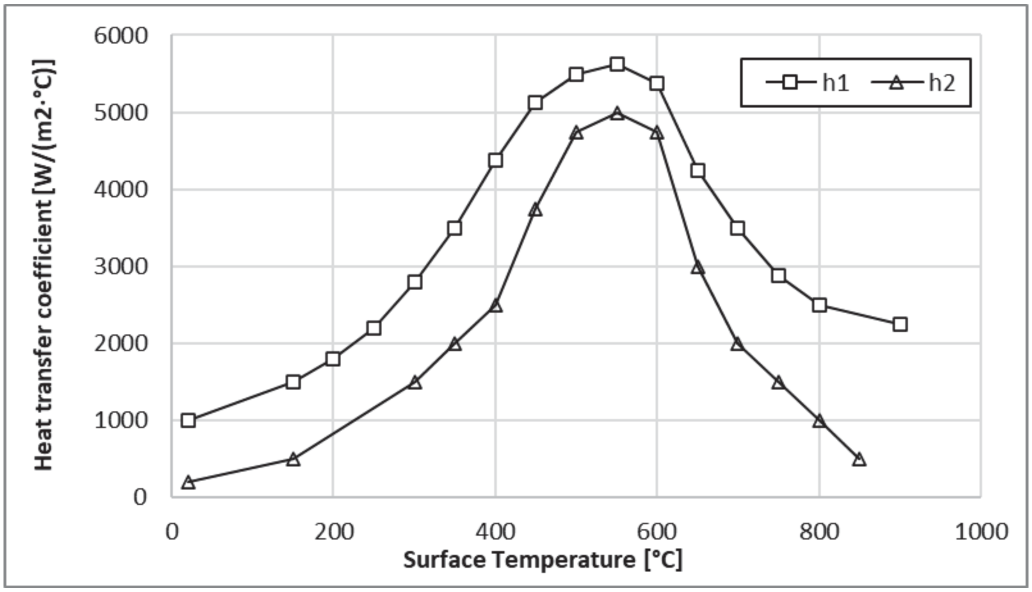

Figure 0.3 Typical HTC for quench oil suggested by SAFRAN

The modeling of the thermal BC is another question that needs to be addressed. As a matter of fact, this is exactly the challenge faced in practice by the industrial partner. Note that the suggested BCs are often based on expanded results from the library of commercial software (see Figure 0.3). Such values need to be tweaked following a trial-and-error process, which becomes tedious and highly inefficient, as it must account for the wide variety of cases on the workpiece. The complexity of the workpiece geometry inevitably leads to multiple surfaces entering the bath with different orientations, with regards to the fluid, including fully horizontal, or even concave locations for the tubular sections. Similarly, the workpiece encounters different flow conditions while quenching, due to its length and size, which affects the thermal BCs. There is no doubt that multiple thermal BCs appear on the workpiece at once, hence a methodology is needed to model the HTC based on varying parameters. In this study, the influence of the probe's size, in the form of thickness, and locations on the quenching tooling, have been prioritized. The former variable is highly valuable as the intended application (i.e., MF, see Figure 0.1) contains ruling sections with different thicknesses, while the latter inheritably accounts for the local flow conditions on the working space.

The present work has been defined in this context and addresses the identified gaps in the literature with regards to the adequate means to characterize industrial quenching processes, the numerical tools needed to estimate local BCs, the development of a database exploring the heterogeneity of the system, influence of probe orientation, influence of probe geometry and size; and a modeling strategy to adjust the thermal BC during the complete process. Thus, this document is organized as follows:

Chapter 1 provides a literature review of the general knowledge regarding the fields involved in heat treatment and quenching operations and its inevitable byproduct: distortion. Then, the basic mechanisms of the different phenomena occurring during quenching by immersion are introduced, as well as the most common correlations found in the literature. It is followed by a review of quench probes studies, including standard and nonstandard geometries, instrumentation strategies and good practices. Lastly, an overview of the inverse heat transfer problem is included, addressing some of the solving techniques and difficulties it presents. The chapter concludes with a summary of the challenges to be addressed in this project and the objectives of this study.

Chapter 2 presents the research approach applied in this project, which can be divided into the following main steps: characteristics of industry-oriented quench probes whose technical drawings can be found in ANNEX I, the in-situ test campaign and its corresponding axes of study, the interpretation of experimental results, the strategy to estimate the thermal boundary conditions, and the mathematical modeling of the thermal boundary conditions.

Chapter 3 introduces the technical information with regards to the experimental materials and methods. It describes testing facilities, test equipment, instrumentation of quench probes, and the test protocol and test setup used during the test campaign.

Chapter 4 presents the experimental results to evaluate bath heterogeneity and the influence of probe's orientation. The discussion is centered on the differences with available data from the literature and the boundary condition estimated for a reference quench probe. ANNEX II follows up to this chapter by presenting the boundary conditions for cases accounting for different orientations of the probe.

Chapter 5 details the analysis of the air transfer step of the reference industrial process. A method to estimate the boundary condition for different probes based on the qualitative identification of control points is introduced in this chapter. The discussion is centered on the influence of the probe's size and the oversimplification when considering lump bodies as per classic heat transfer analysis. In fact, under the conditions of this study, geometries that qualify as lump bodies require further adjustments on their BC to obtain accurate results.

Chapter 6 is solely focused on the immersion step of the process. It provides a systematic review of the cooling regimes (i.e., film boiling, transition boiling, nucleate boiling and convection), its transition temperatures and duration during immersion. Regression models are developed to account for the probe size as a function of the Biot number.

Chapter 7 presents the modeling strategy of the boundary condition for both the air transfer step and the immersion step. The mathematical expressions account for the influence of the probe's size on the temperature dependent heat transfer coefficient. Validation is provided using thermal measurements of an independent probe quenched under comparable conditions. Additional results contributing to the mapping of the temperature dependent HTC can be found in ANNEX III and ANNEX IV. Both annexes consider a hollow cylinder as a test probe, thus analyzing the evolution of the boundary along the bore and outer surface. Discussion elaborates on the differences caused by the probe's geometry.

ANNEX V contains supporting evidence of the need to adjust the BC based on the probe's size. Numerical simulations interchanging the BC from probes with different sizes demonstrate the need to account for such variable in the modeling strategy.

ANNEX VI and ANNEX VII follow up on the methodology outlined in **Chapter 7** by developing the corresponding models for a different test setup, confirming the applicability of the proposed strategy. Lastly, ANNEX VIII provides additional evidence of the influence of the probe size on the hollow cylinder probe confirming the need to account for such variable on different probe geometries.

The Conclusions section links the outcomes of the thesis towards the initial objectives, while further works are listed in the Recommendations section.

CHAPTER 1

LITERATURE REVIEW

1.1 Heat Treatment & Quenching

The manufacturing process of high-performance steel components typically requires a heat treatment process to yield the required mechanical properties (Simsir, 2014). This is achieved by obtaining the very strong and hard phase called martensite as a result of a rapid cooling process, commonly known as the quench hardening process. Depending on the cooling technique, the rapid cooling can be classified as either immersion quenching, spray quenching or gas quenching (Samuel & Prabhu, 2022b). This project is solely focused on immersion quenching. This technique allows to process large and heavy loads, which is convenient to manufacture large landing gear components at a high industrial cadence.

The heat treatment and quench hardening process involves the combination of multiple fields: thermal, metallurgical and mechanical, thus dealing with a complex coupled multiphysical process. Figure 1.1 presents the relation/coupling between the main physical fields. These interactions make the quench hardening process highly complex. Unfortunately, this process may lead to production loses due to inherent challenges such as quench hardening induced distortion, cracking, undesired microstructure distribution and residual stresses (Simsir & Gur, 2008). The following subsections address each of the physical fields involved aiming to provide a basis to assimilate their influence on the inherent problematics of the process.

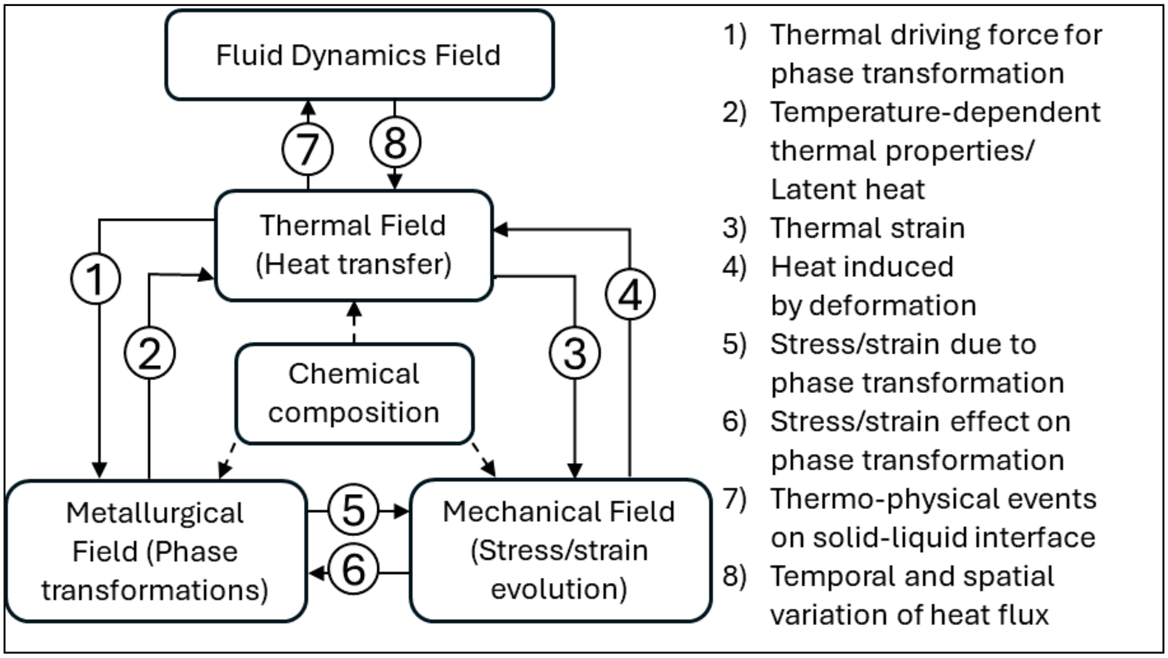

Figure 1.1 Main physical fields and couplings during heat treatment
Modified and redrawn from Simsir (2014, p. 413)

1.1.1 Thermal Field

Heat transfer during the quenching process can be catalogued as the driving force of the other phenomena (phase transformation and thermal stresses). The evolution of the thermal field during quenching directly affects the microstructure and the physical and mechanical properties of the material. Therefore, the accuracy of the simulation and prediction of both metallurgical and mechanical fields depends on the accurate determination of the thermal field.

Classic heat transfer textbooks (Bergman, Lavine, Incropera & Dewitt, 2011) present the three main modes of heat transfer: conduction, convection and radiation. As quenching occurs by immersion, heat exchange occurs between the solid and the liquid. Within the solid, the mathematical relation that expresses the temperature distribution in a conduction analysis is known as the heat diffusion equation, which in Cartesian coordinates is expressed as follows:

$$\frac{\partial}{\partial x}\left(k\frac{\partial T}{\partial x}\right)+\frac{\partial}{\partial y}\left(k\frac{\partial T}{\partial y}\right)+\frac{\partial}{\partial z}\left(k\frac{\partial T}{\partial z}\right)+Q'=\rho C_p\frac{\partial T}{\partial t} \tag{1.1}$$

The heat diffusion equation considers the temperature dependency of the material properties: the thermal conductivity (k), density (ρ) and specific heat (Cp), or the ratio of the heat conducted through the material to the heat stored per unit volume, also known as thermal diffusivity (α). Similarly, the internal heat source (Q') accommodates the latent heat release during phase transformation. The general form shown in Eq. 1.1 can be simplified, for instance, if the heat conduction was analyzed in a one-dimensional direction and expressed in either cylindrical or spherical coordinates.

The solution of Eq. 1.1 requires the definition of initial and boundary conditions. The former can be specified as the initial known temperature (i.e., furnace temperature) over the domain Ω, such that:

$$T(x,y,z,t)=T(x,y,z) \quad \forall\, x,y,z\ \in \Omega \tag{1.2}$$

The boundary conditions are defined in classic heat transfer textbooks as either Dirichlet (first kind), Neumann (second kind) or third kind. A Dirichlet-type boundary condition uses temperature distribution at the surface Ψ, giving the following relation:

$$T_s=T(x,y,z) \quad \forall\, x,y,z\ \in \Psi \tag{1.3}$$

The Neumann-type boundary condition defines the evolution of the heat flux (q') in the normal (η) direction to the surface, such that:

$$-k(T)\frac{\partial T}{\partial \eta}=q' \tag{1.4}$$

With a boundary of the third kind, the heat balance at the surface is expressed by Newton's Law of cooling in classic heat transfer textbooks, such as:

$$q' = h(T_\infty - T_s) \tag{1.5}$$

Where h is the heat transfer coefficient, T_∞ is bulk temperature of the fluid, and T_s is the surface temperature. One of the biggest challenges, if not the most critical one, comes with the accurate definition of h. It is usually determined experimentally and depends on variables like surface geometry, the nature of fluid motion, fluid properties, etc. The identification of h becomes even more challenging, as the cooling regimes during quenching by immersion must consider the multiphase nature of the liquid often encountered on vaporizable quenchants at high temperatures. A detailed description of the different cooling regimes during quenching is included in further subsections.

Given the complexity of the problem, there is no analytical solution to determine the thermal field evolution during the quench hardening of martensitic steel. This leads to the utilization of numerical tools to predict the thermal field. However, the accuracy at which h is determined can impact the reliability of quenching simulation results (Danev, Gospodinov, Radev & Ilieva, 2020; Samuel & Prabhu, 2022b). Hence, the need to develop methods and tools to accurately predict the boundary conditions that can be used in the thermal simulation of the quenching process.

1.1.2 Metallurgical Field

Quenching of martensitic steels is considered as a temperature dependent process, thus time independent once initiated (Koistinen & Marburger, 1959). The kinetics of martensitic phase transformation are generally modeled as per the Koistinen-Marburger (KM) equation, equation, which is expressed as:

$$\xi_m = (1 - \underbrace{\exp\left(-\beta_{tr}(M_s - T)\right)\,)}_{\xi_a} \tag{1.6}$$

Where ξ_m and ξ_a are the fraction of martensite and the volume fraction of austenite respectively. M_s is the martensite start temperature, T is the temperature below M_s, and β_{tr} is the rate of transformation parameter.

The transformation of austenite into different metallurgical products is determined by the cooling rate and its stability range, which is closely linked to the carbon content (Atkins, 1980). One must note that martensitic transformation comes with an increase in the volume of the material. This can be observed in dilatometry results, as shown in Figure 1.2. However, if cooling is insufficient to fully transform austenite into martensite, a mixture of martensite and bainite may occur. This can be caused by the combination of multiple factors, such as the size of the heat-treated component, poor heat exchange conditions, or even low hardenability of the alloy. Different phases have different specific volumes, thus a mixture of phases across the thickness of the component would likely develop into a varying distribution of internal stresses, compression stresses at the surface and tension stresses at the core, thus inducing distortion of the treated geometry.

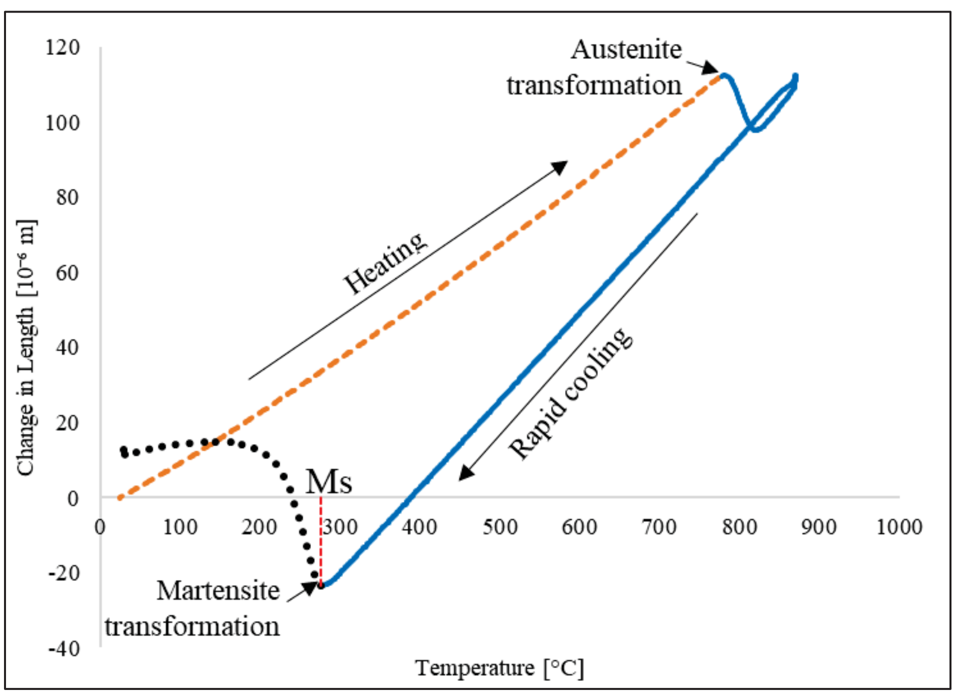

Figure 1.2 Dilatometry results of 300M steel
Reproduced and adapted with the authorization of SAFRAN

1.1.3 Mechanical Field

The mechanical field during the quenching process is solicited, for there is deformation of the specimen and the internal stress generation (Simsir, 2014). It is often considered the most sophisticated of the three fields due to material laws and coupling interactions. Material models for the simulation of quenching can be classified into elasto-plastic models, elasto-viscoplastic models and unified plasticity models (Sadeghifar et al., 2024, 2025; Simsir & Gur, 2008). The formulation of constitutive equations for most of the quenching models considers an additive decomposition of the strain tensor. Thus, the total strain tensor is decomposed into multiple terms as follows (Samuel & Prabhu, 2022b):

$$\varepsilon = \varepsilon^{e} + \varepsilon^{p} + \varepsilon^{th} + \varepsilon^{pt} + \varepsilon^{tr} \tag{1.7}$$

where $\varepsilon^{e}, \varepsilon^{p}, \varepsilon^{th}, \varepsilon^{pt}, \varepsilon^{tr}$ represent the different strain components: elastic, plastic, thermal, phase transformation and transformation induced plasticity strain.

The global thermomechanical properties must be approximated while considering the evolution of the transformation of different phases during quenching. Changes in the microstructure of the component affect the mechanical properties of the phase mixture. Thus, predicting the overall mechanical properties becomes a major problem. The relation between thermal and mechanical fields includes the spatial variations on the component due to the thermal contractions and expansions caused by temperature gradients. This is especially relevant for rapid cooling processes such as quenching (Simsir, 2014).

1.2 Distortion During Quenching

Understanding the roles and interactions between the three main fields involved during heat treatment and quenching are key to grasp the actual problematic: the inherent changes in the geometry and size of a workpiece, also known as distortion. In practice, distortion is almost impossible to fully eliminate, instead, strategies to diminish and reduce distortion are the most viable solution (Narazaki & Totten, 2007). One must note that the final geometry of a workpiece can be influenced by the manufacturing processes before heat treatment. However, distortion becomes noticeable and often unpredictable after heat treatment and quenching operations. The basic mechanisms that cause distortion are typically divided into relief of residual stresses, changes in volume due to thermal gradient, and volumetric changes due to phase transformation (Narazaki & Totten, 2007).

During quenching, distortion occurs because the internal loading mechanisms oppose each other. Its evolution is not entirely intuitive though, as the workpiece cools down, the internal loading mechanisms evolve as well, thus dealing with a non-linear problem (Narazaki et al., 2012) as one or more stress state shifts might occur during quenching. Moreover, the elastic limit of metallic materials is strongly temperature dependent, it decreases with increasing temperatures, leading to plastic deformations when the internal stresses exceed the yield strength of the material (Liscic, 2006).

Taking a steel-made cylinder without phase transformation as a reference (Liscic, 2006), the surface of the cylinder will contract due to the rapid cooling once in contact with the quenchant while the core of the cylinder remains at a high temperature. This imbalance produces tensile stresses at the surface and compressive stresses at the core leading to stretching the surface and contracting the core (see Figure 1.3). If the stresses exceed the yield strength of the material, then plastic deformation occurs. The stress magnitudes start to reduce after reaching the peak thermal gradient between zones, shown at t_{max} in Figure 1.3. Each zone has a different stress evolution, and due to the plastic deformation, they can no longer coexist in a stress-free state. As cooling continues, the extension and compression caused by compressive and tensile stresses continue to develop while also opposed by the remaining temperature differences between both zones. At the end of quenching, thermal shrinkage has produced compressive stresses at the surface and tensile stresses at the core, as shown in Figure 1.3 (Liscic, 2006).

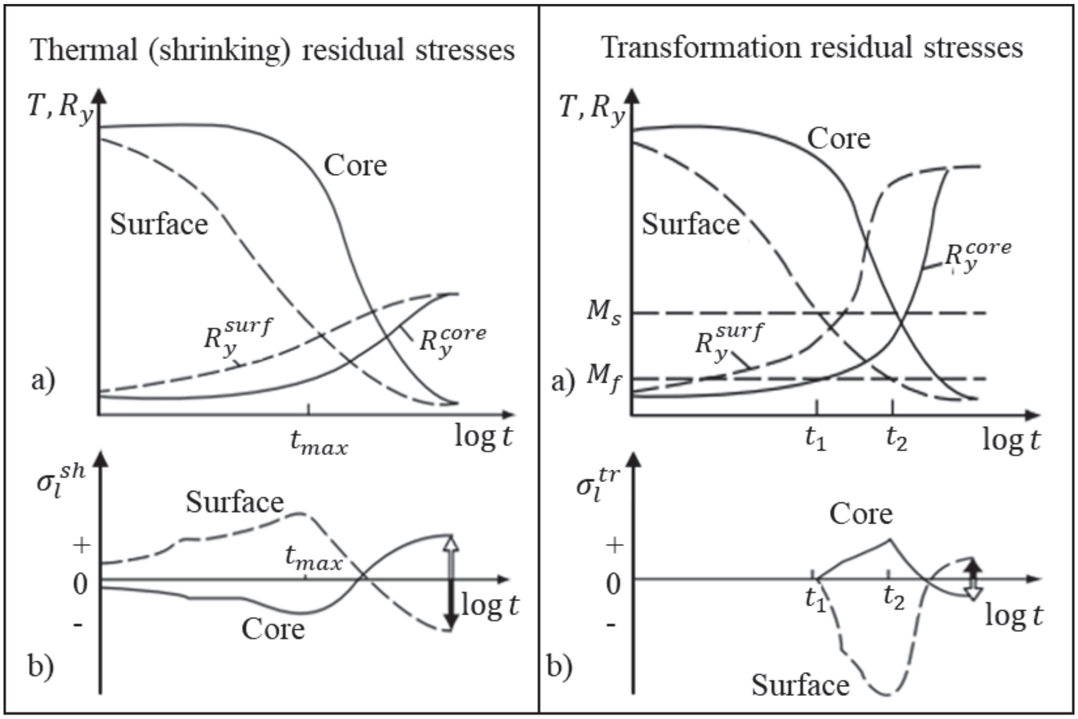

Figure 1.3 Development of residual stresses for simplified cases: thermal shrinking without transformation (left) and transformation without thermal shrinking (right) (a) evolution of temperature and yield strength (R_y) for core and surface, (b) residual stresses at core and surface Modified and redrawn from Liscic (2006, p.320)

A second reference case for a steel-made cylinder with phase transformation but no thermal expansion is shown in Figure 1.3 (Liscic, 2006). Residual stresses start developing upon reaching transformation temperature, which occurs first at the surface (at t_1 in Figure 1.3), resulting in compressive stresses in the surface and tensile stresses at the core. Once the core reaches transformation temperature (at t_2 in Figure 1.3), then the volume increase at the core progressively reduces the stress magnitudes in both zones. Given that opposing plastic deformation occurs, and the difference in size between zones, the residual stresses evolve differently passing zero at a different timing. The imbalance continues developing until the end of cooling, leading to compressing stresses in the core and tensile stresses at the surface, as shown in Figure 1.3 (Liscic, 2006).

Both thermal and transformational stresses appear during the quench hardening of martensitic steels, the combination of these phenomena makes distortion much harder to predict. Unfortunately, they can not be described by simply imposing the simplified cases. It is fundamentally essential to determine the temperature evolution (cooling) of the treated load. By doing so, the thermal imbalance can be predicted, as well as the initiation time of transformation for both surface and core, as they dictate the evolution of hardening residual stresses (Liscic, 2006). In some extreme cases, the accommodation of volume variations at the core and surface is no longer possible, leading to quenching cracks (see Figure 1.4).

Figure 1.4 Quench test specimen made of
300M steel (treated multiple times)
Reproduced with the authorization of SAFRAN

The size of the heat-treated load and the equivalent carbon content of the alloy have a substantial impact on the cooling history and transformation of the material, inherently influencing the evolution of internal stresses during quenching. Moreover, the process characteristics, such as quenchant type, agitation levels, part orientation, and heterogeneities, add up to the challenge of simulating and predicting the final geometry of workpieces treated under industrial conditions.

Attempts to simulate quenching processes often rely on simplified geometries, like the navy-c ring (Beckermann & Carlson, 2011; da Silva et al, 2012), and groove probe (Lopez-Garcia, Medina-Juarez & Maldonado-Reyes, 2022) to measure distortion under controlled environments to validate simulation models before addressing larger and complex geometries. Even these types of simplified studies often rely on the adequate definition of the thermal BCs. This is especially true for simulations where no further consideration is given to the fluid flow; thus, the BC relies on the definition of HTC or surface fluxes. Even more complex simulation studies where fluid flow is considered on ring geometries (Banka, Ferguson & Mackenzie, 2013) have indicated the relevancy of capturing the current evolution of the thermal boundary conditions.

1.3 Typical Heat Transfer During Immersion Quenching

During quenching by immersion, the boundary condition at the surface-fluid interface is a combination of multiple physical phenomena. The evolution of these phenomena dictates the magnitude and intensity at which heat is extracted from the solid towards the fluid, thus directly influencing the thermal BC. It is widely accepted that the typical quenching by immersion into a vaporizable quenchant has the following four cooling regimes: film boiling, transition boiling, nucleate boiling, and convection, as shown in Figure 1.5.

The following subsections describe the basic mechanisms for each cooling regime as well as the correlations available in the literature. Further remarks are included at the end of the section discussing the limitations and applicability of those correlations. Modeling the thermal BC during quenching by immersion remains a challenge, yet of first order of importance as the thermal field is the driving force of the metal-mechanical fields, a key factor to accurately predict the final distortion of a workpiece.

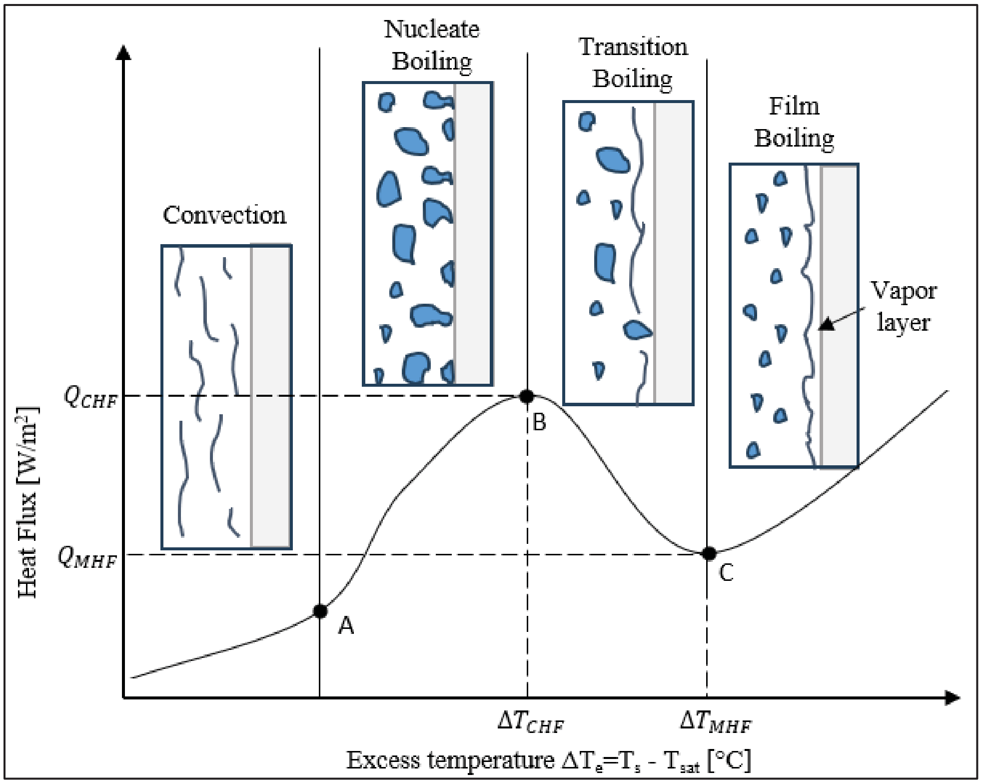

Figure 1.5 Typical quenching curve and cooling regimes

1.3.1 Film Boiling

Generally, heat-treated loads will be at higher temperatures than the boiling point of the quenchant. Such conditions create a vapor blanket around the surface of the load, isolating the surface and reducing the heat extraction rate. The surface will continue to cool down until the vapor blanket can no longer be supported and starts to collapse. The minimum amount of heat flux required to sustain the vapor blanket is known as minimum heat flux (q_{MHF}), shown schematically as point C in Figure 1.5. Point C in Figure 1.5 is referred with different names in the literature, such as Leidenfrost point, “rewet” temperature, onset of stable film boiling temperature; such a name depends on the method used to measure it (Darr, Dong, Glikin, Hartwig & Chung, 2019).

Right upon immersion, the amount of heat extracted from the body is referred to as the initial heat flux density (q_{in}). For film boiling to appear, the magnitude of q_{in} must be bigger than the first critical heat flux density (q_{cr1}). q_{cr1} is generally understood as a property of the quenchant, it represents a peak flux value upon the shock-film boiling, which is required for bubble nucleation first to occur just before stabilizing and forming the vapor blanket on the surface (Kobasko, Moskalenko, Totten & Webster, 1997). As the occurrence of q_{cr1} is extremely fast, often appearing at 0.1 s after immersion, q_{cr1} has been associated to the second critical heat flux density (q_{cr2}), which represents q_{MHF}, as per the relation:

$$q_{cr1} = 5 \times q_{cr2} \tag{1.8}$$

There are different ratios for the relation between q_{cr1} and q_{cr2}, as well as two main approaches to model them, either with regards to the stability of the vapor film formation or bubble growth formation and departure (Kobasko et al., 1997). Nevertheless, the general agreement is that q_{cr2}, and therefore q_{MHF}, can be characterized for a given quenchant using experimental means, such as quench probes (Liscic & Singer, 2014).

In practice, the duration of the film boiling regime depends on multiple factors, such as the mass and shape of the part, quenchants properties, bath temperature, agitation rates (Liscic & Singer, 2014). The orientation of the load can influence its duration, for instance, a bottom side of a part will retain most of the bubbles, having difficulty leaving the surface and rising upwards even while the surface might be cooled down. Similarly, blind holes and concave geometries are likely to experience longer film boiling than outer and exterior surfaces (Liscic & Singer, 2014).

1.3.1.1 Minimum Heat Flux

Analytical solutions have been developed to estimate q_{MHF}, point C in Figure 1.5. The classic work of Zuber (1959) used stability theory to derive the following expression for a horizontal surface:

$$q_{MHF}^{Z} = C\rho_v h_{fg}\left(\frac{g\,(\rho_l - \rho_v)\sigma}{(\rho_l + \rho_v)^2}\right)^{1/4} \tag{1.9}$$

where ρ_l, ρ_v are the densities of liquid and vapor phases, g the gravitational constant, σ the surface tension, h_{fg} is the latent heat of vaporization, and the constant C given with a value of 0.35. Further developments carried out by Berenson (1960) adjusted the expression as follows:

$$q_{MHF}^{B} = 0.09\rho_v h_{fg}\left(\frac{g\,(\rho_l - \rho_v)}{\rho_l + \rho_v}\right)^{1/2}\left(\frac{\sigma}{g(\rho_l - \rho_v)}\right)^{1/4} \tag{1.10}$$

More recently, a mechanistic model was developed under saturated pool boiling while considering the decrease in the vapor blanket on the surface as time progresses. Such decrease is caused by the combined effects of the phase change at the liquid-vapor interface, and the subsequent release of vapor due to instabilities along the vapor peaks (Cai, Mudawar & Liu, 2020). Thus, q_{MHF}^{C} is given as:

$$q_{MHF}^{C} = 0.01947\left(\frac{\rho_l}{\rho_v}\right)^{-0.2029}\rho_v h_{fg}\left(\frac{\sigma g(\rho_l - \rho_v)}{\rho_v^2}\right)^{1/4} \tag{1.11}$$

1.3.1.2 Minimum Heat Flux Temperature

Point C in Figure 1.5 can also be associated to the temperature value at which q_{MHF} occurs, labelled herein as T_{MHF}. In fact, it has been argued that temperatures reported in the literature for similar conditions are often more consistent than values of q_{MHF} (Cai et al., 2020). Prediction models for T_{MHF} can be traced to the works of (Berenson, 1961) who derived the following expression:

$$T_{MHF}^{B} = T_{sat} + 0.127\frac{\rho_v h_{fg}}{k_v}\left(\frac{g\,(\rho_l - \rho_v)}{\rho_l + \rho_v}\right)^{\frac{2}{3}}\left(\frac{\sigma}{g(\rho_l - \rho_v)}\right)^{\frac{1}{2}}\left(\frac{\mu_v}{g(\rho_l - \rho_v)}\right)^{\frac{1}{2}} \tag{1.12}$$

Where k_v is the thermal conductivity of the vapor, and μ_v is the vapor viscosity. Berenson's model has been modified to account for the transient phenomena of wetting the heated wall surface by the liquid, which then leads to evaporation of the microlayer (Henry, 1974). Thus, Henry's model, which was fitted to pool quenching data for different fluids (water, n-pentane, ethanol), is given as the following expression:

$$T_{MHF}^{H} = T_{MHF}^{B} + 0.42(T_{MHF}^{B} - T_l)\left[\left(\frac{\beta_l}{\beta_w}\right)^{\frac{1}{2}} \frac{h_{fg}}{c_{p,w}(T_{MHF}^{B} - T_{sat})}\right]^{0.6} \tag{1.13}$$

Where β is the thermal effusivity computed as the product between conductivity, density and specific heat capacity ($\beta = k\rho c_p$). This represents the ratio between liquid (β_l) and material of the wall (β_w) which postulates that conduction drives the thermal gradient occurring during the transient wetting.

Further correlations have been developed based on Berenson's and Henry's work. For instance, the influence of roughness was considered by adding a ratio of surface roughness and adjusting the constants of the right-hand side terms in Eq. 1.13 (Peterson & Bajorek; 2022). Alternatively, (Cai et al., 2020) developed a correlation that considers the Nusselt number to predict T_{MHF}^{C}, given as:

$$T_{MHF}^{C} = T_{sat} + 0.1223\left(\frac{\rho_l}{\rho_v}\right)^{-0.2029} \frac{\rho_v h_{fg}}{Nu_v k_v}\left(\frac{\sigma^3}{g\rho_v^2(\rho_l - \rho_v)}\right)^{\frac{1}{4}} \tag{1.14}$$

An overview of different correlations to predict T_{MHF} can be found in the works of (Darr et al., 2019), and physics informed neural networks (Kim, Hurley & Duarte, 2022). Experimental work on film boiling and vapor collapse on different geometries and surfaces reported that a decrease in the surface superheat decreases the surface heat fluxes and vapor film thickness for all geometries alike (plate, spheres). Bath temperature (water) strongly influences the heat transfer coefficient and heat flux during film boiling (Jouhara & Axcell, 2009).

1.3.1.3 Film Boiling HTC

Classic literature on film boiling include analytical expressions to estimate the heat transfer coefficients during film boiling (h_{FB}). Berenson (1961) investigated film boiling on a horizontal flat surface considering the phenomena as a hydrodynamic instability problem driven by Taylor's instability of the liquid-vapor interface. Such an approach yields the following relation of the heat transfer coefficient during film boiling (Berenson, 1961):

$$h_{FB}^{Ber} = 0.425\left(\frac{k_v^3\,\rho_v\,g\,(\rho_l-\rho_v)h_{fg}{}'}{\mu_v\,\Delta T_{sat}\,\lambda_c}\right)^{1/4} \tag{1.15}$$

Where k_v is the thermal conductivity of vapor, $\rho_{l,v}$ is the density of liquid and vapor, g the gravitational constant, μ_v represents the dynamic viscosity of vapor, ΔT_{sat} accounts for the overheat temperature ($\Delta T_{sat} = T_{bulk} - T_{sat}$), and λ_c is the critical wavelength, defined as:

$$\lambda_c = \left(\frac{\sigma}{g(\rho_l-\rho_v)}\right)^{1/2} \tag{1.16}$$

Thus, λ_c is given by the relation of surface tension (σ), and densities ($\rho_{l,v}$). In Eq. 1.15, $h_{fg}{}'$ can be defined as:

$$h_{fg}' = h_{fg} + 0.5\,c_{pv}\Delta T_{sat} \tag{1.17}$$

Where c_{pv} is the specific heat at constant pressure of the vapor and h_{fg} the latent heat of vaporization. Interestingly, the relation proposed by Berenson is comparable to the one developed by Bromley (1949) who defined the heat transfer coefficient for film boiling on a horizontal cylinder as:

$$h_{FB}^{Brom} = 0.62\left(\frac{k_v^3\,\rho_v\,g\,(\rho_l-\rho_v)h_{fg}{}'}{\mu_v\,\Delta T_{sat}\,D}\right)^{1/4} \tag{1.18}$$

One must note that Berenson and Bromley relations differ on the magnitude of their constants (0.425 and 0.62) and the replacing the critical wavelength (λ_c) by the cylinder diameter (D) on Bromley's definition. Further studies by Breen & Westwater (1962) revealed the limitation of Bromley's relationship when predicting HTC for cylinders with very large and very small diameters. Thus, a relationship was proposed by assuming the solution should approach that of Berenson (Nelson & Pasamehmetoglu, 1992):

$$h_{FB}^{B\&W} = \left(\frac{0.59-0.69\,\lambda_c}{D}\right)\left(\frac{k_v^3\,\rho_v\,g\,(\rho_l-\rho_v)h_{fg}{}'}{\mu_v\,\Delta T_{sat}\,\lambda_c}\right)^{1/4} \tag{1.19}$$

One must note that the relations outlined in Eq. 1.15, Eq. 1.18, and Eq. 1.19 for h_{FB}, as well as those to predict q_{MHF}, T_{MHF} rely on the physical properties of the liquid and its vapor. Such approach presents an additional challenge when the properties of the quenchant, in both of their phases, are unknown.

1.3.1.4 Wetting Front

The moment when the vapor blanket "collapses" during quenching is often referred as "quench", "re-wetting" or "wetting" front (Nelson & Pasamehmetoglu, 1992). It represents the end of film boiling, but it does not occur at the same instance in time on the entire surface. This has been demonstrated for standard specimens (Ramesh & Prabhu, 2014a) and is especially true for large components subject to immersion processes as the lower end starts to cool down before the upper portion of the specimen. Hence, different cooling regimes may coexist at the same time along the surface of the specimen as represented in Figure 1.6.

Experimental studies explored the evolution of the wetting front on a conical-end probe (Cruces-Resendez, Hernandez-Morales & Guzman, 2021). The velocity of the wetting front increases when the start temperature of the specimen decreases as well as at higher free-stream water velocity. The dependency of the wetting front velocity on surface temperature was also reported for hollow cylinders (Frerichs & Luebben, 2009).

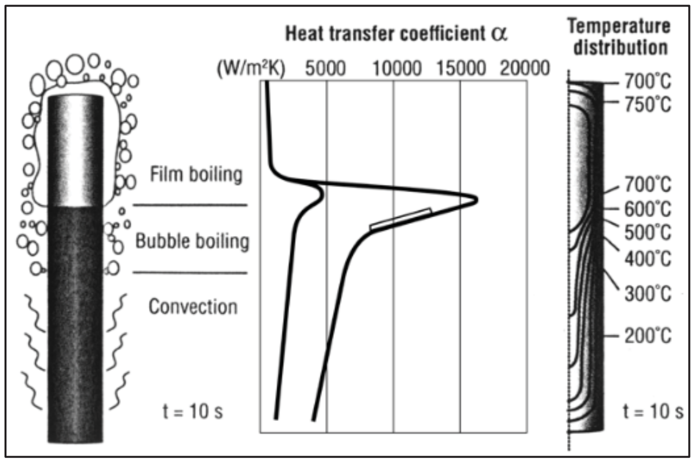

Figure 1.6 Simultaneous appearance of the different heat transfer mechanisms during quenching
Extracted from Liscic & Singer (2014, p. 127)

1.3.2 Transition Boiling

The transition boiling regime exists between points B and C in Figure 1.5. Contrary to film boiling that is often represented by steady-state correlations, transition boiling and the subsequent summit are transient-dependent (Nelson & Pasamehmetoglu, 1992). Due to its strong unsteadiness, this regime has received little attention compared to the other cooling regimes but has been investigated using transient calorimeter or quenching techniques. Interestingly, transition boiling curves follow different routes for heating or cooling processes (Ghiaasian, 2017; Monde, Liu, Mitsutake & Zin, 2006; Ungar & Eichhorn, 1996) as was experimentally confirmed for methanol under saturated pool boiling conditions by (Ungar & Eichhorn, 1996) as shown in Figure 1.7.

From Figure 1.7, the curve with decreasing temperature has lower fluxes than the ones with increasing temperatures. The reason for such variation has been attributed to the role of surface tension in expanding (heating) and retreating (cooling) processes (Witte & Lienhard, 1982) or the associated heat capacity of the heated solid (Monde et al., 2006). Note that the term “film transition boiling”, first introduced by (Witte & Lienhard, 1982), is used to refer to the transition from film boiling to nucleate boiling on a cooling process. Then, when the boiling curve follows a heating process, it is referred to as “nucleate transition boiling”. As this study is solely focused on a quenching process where no heating exists, the term transition boiling is used for this regime in this document.

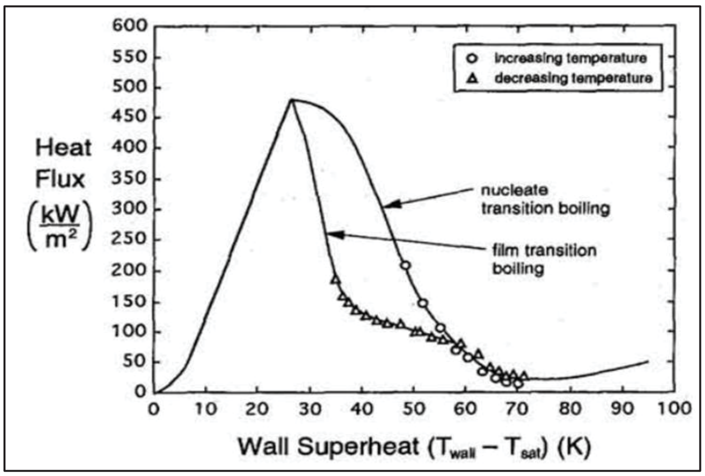

Figure 1.7 Transition boiling curves for saturated methanol for heating and cooling processes
Adapted from Ungar & Eichhorn (1996, p. 660)

The end of the transition boiling regime, associated with point B in Figure 1.5, has been the center of discussion, as some authors have reported that its magnitude is consistent for heating and cooling processes alike (Ungar & Eichhorn, 1996), whereas others have reported that the maximum heat flux is lower in magnitude for cooling processes (Monde et al., 2006). The latter have associated that the value of the heat flux is dominated by the ability of the solid to supply heat to the liquid during cooling. Furthermore, experimental testing under subcooling conditions indicates that the heat flux in the transition boiling regime increases with the degree of subcooling (Monde et al., 2006).

For quenching operations, it was demonstrated that the starting temperature of the specimen decreases the magnitude of the surface heat flux during transient boiling for quenching in subcooled water processes (Lu, Bourouga & Ding, 2013). Note that there is no general theory to model the surface heat flux during transition boiling (q_{TB}). Thus, models often rely on linear interpolation between the two reference points (q_{MHF} and q_{CHF}) delimiting transition boiling on the boiling curve, labelled as points B and C in Figure 1.5. One of such proposals is expressed as (Kolev, 2007):

$$q_{TB}^{Kol} = q_{MHF}\left(\frac{q_{CHF}}{q_{MHF}}\right)^{m_{TB}} \tag{1.20}$$

Where the parameter m_{TB} is given by the following relation:

$$m_{TB} = \frac{\ln\left(\Delta T_{MHF}/\Delta T_w\right)}{\ln\left(\Delta T_{MHF}/\Delta T_{CHF}\right)} \tag{1.21}$$

In Eq. 1.21, ΔT_{MHF} and ΔT_{CHF} are the difference between surface temperature and the reference flux, either q_{MHF} or q_{CHF} respectively, and ΔT_w is the difference between wall temperature and the saturation temperature of the fluid.

Interestingly, such approach of utilizing linear interpolation between the reference fluxes is applied on commercial CFD software, such as AVL Fire (Kopun, Skerget et all., 2014; Kopun, Zhang, et al., 2014), where the flux during transition boiling is computed as:

$$q_{TB}^{Kop} = q_{CHF}\Psi_{TB}+q_{MHF}(1-\Psi_{\mathrm{TB}}) \tag{1.22}$$

Where Ψ_{TB} is a weighting parameter given as:

$$\Psi_{\mathrm{TB}} = \psi_{tb}\frac{T_{CHF}}{T_w - T_{CHF}} \tag{1.23}$$

Where T_{CHF} is the critical heat flux temperature, ψ_{tb} represents the probability of vapor collapse when switching from film boiling to transition boiling, defined as the wetting parameter that varies between 0.1 to 0.6 (Srinivasan, Moon, Greif, Wang & Kim, 2010). Thereby, modeling of the transition boiling heat flux relies on the definition of the reference fluxes and their corresponding temperatures.

1.3.3 Nucleate Boiling

The subsequent cooling regime after transition boiling, for a cooling process, is nucleate boiling. This regime is encompassed between points A & B in Figure 1.5, known as the Onset of Nucleate Boiling (ONB) and Critical Heat Flux (CHF) respectively. This cooling regime, although widely study in the literature, presents a challenging and complex phenomena where heat is being removed from the surface by a combination of vapor and bubbles (Unal, Daw & Nelson, 1992). Thus, boiling is characterized by the formation of vapor bubbles, its grown and detachment from the surface. Classic literature further subdivides nucleate boiling into subregions referred as: incipient boiling, discrete bubble region, first transition region (where vapor jets appear), vapor mushroom region, until reaching the CHF (Unal et al., 1992) as shown in Figure 1.8.

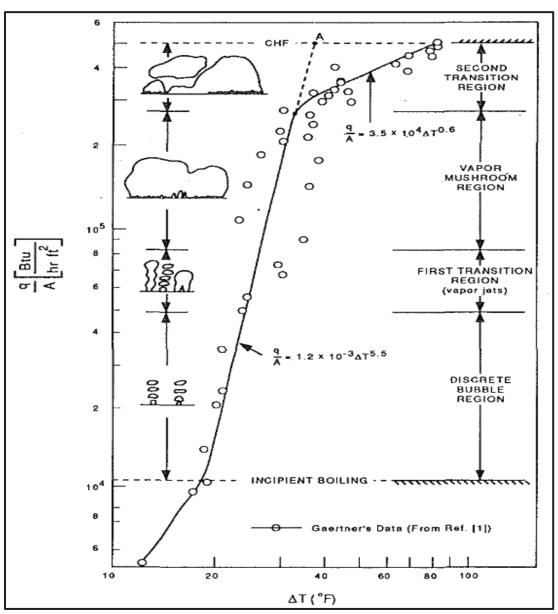

Figure 1.8 Subdivision of boiling regions for water boiling
Extracted from Gaertner (1965, p.20)

The boiling subregions shown in Figure 1.8 were observed under saturated conditions, when the temperature is controlled and progressively increased, and the resulting heat flux is the independent variable (Faghri & Zhang, 2020). However, quenching operations involve a cooling process where the surface temperature decreases, thus the subregions appear in reverse order. Nonetheless, the evolution of these subregions has been considered as secondary in relevancy during quenching, as the predominant rapid cooling steep occurs during transition boiling, the previous cooling regime, while the contribution of nucleate boiling takes effect when the wall superheat is of the order of 30K to 40K (Srinivasan et al., 2010).

The magnitude of the heat flux rapidly increases with the excess temperature (ΔT_e) during boiling, as shown in Figure 1.8. The most common expression to compute the heat flux during this condition is the correlation developed by (Rohsenow, 1952), which can be written as:

$$q_{NB}^{R} = \mu_l h_{fg} \left[\frac{g(\rho_l - \rho_v)}{\sigma}\right]^{0.5} \left(\frac{C_{p,l}(\Delta T_e)}{C_{sf} h_{fg} Pr_l^n}\right)^3 \tag{1.24}$$

For which the constant C_{sf} and exponent n depend on the liquid-surface combination, often given in textbook tables (Bergman et al., 2011; Faghri & Zhang, 2020) while the liquid properties should be evaluated at saturation temperature. Clearly, the expression in Eq. 1.24 does not account for shape nor orientation, while also limited to clean surfaces and may lead to high errors (up to $\pm 100\%$). Thus, it is recommended to use such relation at low excess temperatures ($\Delta T_e < 10°C$) (Bergman et al., 2011).

During nucleate quenching, heat exchange is influenced by various bubble dynamic parameters (i.e., bubble departure diameter, nucleation site density, bubble growth rate, bubble departure frequency). A review of different correlation models accounting for the influence of these parameters on the heat flux and heat transfer coefficient during nucleate boiling can be found in (Mohanty & Das, 2017). Note that to utilize those correlations, it is necessary to determine the thermophysical properties of the fluids, which are also needed to estimate the bubble dynamic parameters.

1.3.3.1 Critical Heat Flux

In applications such as design of heaters and boilers or nuclear reactors, knowledge of the critical heat flux (q_{CHF}) is critical as it denotes the operational limit before drastically leading to the burnout point. For transient cooling processes, such as quenching, q_{CHF} indicates the beginning of nucleate boiling. It has been reported that q_{CHF} obtained with a transient cooling technique (i.e. quenching) are likely to be lower than those obtained on steady-state condition (Katto, 1994). Due to its physical significance, q_{CHF} is often used as a parameter or reference when modeling transition boiling as explained in the previous subsection. There are multiple correlations in the literature that predict q_{CHF}. The models differ depending on the mechanism that produce the CHF. These are referred as hydrodynamic instability, macrolayer dryout, bubble interference, hot/dry spot, and interfacial lift-off (Fang & Dong, 2017; Liang & Mudawar, 2018).

Notably, most of the published work is founded on the hydrodynamic instability model proposed by Zuber (1959). The model states that the CHF occurs when vapor jets at the nodes of the Taylor waves exceed the velocity allowed by the Helmholtz instability (Zuber, 1959). Such phenomena prevent the liquid to move downwards towards the surface as the vapor is moving upwards, thus leading to the CHF. The initial relation proposed by Zuber to estimate q_{CHF}^{Z} is given as:

$$q_{CHF}^{Z} = K\rho_v h_{fg}\left(\frac{g\,(\rho_l-\rho_v)\sigma}{{\rho_v}^2}\right)^{\frac{1}{4}}\left(\frac{\rho_l}{\rho_l+\rho_v}\right)^{\frac{1}{2}} \tag{1.25}$$

Where the constant K is often reported in the literature as 0.131. Modifications to Zuber's constant are commonly encountered to account for some parametric effects.

Other models such as "macrolayer dryout" postulate that CHF is triggered by the drying of the film beneath large mushrooms shapes bubbles, just before the departure of coalesce bubbles

(Haramura & Katto, 1983). Yet, the macrolayer dryout model to predict q_{CHF}^{HK} can be considered as a refinement of Zuber's relation, as q_{CHF}^{HK} can be expressed as:

$$\frac{q_{CHF}^{HK}}{q_{CHF}^{Z}} = 5.5\left(\frac{A_g}{A_w}\right)^{\frac{5}{8}}\left(1-\frac{A_g}{A_w}\right)^{5/16}\left[\left(\frac{\rho_l}{\rho_g}+1\right)/\left(\frac{11\rho_l}{16\rho_g}+1\right)^{3/5}\right]^{5/16} \tag{1.26}$$

Where:

$$\frac{A_g}{A_w} = 0.0584\left(\frac{\rho_g}{\rho_l}\right)^{1/5} \tag{1.27}$$

The estimation of the thickness of the macrolayer has produced multiple iterations of this strategy, yet it remains one of the major uncertainties of this method (Fang & Dong, 2017).

The remaining models consider different mechanisms that cause the CHF. The bubble interference models postulate that CHF occurs when bubbles coalesce radially given high departure frequency and bubble number at high superheats, thus preventing the liquid from reaching the surface inducing CHF (Rohsenow & Griffith, 1955). The hot/dry spots model considers the irreversible growth of the dry spot area on the surface, as there is no rewetting of the surface after the bubble departure, which then leads to CHF. Whereas the lift/off mechanism (Galloway & Mudawar, 1993) postulates that the vapor momentum will become strong enough to lift off the liquid from the surface. The formulation can be simplified to an expression close to Zuber's model with an adapted value for the constant K for saturated conditions.

1.3.3.2 Parametric Effects on CHF

Multiple studies aim to improve the predictive capability of Zuber's model by accounting for parametric effects. For instance, Zuber's expression (Eq. 1.25) is independent of surface conditions, although the influence of certain variables such as contact angle and roughness on

q_{CHF} has been debated over decades. It has been reported that better wettability, by means of smaller contact angles, leads to smaller bubble departure diameter and higher departure frequency, thus increasing the heat exchange and leading to higher HTC for the same excess temperature (Ghiaasiaan, 2017).

Surface roughness is reported to have a positive impact on the heat extraction during nucleate boiling. Bubble diameter, departure frequency, and active site density are affected by surface roughness (McHale & Garimella, 2010). Even q_{CHF} has been reported to increase in rough surfaces as per (Kim, Jun, Laksnarain & You, 2016). They developed a proposal to account for roughness (R_a) and contact angle (Φ) while considering the mean spacing between roughness peaks (S_m), thus adjusting the constant K in Eq. 1.25 as follows:

$$K^{Kim} = 0.811\left(\frac{1+cos\Phi}{16}\right)\left(\frac{2}{\pi}+\frac{\pi}{4}(1+cos\Phi)+\frac{351.2cos\Phi}{1+cos\Phi}\left(\frac{R_a}{S_m}\right)\right)^{\frac{1}{2}} \quad (1.28)$$

q_{CHF} is also affected by operating pressure, especially when reduced considerably with regards to atmospheric conditions as the vapor specific volume increases significantly. Although this variable is of interest for systems whose operating pressure can be adjusted, not the case for immersion quenching, it is relevant to note that correlations in the literature still rely on adjusting the constant K in Eq. 1.22 as proposed by (Wang, Li, Zhang, Xie & Ma, 2016), to account for its effects as follows:

$$K^{W} = 0.18 - 0.14\left(\frac{P}{P_c}\right)^{5.68} \quad (1.29)$$

Nucleate boiling can be affected by the orientation of the surface with regards to the fluid, a common case encountered in industrial workpieces. Findings in the literature indicate that pool boiling decreases as the specimen goes from a vertical setup towards a horizontal downward facing surface as shown in Figure 1.9. Adjustments to the constant K in Zubber's expression have been made to account for the influence of orientation, as reported by (Liang & Mudawar, 2018). Yet, it has been suggested that there are at least three different pool boiling regions depending on the vapor behavior just before q_{CHF}: downward facing, near-vertical, and upward facing (Howard & Mudawar, 1999) concluding that a single overall pool boiling model cannot account for all the influence of heaters surface orientation under saturated conditions (Howard & Mudawar, 1999).

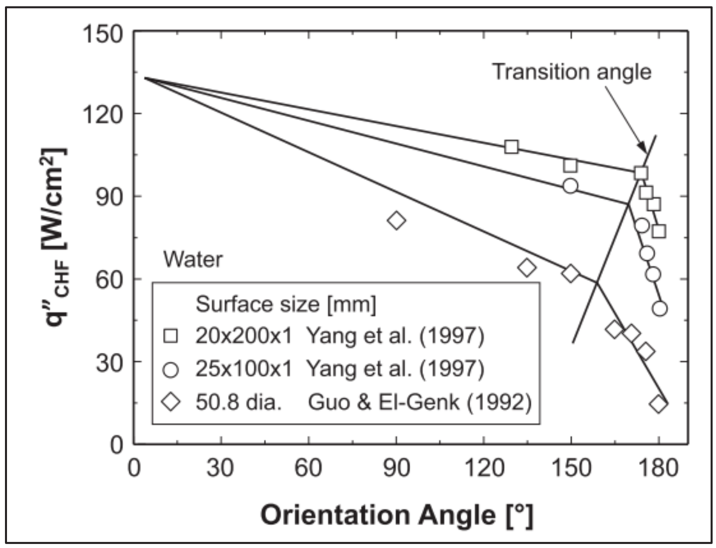

Figure 1.9 Effect of orientation on critical heat flux
Adapted from Yang, Baek & Chang (1997, p. 1097)

The influence of subcooling on the CHF has been reported for horizontal and vertical small tubes (Pattanayak & Kothadia, 2022). A decrease in the pool temperature increases the CHF regardless of configuration and specimen size. A similar behavior was reported for transient cooling of cylindrical bodies (Zabirov et al., 2021). A strategy to account for the subcooling temperature is given as (Hua & Xu, 2000):

$$\frac{q_{CHF,sub}}{q_{CHF,sat}} = 1 + K_{sub}\, Ja/\, Pe^{1/4} \tag{1.30}$$

Where Ja and Pe are the Jacob and Peclet numbers given by:

$$Ja = \frac{\rho_l C_p \Delta T_{sub}}{\rho_v h_{fg}} \tag{1.31}$$

$$Pe = \frac{\sigma^{3/4}}{\alpha_v[g\ (\rho_l - \rho_v)]^{1/4}\rho_v^{1/2}} \tag{1.32}$$

Note that the constant K_{sub} in Eq. 1.30 is given as 0.345 (Hua & Xu, 2000), although other studies have reported a different value ($K_{sub} = 4.28$) based on experimental results (Elkassabgi & Lienhard, 1988).

1.3.4 Convection

The final cooling regime of quenching is convection, which is often studied as either forced convection or natural convection. The former refers to conditions where fluid flow is induced by external means such as fans, the latter is caused by buoyancy forces on the fluid. This is caused by the density gradients in the liquid heated by the quenched surface (Lienhard V & Lienhard IV, 2024).

During quenching, the convective regime typically has the lowest heat extraction rates, especially for natural convection as its efficiency depends on the thermo-physical properties of the fluid, and the temperature gradient between surface and bath. The local heat transfer coefficient during natural convection ($\overline{h_{c,n}}$) can be expressed as (Lienhard V & Lienhard IV, 2024):

$$\overline{h_{c,n}} = \overline{Nu_l}k/L \tag{1.33}$$

Where k and L are the thermal conductivity of the fluid and characteristic length respectively, while Nu_l is the local Nusselt number given by the expression developed by (Churchill & Chu, 1975) as:

$$\overline{Nu_l} = \left[0.825 + \frac{0.387Ra^{1/6}}{[1 + (0.492/Pr)^{9/16}]^{8/27}}\right]^2 \tag{1.34}$$

Where Ra is the Rayleigh number and Pr the Prandtl number given as:

$$Ra = \frac{g\beta\Delta T_{wf}L^3}{\nu\alpha} \tag{1.35}$$

$$Pr = \nu/\alpha \tag{1.36}$$

Where β represents the thermal coefficient of expansion, ν is the kinematic viscosity, α is the thermal diffusivity, g is the gravity, and ΔT_{wf} is the difference in temperature between wall and fluid. The above formulations can be used to approximate the heat transfer coefficient even if the surface temperature slightly exceeds the saturation temperature of the liquid, just below the bubble inception point during pool boiling (Lienhard V & Lienhard IV, 2024). This can be schematically illustrated in Figure 1.5, the reference point A indicates the end of the convection domain and the beginning of boiling, with nucleation and slight superheating exceeding the saturation temperature.

1.3.5 Remarks on the Boiling Curve

Modeling the boiling curve for quenching remains a scientific challenge as the available formulations present certain limitations. The above correlations are applicable to restricted domains for certain canonical geometries (sphere, cylinder, plate), specific surface conditions, orientations, and testing conditions. Moreover, the applicability of such models is still an open question as most of the correlations were obtained for pool boiling, steady state conditions. As outlined, there is a general understanding that transient cooling testing, i.e. quenching, leads to different boiling curves than those obtained with the reference conditions.

Furthermore, the thermophysical properties of the quenchant in its liquid and gaseous phases are necessary to utilize the above correlations. In fact, some of the previously mentioned constants still need to be experimentally identified as for the case under study there is no access to the quenchant's thermophysical properties. Even so, this would still be insufficient to fully plot the boiling curve, particularly the nucleated portion.

Alternatively, it is possible to identify the BCs in the form of surface heat fluxes or heat transfer coefficients by characterizing the quenching process and then solving the inverse heat transfer problem. This approach should provide an insight into the actual conditions of the process, meaning that the heterogeneities of the process should be captured during the experimental characterization.

As is presented in the next section, multiple researchers have successfully identified the evolution of the thermal BCs using different geometries of instrumented metallic bodies, also referred as quench probes. This approach comes with additional challenges in terms of sizing of the quench probes, instrumentation strategies, test conditions, as well as methods to solve the inverse problem, which will be addressed further on.

1.4 Quench Probes

The simplest quenching probe can be conceived as a metal part instrumented with a sensor measuring its internal temperature as shown in Figure 1.10. Experimentally acquired cooling curves provide insight into the cooling characteristics of the quenching medium and the working environment. In fact, acquisition of the cooling curve using in-body measurements has been an integral part of the standard procedures to evaluate the quenchant capabilities. However, the dimensions of the quench probe, material, and instrumentation strategy can vary widely. Even the simplest geometry (i.e. plate) can be instrumented in multiple configurations depending on the case of study: 1D or 2D case (Wallis, 2010), hence requiring special attention.

Utilizing quench probes to obtain internal measurements prevents the fin cooling effect on surface-mounted sensors. Such phenomena lead to lower temperature readings than the actual values at the base material of the specimen while typically presenting strong disturbances (oscillations) that require compensation methods (Tszeng & Saraf, 2003). Moreover, quench probes have the advantage to directly quantify the heat flux at the solid-liquid interface, making it possible to inverse identify surface heat flux and HTC to feed the thermal-metallurgical-mechanical simulation (Wallis, 2010).

This section discusses the following types of probes: standard probes, modified standard probes and non-standard quench probes. Standard probes are introduced first, including the most common standards around the world used to obtain cooling curves. It is followed by a discussion on the studies that use quench probes similar in dimensions to standard specimens but made of different materials while considering alternative instrumentation strategies. Lastly, the discussion is centered on quench probes that have been developed with the sole purpose of characterizing industrial processes.

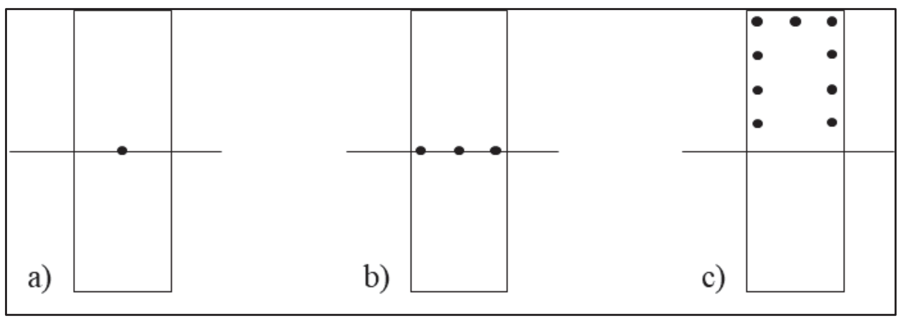

Figure 1.10 Typical thermocouple arrangement for a) single thermocouple, b) multiple thermocouples for 1D case, and c) 2D

1.4.1 Standard Probes

There are several testing standards, which require a "quench probe", published by different entities all over the world, as summarized in Table 1-1. The relevancy of any standard method can not be neglected; they are extremely useful for comparison and quality purposes among different quenchants. These standards consider high conductivity materials and small quench probes (see Table 1-1). Such characteristics lead to assuming a lumped condition in the quench probe, thus neglecting the thermal resistance through the body while recording the thermal history at one measurement point at the geometrical center of the specimen.

Standard procedures are far from truly characterizing the boundary conditions on real workpieces. The material and size of the specimen are likely to differ from standard procedures; these factors influence the internal thermal resistance and temperature gradients inside the specimen as well as the boundary conditions on the surface. Similarly, standard procedures define reference temperatures for both specimen and bath while enforcing immediate immersion on the bath. These factors might differ on real-life operations and require special attention to truly capture their influence during quenching. Nevertheless, standard procedures provide the basis of multiple works that rely on the standard probes as their primary specimen attesting their relevancy as exploratory means, as will be described in the next subsection. One must note that the industrial partner continuously performs testing as per standard procedure (ASTM D 6200) to record the characteristic cooling curve, such results are considered as baseline cooling curve in this study.

Table 1-1 Summary of standard procedures (Liscic & Singer, 2014)

Standard	**Material**	**Size [mm]**	**Instrumentation**	**Temp [°C]**
ISO 9950 (International)	Alloy 600 [a]	Ø12.5 x 60 [a]	1 TC at geometrical center	Probe: 850±5 Bath: 40±2
JIS K 2242 (Japan)	Silver 99.999%	Ø10 x30	1 TC inserted laterally at half length	Probe: 810±5 Bath: 80, 120, 160
SH/T0220-92 (China)	Silver 99.999%	Ø10 x 30	1 TC at geometrical center	Probe: 810±5 Bath: 80±2
[a] Similar probe used in American Standards for Testing and Materials (ASTM) ASTM D 6200, ASTM D 6482-6, ASTM D 6549-06 and ASTM D 7642-10				

1.4.2 Modified Standard Probes

Using modified standard probes is a common practice among researchers as the data can be compared directly against standard procedures. This section discusses the benefits and limitations of such practice based on multiple authors that have explored different instrumentation strategies, specimen material, start temperature, and even geometrical modifications of the standardized cylindrical quench probe. A list of the works using a modified standard cylindrical probe (Ø12.7 mm) are included in Table 1-2.

The instrumentation strategies vary widely between studies as the number of sensors, and their placement is mainly driven by the author's rationale. Hence, the number of combinations is almost limitless. However, two main instrumentation strategies can be distinguished, either additional sensors are placed along the axis of the cylinder at different depths, or along the same radius line while maintaining a sensor at the center of the specimen (see Figure 1.11).

The first instrumentation strategy (i.e., sensors at varying depths) explores the rewetting kinematics along the length of the specimen, thus identifying the different time and temperature when the film boiling ends and gives places to nucleate boiling at different stations depth wise of the specimen. It was found that transition from film boiling to nucleate boiling does not occur at the same time everywhere (Ramesh & Prabhu, 2014b; Samuel & Prabhu, 2022a). The second instrumentation strategy (i.e., multiple sensors along the same radius line) captures the temperature gradient across the specimen thickness (Cruces-Resendiz et al., 2021). A common finding was the difference in temperature between core and subsurface measurements even when using such relatively small specimens (Ø12.7 mm) as reported by (Hernandez-Morales, Cruces-Resendez & Duran-Garcia, 2025; Ramesh & Prabhu, 2014b)

A major takeaway from the different studies is the common understanding of placing at least one sensor as close as possible to the main surface of exchange. This allows the experimental results, in the form of cooling curves, to better represent the thermal history and phenomena occurring at the surface as readings in the center of the specimen will present an inherent delay in time when compared to the surface. Note that there is no clear standard value for the subsurface distance (γ), although a value of 2 mm appears often among researchers using this type of specimens (see Table 1-2).

Most of the authors aim for material without phase transformation. Thus, the inverse problem can be solved without the added complexity of the phase transformation of the material. Several studies have used steel made specimens (see Table 1-2) aiming to better represent the type of material under real life operations rather than high conductivity materials from standard procedures.

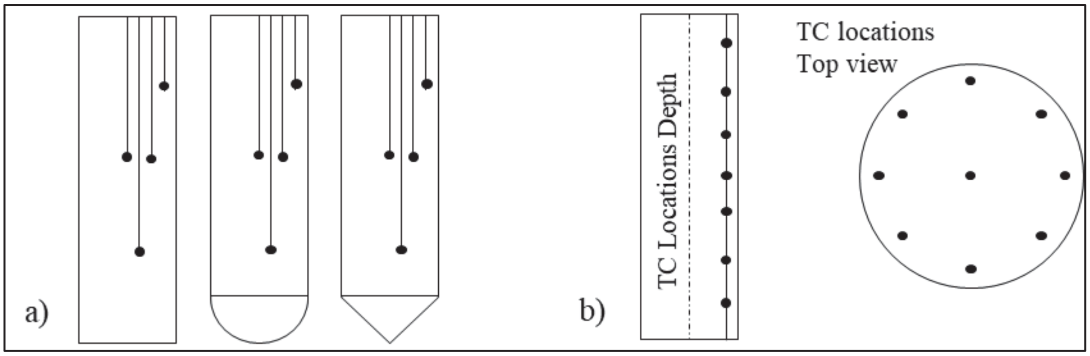

Figure 1.11 Modified standard quench probes a) Probes with different end geometry
Modified and redrawn from Hernandez-Morales et al. (2025, p. 148)
b) Instrumentation for axial and radial assessment
Modified and redraw from Ramesh & Prabhu (2014a, p. 436)

Studies addressing the start temperature of the specimen indicate that the peak surface heat flux decreases in magnitude and appears at lower temperatures when lowering down the start temperature (Hernandez-Morales, Lopez-Sosa & Cabrera-Herrera, 2012). These results are consistent even when using different specimens: IVF probe and CHTE probe, with a single sensor in the core of the specimen (Maniruzzaman, Dai & Sisson, 2012). Furthermore, a linear relation between HTC peak as a function of soak temperature has been developed confirming the strong correlation relation between these variables when using small quench probes (Maniruzzaman et al., 2012).

The influence of the end-geometry of the quench probe has been explored using different designs: flat, conical, and hemispherical, as shown in Figure 1.11 (Hernandez-Morales, Cruces-Resendez & Tellez-Martinez, 2019; Hernandez-Morales et al., 2025). Their findings demonstrate the impact of such feature on the thermal history of small specimens whose length is roughly about 50 mm (see Table 1-2). For instance, the flat-end probe induces a more prolonged film boiling stage than the other geometries. Similarly, cooling rates were reported to be lesser in magnitude for the flat-end geometry when compared to the other geometries.

Overall, modified standard probes have been extremely useful to obtain insightful information, yet they remain small in dimensions without accounting for any type of factors encounter under real life operations.

Table 1-2 Studies with quench probes similar to standard specimens to characterize immersion quenching

Author (s)	**Probe Body**[a]	**Instrumentation**[b]	**Quenchant**[c]	**Start Temp**
(Cruces-Resendez et al., 2021)	Cylinder with conical end Ø12.7 x 51 mm (plus cone) AISI 304SS	3 TCs, axially distributed along same radius $\gamma = 2.3;\ \varphi = 0.1$	Water at 60°C $\vartheta = 0.2, 0.6$	950°C and 850°C
(Hernandez-Morales et al., 2019)	Cylinders (conical and hemispherical end) Ø12.7 x 51 mm (plus cone /hemisphere) AISI 304SS	3 TCs, placed at tid-length, both core and subsurface $\gamma = 1.5$	Water at 60°C $\vartheta = 0.2, 0.6$	--
(Hernandez-Morales et al., 2025)	Cylinder (flat, conical, and hemispherical ends) Ø12.7 x 54.3 mm plus end geometry AISI 304SS	4 TCs, one at geometrical center, three axially distributed along same radius $\gamma = 2.3;\ \varphi = 0.1$	Water at 60°C $\vartheta = 0.2, 0.6$	850°C
(Maniruzzaman et al., 2012)	Cylinder IVF and CHTE probes Ø12.5 x 60 mm Ø9.5 x 38.1 mm INCONEL, SAE 4140	1 TC, only at geometrical center $\varphi = 0.02$	Mineral oil	IVF: 850°C to 450°C CHTE: 900 °C to 400°C
(Ramesh & Prabhu, 2014a)	Cylinders Ø12.5 x 60 mm Inconel 600	9 TCs, one specimen with TCs axially distributed and one radially $\gamma = 2;\ \varphi = 0.1$	Mineral oil	850°C
(Samuel & Prabhu, 2022a)	Cylinder Ø12.5 x 60 mm Inconel 600	5 TCs, distributed axially and geometrical centre $\gamma = 2;\ \varphi = 0.1$	Oils at 30°C	860°C

[a] Probe geometry dimensions $[mm]$ and material
[b] Instrumentation strategy, distance to surface (γ, $[mm]$), and acquisition frequency (φ, $[s]$)
[c] Quenchant type, temperature [°C] and flow velocity (ϑ, $[m/s]$)

1.4.3 Non-Standard Quench Probes

This section discusses the implementation of non-standard quench probes, i.e., specimens whose dimensions are bigger than those of standard specimens, as means to characterize quenchants. In this manner, some of the concerns due to the difference in mass between standard specimens and common workpieces are addressed. Thus, non-standard probes avoid cooling too quickly and higher heat extraction rates, the main drawbacks when using standard specimens (Liscic & Singer, 2013). Moreover, additional parameters of interest such as material and instrumentation strategies of the non-standard probes are discussed in this section. In theory these non-standard probes could potentially capture the heterogeneities of industrial-sized quenching bath, clearly a shortcoming of testing under laboratory conditions.

1.4.3.1 Cylindrical Non-Standard Quench Probes

One could argue that most non-standard quench probes follow a cylindrical geometry. Several studies evaluating immersion quenching with cylindrical probes are listed in Table 1-3. Arguably, the most well-known non-standard quench probe is the Liscic/Petrofer probe shown in Figure 1.12 (Liscic, 2016). Such specimen was designed to capture the thermal gradient along the thickness of the specimen under industrial conditions. In fact, the influence of probe size was explored by testing three different probe diameters while maintaining the same length over diameter ratio of 4. Interestingly, it was found that the HTC did change with the specimen diameter while the largest specimen did not present film boiling (Liscic, Singer & Beitz, 2011).

The influence of quench probe size has been reported to impact the peak HTC, as it decreases as the probe diameter increases (Behrem & Hrnjica, 2018). This is reflected in a decrement of the experimentally acquired maximum cooling rates. Notably, it has been reported that peak surface heat flux decrease and appear at lower temperatures as start soak temperature decreases, making film boiling become less notorious as start temperature decreases (Babu & Prasanna, 2010). These findings confirm the influence of both size and soak temperature during immersion quenching.

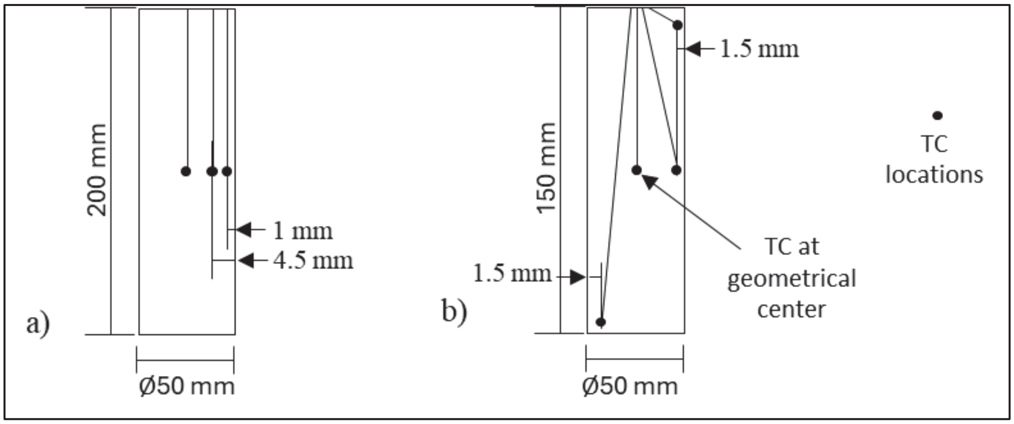

Figure 1.12 Schematic of non-standard cylindrical quench probes
a) Liscic-Petrofer quench probe
Modified and redrawn from Liscic (2016, p. 206)
b) Quench probe with multiple TCs along probe axis
Modified and redrawn from Behrem & Hrnjica (2018, p. 64)

Non-standard specimens can be used to explore process parameters such as quenchant velocity and bath temperature in addition to the specimen size (Ø25, 38 & 51mm) (Monroe & Bates, 1983). Their findings demonstrate that the maximum cooling rate at the core decreases as the specimen size increases. Moreover, they concluded that the quenchant flow velocity becomes more influential as the bath temperature increase for the largest probe (Ø51 mm). Furthermore, non-standard probes can be made of the same alloys as those used in the actual components while testing the quenchants in their on-site conditions (Prasanna Kumar et al., 2014).

Another relevant takeaway comes with the means to ensure the position of the sensor, techniques include the utilization of threated/taps to instrument the specimen (Monesh Kumar, Rahul, Sathyaseelan & Babu, 2023). Similarly, accurate enough results have been reported for subsurface sensors placed up to 4 mm off the surface (Prasanna Kumar et al., 2014). Although the consensus remains to place the subsurface sensor as close as possible to the surface.

Even though inverse methods are discussed in detail in the following section, many of the studies listed in Table 1-3 include their inverse methods to determine their BCs. Although, non-standard probes may require more complex methods to solve the inverse heat transfer problem than the standard specimens.

Table 1-3 Non-standard cylindrical quench probes studying immersion quenching

Author (s)	Probe Body[a]	Instrumentation[b]	Quenchant[c]	Start Temp
(Babu & Prasanna, 2010)	Ø20 x 50 mm 304L	2 TCs, mid-length, core and subsurface $\gamma = 2;\ \varphi = 0.1$	Water at 31°C	950°C to 400°C
(Behrem & Hrnjica, 2018)	Ø25 x 50 mm Ø50 x 150 mm Ø75 x 225 mm AISI 304	4 TCs, geometrical center & distributed along axis $\gamma = 1.5;\ \varphi = 0.5$	Water at 40°C	850°C
(Heming, Xieqing, & Jianbin, 2003)	Ø20 x 60 mm Ø40 x 120 mm Steel	2 TCs, Mid-length, core and subsurface $\gamma = 1$	Water at 20°C	850°C
(Liscic, 2016)	Ø50 x 200 mm Inconel-600	3 TCs, Mid-length, distributed along same radius $\gamma = 1;\ \varphi = 0.02$	Mineral oil at 28, 60°C Water at 22°C	850°C
(Liscic et al., 2011)	Ø20 x 80 mm Ø50 x 200 mm Ø80 x 320 mm Inconel-600	1 TC at mid-length subsurface $\gamma = 1$	Mineral oil at 50°C	850°C
(Monroe & Bates, 1983)	Ø25 x 100 mm Ø38 x 152 mm Ø51 x 204 mm AISI 304SS	1 TC at geometrical center	Oil at 30, 60 and 70°C	900°C
(Nayak & Prabhu, 2018)	Ø25 x 30 mm Ø50 x 30 mm 304SS	3TCs and 5TCs, mid-length distributed along same radius $\gamma = 1.5, 2;\ \varphi = 0.1$	Mineral, sunflower, karanja, and neem oil	860°C
(Prasanna Kumar et al., 2014)	Ø25 x 100 mm Steels: C45, 41Cr4, 100Cr6, 8822 H, SA 542, 52 100, 4140, SUP 9	1 TC at subsurface $\gamma = 4$	Oils (Castrol 798, Nippon 303) and Polymer solutions	850°C
(Sugianto, Narazaki, Kogawara & Shirayori, 2009)	Ø20 x 60 mm Steels: JIS SUS304 (AISI 304) and JIS S45C (AISI 1045)	6 TCs axially distributed (4 levels), radially (2 radii), and geometrical center $\gamma = 1;\ \varphi = 0.01$	Water $\vartheta = 0.3, 0.7$	850°C

[a] Probe dimensions $[mm]$ and material
[b] Instrumentation strategy, subsurface distance ($\gamma, [mm]$), acquisition frequency ($\varphi, [s]$)
[c] Quenchant type, temperature [°C] and flow velocity ($\vartheta, [m/s]$)

1.4.3.2 Other Non-Standard Quench Probes

A large group of non-standard quench probes have been developed to address other cooling processes such as spray quenching, gas quenching or even a different geometry other than a cylinder. A summary of these non-standard probes is presented in Table 1-4. Among the different geometries, researchers have opted to instrument geometries like plates, step plates, bars or rods.

Among the most innovative devices one can find the double-rod quench probe (Kim & Oh, 2001). This original device was made of two rods of the same length, one of which contained all the sensors mechanically installed on local groves as shown in Figure 1.13. Thus, the sensors were allocated at the mid-length of the specimen once assembled. The sensors provided the thermal history in the circumferential direction at a constant distance off the main surface of exchange. Although innovative, the proposal requires additional care on the installation, sealing and welding of the two rods, as well as the local perturbations of the thermal field are to be expected due to the direction of the sensors.

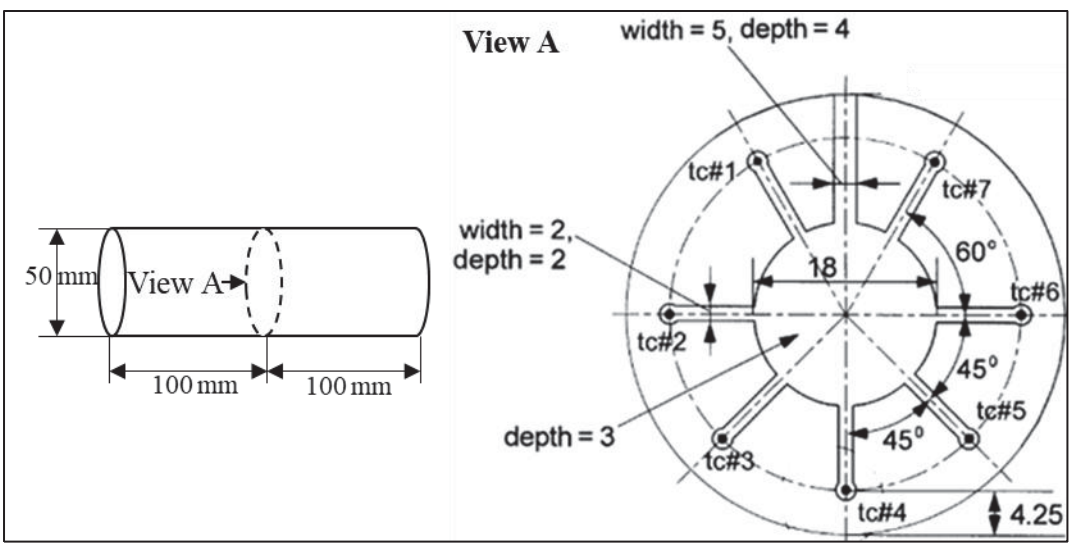

Figure 1.13 Schematic of double-rod quench probe
Modified and redrawn from Kim & Oh (2001, p. 160)

Alternative designs include a probe body with a blind hole to channel the sensors to a required depth as shown in Figure 1.14 (Ferguson, Li & Freborg, 2013). This design facilitates drilling as the actual depth of the hole for the sensors is reduced considerably. Moreover, it reduces the mass of the specimen when compared to a solid cylinder, which becomes practical when testing larger specimens. Such design allows for placing sensors at different positions in the axial and circumferential locations, it is also capable to be tested under industrial conditions (Ferguson et al., 2013).

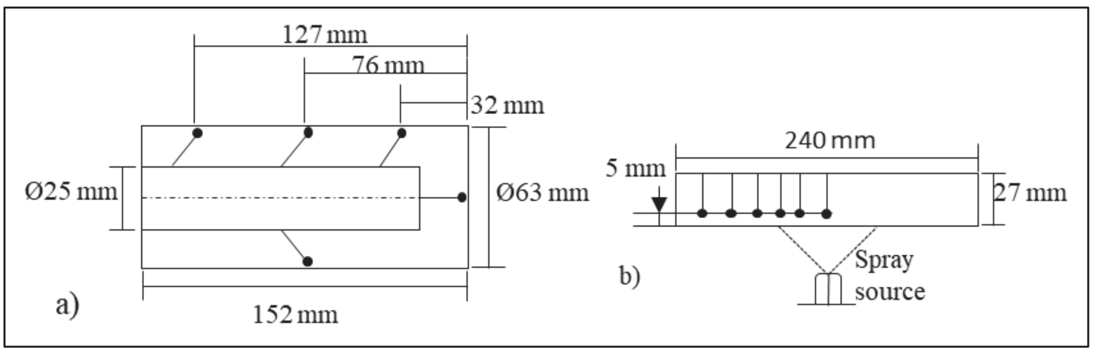

Figure 1.14 Schematic of non-standard quench probes a) Blind-hole quench probe
Modified and redrawn from Ferguson et al. (2013, p. 224)
b) Plate quench probe used to characterize spray quenching
Modified and redrawn from Fan et al. (2022, p. 3)

Studies on gas quenching have provided relevant information in the form of three criteria for heat transfer analysis: average cooling rate at different temperature range, cooling time every drop in 100°C and surface heat fluxes (Monesh Kuhmar et al., 2023). Moreover, an article presenting the recommendations of the German Research Committee for Quenching describes the following guidelines for determination of HTC during gas quenching (Luebben, Lohrmann, Segerberg & Sommer, 2009):

- A ratio of length to diameter of at least three (3).
- The hot junction of a thermocouple should be located, relative to the main heat exchange surface, at most, at a depth equivalent to one-tenth of the specimen radius.
- Use of transformation less materials, such as Inconel 600 or an austenitic stainless steel.
- Bores for the sensors should be parallel to the main heat exchange surface, which avoids disturbing the temperature field.

Table 1-4 Non-standard quench probes (multiple geometries) for quenching processes

Author (s)	Process	Probe[a]	Instrumentation[b]	Quenchant[c]	T_{start} [°C]
(Fan et al., 2022)	Spray quenching	Plate 240 x 240 x 27 mm Al 7055-H112	6 TCs distributed along plate axis. Drilled normal to surface of exchange $\gamma = 5$	Water at 25°C	450
(Ferguson et al., 2013)	Immersion	Bar Ø64 x 152 mm 304SS	5 TCs distributed axially and along circumference of the body $\varphi = 0.01$	Water $\vartheta = 6.6{,}7.2$	875
(Fernandes & Prabhu, 2007)	Lateral quenching	Cylinders Ø28 x 56 mm Ø44 x 88 mm AISI1040	2 TCs placed at mid-length, core and subsurface $\gamma = 2$	Brine, water, palm oil and mineral oil at 30°C	870
(Kim & Oh, 2001)	Immersion (transverse flow) & air quench	Rod Ø50 x 200 mm S45C - steel (AISI 1045)	7 TCs allocated at mid-length, distributed along the circumference $\gamma = 4.25;\ \varphi = 0.08$	Water and air (forced convection)	500
(Kopun et al., 2014)	Immersion	Step plate Variable thickness: 4 to 16 mm, 200 x 149 mm AlSi7MgCu0	3 TCs centred on surface, each one on three different steps	--	--
(Li, Wells, Cockcroft & Caron, 2007)	Spray quenching	Cylindrical plate Ø280 x 12.7 mm AISI 316	7 TCs placed along same diameter line. Drilled normal to the main surface $\gamma = 1;\ \varphi = 0.001$	Water at 15°C	1000 to 400
(Monesh Kumhar et al., 2023)	Gas quenching	Cylinder Ø20 x 50 mm 304SS	2 TCs placed on the same radius on opposite sides $\gamma = 2;\ \varphi = 0.1$	--	850

[a] Probe geometry, dimensions $[mm]$, and material
[b] Sensors strategy, distance to surface ($\gamma, [mm]$), and acquisition frequency ($\varphi, [s]$)
[c] Quenchant type, temperature [°C] and flow velocity ($\vartheta, [m/s]$)

Table 1 4 Non-standard quench probes (multiple geometries) for quenching processes (cont'd)

Author (s)	Process	Probe[a]	Instrumentation[b]	Quenchant[c]	T_{start} [°C]
(Xiong, Wang, Xiong, Lu & Yang, 2020)	Immersion	Rods (hemispherical end) Ø20 x 115 mm Fe25Cr5Al and Zircaloy-4	4 TCs axially distributed (4 levels), radially (2 radii), and geom center $\gamma = 1.5;\ \varphi = 0.02$	Water	600
(Yamada et al., 2010)	Immersion	Rods (hemispherical end) Ø32 x 48 mm Silver	1 TC at center $\varphi = 0.25$	Water at 70°C to 100°C	600

[a] Probe geometry, dimensions $[mm]$, and material
[b] Sensors strategy, distance to surface (γ, $[mm]$), and acquisition frequency (φ, $[s]$)
[c] Quenchant type, temperature [°C] and flow velocity (ϑ, $[m/s]$)

Research carried out on spray quenching differs on the geometry of the specimen itself as researchers often prefer a plate like geometry rather than a cylinder. Due to the nature of the process, local cooling by spray, the instrumentation leads to the sensors being installed normal to the main surface of exchange, as shown in Figure 1.14 (Fan et al., 2022; Li et al., 2007).

Previous studies have addressed the influence of start temperature for spray quenching, which has been reported to decrease peak heat fluxes as well as the film boiling. Interestingly, the slope of nucleate boiling regimes and convective boiling remain constant and independent of the soak temperature (Li et al., 2007). Notably, these studies address the influence of thermocouple installation on the thermal history, even suggesting a correcting methodology when the sensors are normal to the main surface of heat exchange (Caron, Wells & Li, 2006).

1.4.4 Remarks on Quench Probes

Cleary, there is a variety of research studies that have implemented quench probes to characterize quenchants and processes. The works cited in this section, summarized in Table

1.2 to Table 1.4, can be taken as reference to developing custom-made quench probes. The following remarks enclose the main takeaways based on those studies.

Firstly, the geometry and dimensions of the quench probe can be a subject of discussion. Most studies exploring immersion quenching consider a cylindrical specimen, which becomes useful for modeling purposes (i.e., simplification for 1D axisymmetric model). However, cylindrical geometries maintain an open question with regards to the actual direction of the heat flux. Interestingly, plate-like quench probes, which would certainly avoid such problematic, are not a common geometry for immersion processes. Authors have suggested minimum ratios between length and diameter (i.e., >4) to avoid end cooling effects. For the case herein, the cooling of the specimen during the air transfer step and subsequent immersion can not be ignored.

Secondly, the general consensus is to place the in-body sensors as close as possible to the surface of exchange, yet the instrumentation strategy, including the number of sensors and their position, remains a decision to be made by the researchers on a case-by-case basis. Often, the type of phenomena of interest will likely dictate the final instrumentation strategy. Nonetheless, placement of the sensors should be carefully chosen; further compensation strategies might be required if the local thermal field is affected.

Thirdly, it has been proved that variables such as probe size, start temperature of the specimen, and quenchant temperature have an influence on the cooling curves. Hence, the thermal BCs are likely to evolve due to those variables. Exploring the influence of such variables under the condition of this study comprehend a key element on the development of a database containing characteristic cooling curves.

The quality of the data obtained with the quench probes has a strong influence on the solution of the inverse heat transfer problem (IHTP). As a reminder, test data becomes the input for the IHTP. Likewise, the factors outlined before (i.e., probe geometry, instrumentation) have an influence on the selection of the methodology and postulates when solving the IHTP.

1.5 The Inverse Heat Transfer Problem

The IHTP must be solved to estimate the thermal BCs at the surface-fluid interface between the quench probe and the quenchant. This section includes the definition of the IHTP, followed by classification of the type of IHTP, and the solving techniques available in the literature. The section concludes by discussing the difficulties of solving the IHTP and elaborating on the accuracy levels, reported in the literature, that identify thermal BCs during quenching by solving the IHTP.

1.5.1 Definition of the IHTP

In heat transfer, the direct problem deals with the estimation of the temperature distribution within a medium for a given boundary condition and thermophysical properties. On the other hand, the IHTP is concerned with the estimation of an unknown variable based on the response of the system. This can be rephrased as follows "in the direct problem the causes are given, the effect is determined; whereas in the inverse problem the effect is given, the cause is estimated" (Ozisik & Orlande, 2000).

The IHTP is an ill-posed problem contrary to the direct problem. For a problem to be considered as well-posed, the following criteria must be met: a solution must exist, it must be unique; and the solution shall be stable under small changes to the input data (Ozisik & Orlande, 2000). However, for the inverse problem, the uniqueness of the solution can be proved only for some special cases and the sensitivity to random errors requires special techniques to satisfy the stability condition.

For instance, taking as reference a one-dimensional slab of thickness δ without heat generation, the general form of the heat diffusion equation is given by:

$$\frac{\partial}{\partial x}\left(k\frac{\partial T}{\partial x}\right) = \rho c\frac{\partial T}{\partial t} \tag{1.37}$$

The direct problem requires BCs to be defined at the surface (as given in Eq. 1.3 to Eq. 1.5). Hence the causes (BCs) are known, and its effect (i.e., thermal history) is to be determined by solving Eq. 1.37. However, for the inverse problem the internal temperature (i.e., the effect) is known at an internal location x_{test}, for the complete time interval of interest:

$$T(x_{test}, t_i) = T_{test}(t_i) \quad at \quad (0 < x_{test} < \delta) \;\; for\,(0 < t_i < t_{end}) \tag{1.38}$$

Thereby, the IHTP uses the known thermal history to estimate the unknown boundary condition as represented schematically in Figure 1.15. The inverse approach is applicable to other unknown variables and is also applicable to the different heat transfer modes.

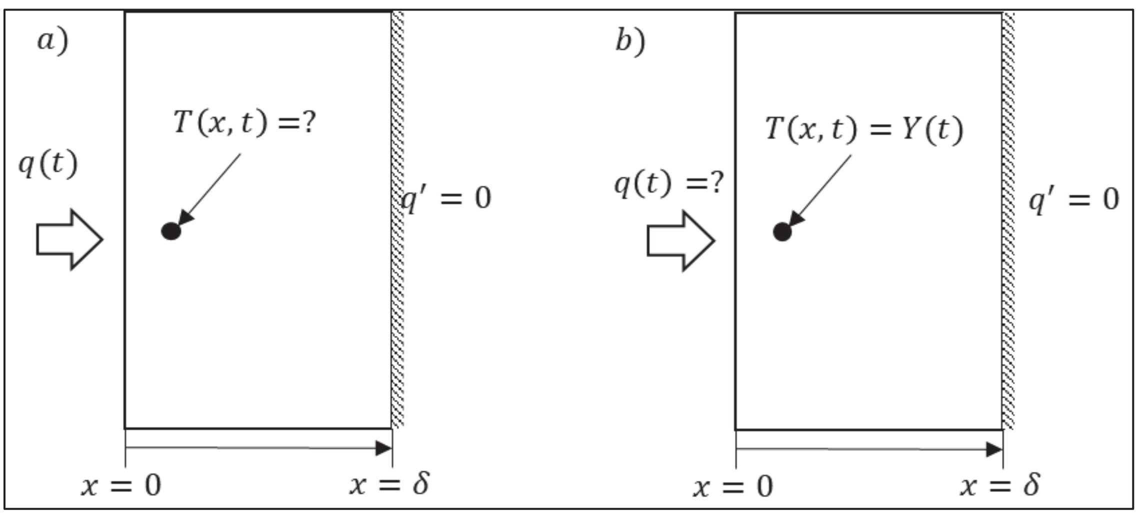

Figure 1.15 Schematic of a 1D slab of thickness (δ) subject to a heat flux (q) at x=0,
a) direct problem where $q(t)$ is known, but temperature distribution $T(x,t)$ is unknow,
b) inverse heat conduction problem where $q(t)$ is unknown
Adapted from Woodbury, Najafi, de Monte & Beck (2023)

1.5.2 Classification of the IHTP

The classification of the IHTP widely depends on the author's approach. For instance, Ozisik & Orlande (2000) proposed two main groups of IHTPs either based on the nature of the heat transfer process or depending on the causal characteristic to be estimated. The first group associates the IHTP based on the heat transfer phenomena such as conduction, convection, radiation, or a combined effect among them. When the transient temperature measurements at one or more interior locations of a given body are known, and the surface heat flux or surface temperatures are unknown, the problem is referred to as the inverse heat conduction problem (IHCP), as defined by (Woodbury et al., 2023). The second group uses a causal characteristic classification, as given in Figure 1.16, which associates the IHTP to one of five characteristics of the heat diffusion equation. Using this classification, the work herein has only one unknown characteristic: the boundary conditions. All the other causal characteristics are either known (i.e., geometric characteristics, initial condition), taken from the literature (i.e., thermophysical properties), or neglected (i.e. source term).

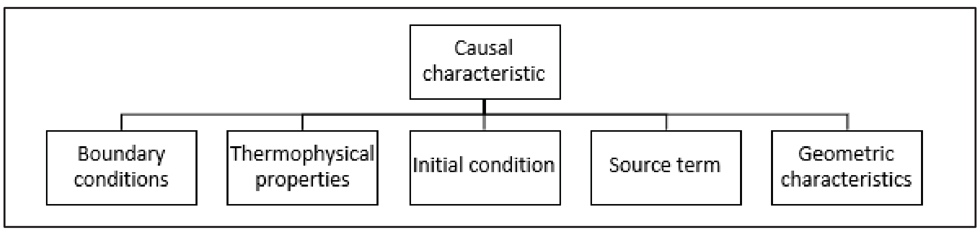

Figure 1.16 Classification of IHTP as per Ozisik & Orlande (2000, p. 8)

According to (Woodbury et al., 2023), the IHCP can be assigned into one or multiple categories based on the methods used to solve the IHCP. Thus, the proposed categories consider the ability of the method to treat linear or nonlinear cases, the method of solution of the heat conduction equation (i.e., exact solutions, finite difference, finite element), the time domain used (i.e., only present time, future time step, complete time domain), and the dimensionality of the IHCP (i.e., 1D, 2D or 3D). As will be seen in the upcoming section, the initial solving techniques were developed for one-dimensional cases while solving a 2D or 3D case would increase the complexity of the problem. Solving the inverse problem often involves the minimization of an objective or penalty function as part of the formulation. The procedures used to accomplish such minimization are also another means to classify the type of inverse problem (Colaço & Dulikravich, 2011).

1.5.3 Solving Techniques

This section presents an overview of the different techniques and strategies to solve inverse problems. Classic methods are introduced first, followed by iterative and alternative methods developed through the years. The discussion is centered on the limitations and applicability of such methods, especially with regards to the conditions under study (i.e., non-homogenous conditions before immersion, multiple unknown thermal BCs, temperature dependent material properties). Documentation related to the application and solution of the IHTP is widely available in the works of (Colaço & Dulikravich, 2011; Ozisik & Orlande, 2000; Woodbury et al., 2023).

1.5.3.1 Classic Techniques

The initial works on the inverse identification of the surface heat flux for one-dimensional transient thermal problems are often attributed to (Beck, 1968; Stolz, 1960). The unknown flux was estimated by inverting the convolution integral using thermal measurements from a single point, allowing the time-dependent calculation of the response of the body to follow a variable excitation thanks to the superposition of linear solutions. The convolution integral, also called Duhamel integral, is represented by the expression below:

$$T(x,t) - T(x,0) = \int_{0}^{t} q(0,\lambda)\frac{\partial\phi(x,t-\lambda)}{\partial t}\partial\lambda \tag{1.39}$$

Where, q represents the surface heat flux, $\partial\phi/\partial t$ the time derivative of the response of the body, $T(x,0)$ is the initial temperature, $T(x,t)$ represents the temperature variation, and λ is the time step. Then, using the principle of state superposition that allows the summation of temperature responses in a body caused by steps of surface heat flux, Stolz calculated the evolution of the temperature at a given point ($\Delta T(x, j\Delta t)$), given the increments of surface heat flux (Δq_i) for a direct problem using the following expression:

$$\Delta T(x, j\Delta t) = \sum_{i=0}^{j} \Delta q_i \phi(x, (j-i)\Delta t) \tag{1.40}$$

Where the term, $\phi(x, (j-i)\Delta t)$ is the response for $[1;j]$ time steps. The step response can be identified by analytical calculations, experimental results, or numerical approximations, such as with the finite difference method (Beck, 1968; Stolz, 1960). Note that this expression is valid for a uniform and constant initial temperature of the body. Solving the direct problem can be achieved by writing such expression (Eq. 1.40) in matrix form (Wells & Daun, 2009). Then, assuming constant thermal properties of the material, the inverse identification of the surface fluxes can be calculated by inverting the matrix form of Eq. 1.40, as follows:

$$\Delta q_{j-1} = \left[-\sum_{i=0}^{j-2} \Delta q_i \phi(x, (j-i)\Delta t) + Y(x, j\Delta t) \right] \cdot [\phi(x, \Delta t)]^{-1} \tag{1.41}$$

Where Y represents the measured temperature variation. It was reported that the above method is stable provided that the selected time step is sufficiently large (Beck, 1968; Stolz, 1960). Otherwise, the inversion result can oscillate until it becomes completely degenerate which was attributed to the errors (i.e., inaccurate temperature and position of sensors) present in the input data (Stolz, 1960). Alternatively, it was suggested that increasing the time step length decreases the amplitude of oscillations in the inverted results (Wells & Daun, 2009), which then leads to the implementation of regularization techniques. Nonetheless, classic methods are suitable for uniform and constant initial conditions, constant material properties, thus questioning its applicability when dealing with real-life conditions during quenching by immersion.

Regularization

Regularization is defined as any modification of an originally ill-posed problem that mathematically brings it closer to a well-posed problem (Woodbury et al., 2023). Unfortunately, although it can limit oscillations, regularization introduces biases to the estimates. These biases reduce the sensibility of the system and make the proposed solutions inaccurate. Thus, any regularization technique requires a trade-off between stability of the calculation without overly biasing the results (Woodbury et al., 2023).

One of the most cited techniques is Tikhonov regularization. It consists of modifying the least squares method by adding a stabilization term containing a regularization parameter, which is a constant to be defined (α_0). In inverse heat transfer problem, the Tikhonov regularization is often presented expressed in its zeroth order as follows (Ozisik & Orlande, 2000; Woodbury et al., 2023):

$$S = \sum_{i=1}^{n} (Y_i - T_i)^2 + \alpha_0 \sum_{i=1}^{n} q_i^2 \tag{1.42}$$

Where, S denotes the objective function or the penalty function; Y_i is the experimental temperatures; T_i is the calculated temperature values according to the different heat flux steps q_i, and α_0 is the regularization parameter. Thus, the challenge when implementing regularization techniques lays on defining the adequate α_0. The application of Tikhonov regularization is usually done on the full-time domain (Beck, Blackwell & Haji-Sheikh, 1996; Woodbury et al., 2023). Following such approach comes with potential drawbacks when α_0 is not properly defined, iterations might be required over the full-time domain, thus decreasing the overall efficiency of the method.

Function Specification Method

The IHCP can be treated by assuming a functional form of the surface heat flux referred as the Function Specification Method (FSM). The function itself can be of any form, straight lines or polynomials of any degree (Samadi, Woodbury & Beck, 2018). FSM can be applied simultaneously to the whole domain or sequentially one segment after the other. The sequential function specification method (SFSM), commonly referred as the Beck's method, adds regularization by considering data from future time steps (Beck, 1968; Woodbury et al., 2023). SFSM considers a function form of the flux $q(t)$ for times t_M, t_{M+}, t_{M+n-1}, thus temporally holding the heat flux value over the future time steps (n). This method takes advantage of the diffusive nature of transient heat conduction as any input at the surface is both lagged and damped (Woodbury et al., 2023). In its linear form, the sum of squares is used to compute the square differences between measured and calculated data as follows:

$$S = \sum_{i=1}^{n} \left(Y_{M+i-1} - T_{M+i-1}\left(q_M, q_{M+1,} \dots, q_{M+r-1}\right) \right)^2 \tag{1.43}$$

In the SFSM, the number of future time steps (n) represents a mean of regularization as additional measurements are brought in without increasing the number of heat fluxes to estimate. However, there are certain elements to consider when using the linear form of this method. For 1D problems with two boundaries on the spatial domain, one of them must be known, often considering adiabatic conditions by either isolating one side of the geometry, or symmetry planes or axes. When the problem becomes non-linear, such as when thermal properties are functions of temperature, iterations on the value of the fluxes are necessary to solve the inverse problem (Beck, 1970; Woodbury et al., 2023).

The capabilities of the method to estimate multiple BCs at once might require further developments, as it is often deployed for finding one unknown BC for a 1D case. Similar to regularization techniques, iterations might be required when dealing with more complex problems. Thus, solving the IHTP can easily become an optimization problem that requires iterative methods, as is outlined in the upcoming section.

1.5.3.2 Iterative Methods

Several authors (Colaço & Dulikravich, 2011; Ozisik & Orlande, 2000; Woodbury et al., 2023) recognize that iterative methods are necessary to perform inverse identification of nonlinear transient heat transfer problems. Mathematically speaking, these techniques do not require inverting the direct solution but rather using optimization techniques to minimize a penalty function. Thus, iterative methods can deal with a wider range of BCs and variables than the previous solving techniques while still providing accurate results. The main question remains which method might be the most suitable, as iterative methods may require the development of complex optimization solvers, while computational power can rapidly increase depending on the selected method.

The penalty function is often found in the form of the square differences between test temperatures and simulated values (Felde, 2012):

$$S = \sum_{i=1}^{n} (Y_i - T_i)^2 = min \tag{1.44}$$

Iterative methods can be divided into gradient (deterministic) and non-gradient based (stochastic) (Colaço & Dulikravich, 2011). Deterministic methods, such as the conjugate gradient method (CGM), are often found in the inverse heat transfer literature (Colaço & Dulikravich, 2011; Woodbury et al., 2023). Modified gradient based strategies have been applied to solve the IHCP for 1D case with triangle-, sine-, and square wave functions of the heat flux (Tourn, Alvarez-Hostos & Fachinotti, 2021a), and have proved to be accurate and performing enough for estimating HTC for 1D and 2D cases for immersion quenching (Buczek & Telejko, 2013; Felde, 2012). Note that these techniques are often applied to the complete time domain of the system.

Stochastic methods rely on iterative procedures that do not require computing the gradient of the penalty function. This can be achieved, for example, by bounding or brute force. Although potentially more costly in computing power and processing time, these methods can converge into a global minima, a potential advantage when compared with deterministic methods as they may converge into local minima instead (Colaço & Dulikravich, 2011).

1.5.3.3 Alternative Methods

Alternatively, researchers have proposed dealing with the IHCP on complex geometries by dividing the domain into sections where the IHTP is solved locally (Duda & Konieczny, 2019).

These techniques solve the direct problem for the domain enclosed within the sensors position (Liscic, 2016; Liscic et al., 2011; Sanchez-Sarmiento & Cavaliere, 2021) and then estimating the BC on the remaining region of the domain. The temperature field reconstruction (TFR) (Sanchez-Sarmiento & Cavaliere, 2021) and the temperature gradient method (TGM) follow such approach. The latter is founded on the physical relation between the surface flux and the product of the temperature gradient at surface multiplied by the conductivity of the material (Liscic, 2009):

$$k(T)\frac{\partial T}{\partial x} \cong -k(T)\frac{T_{surf} - T_{x_{known}}}{x_{known}} = q \tag{1.45}$$

In the TGM, temperature-dependent properties can be adjusted per time step (Liscic, 2016; Liscic et al., 2011). The method relies on sensors placed close to the surface, a maximum depth of 1.5 mm off the surface is recommended for this method as deeper sensor’s would reflect on lower magnitudes of the estimated BCs (Hernandez-Morales et al., 2019). The maximum in-depth distance is suggested for a sensor parallel to the main surface of exchange, consistent with the subsurface distance as per the Liscic/Namnac probe (Liscic, 2009). However, the instrumentation of such probe is more complex to implement as the thermocouples are inserted either obliquely or perpendicular to the exchange surface, which goes against the recommendations reported by (Luebben et al., 2009).

Researchers have also proposed the implementation of genetic algorithms (GA) (Felde, 2012) and artificial neural networks (ANN) (Bouissa, Shahriari, Champliaud & Jahazi, 2019). The former was compared against other iterative methods, such as CGM, producing an improvement in its accuracy (smaller cost function) although at a higher computational cost (computing time) (Felde, 2012). ANN has been used to predict HTC as a function of temperature for a 3D simulation of a large steel block, its architecture uses a back-propagation algorithm using one hidden layer as described by (Bouissa et al., 2019). Additional regularization techniques can be found in the works of (Tourn, Alvarez-Hostos & Fachinotti, 2021b) for a 1D linear case considering square- and triangular-wave signals.

1.5.4 General Difficulties on Solving Inverse Problems

The difficulties of solving the inverse heat transfer problem for a semi-infinite solid at zero temperature based on the behavior of the surface heat flux at the surface were addressed by (Ozisik & Orlande, 2000). It was reported that the phase shift of the temperature response increases as the measurement point is further away from the surface. Similarly, the amplitude of the oscillatory response decreases with the distance of the measurement point from the surface and increasing excitation frequency. This behavior is described as the damping effect by (Woodbury et al., 2023) and previously addressed by (Beck, 1970). The combination of uncertainty and lack of measurement sensitivity can greatly complicate the inverse identification techniques. This could lead to unnecessary iterations to reach an acceptable degree of accuracy on the proposed solution, or potentially not even represent the actual conditions at the surface. As the measurements are further away from the surface, the sensitivity to the fluctuations on the surface decreases. Thereby, the general understanding is that experimental measurements are to be taken as close as possible to the surface without affecting the local thermal field.

Inverse heat transfer problems are mathematically ill-posed, they greatly amplify small input errors in the output results of the inversion, a notorious difficulty described by several authors (Colaço & Dulikravich, 2011; Ozisik & Orlande, 2000; Woodbury et al., 2023). Some authors have proposed smoothing the input data in order to reduce the disturbances that exist in the data recorded by thermocouples (Liscic, 2016; Liscic et al., 2011) or even smoothing the output result of the inversion to attenuate residual oscillations (Stolz, 1960).

Another question comes with the computing power required for solving inverse problems, especially when implementing iterative methods. Deterministic methods are generally less expensive that stochastic ones, although evaluating the cost function and computing the sensitivity coefficients in the form of derivatives might increase the computational cost (Colaço & Dulikravich, 2011). Even more sophisticated techniques like GA might not necessarily provide an improvement on computation power when compared with traditional gradient methods (Felde, 2012).

1.5.5 Solving the Inverse Problem for Quenching Cases

Given that the present study is interested in immersion quenching, this subsection provides an overview of the works of different authors addressing similar processes (or rapid cooling processes, like spray quenching), and the accuracy levels of their methods used to estimate the BCs. There is no clear consensus on which method is best for a given case, in fact, the methods and metrics vary between studies. Thus, a fair comparison between studies should account for the assumptions, postulates and rationale of the authors. This includes, but not limited to, the dimensionality of the problem (i.e., 1D, 2D, axisymmetric, etc.), differences in processes (i.e., specimen's temperature, range of temperature), and even their test specimens (i.e., probe size, material, etc.).

The works in the literature estimate different types of BCs, such as HTCs (Behrem & Hrnjica, 2018; Buczek & Telejko, 2013, Fan et al., 2022; Liscic & Singer, 2013), surface heat fluxes (Babu & Prasanna, 2010; Prasanna Kumar et al., 2014; Ramesh & Prabhu, 2016; Ramesh & Prabhu, 2014a), as well as surface temperature (Jahedi, Berntsson, Wren & Moshfegh, 2018). Hence, choosing the solving technique and type of thermal BC for the IHPT is subject to the researchers. Nevertheless, the works available in the literature can provide a reference of the accuracy levels expected when estimating the thermal boundary conditions for an immersion quenching process.

Authors in the literature assess the accuracy of their methods by different means, including maximum temperature difference (Behrem & Hrnjica, 2018), relative error ((Behrem & Hrnjica, 2018), and error interval (Babu & Prasanna, 2010). Those account for the difference between test data and a proposed solution using a cooling curve. Moreover, the cooling rate curve, i.e., the derivative of the cooling curve, has also been included in the metrics for computing mean relative difference (MRD), mean absolute difference (MAD), and standard error (SE) (Sanchez-Sarmiento & Cavaliere, 2021).

The values of maximum temperature difference are easily quantifiable regardless of the method, yet the magnitude of their values varies widely. For instance, Behrem & Hrnjica (2018) reported a difference of 40°C between test and proposed solution, whereas Liscic & Singer (2013) report a temperature difference within a range of $\pm$15°C. Note that the former study solved a 2D axisymmetric case using a hybrid optimization algorithm to estimate the HTC, whereas the later dealt with a 1D axisymmetric problem implementing the TGM. Regardless of the differences in methods, multi-dimensional problems inevitably increase the complexity of the problem and potentially affect the accuracy of the proposed solution. Nonetheless, the largest difference in temperature tends to appear at high temperatures (Babu & Prasanna, 2010; Liscic & Singer, 2013).

The relative error is also a common metric in the literature. Multiple authors have reported results for immersion quenching whose errors remain below 5% (Babu & Prasanna, 2010; Behrem & Hrnjica, 2018; Prasanna Kumar et al., 2014; Ramesh & Prabhu, 2014a; Ramesh & Prabhu, 2016). Some of these authors have worked with 2D geometries using the FSM (Babu & Prasanna, 2010), or 2D axisymmetric case (Behrem & Hrnjica, 2018). However, when considering phase transformation, errors may increase to the range of 15 to 25%, even for a 1D axisymmetric case (Samuel, Nayak, Rao & Prabhu, 2023). Ramesh & Prabhu (2014a; 2016) concluded that increasing the number of zones (or segments, as called by the authors) improved the accuracy of the estimated boundary condition, as one single zone error was reported as high as 35% whereas an 8-zones model reduced the error down to <5%. It must be noted that the rationale of the authors of increasing the number of zones was mainly driven by the instrumentation strategy on the test specimen as sensors were strategically placed along the axial and radial directions.

Furthermore, implementing iterative algorithms often require the definition of one or more stopping criteria. Fan et al., (2022) suggested an average error of 3% on the identified HTC to stop their algorithm. Pati et al., (2019) proposed a stringent stopping criterion, in the form of a minimum error of 0.001°C, at multiple measurements points. Samuel, Nayak, Rao & Prabhu (2023) considered flux variations less than 0.5% as stopping criteria.

Most studies above were obtained for quench probes similar or close to standard probes with Ø ≤ 20 mm (Babu & Prasanna, 2010; Buczek & Telejko, 2013; Prasanna Kumar et al., 2014; Ramesh & Prabhu, 2014a; Samuel, Nayak, Rao & Prabhu, 2023). For immersion quenching, the works of Behrem & Hrnjica (2018) and Liscic & Singer (2013) can be considered the most industry-oriented cases, as their specimens are considerably larger than standard specimens. Behrem & Hrnjica (2018) solve the IHTP for specimens with different diameters (Ø25, 50, 75 mm), it was reported that the smallest specimen produced the larges relative errors, yet always below 5%. Liscic & Singer (2013) with the Petrofer quench probe (Ø50 mm), solved the IHTP using the TGM for an axisymmetric 1D case. They reported temperature differences within a range of ±15°C. Note that the largest errors are reported for the sensor at the center of the specimen, especially at high temperatures, while sensors closer to the surface have error lesser in magnitude.

1.6 State of the Art, Challenges and Objectives

The main objective of this thesis is to develop methods and means to experimentally characterize and model the thermal boundary condition during immersion quenching under industrial environments. The work included herein is limited to the thermal field evolution during quenching.

The following lines describe the detailed objectives that will be addressed in this document:

1. Develop the experimental means to characterize industrial quench systems that represent the process and geometries of typical workpieces.

The *first objective* directly addresses the need for industry-oriented test equipment, including specially designed quench probes, to account for the actual shopfloor conditions. The limitations of standard testing using small specimens, which fail to represent industrial processes, and produce higher cooling performances and extraction rates, would be entirely avoided. Nevertheless, the quench probes must represent the geometry of the workpiece, as the local conditions might be altered based on the specimen's geometry. These questions and challenges are addressed in this document in multiple ways. Figure 1.17 highlights the chapters and annexes containing information regarding objective 1.

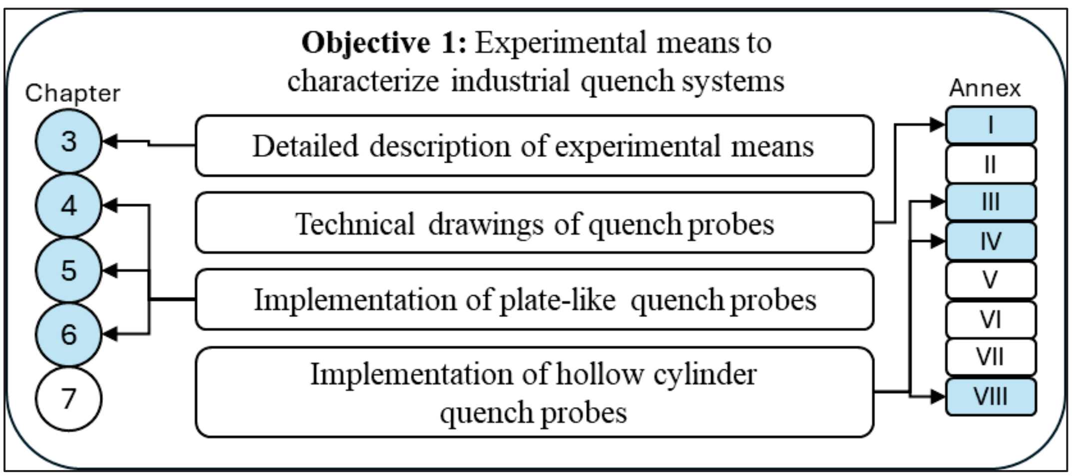

Figure 1.17 Chapters and annexes presenting information regarding objective 1

2. Develop numerical tools to estimate local boundary conditions during the air transfer step and immersion step of the reference process (max 5% relative error).

For the *second objective,* the tools to identify the local boundary conditions must consider both the air transfer step, which is often ignored in the literature, and the immersion step. Further refinements might be required for the air transfer step as textbook correlations, which may provide acceptable results in practice, are not representative of the actual process. Furthermore, the accuracy levels reported in the literature, to estimate the thermal BCs by solving the IHTP during quenching, are deemed acceptable for errors values around 5%, regardless of the technique or methods implemented to solve the IHTP. The work carried out by (Lemyre-Baron,

2025) is taken as reference after successfully identifying baseline boundary conditions for the industrial process of interest fulfilling the above criteria. The numerical tools used in this document are described in different chapters and annexes, as indicated in Figure 1.18.

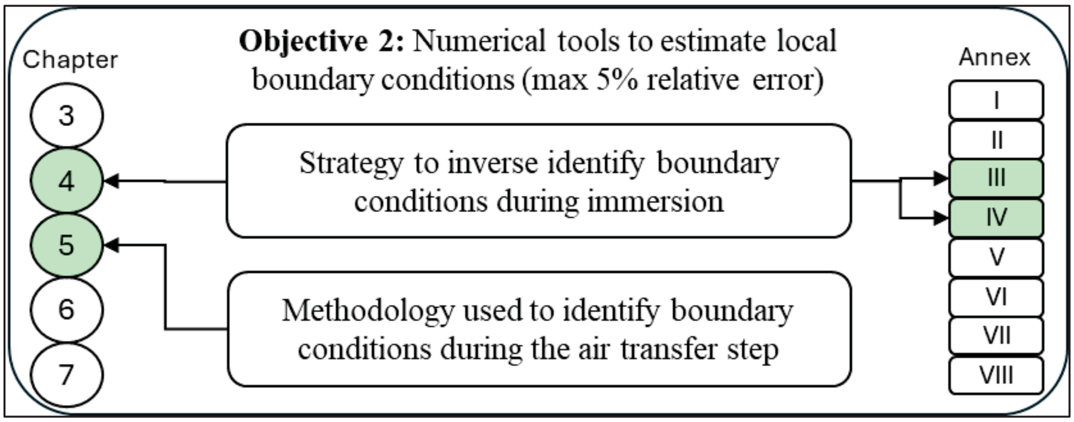

Figure 1.18 Chapters and annexes presenting information regarding objective 2

3. Produce database of cooling curves and thermal boundary conditions to analyze the influence of process variables (i.e., bath heterogeneity, probe orientation, position on HT-rig), and quench probe variables (i.e., probe size and probe geometry).

The *third objective* will produce an undoubtedly unique database on its own. There is no reference available in the literature, representing industrial environments to the level of detail described in this document. The database is built up of experimentally acquired cooling curves and identified thermal boundary conditions (i.e., temperature dependent heat transfer coefficients). The influence of the variables of interest is discussed in different chapters and annexes, as shown in the schematic in Figure 1.19. Notably, the data presented in this study provide reliable and representative BC of an actual industrial process. Therefore, the identified BC can be easily applied on quenching simulations.

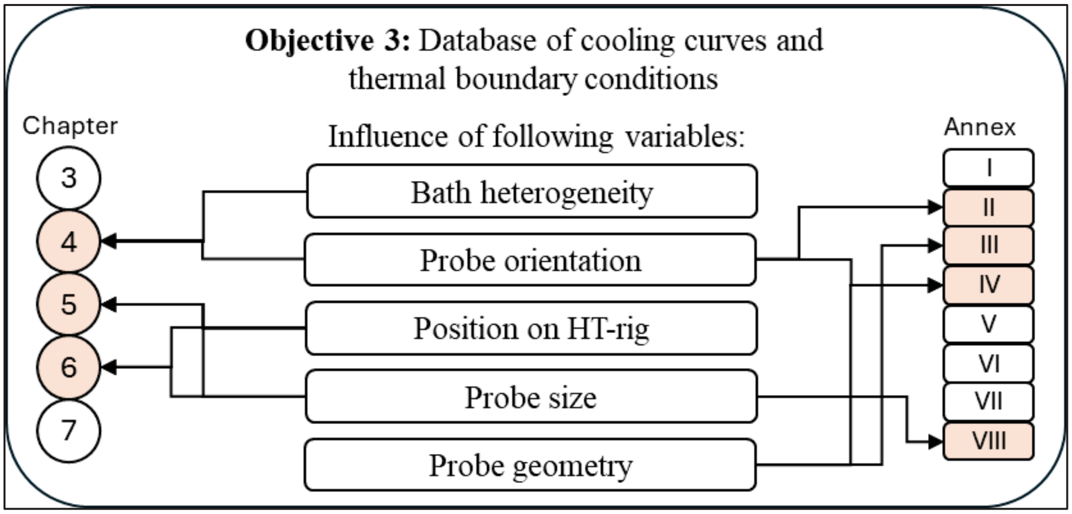

Figure 1.19 Chapters and annexes presenting information regarding objective 3

4. Develop a mathematical modeling strategy to adjust the local boundary conditions to account for the influence of specimen size

With regards to the *fourth objective,* the modeling strategy to adjust the thermal boundary conditions based on the specimen size directly challenges the general understanding of the HTC as an intensive property for a given surface-fluid combination. Modeling assumptions such as simplification as lumped bodies, often used in the literature, prevent capturing the thermal gradient inside the body, and assume the same BC on the surfaces. These considerations, although useful, fail to properly represent the conditions during both the air transfer step and immersion step. Hence, the mathematical models will provide the flexibility to adjust the local BC based on the cooling regimes, thus accounting for the physical phenomena occurring at the surface. Figure 1.20 indicates the chapters and annexes discussing the questions, challenges and proposed models for the fourth objective.

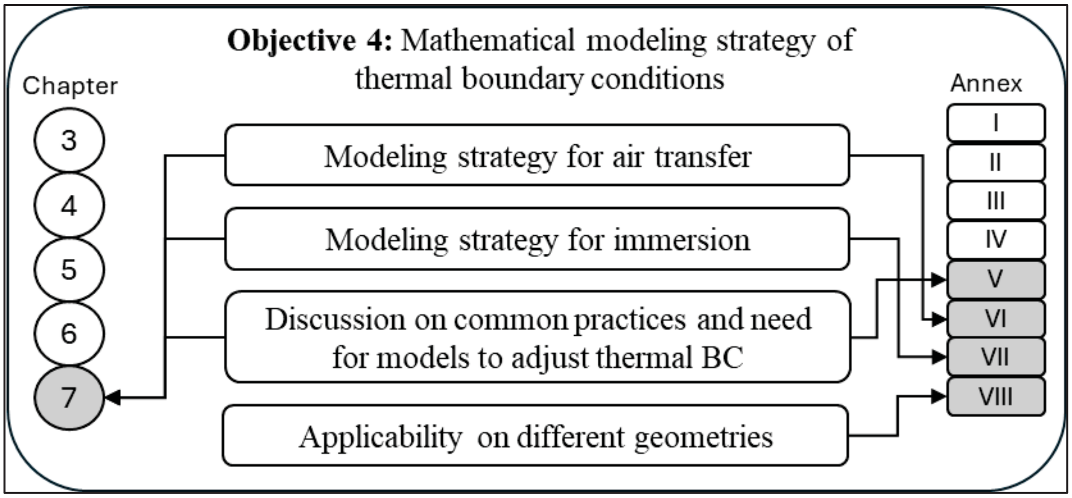

Figure 1.20 Chapters and annexes presenting information regarding objective 4

CHAPTER 2

RESEARCH APPROACH AND ORGANIZATION OF DOCUMENT

2.1 Research Approach

The main tasks of the work herein can be segregated into the following categories: 1) development of industry-oriented quench probes, 2) in situ test campaign, 3) interpretation of test results, 4) identification of thermal BCs, and 5) modeling of the BCs. The first task (label 1 in Figure 2.1), directly addresses the *first objective* outlined before. The subsequent tasks, second to fourth, were defined to fulfill the *third objective: database of cooling curves and thermal BCs.* The *second objective* (i.e., numerical tools to estimate thermal BC) required a parallel development fully achieved by completing task 4 (label 4 in Figure 2.1). The *fourth objective* is accomplished as part of task 5 of the research approach.

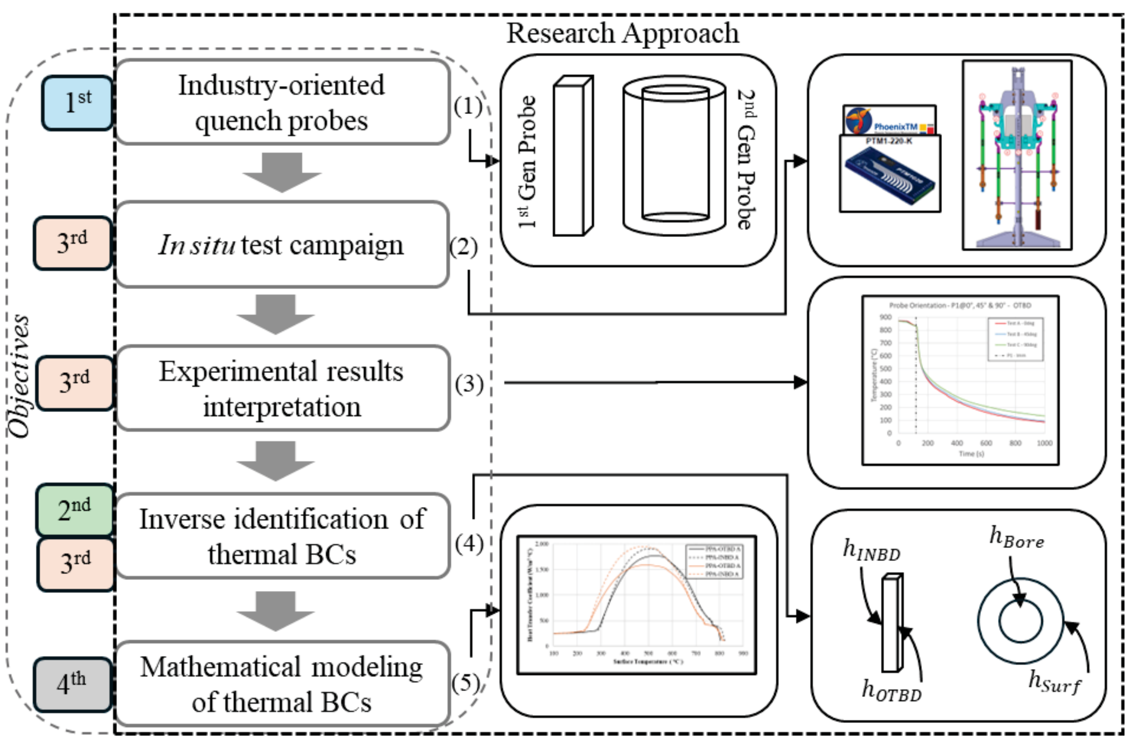

Figure 2.1 Main steps of this research project

The outcomes of this work are the characteristic BCs, in the form of heat transfer coefficients, representative of the industrial process under study. However, the work herein challenges multiple postulates commonly used in engineering practice and academia. Undoubtedly, the influence of the specimen's size on the HTC, and the proposed strategy to mathematically model the BC to account for such phenomena is one of the main outcomes of this research.

Even though most of the research activities were carried out gradually as shown in Figure 2.1, they are not entirely independent from each other. The following subsections provide additional details as well as the interrelation between them.

2.1.1 Industry-Oriented Quench Probes

Industry oriented quench probes are required to adequately characterize the industrial facilities of the industrial partner. Plate-like geometries were chosen as the 1st generation of quench probes. An extensive work has been carried out by (Lemyre-Baron, 2025) addressing the sizing and instrumentation of a 50.8 mm thick stainless-steel plate. General guidelines from such work were considered such as the sensor's distance to the surface, depth of the sensors inside the specimens, minimum length over thickness ratio, and general instrumentation approach. The typical geometry of a quench plate probe is shown in Figure 2.2.

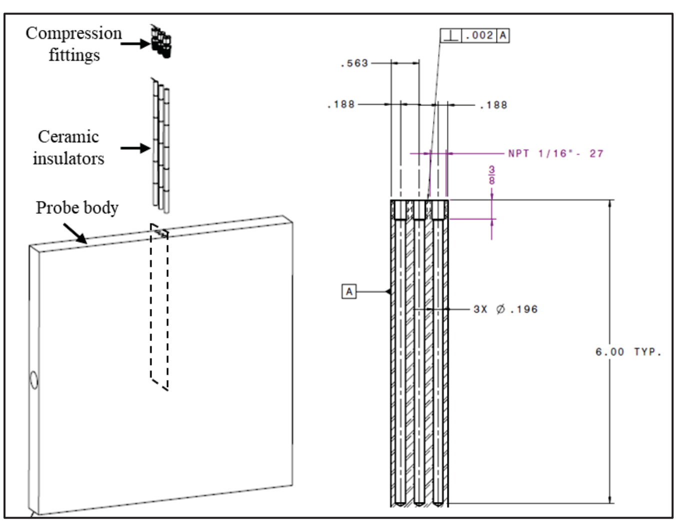

Figure 2.2 Typical quench probe (units in Imperial)

The instrumentation remains consistent as three sensors were distributed along the specimen's thickness. These sensors were fixed with compressor fittings at the top surface. Likewise, the sensors always remain parallel to the main surface of exchange as outlined by (Lemyre-Baron, 2025).

The work herein explores the influence of the specimen's size, thus varying the thickness of the body. The resulting geometries are labelled as PPA, PPB, and PPC, along the different chapters. Although conceptually it only involves the thickness of the plate, care must be taken as the clearance between compression fittings at the top surface could be compromised as well as the assembly points on the side of the plate geometry (see Figure 2.2).

Utilizing plate-like geometries comes with clear advantages with regards to modeling considerations. For instance, these geometries ensure that the heat exchange occurs through the main surfaces, and providing the right sizing, it leads to a 1D transient heat transfer problem. This also reduces the level of complexity when solving the IHTP. In addition, plate like geometries are practical to manipulate and assemble, they also provide flexibility to adjust their orientation with regards to the oil flow. Moreover, the size and weight constraints were easily met, thus functional for testing under industrial conditions.

In addition to the plate-like quench probes, a tube-like geometry, referred herein as hollow cylinder (HC) was used to characterize the industrial environment. The HC probe is shown in Figure 2.3. Such geometry provides insightful information of the boundary conditions for outer surfaces and inner bore surface, it is referred as the 2nd generation of quench probes. The good practices from the plate-like probes were considered, which eased the decision-making during its development. However, additional challenges arise such as assembly strategy, compatibility with tooling, and weight limitations. Detail drawings of the probe geometries, plate and hollow cylinder can be found in ANNEX I

The influence of probe geometry can be assessed by comparing the experimental data from each probe, as well as analyzing the identified thermal BCs. Although secondary to the main work herein, the results for tube-like geometries can be found in ANNEX III and ANNEX IV. They provide a basis for further developments, including evaluation of assumptions made during modeling of the thermal boundary conditions of plate-like geometries. Nevertheless, the work herein provides industrially acquired thermal boundary conditions, for plate like geometries and hollow cylinders.

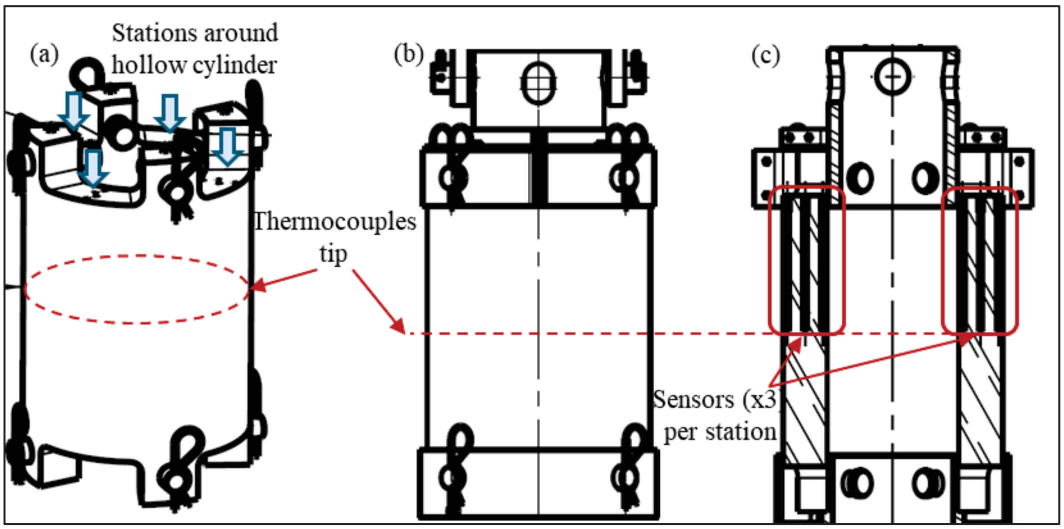

Figure 2.3 Hollow cylinder (HC) quench probe a) iso view, b) assembly setup, c) cut-view of assembly

2.1.2 In-situ Test Campaign: Characterization of Industrial Environment

The second step of the global methodology encompasses the experimental work at the industrial partner facilities. The in-situ test campaign was conducted with the utilization of an actual heat treatment rig (HT-rig) and following a typical industrial procedure of the quenching step, which includes the transfer through air of the heat-treated load from the furnace to the quench bath where immersion quenching is completed. A detailed description of the experimental means and methods is included in CHAPTER 3. In this subsection, the rationale and intend of the in-situ test campaign is described.

The in-situ campaign explores the following axes: heterogeneity of the quench bath, influence of probe orientation, and influence of probe size, as shown in Figure 2.4. It is important to mention that the testing capabilities of the system could encompass a wider range of axis of study, such as surface finishing, bath temperature, immersion speed, etc. Such variables, although relevant for the scientific community, are beyond the scope of this work due to the intended application in accordance with the industrial partner expectations.

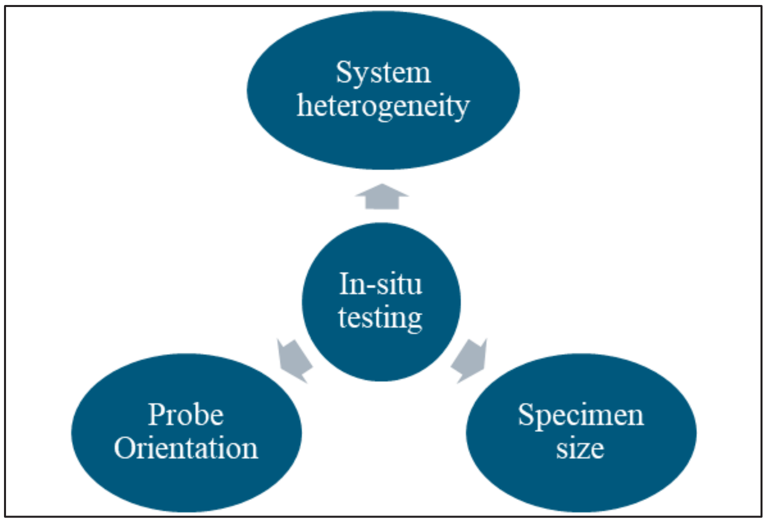

Figure 2.4 Axes of interest for in-situ test campaign

The first axis, heterogeneity of the quench bath, aims to identify the variations in the local boundary conditions along the working space. Such variation can be helpful to dictate the degree of refinement required to properly define the thermal BCs when running the numerical simulations of the process. The second axis, influence of probe orientation, responds to the reality faced with industrial components whose surfaces might not be parallel to the oil flow during immersion quenching. Thus, the quench probes orientation is adjusted with regards to the oil flow. This axis is explored for both generation of probes, plate-like (see CHAPTER 4 and ANNEX II) and hollow cylinder (see ANNEX III and ANNEX IV).

The third axis, the influence of probe size, is arguably the main subject of interest in the main body of this work. This is addressed in CHAPTER 5 and CHAPTER 6 during the air transfer and the immersion step, respectively. The experimental work shows that the HTC can not be considered as an intensive property of a given surface-fluid combination. This was demonstrated by the work carried out for the mathematical modeling outlined in CHAPTER 7. Further details with regards to the in-situ test campaign can be found in Section 3.6.

The axes outlined above were explored for both generations of quench probes. Comparison between results for the 1st and 2nd generation probes capture the influence of the probe geometry. Details about the exploratory work per axis are distributed in this document as per Table 2-1. The work includes the experimentally acquired cooling curves which became the input to estimate the BCs by solving the IHCP.

Table 2-1 Distribution of the in-situ test campaign per axes

Probe	**Axis**	**Details**	**Chapter(s)**	**Annex(es)**
1st Gen	Repeatability	Test results	4, 5, 6	--
	System Heterogeneity	Position on HT-rig	5, 6	--
		Symmetry	4	--
	Probe Orientation	Ver/Inc/Hor	4	II, IV
	Specimen size	Effect with Position	5, 6	II
		Effect with Orientation	--	II
2nd Gen	Heterogeneity	In-body stations	--	III, IV
	Specimen size	Outer diameter	7	V-VIII
	Orientation	Ver/Hor	--	IV

2.1.3 Experimental Results Interpretation

The experimental data was analyzed systematically as per the main steps summarized in Figure 2.5. Given the extensive in situ test campaign, the analysis and interpretation require an adequate classification of the test data. Such step firstly involves the recording of test setup configuration, quench conditions, traceability of sensors' location on the test specimens and the corresponding channels on the data logger. Then, the test data must be properly aligned with regards to the immersion time of the specimen to allow for direct comparison among different test cases.

The critical step of the methodology is the identification of characteristic points corresponding to the physical phenomena, mathematical significance, and relevancy to the process. Such points are described in detail in CHAPTER 5 for the air transfer and CHAPTER 6 for the immersion step. These points allow a quantitative comparison between a given case of interest. Moreover, the identification of characteristic points on the test data provided the basis for one of the inverse identification methods, as described in CHAPTER 5, as well as identifying the equivalent characteristic points on the temperature dependent surface heat flux curve as explained in the subsequent modeling subsection and CHAPTER 7.

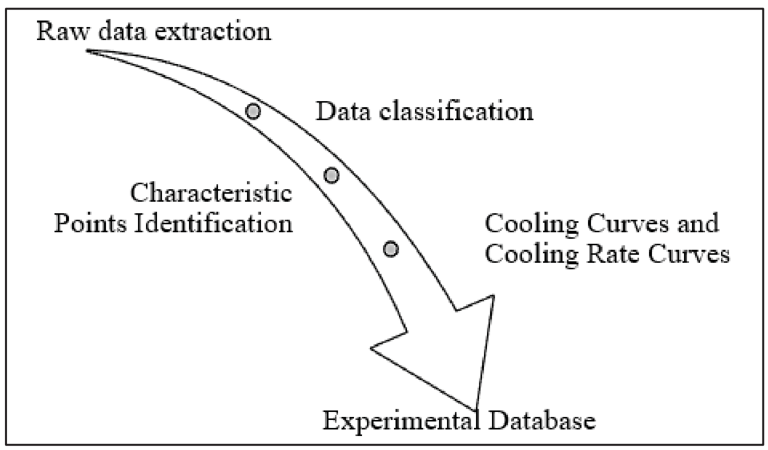

Figure 2.5 Interpretation of test data

The utilization and interpretation of the test data is used vastly along the different chapters and annexes of this study. It is recommended to the reader to familiarize with the labeling of the specimens' surfaces and location of the sensors to ease the reading on a given chapter. In general, the main surfaces of exchange are labelled based on their orientation, either Outbound (OTBD) or Inbound (INBD) with regards to the mid-plane of the tooling (see Figure 2.6). Cases exploring the influence of surface orientation would also require further update on the labeling, as shown in Figure 2.6. Likewise, plate quench probes are labelled as PPA, PPB or PPC depending on the specimen size.

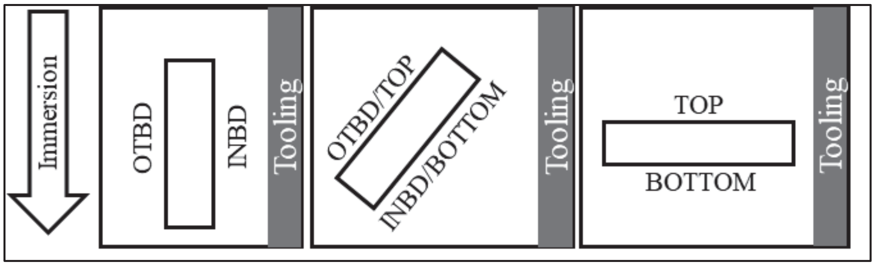

Figure 2.6 Labeling of main surfaces of exchange for plate probes

2.1.4 Thermal Boundary Condition Identification

The identification of the thermal boundary condition requires solving the IHTP. In this study, iterative procedures were implemented to identify the thermal BCs as they are capable to deal with the non-linearity of the transient heat transfer problem while identifying multiple unknown BCs. A stochastic method was developed for the air transfer step, explained in detail in CHAPTER 5, while a gradient based method is used for the immersion step, as implemented by (Lemyre-Baron, 2025). The main steps of both methods are described in Figure 2.7. First, the temperature evolution at the surface of the quench probe is reconstructed, before extracting the surface heat flux from a finite element (FE) simulation whose boundary conditions are the reconstructed thermal profiles. Then, the HTC can be computed and used as boundary condition on a refined FE model to verify the proposed values. In essence, both tools differ on the solving technique during the first step of the methodology (i.e., surface temperature identification).

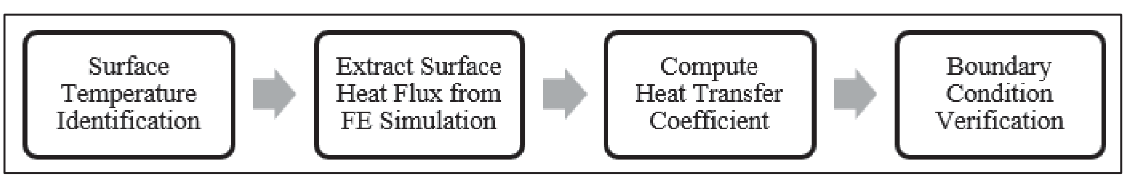

Figure 2.7 Strategy to identify thermal boundary conditions

Therefore, this study deals with the IHTP as an optimization problem for which iterative methods were implemented. The minimization of the penalty function (i.e., in the form of sum of squares between measured and predicted results) follows different strategies per method.

For the air transfer step, an iterative technique evaluates the thermal profile based on Hermite polynomials as described in CHAPTER 5. The immersion step uses a damped Newton solver algorithm to iteratively optimize linear piecewise surface temperature profiles as outlined in CHAPTER 4, additional details can be found in (Lemyre-Baron, 2025). The accuracy of the proposed solution as per both methods is evaluated with the root mean square error (RMSE) at the sensor's location and the relative error between simulation and test values. The verification cases were run for both air transfer and immersion. Results of such verification step are presented in CHAPTER 7.

The identified thermal BCs are one of the main outcomes of this study. Providing a good degree of accuracy of the identified BCs, as outlined in CHAPTER 7, the identified values closely represent real-life industrial operations, thus accounting for the environmental conditions and peculiarities non accounted for under laboratory settings. Moreover, the predicted BCs would, in theory, improve the accuracy of the thermal numerical simulation of the quenching process.

Therefore, the produced temperature dependent HTCs for the different test cases as per the axes of interest (see Figure 2.4) can be catalogued as part of a unique database of industry-oriented thermal boundary conditions for plate-like geometries and hollow cylinders.

2.1.5 Mathematical Modeling of Thermal Boundary Condition

Mathematical models of the thermal BCs during quenching have been developed as part of this study. Such models address the influence of the specimen's size as described in detail in CHAPTER 7, and ANNEX V to ANNEX VIII. Even though solving the IHTP can be used to develop a database of thermal BCs, as outlined in previous subsections, it requires the experimental work to characterize the actual process. Such experimental work can not be avoided when no data is available and is still required for validation purposes. However, it is unpractical to test an infinite number of geometries to obtain a whole domain database of thermal BCs.

The models developed in this study address one of the real-life challenges as industrial components have different ruling sections and sizes. The decision to prioritize the influence of the specimen size was driven by the findings reported in published work reported in CHAPTER 5 and CHAPTER 6. Thereby, the strategy presented in CHAPTER 7 addresses the air transfer step and immersion step separately. Such approach ensures the accurate prediction of the thermal field of the heat-treated specimen before immersion into the quenchant.

Once immersion occurs, the multiple physical phenomena at the surface-fluid interface are captured by modeling each of the cooling regimes separately: film boiling (FB), transition boiling (TB), nucleate boiling (NB) and convection (C), as shown schematically in Figure 2.8. Each of the models is bounded by characteristic points of physical significancy, which aids in defining the connection between each of the cooling regimes. Thus, the minimum heat flux (Q_{MHF}) defines the boundary between FB and TB, the critical heat flux (Q_{CHF}) indicates the boundary between TB and NB, while the onset of nucleate boiling (Q_{ONB}) marks the end of NB and beginning of convection (see Figure 2.8).

The proposed models are first verified against internal measurements of the reference specimens and validated with regards to test data for a specimen whose dimensions fall within the range of this study. Note that the model's verification and validation are restricted to the thermal field (i.e., temperature measurements) only.

An adequate definition of the thermal boundary condition for simulation of the quenching process shall improve the accuracy on the thermal simulation, and potentially, final distortion prediction. The present work with regards to the mathematical modeling is limited in this work to plate-like geometries, yet evidence is provided in ANNEX VIII that such variable must be accounted for cylinder-like geometries.

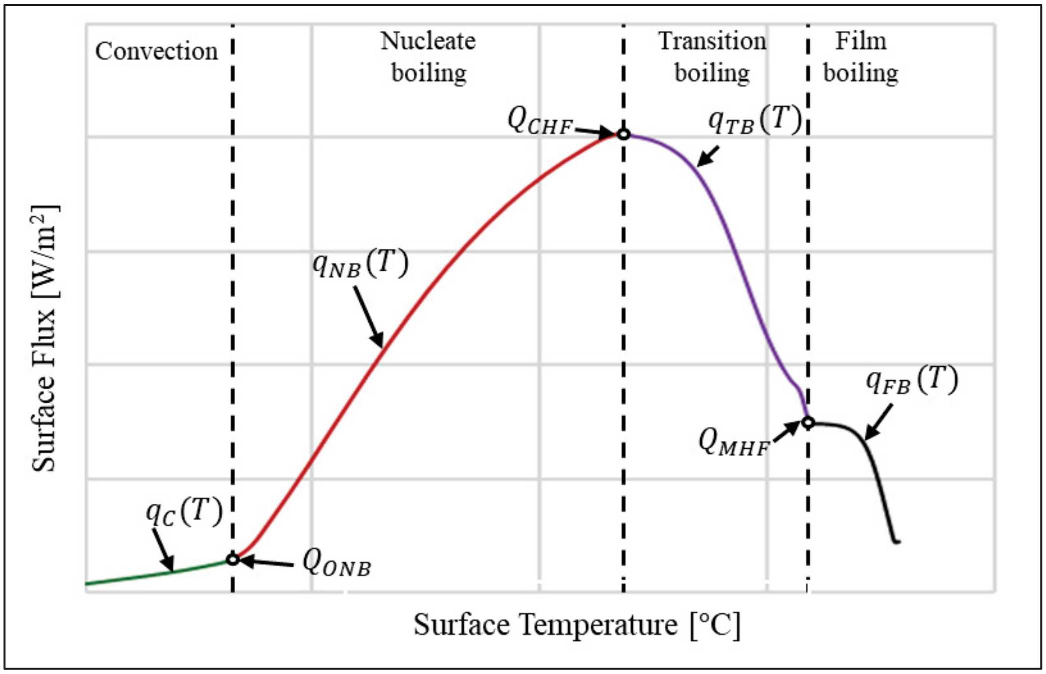

Figure 2.8 Thermal boundary conditions models during immersion

2.2 Document Organization

Thus far, this thesis has covered the existing literature addressing heat treatment and quenching, the physical phenomena, characterization methods and strategies to solve the inverse problem in the previous chapter. It is followed by the present chapter describing the main steps of the research strategy employed in this study.

The subsequent chapters and annexes provide a combination of test methods and data, strategies to identify boundary conditions by solving the inverse heat conduction problem, the resulting boundary conditions, and mathematical modeling of such boundary conditions. An overview of the content per chapter is included in Figure 2.9 to guide the reader, although the following lines provide an overview of the content per chapter/annex.

		Test Methods	Test Data	Inverse Method	Thermal BC [q(T), h(T)]	Model Build up	Model V&V
Chapter	3	✓					
	4	✓	✓	✓	✓		
	5	✓	✓	✓	✓		
	6	✓	✓				
	7				✓	✓	✓
Annex	I	✓					
	II			✓	✓		
	III	✓	✓	✓	✓		
	IV	✓	✓	✓	✓		
	V				✓	✓	
	VI				✓	✓	✓
	VII				✓	✓	✓
	VIII				✓	✓	✓

Figure 2.9 Content distribution per chapter and annex

Chapter 3 is the main reference with regards to test methods and materials; it details the technical information of the experimental work carried out throughout this study. A description of the testing facilities, test equipment, instrumentation of test specimen, and positioning system is included in this chapter. The chapter provides the test protocol under industrial environments and different test setup performed during the test campaign.

Chapter 4 evaluates two main axes of the experimental work: bath heterogeneity and specimen's orientation (see Figure 2.4). It also includes an overview of the inverse method used to estimate the boundary conditions of a plate probe. The resulting boundary conditions as per the specimen's orientation are shown in ANNEX II. Additional results combining the influence of location and orientation for different probes are included in such annex.

Chapter 5 focuses on the air transfer step of the industrial quenching process. It includes the qualitative identification of control points according to the process characteristics and test setup. The chapter also includes a methodology to estimate the boundary conditions for quench probes with different sizes. In fact, findings indicate that the boundary conditions must account for the influence of size, even for specimens that would be considered as lumped bodies as per classic heat transfer analysis.

Chapter 6 introduces the systematic review of the cooling processes during the immersion step. Different specimens and test setup are analyzed to determine the evolution of the transition temperature and duration of the cooling regimes during immersion quenching. Findings indicate that such transition points between regimes are influenced by the specimen's size and the relative duration of the regimes follows a non-linear behavior.

Following on the findings described in Chapter 5 and Chapter 6, **Chapter 7** introduces a mathematical modeling strategy to adjust the thermal BCs as a function of the Biot number, thus accounting for the size of the specimen. The two steps, air and immersion, are treated separately thus providing flexibility to treat the BC per step.

ANNEX III and ANNEX IV present the experimental test results and resulting boundary conditions for a hollow cylinder specimen and compared against the baseline plate-like probe. The latter ANNEX IV includes the influence of orientation for horizontally quenched specimens. Thereby, both annexes contribute to the axes of study as per Figure 2.4.

Supporting results for the models described in Chapter 7 are included in ANNEX V, where a crossover of the BC for plate probes with different size demonstrates the need to account for such variable in the modeling strategy. Moreover, the models described in Chapter 7 are developed for an additional setup and presented in ANNEX VI and ANNEX VII for the air transfer and immersion respectively. Lastly, ANNEX VIII presents the influence of probe size for the hollow cylinder, confirming the need to account for the influence of size for a different geometry.

CHAPTER 3

EXPERIMENTAL MATERIALS AND METHODS

This chapter presents the experimental materials and methods used in this study. Special attention is given to the heat treatment and quenching infrastructure of the industrial partner, SAFRAN Landing Systems, whose typical process and its inherent particularities were under study in this work. The chapter includes technical specifications of the acquisition system and test set up used during the test campaign.

3.1 Industrial Facilities: Layout and Tooling

The industrial partner facilities include an autenitization furnace, classified as a Class 4 furnace, with a temperature uniformity equal or better than ±10 ºC as per AMS 2750. The quench tank is a four-meter-high (≈50 k liters of oil) allocated next to the furnace as shown in Figure 3.1. Given the layout of the facilities, the heat treated load must be transferred from the pit furnace to the quench bath through air. Such air transfer requires an specific procedure as follows: upon opening the furnace, the HT-rig is locked up (0), the heat-treated load is extracted vertically (1) using an overhead crane, it continues its vertical movement until reaching a pre-defined height to clear the furnace (2), then it travels through air laterally (3) until reaching the top of the quench bath (4); the system descends before being immersed into the quenchant (5) and continues all the way down in the tank (6) where it completes its cooling. This procedure is depicted in Figure 3.1.

For the purpose of this study, the air transfer from furnace to quench bath has been assigned a duration of 120 s. Note that any standard procedure advocates for immediate immersion, thus reducing any transferring to a minimal as it creates thermal gradients inside the quenched specimen and heterogenous condition before immersion. However, such step is inevitable when dealing with industrial environments like the one under consideration. The immersion speed of the system is estimated at 203 mm/s, which remains constant along the test campaign. The quench bath has a 3-propeller agitation system that reinjects the oil flow at the bottom of the tank, a deflector is placed at the bottom redirecting the oil flow upwards. Agitation levels are maintained constant through the entire test campaign. Similarly, oil bulk temperature remains consistent for every single test run.

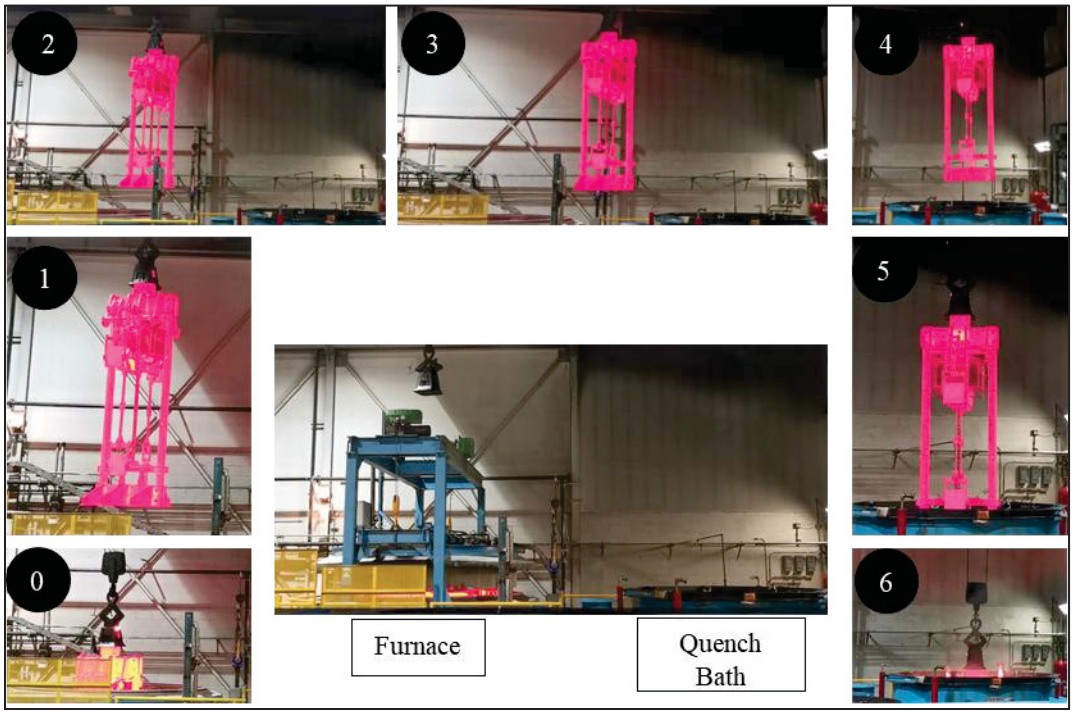

Figure 3.1 Typical quench process
Photos courtesy of SAFRAN

Under normal operations, a heat-treated load is made of the HT-rig that holds multiple components at once. For instance, a load containing A320 components has four parts loaded on the HT-rig as shown in Figure 3.2. The size and dimensions of these components is considerably bigger than any standard specimen quenched under laboratory procedures. Furthermore, the geometry of the tooling combined with the potentially different flow velocities along the HT-rig height, may produce different heat extraction rates that might induce heterogeneities while quenching. For the study presented herein, the HT-rig depicted in Figure 3.2 was used as the baseline item. As will be explained in further subsections, the data acquisition system, and probe propositioning system were purposely designed to be assembled on such HT-rig.

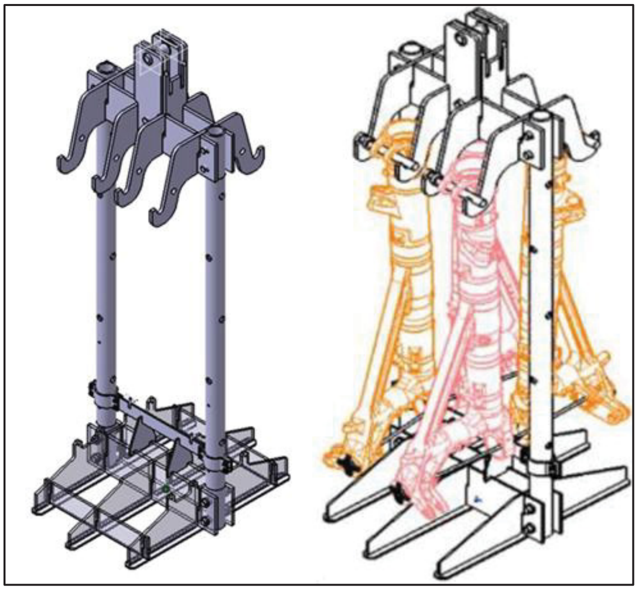

Figure 3.2 Typical heat-treated load
Courtesy of SAFRAN

3.2 Data Acquisition System

The experimental data during the test campaign was recoded using an “in-process” Phoenix TM system. The system has been designed to record the thermal evolution while going through the complete heat treatment and quenching process, hence capable to withstand the intense heat inside the furnace and thermal gradients during quenching. Using such system eases the manipulation of the test set up as there are no external devices nor items outside the envelope of the tooling.

3.2.1 Data Logger

The acquisition system is a Phoenix TM PTM1220 high temperature data logger with an accuracy of 0.3°C and a resolution of 0.1°C with a maximum capacity of 20 thermocouples. The logger was calibrated and passed as a field test instrument per AMS 2750 while all the mineral insulated type K thermocouples were calibrated as per ASTM E220. The correction factors for each of the data logger channels were accounted by the software Phoenix TM. Likewise, the thermocouple’s deviation as per their batch certificate were filled into the

Phoenix software, thus final data series output already considers both correction factors. Evidence of the thermocouple deviation at different temperatures is shown in Figure 3.3 showing the acceptability of the thermocouple batch for the temperature range of interest <900°C. Note that multiple batch were used during the test campaign, each of them fulfill the criteria as per AMS 2750 limits The sampling rate of the data logger is set to 5 Hz for every test while recording starts at 100°C.

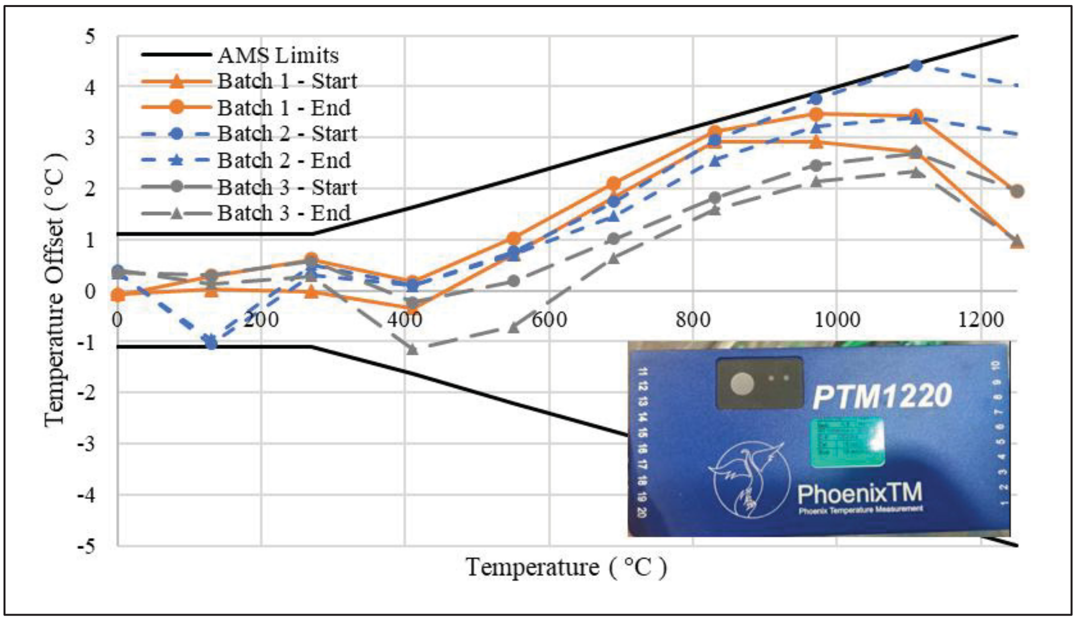

Figure 3.3 Thermocouples' deviation and data logger Phoenix TM PTM1220

3.2.2 Thermal Barriers

To withstand the temperature range of the heat treatment process and the thermal gradient while quenching, the data acquisition system is protected by a TS12 series barriers carefully engineered by Phoenix TM. The insulating system is made of two main layers: an internal thermal barrier with heat sink (that changes from solid to liquid upon reaching 58°C as per user's manual), and an outer sacrificial insulation layer (can not be used more than one quenching cycle). In addition, oil tight seals and a graphite gasket are installed at the entrance of the inner insulation layer. Schematic in Figure 3.4 illustrates the main items of the insulating barriers.

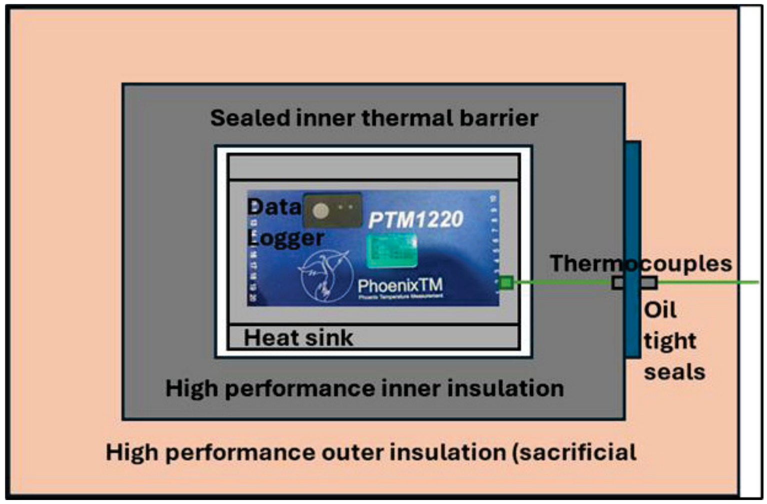

Figure 3.4 Insulation system for data logger Phoenix TM

The data logger is placed inside the heat sink in the form of a retractable tray, as shown in Figure 3.5. Each of the thermocouples must be connected to the data logger before the trey is installed inside the inner thermal barrier. The front end of the barrier is sealed using oil tight seals and a graphite gasket (see Figure 3.5). Afterwards, the sealed inner thermal barrier is allocated inside the outer insulation sacrificial thermal barriers (Figure 3.5). The system has a maximum operating temperature of 1000°C. There is a maximum operating time, depending on temperature and procedure, that must be consulted with the supplier to prevent excessive heating, even after a quenching is completed.

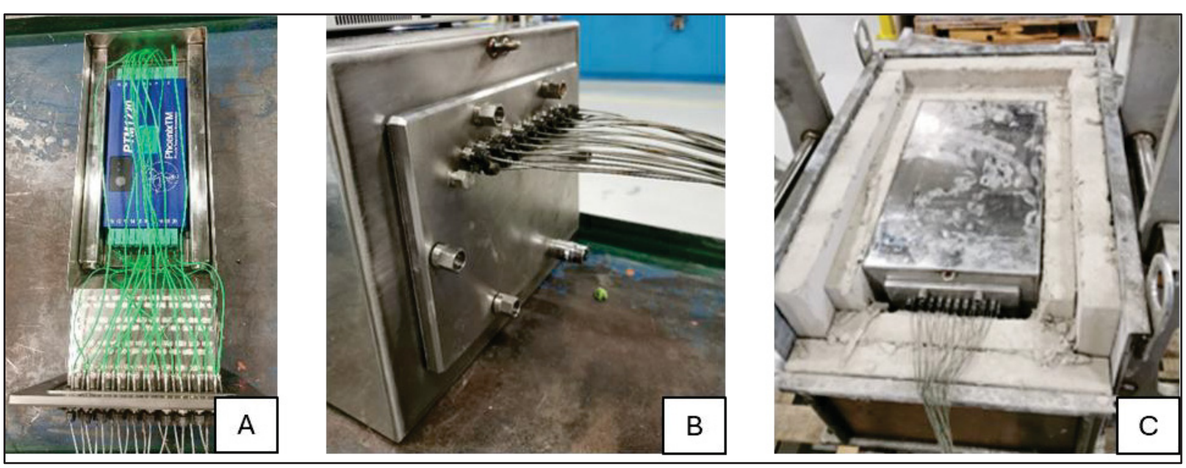

Figure 3.5 Test equipment: a) Data logger on heat sink, b) Front view of sealed inner thermal barrier, c) outer insulation barriers before closing

After a test cycle, the sacrificial external barriers remain at high temperatures and may contain oil residuals (also at high temperatures), see Figure 3.6. The removal of these insulation layers must be done with extreme care and disposed immediately after a test run. Once the inner insulation box is removed off the external layer, the data logger can be retrieved by removing the front plate of the box and pulling out the trey (heat sink). Note that condensation may appear on top of the heat sink (see Figure 3.6). Such condition is not a concern since the logger itself is sealed against moisture ingress for the battery and electronics compartment

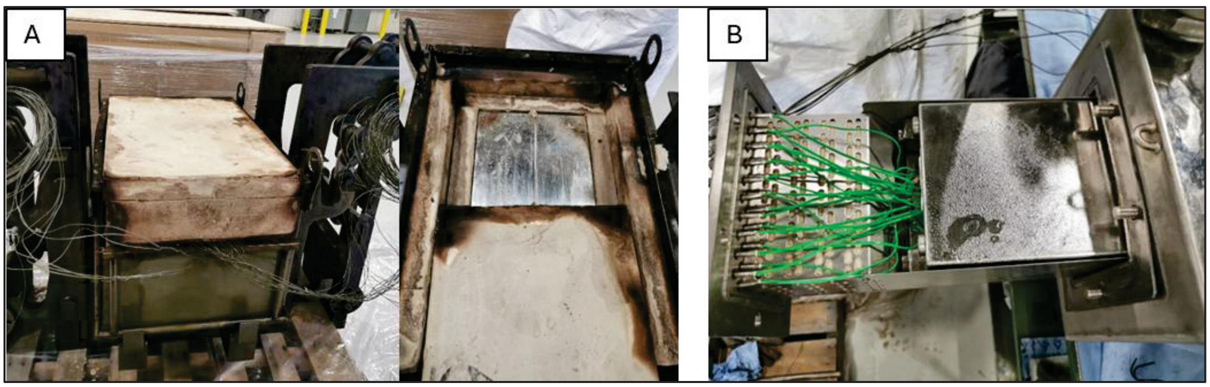

Figure 3.6 Condition of test equipment after test run a) outer insulation barriers with burning marks and oil residuals, b) heat sink with water drops due to condensation

3.3 Instrumentation of Quench Probes

The quench probes used in this study were instrumented with multiple type-K thermocouples connected to the datalogger to record the thermal history. Each thermocouple was mechanically secured at two locations. One side was secured to the front plate of the sealed inner thermal barrier, and the other end is fixed at the top end surface of the quench probe as shown in Figure 3.7. Each of these locations were carefully thigh with compression fittings that hold the sensors in place through the complete test run, ensuring the contact with the end of the bore where the thermocouple is inserted. Ceramic insulators (see Figure 3.7) were installed altogether with the thermocouple wire along the depth of the bore. This reduces any heat exchange along the bore walls to a minimal, and aids to direct the tip of the thermocouple to the center of the bottom end of the bore.

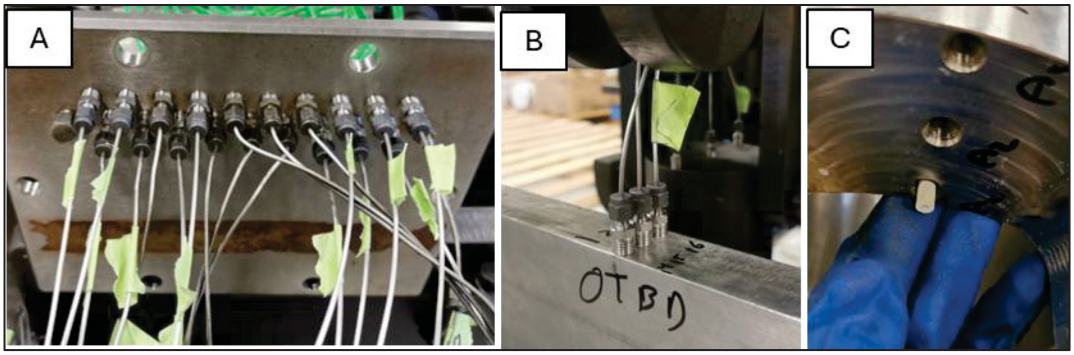

Figure 3.7 Thermocouple installation on a) front plate of insulating box, and b) top surface of quench probe, c) typical ceramic insulator

3.4 Probe Positioning System

A probe positioning system (PPS) was designed to be retrofitted onto a production HT rig as depicted in Figure 3.8. The data acquisition system protected by the insulating box is nested in the PPS at the highest allowable location of the HT-rig. This is to avoid perturbing the oil flow during immersion (i.e., undesired wakes or turbulences).

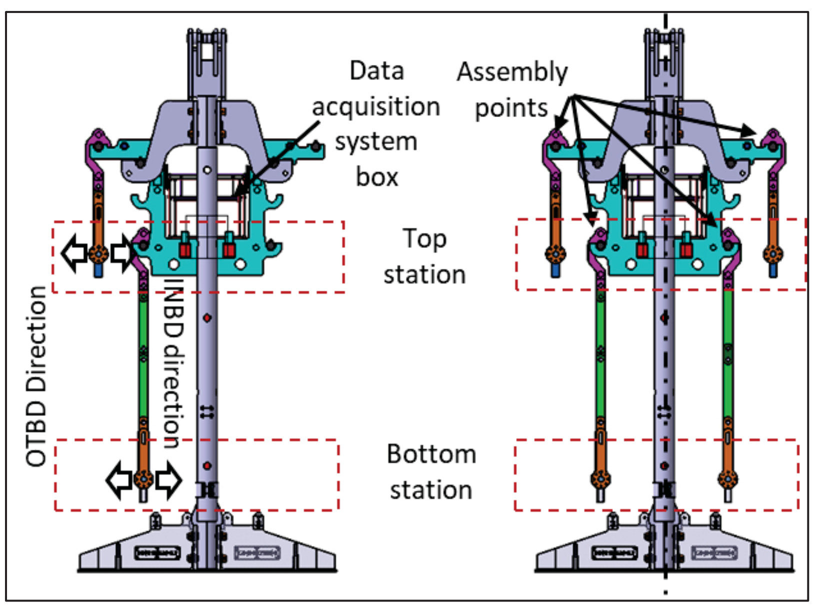

Figure 3.8 Probe positioning system (PPS) on HT-rig
Courtesy of SAFRAN

The design of the PPS provides flexibility for allocating quench probes at different heights; thus, it is possible to capture the local conditions at the top and bottom of the HT-rig. Similarly, the PPS has multiple anchor points to test a maximum of 4 specimens on a single test run. This feature allows to assess the heterogeneity of the quench bath. Likewise, the orientation of the specimens can be adjusted with regards to the oil flow. The orientation of the main surface of exchange of the quench probe with regards to the tooling must be registered for every test. The surfaces are labelled as either INBD, looking towards the mid-plane of the HT-rig, or OTBD, opposite to the tooling as shown in Figure 3.8.

The PPS is capable of hosting different and more complex quench probes designs as shown in Figure 3.9, providing that the test configuration does not exceed the maximum load per anchor point. Alternatively, more than one anchor point can be used to hold the test setup. This provides the ability to either increase the size of the tested specimen or modify the orientation of the test setup as shown in Figure 3.9.

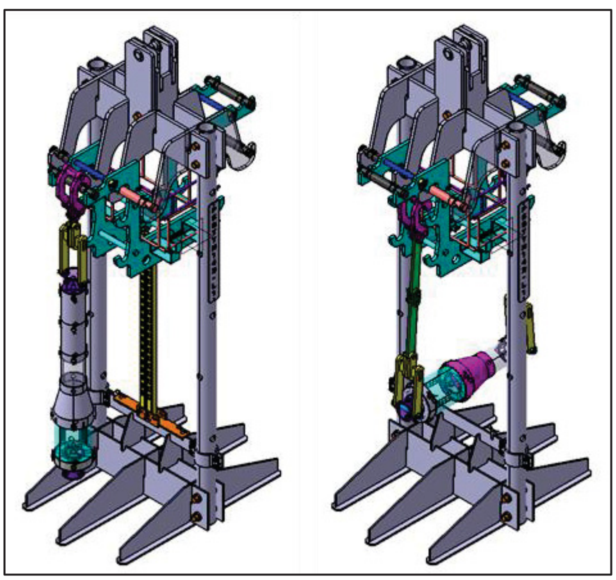

Figure 3.9 PPS capabilities to host alternative quench probe designs
Courtesy of SAFRAN

3.5 Test Protocol

The main steps of the test protocol are depicted in Figure 3.10. The initial step, labelled as system preparation, includes the installation and labeling of the thermocouples, programming of the data logger, identification of data logger channels, assembly of insulating layers, and setup of the quench probes in the desired transport configuration. Once ready, the system can be transported to the heat treatment facilities (Step 2) where the final assembly on the HT-rig is completed (Step 3). It is during this step that the actual test configuration is arranged on the HT-rig, it requires additional manipulation as the height and orientation of the specimen might be adjusted. Afterwards, a final visual inspection is carried out on each probe to ensure proper assembly and adequate conditions of the thermocouples before proceeding to the heat treatment & quenching cycle.

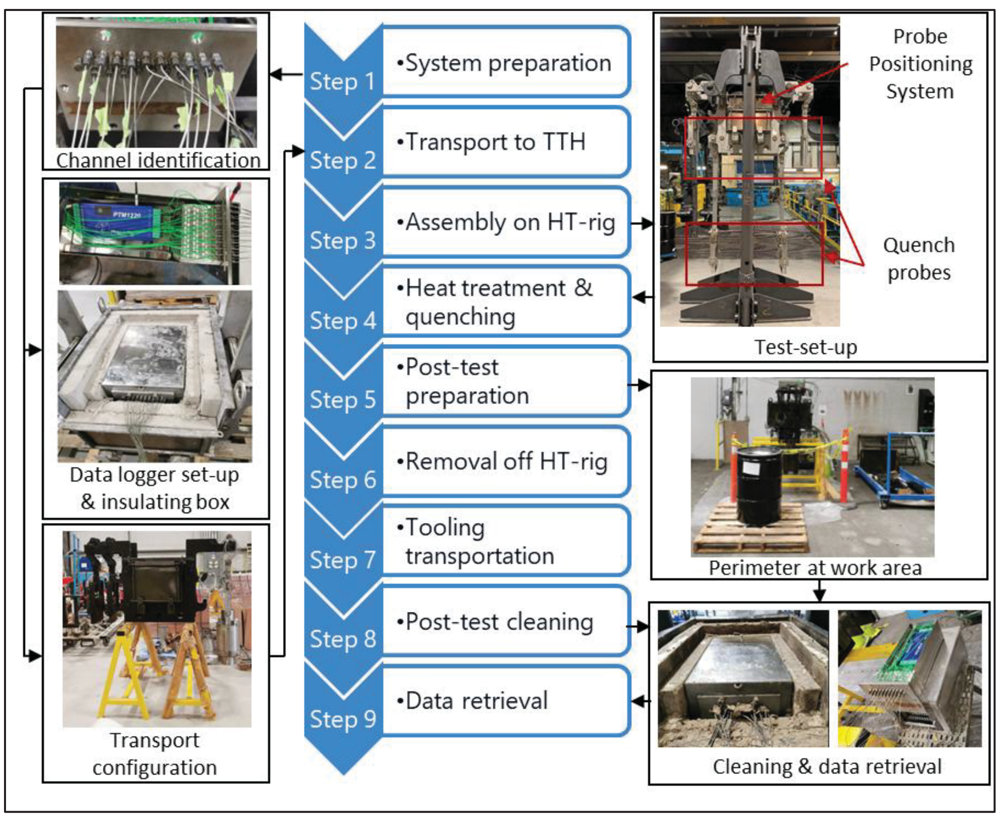

Figure 3.10 Main steps of test protocol
Photos courtesy of SAFRAN

While the test load is going through the Step 4 of the protocol, the preparations for the next tasks must be carried out (Step 5). This includes the designation of a working area for the final cleaning and retrieval of the data logger and acquisition of personal safety equipment (i.e., safety masks, high-temperature resistant gloves). Safety and health protocols must be followed as per the on-site guidelines, especially while disposing the sacrificial insulating bricks.

Once the heat treatment and quenching are completed (Step 4), the system shall be removed off the HT-rig which requires setting up the system back to its transport configuration (Step 6). Then, the system is moved to a designated working area (Step 7) where the last two steps of the protocol can be completed. The cleaning and data retrieval require the extraction of the inner insulating box to access the data logger inside. The external insulating panel must be disposed by the end of a test run. The data logger continues recording until its manually stopped upon successfully extracting the trey from the inner box, see Figure 3.6.

The typical timing of the main activities of the test protocol are listed in Table 3-1. Note that activities listed in Table 3-1 require the support of qualified personnel in the shopfloor, including the operation of lifting devices and the heat treatment facilities. This information can be used to coordinate with the heat treatment and production departments to ensure availability of the personal and equipment without altering the production cadence.

Table 3-1 Typical timing per step during test

Step	Time	Comments
Assembly on HT-rig	20min	Assembly on HT-rig using forklift
Final test setup	40min	Final adjustment of probe position using overhead crane
Furnace time	2hr	Activate atmosphere control
Oil quench	45min	Ensure agitation system is active
Water cleaning/rinse	15min	Remove oil & water excess
Removal off HT-rig	25min	System goes back to transport configuration
Cleaning & data retrieval	45min	Dispose sacrificial insulating layers

3.6 Test Campaign

The work herein has characterized the facilities of the industrial partner taking advantage of the different quench probes and capabilities of the PPS. A typical heat treatment rig was subdivided into different regions as depicted in Figure 3.11. The grid can be used to allocate a given test specimen in the working environment which then can be used to identify and select comparison cases as per the axis of study of the work herein.

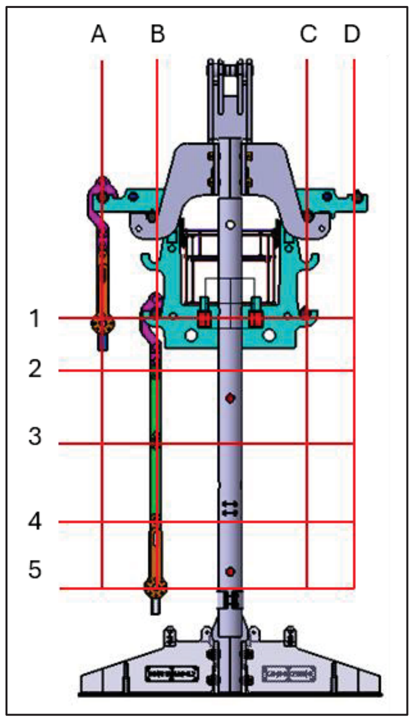

Figure 3.11 Test grid on HT-rig
Courtesy of SAFRAN

As described in the previous chapter, the main axes of study can be summarized as follows: heterogeneity of the bath, influence of probe orientation, and influence of probe size. A list of the experimental work carried out to explore these axes is included in Table 3-2. In summary, the influence of probe size is explored by test runs 1 to 6, heterogeneity of the system can be assessed with test 1-3 vs test 4-6 for a bottom vs top comparison, or test 1 vs test 7 for an evaluation of symmetry. The influence of probe orientation is analyzed based on test 1, and test 8 through 13 while also exploring the evolution of such variable along the height of the bath. Moreover, influence of probe geometry is explored with test 14 to 16. The table includes a reference to the section in this document where such test is under consideration and discussion. Note that such discussion may be focused on the experimental results itself, or the identification of the boundary condition following the solution of the inverse problem.

Table 3-2 Test campaign overview

<table>
<tr><th>ID</th><th>Probe</th><th>Row</th><th>Column</th><th>Orientation</th><th>Section</th></tr>
<tr><td>1</td><td>PPA</td><td>1</td><td>A</td><td rowspan="7">Vertical (0 deg)</td><td>Chapter 4, 5, 6, 7</td></tr>
<tr><td>2</td><td>PPB</td><td>1</td><td>D</td><td rowspan="5">Chapter 5, 6, 7</td></tr>
<tr><td>3</td><td>PPC</td><td>1</td><td>A</td></tr>
<tr><td>4</td><td>PPA</td><td>5</td><td>B</td></tr>
<tr><td>5</td><td>PPB</td><td>5</td><td>C</td></tr>
<tr><td>6</td><td>PPC</td><td>5</td><td>B</td></tr>
<tr><td>7</td><td>PPA</td><td>1</td><td>F</td><td>Chapter 4</td></tr>
<tr><td>8</td><td>PPA</td><td>5</td><td>B</td><td>Inclined (45 deg)</td><td rowspan="2">Chapter 4, Annex II</td></tr>
<tr><td>9</td><td>PPA</td><td>5</td><td>B</td><td>Horizontal (90 deg)</td></tr>
<tr><td>10</td><td>PPC</td><td>5</td><td>B</td><td>Inclined (45 deg)</td><td rowspan="4">Annex II</td></tr>
<tr><td>11</td><td>PPC</td><td>5</td><td>B</td><td rowspan="3">Horizontal (90 deg)</td></tr>
<tr><td>12</td><td>PPC</td><td>3</td><td>B</td></tr>
<tr><td>13</td><td>PPC</td><td>4</td><td>B</td></tr>
<tr><td>14</td><td>HC-A</td><td>2</td><td>D</td><td>Vertical (0 deg)</td><td>Annex III, VIII</td></tr>
<tr><td>15</td><td>HC-A</td><td>4</td><td>C</td><td>Horizontal (90 deg)</td><td>Annex IV</td></tr>
<tr><td>16</td><td>HC-B</td><td>2</td><td>D</td><td>Vertical (0 deg)</td><td>Annex VIII</td></tr>
</table>

CHAPTER 4

ANALYSIS OF INDUSTRIAL QUENCHING (AIR TRANSFER + OIL IMMERSION) AND THE COOLING REGIMES AFTER IMMERSION

Gamaliel Salazar[a], Jean-Sebastien Lemyre-Baron[a], Mohammad Jahazi[a], Henri Champliaud[a], Antoine Tahan[a]

[a] Department of Mechanical Engineering, École de technologie supérieure, 1100 Rue Notre-Dame Ouest, Montreal, QC, Canada

Paper published in *Heat Treat 2023: Proceedings of the 32nd ASM Heat Treating Society Conference*, October 2023

Abstract: Standard laboratory test methods are useful to compare the cooling performance and cooling regimes of different quenchants under controlled environments where quenching occurs almost immediately. In reality, many industries rely on systems that require transferring through air from the austenitizing furnace to the quench tank. In this project, a special quench probe apparatus is used to characterize an industrial quenching process involving air transfer followed by quenching in low viscosity oil. The probe system allows investigation of the non-homogeneous condition before immersion. The heterogeneity of the process, through air and in the oil, is captured by modifying the position and orientation of the quench probes among many experiments. Multiple characteristic points were identified during the boiling stage due to its physical significance to produce time dependent analytical curves built up through piecewise polynomial interpolation while an optimization algorithm models the convective stage. Inverse analysis is carried out with the data captured by the probes to estimate time dependent temperature boundary conditions. The output can further be computed into a temperature dependent heat transfer coefficient curve. Results indicate that the phenomena occurring after immersion differ from laboratory results thus demonstrating the significance of characterizing the actual industrial process.

4.1 Introduction

Quench hardening of steel is a common manufacturing process. The desired mechanical properties are attained by altering the physical properties of the material following a given heating and cooling cycle. Martensitic steel, a very hard material, is obtained by heating steel above its austenitizing temperature and then cooling it down very rapidly. Mineral oil is commonly used as a quenchant nowadays due to its ability to transfer heat rather rapidly, however less severely than water. Additives also allow the performance and properties of mineral oils to be adjusted.

Standard test methods (ASTM D6200-21, 2021; ISO 9950:1995, 1995) used to assess quenching oils performance rely on cooling curve analysis. Small cylinders (Ø12.5mm x 60mm) made of Inconel 600 fitted with a thermocouple will achieve, under laboratory conditions, almost immediate immersion into the quenching media vessel. As has been pointed out previously (Kobasko & Liscic, 2017), small probes generate a more obvious film boiling signature due to higher initial flux densities than their real-life counterparts. Similarly, experiments carried out to study the influence of probe diameter on heat transfer coefficient (HTC) found that film boiling progressively vanished with larger diameter probes (Liscic et al., 2011). Hence, experimentally identified HTC may not be directly generalized to any geometry. Finding applicable HTC values for components varying in size and in complexity poses a real challenge, especially when dealing with components exhibiting varying wall thickness.

Multiple methodologies have been proposed to interpret data acquired through standard testing (Canale, Lou, Yao & Totten, 2009). It is widely accepted that parameters such as max cooling rate, temperature at max cooling rate, and time to reach transformation temperature (Ms) can describe the overall performance of a quenchant regardless of the experimental procedure. However, a more detailed monitoring of the thermal history is preferred to identify the different cooling regimes during immersion quenching. Cooling curve analysis has been used to compare the properties of multiple vegetable oils to commercially available petroleum oil-based quenchants by following the procedure ASTM D6200 (Simencio Otero et al., 2018). The authors used the Tensi probe demonstrating the benefits of using multiple sensors inside the same probe body. This strategy permits a better understanding of additional phenomena occurring at different locations along the probe.

One of the few studies dealing with a transferring step between the oven and the quench tank can be found in the work of (Ferguson et al., 2012, 2013). A water quenching process is investigated using a 304SS bar with a diameter of 63.5 mm over length of 152.4mm. This study points out the importance of capturing transfer time and temperature drop before immersion quenching as their report temperature drops around 20°C to 30°C during their transfer period. The authors emphasize the need to develop industrially oriented equipment to characterize large heat treatment facilities to model the process more accurately.

For this project, experiments are carried out in the heat treatment and quenching system at SAFRAN Landing Systems Montreal. A schematic of the typical on-site heat treatment process is presented in Figure 4.1. First, the heat-treated load is extracted from the oven using an overhead crane (1), it then travels through air (2) before being lowered into the oil quench tank (3) where it completes its cooling process (4). The system comprises a four-meter-high quench tank containing +55k liters of oil and a special rig to support the heat-treated parts. Instrumenting components with thermocouples can help to appreciate the cooling performance during oil immersion and to assess the homogeneity during the heat treatment. However, over a complex geometry with varying wall thickness, such as a landing gear main fitting, the identification of the heat transfer coefficient can be challenging.

The industrial partner does perform a continuous assessment of the condition of the quenchant as per ASTM D6200. As per the typical cooling curve (see Figure 4.2), the three stages of quenching are noticeable: an initial vapor stage that collapses around 700°C, followed by a boiling stage with its maximum cooling rate near the 600°C mark while the final convective stage appears once the sample cools down around 350°C. The stability and the conformance of the results from sample to sample throughout the year may comfort the idea that the process is in control, but the cooling rates may still vary widely with the size and shape of a load.

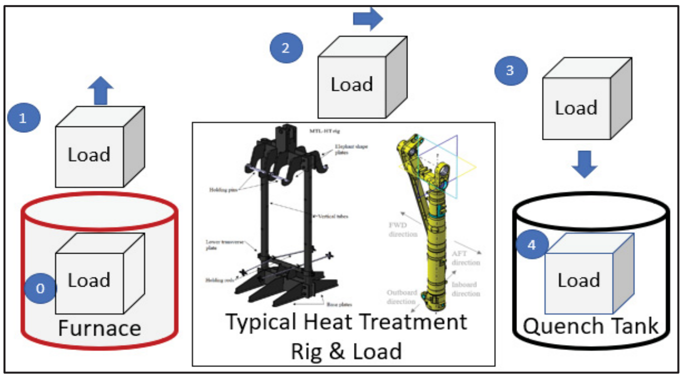

Figure 4.1 Schematic of the Heat treatment process
at the industrial partner site
Courtesy of SAFRAN

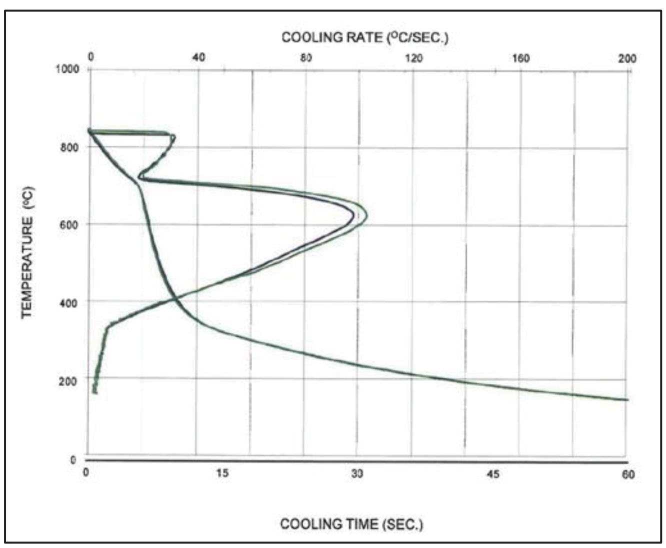

Figure 4.2 Typical cooling curve
Courtesy of SAFRAN

The objective of this study is to characterize the cooling performance of the quenching system at the industrial partner location. Multiple tests are carried out to investigate the repeatability and heterogeneity of the process while evaluating the effect of surface orientation during immersion into the oil quench tank.

4.2 Methodology

4.2.1 Design and Development of Special Quench Probes

The size of the industrial installation requires a quench probe massive enough to retain a surface temperature above 800°C after travelling through air for 120s from the austenitizing oven to the oil quench tank, and still hold enough heat after travelling three meters deep into the oil at a speed of 200 mm/s. A 304.8x304.8x50.8mm 304 stainless steel plate weighing 38 kg instrumented with three thermocouples fits this requirement.

The thermocouple wells are drilled parallel to the two main surfaces reaching down to the mid-length of the plate: two near surface and one at the mid-plane of the plate. It is known that the placement of the thermocouples on the surface or in wells may cause disturbances in the temperature field, rendering inaccurate measurements (Caron et al., 2006; Li & Wells, 2005; Wells & Daun, 2009). Provided that the thermocouples are parallel to the main surface of heat exchange, the effect of the wells on the temperature field at the probe's mid-length should be negligible (Luebben et al., 2009). Heat transfer simulations considering immersion of the probe's body into a quenching medium demonstrate that the difference against a perfect 1D heat flow case without the well is, at most, equivalent to the tolerance of the thermocouple type K. An isometric view of the quench probe and a mid-plane cut at the location of the thermocouples is presented in Fig. 3.

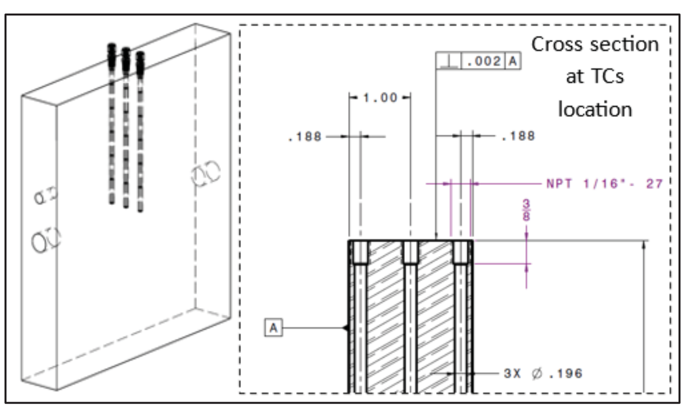

Figure 4.3 Quench probe – P1 (units in Imperial)

4.2.2 Interpretation and Comparison of Test Measurements

The experimentally acquired cooling curves are compared against different datasets depending on the study case. Given that the time before immersion is known for any dataset, such instance is selected as the reference point in time to harmonize multiple datasets. Additionally, the experimental data is converted into time dependent analytical curves through piecewise polynomial interpolation as per the methodology proposed by (Jan & MacKenzie, 2021) that consists of identifying multiple characteristic points of physical (boiling phases, Q_{MHF}, Q_{CHF}) and mathematical significance (1st and 2nd derivatives) where the polynomial between control points over a given width s_i is defined for $(t - t_1) \in [0, s_i]$ as (Jan & MacKenzie, 2021):

$$T_i(t - t_i) = a_i + b_i(t - t_i) + c_i(t - t_i)^2 + d_i(t - t_i)^3 \tag{4.1}$$

While the polynomial constants are defined as follows:

$$a_i = T_i \tag{4.2}$$

$$b_i = \dot{T}(t) \tag{4.3}$$

$$c_i = 3\frac{(T_{i+1} - T_i)}{s_i^2} - 2\frac{q_i}{s_i} - \frac{q_{i+1}}{s_i} \tag{4.4}$$

$$d_i = 2\frac{(T_i - T_{i+1})}{s_i^3} + \frac{q_i}{s_i^2} + \frac{q_{i+1}}{s_i^2} \tag{4.5}$$

As is discussed in the results section, there are several configurations that do not present a clear and stable blanket phase, thus the significant points before the critical heat flux at maximum cooling rate are identified by an optimization approach. Likewise, the transition towards the convective stage, being considerably longer in time and not as pronounced as per standard cooling curve, utilizes an optimization algorithm to identify additional reference points to model the transition towards the convective stage by reducing the penalty function. Nevertheless, the methodology facilitates the comparison of multiple parameters of interest such as temperature by the end of air travel, film boiling (if existent), maximum Cooling Rate, time to reach any temperature of interest (i.e., 300°C equivalent to Ms, etc.) for any set of data.

4.2.3 HTC Identification Strategy

For the project herein, the main steps of the identification of the heat transfer coefficient (HTC) are depicted Figure 4.4. The methodology is founded on the successful inverse identification of HTCs as outlined in previous studies using simple geometries (Bourouga & Gilles, 2010; Malinowski, Hadala & Cebo-Rudnicka, 2022; Ramesh & Prabhu, 2014b) focusing on 1D or 2D heat transfer and using internal temperature measurements. The probe's surface temperature identification strategy uses direct FEM heat transfer solution (Huiping, Guoqun, Shanting & Yigou, 2006; Li, 2003) of the temperature field coupled with a damped Newton solver algorithm (Chapra & Canale, 2010). The latter minimizes the sum of square residuals between simulation and internal measurements by iteratively optimizing linear piecewise surface temperature evolutions using sequential time intervals.

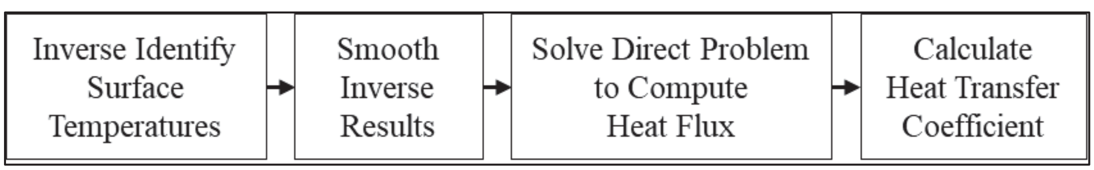

Figure 4.4 HTC identification strategy: main steps

The 1st and 2nd derivatives used to build the Hessian matrix and the gradient vector of the Newton solver equation are approximated by post processing sensitivity simulations of the modeled temperature field using numerical differentiation. The method uses commercial FE software with python scripting to run the algorithm. This allows handling effortlessly temperature dependent physical properties. The heat transfer coefficient is computed afterwards by extracting the simulated surface heat flux when imposing the identified surface temperature evolution to the modeled thermal field. Identifying the time dependent boundary temperature reduces the optimization solution domain to a bounded interval between the initial temperature and the sink temperature.

The identification of the surface temperature may suffer from numerical instability. Longer time intervals help to stabilize the results (Beck, 1970). However, this is accomplished at the expense of a reduced time resolution for the retrieved surface temperature evolution. Without a careful synchronizing, longer time intervals may incorrectly represent steep transitions. To a certain extent, identified cooling curves using smaller time intervals may exhibit contained instability, i.e. without divergence of the global solution. The curves, showing characteristic «saw teeth» can be smoothed out to eliminate non-physical behavior, such as temporarily oscillating temperatures at the surface over a certain period. Least squares B-spline regression, inspired from a point distance minimization algorithm (Flöry, 2009), is used to effectively reduce the undesired oscillations in the retrieved surface temperature from the methodology herein. The smoothed curves are then imposed as time dependent temperature boundary conditions on the FE thermal field model. With the post-processed surface heat flux extraction, the temperature dependent Heat Transfer Coefficient is derived following the well-known Newton's Law of cooling. A verification simulation using the derived HTC model finds the experimental measurements during oil quenching within acceptable values given the uncertainty range of the type K thermocouples as per AMS 2750.

4.2.4 Experimental Means & Test Campaign

The experimental part of this study is carried out at the industrial partner's facilities. Beyond heterogeneity, investigating into the influence of the heat treatment rig may confirm the hypothesis of mutually radiating surfaces during the air transfer. Moreover, heat transfer rates are likely to depend on the position and the orientation of the quench probes. Different orientations are tested as depicted in the schematic in Figure 4.5. Test A represents a 0 deg set up (vertical), Test B considers a 45 deg inclination of the probe while Test C places the quench probe fully horizontal (90 deg).

A probe positioning system (PPS) was designed to be retrofitted onto a production HT rig as depicted in Figure 4.6. This probe support assembly provides flexibility for allocating quench probes at different heights and anchor points while allowing angular displacement. A data acquisition system protected by an insulating box is nested in the PPS at the highest allowable location of the HT-rig. This is to avoid perturbing the oil flow during immersion (i.e., undesired wakes or turbulences). The acquisition system is a Phoenix TM PTM1220 20-channel data logger with an accuracy of 0.3°C & a resolution of 0.1°C. All of the probes are instrumented with mineral insulated type K thermocouples calibrated as per AMS 2750. The sampling rate is set to 5 Hz. The design of the experimental HT-rig allows for a maximum of 4 probes to be installed all at once.

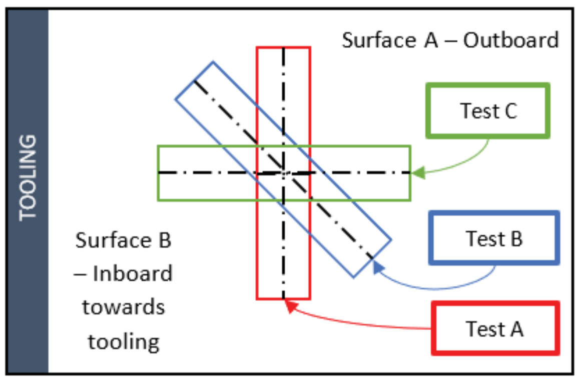

Figure 4.5 Schematic of probe orientation

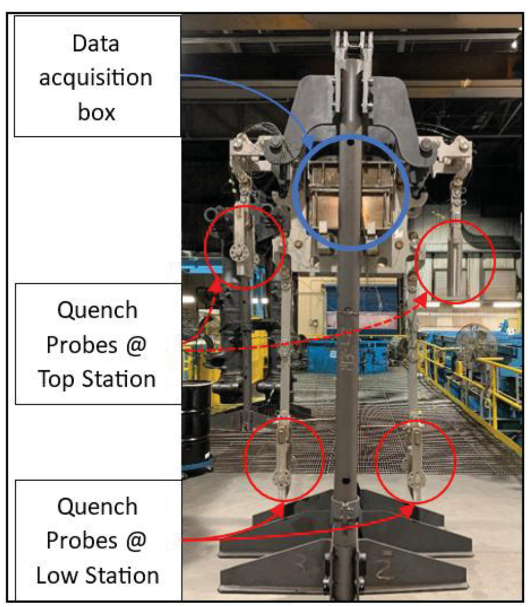

Figure 4.6 Assembly of quench probes
in test rig

4.3 Experimental Results

4.3.1 Experimental Results Repeatability

The repeatability was assessed by placing a quench probe in the exact same location on the experimental assembly for a number of tests (Test A to Test D). Sub-surface thermocouples in the INBD & OTBD surfaces are compared and shown in Figure 4.7. The curves depict the cooling process (air transfer + immersion) until the probes reach 100°C. The time scales of the curves are adjusted to synchronize immersion at 120 seconds. On average, it corresponds to the time required after initiating the extraction from the oven to reach the oil in the quench tank. Measurements obtained during the air transfer have consistent results. The highest temperature difference appears on the INBD surface sensor with 3.3°C (see Table 4-1). However, above 800°C, this discrepancy falls well within the allowable uncertainty range of a type K thermocouple as per AMS 2750.

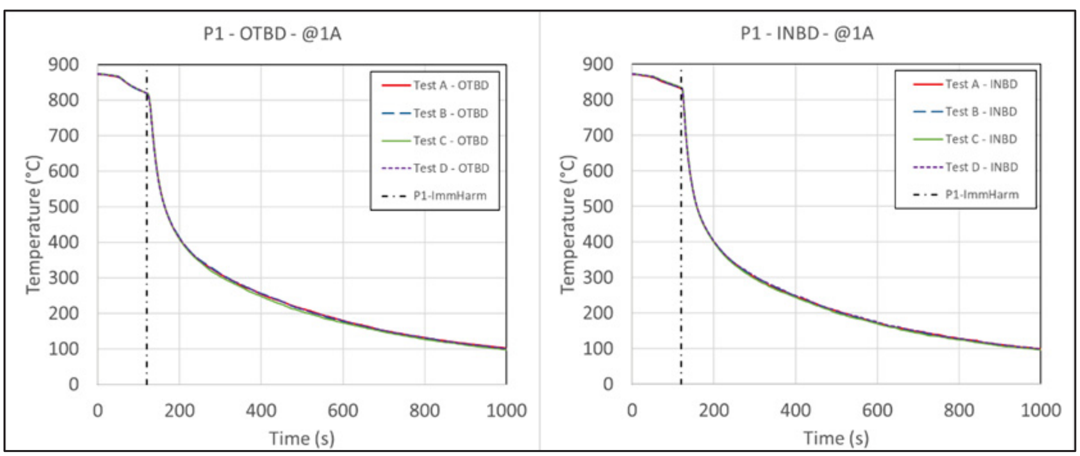

Figure 4.7 Temperature measurements (repeatability) for OTBD (left) & INBD (right) directions

By comparing the curves, the effect of mutually radiating surfaces between the INBD surface and the acquisition box is manifest. The temperature before immersion on the INBD side is always higher than on the OTBD surface as emphasized in Figure 4.8. Although predictable, the characterization of the rig transfer through air demonstrates that the radiation between hot surfaces yields an unsymmetrical temperature profile within the probes before quenching.

Table 4-1 Experimental temperature measurements before immersion (t=120s)

Temperature before immersion (°C)			
Test	OTBD	MID	INBD
A	819.6	844.1	832.1
B	818.4	843.8	831.9
C	819.8	845.6	835.2
D	819.8	844.9	833.3
Max Delta	1.4	1.8	3.3

Similarly, cooling rates of experiments A to D are compared. The first 200 seconds of the process are plotted in Figure 4.9 (for both surfaces INBD & OTBD). The apparent superimposition of the cooling rate curves show consistency even during oil quenching for the highest discrepancy does not exceed 0.7°C/s (see Table 4-2). The most interesting finding is the null vapor stage after immersion of the probe. This is consistent with the findings initially reported by (Kobasko & Liscic, 2017; Liscic et al., 2011) for relatively large cylindrical probes. It is worth mentioning that despite having a higher temperature before immersion, the INBD surface presents a higher maximum cooling rate than the OTBD surface.

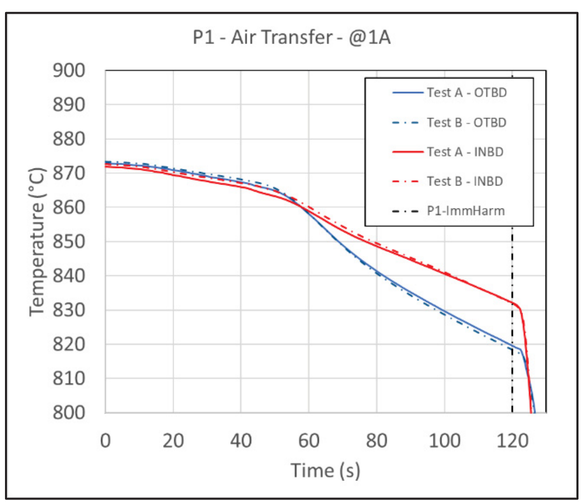

Figure 4.8 Temperature measurements during air transfer

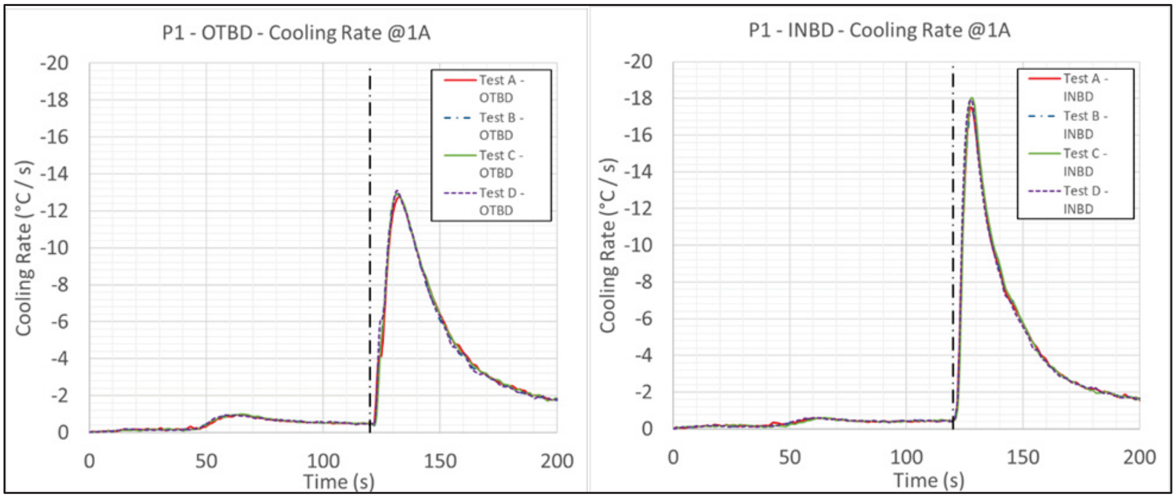

Figure 4.9 Cooling rates from t=0s to t=200s. OTBD (left) & INBD (right) directions

Table 4-2 Maximum cooling rates based on experimental data

Cooling rates (°C/s)		
Test	OTBD	INBD
A	12.8	17.5
B	12.9	17.3
C	12.9	18.0
D	13.1	17.9
Max Delta	0.3	0.7

4.3.2 Heterogeneity of the System

The heterogeneity of the heat treatment process is assessed by the symmetrical condition along the mid-plane of the heat treatment rig. Given that they are placed on opposite sides of the HT-rig, the tests labeled as D & E are compared in Figure 4.10. The cooling curves at higher temperatures are arguably consistent through the air transfer and oil immersion all the way down to the range of 350°C to 300°C. Below that, the differences start to appear as the cooling curves of Test E exhibit slower rates on both surfaces INBD & OTBD. Note that the OTBD surface presents a clearer difference between the two tests. This shows that a stronger symmetry condition exists for surfaces facing inwards or towards the tooling. Coincidentally, the range of temperature at which the differences appear would correspond to the beginning of the convective heat transfer stage in oil. Contrary to standard quenchant testing, the current characterization method does not present a clear end point for the nucleate boiling nor for the beginning of convection.

4.3.3 Probe Orientation

The influence of surface orientation during quenching is assessed by comparing different tests at selected orientations while maintaining the same location on the tooling for all the tests under comparison. For the discussion herein, the surface of the probe labelled as OTBD is facing outboard for the vertical and inclined configurations (Test A at 0 deg & Test B at 45 deg). For the horizontal set-up (Test C at 90 deg) the OTBD side refers to the top surface of the plate. Conversely, the INBD side is the bottom side as schematized in Figure 4.5. The results of these tests are presented in Figure 4.11 and Figure 4.12.

For Test C, the bottom surface develops a prolongated vapor blanket that does not appear for the other two cases A and B. Interestingly, the top surface appears to have a more consistent cooling till reaching 500°C. Below that temperature, the increasing inclination reduces the cooling rate. On Figure 4.12, the robustness of the vapor blanket on the bottom side is manifest when looking at the area below the cooling rate curve of the INBD surface (Test C at 90 deg).

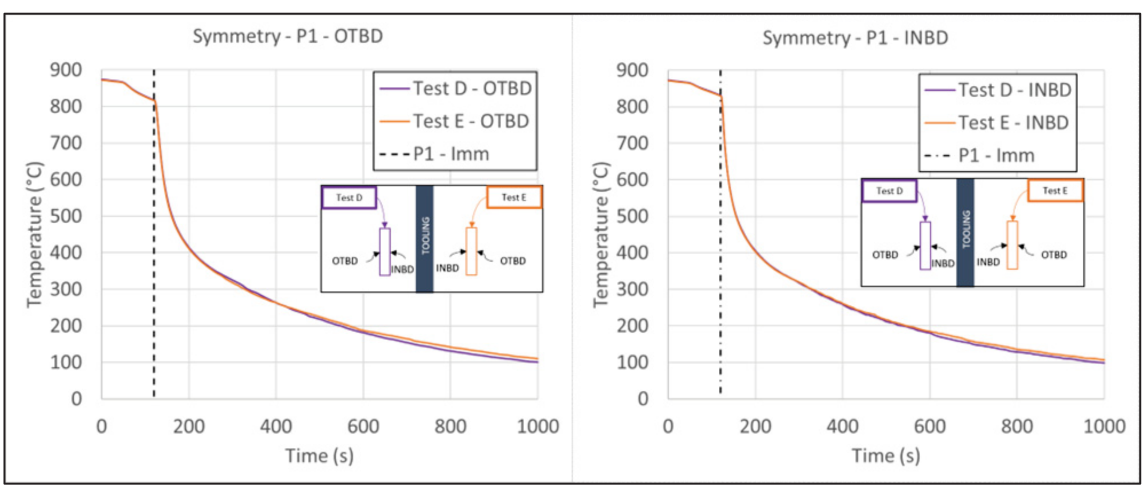

Figure 4.10 Measurements to evaluate symmetry: OTBD (left) & INBD (right) directions

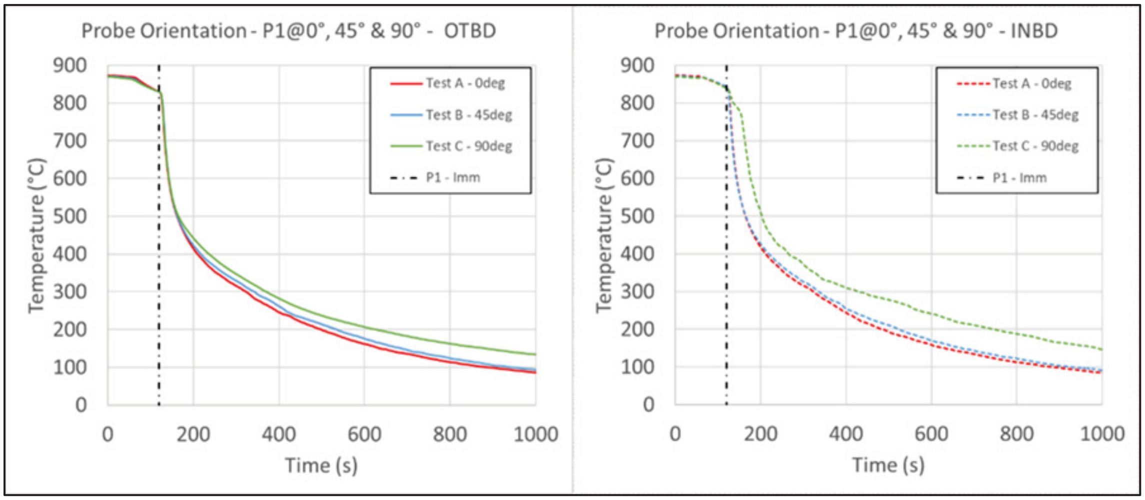

Figure 4.11 Cooling curves for different orientations: vertical, inclined (45deg) & horizontal (90deg) for OTBD (left figure) & INBD (right figure) directions

For now, on the bottom side, the inclination at which the vapor blanket starts to become robust enough to be detected is yet unknown. Since there is no apparent vapor blanket at 45 deg during Test B, the value of the angle where a stable vapor blanket appears should be comprised within the range of 45 deg to 90 deg. Nevertheless, for the purposes of having reference values, the three orientations provide a solid database for further studies.

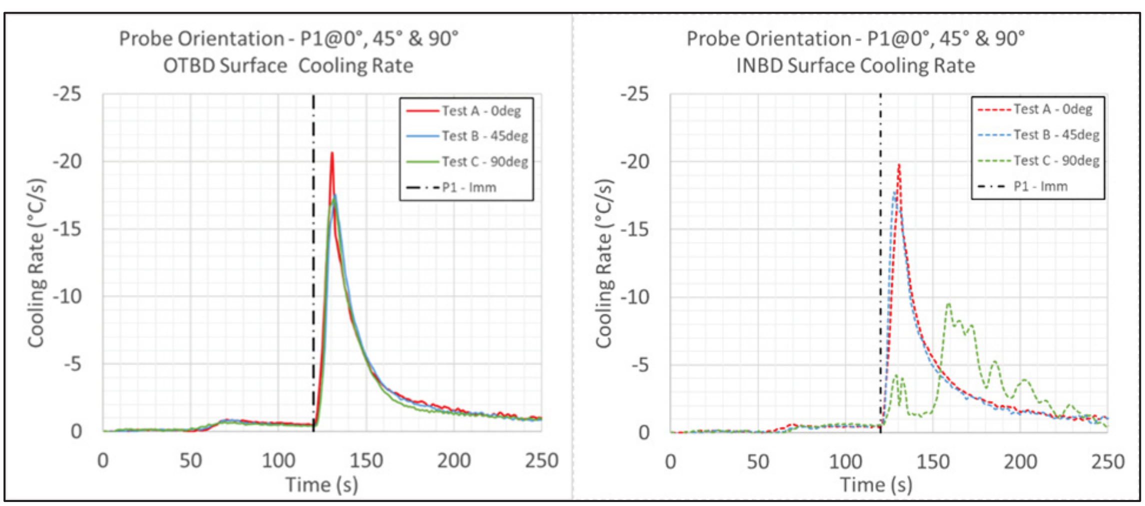

Figure 4.12 Cooling rate curves for different orientations: vertical, inclined (45deg) & horizontal (90deg) for OTBD (left figure) & INBD (right figure) directions

4.4 HTC Identification Results

4.4.1 Surface Temperature Reconstruction and Heat Flux

By using the experimentally acquired measurements, the surface temperature is reconstructed as described in the methodology section. For the discussion herein, the object of this study is to identify the HTC for a vertical plate. The reconstructed surface temperature curves are presented in Figure 4.13. The computed heat flux for both surfaces is presented in Figure 4.14. The results show that the majority of the heat is extracted between immersion at t=120s and the 300s mark when the surfaces reach 300°C, thus most of the heat contained in the quench probe is released in the first 180s after immersion. The INBD side displays a higher heat flux compared to the OTBD after immersion but lower in magnitude during the air transfer (before the immersion mark).

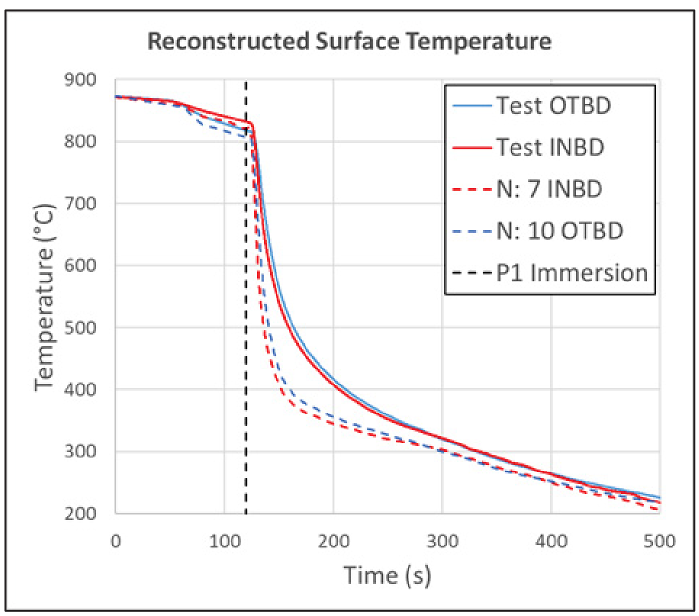

Figure 4.13 Reconstructed surface temperature for a vertical plate (INBD & OTBD surfaces)

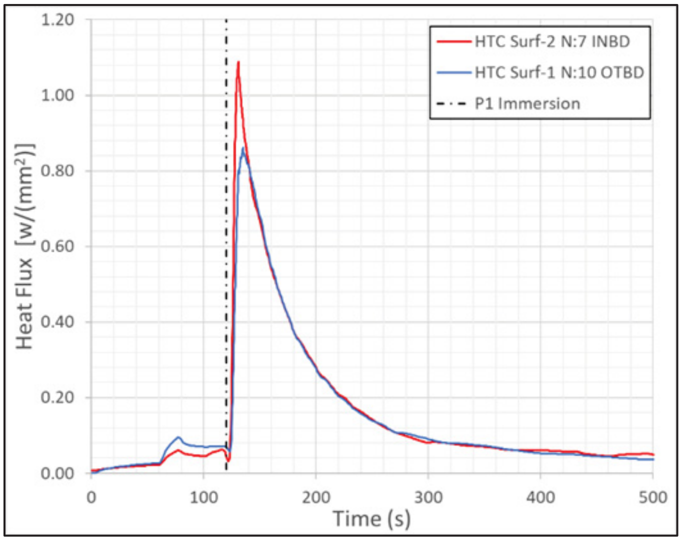

Figure 4.14 Heat Flux computation for
a vertical plate (INBD & OTBD surface)

4.4.2 Baseline HTC

One of the main objectives of the heat transfer characterization of the process is to identify the temperature dependent heat transfer coefficient (HTC) for the INBD and OTBD surfaces of the vertical plate probe (see Figure 4.15). The newly identified HTC is plotted against a previous reference HTC used by the industrial partner that had been originally obtained from DANTE Solutions (DANTE, 2019). The difference in testing methods and materials is arguably the main factor that drives the differences in the shape and magnitude of the HTCs. While the DANTE curve has a clean bell curve with a peak value around 550°C, the newly identified HTC has a rapid increase in magnitude right after immersion while maintaining its highest values for an extended temperature range. The highest value of the newly characterized HTC is barely half of the previous baseline. The only portion of the curve where the HTCs are consistent corresponds to a fully convective stage starting from 250°C downwards.

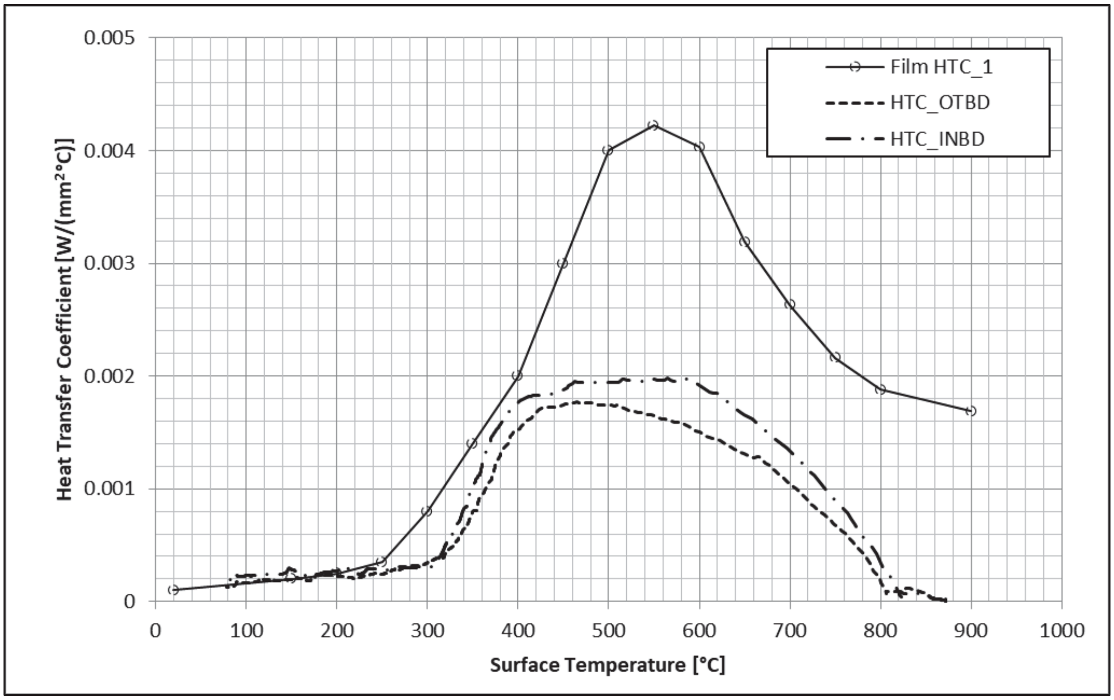

Figure 4.15 Comparison between literature values DANTE (2019, p. 4) and industrially characterized HTC

More importantly, the values obtained under this study do reflect the different conditions before (during the air travel) and after immersion on a given surface for a vertical plate. The characterization methodology can be reproduced for other cases under investigation in this study.

4.5 Conclusions

The proposed characterization methodology successfully captures the different conditions encountered in the industrial quenching process of large steel components. The results presented in this study demonstrate the non-uniform condition of the quench probe due to the air transfer before immersion in quenching oil. The non-homogeneous condition leads to different cooling performances for each surface on the same quench probe.

Contrary to standard laboratory testing results, the absence of the vapor blanket stage is confirmed for the size and conditions of the quench probe used during this test campaign.

Further study cases may address the effect of local thickness of the probes when quenched in the same conditions. The orientation of the quench probe in the quench tank results in different cooling phenomena, especially for probes quenched perpendicular to the immersion direction for which a strong vapor blanket appears right after immersion. However, further investigation is required to determine the angular orientation at which the vapor blanket stage may appear.

The strategy implemented in this study to compute the heat transfer coefficient for a vertical plate can be extended to other configurations and geometries.

Note: ANNEX II presents the resulting boundary conditions considering the influence of probe orientation, not included in this publication.

CHAPTER 5

DETERMINATION OF THERMAL BOUNDARY CONDITIONS USING PIECEWISE HERMITE POLYNOMIALS DURING THE AIR TRANSFER STEP OF AN INDUSTRIAL QUENCHING PROCESS

Gamaliel Salazar[a], Jean-Sebastien Lemyre-Baron[b], Mohammad Jahazi[a], Henri Champliaud[a], Antoine Tahan[a]

[a] Department of Mechanical Engineering, École de technologie supérieure, 1100 Rue Notre-Dame Ouest, Montreal, QC, Canada
[b] Product Improvement Engineering, Safran Landing Systems Canada,13000 Rue du Parc, Mirabel, Quebec, Canada, J7J 0W6

Paper published in *Journal of Thermal Science and Engineering Applications*, July 2025

Abstract: The study herein presents the identification of the thermal boundary conditions during the air travel step before quenching by immersion under an industrial environment. The experimental characterization was done with quench probes instrumented with multiple in-body thermocouples and tested in situ to account for the uneven cooling during the air transfer. A fast-converging numerical approach using an exhaustive search algorithm was developed to solve the inverse heat transfer problem thus estimating the unknown thermal boundary conditions. The approach reconstructs the surface temperature based on Hermite polynomials whose control points were determined as per the system movements and the underlying physics. The solver considers near-solution starting values obtained from converting the test data at subsurface locations into mathematical expressions, thereby bounding the solution domain. The proposed methodology minimizes the Root Mean Square Error (RMSE), it produces RMSE < 2°C and peak max/min errors < 3.5°C confirming the accuracy of the procedure. Findings demonstrate the need to consider the heterogenous conditions even for specimens that qualify for lumped capacitance analysis (Bi<0.1). The irradiative effects can produce a difference in heat flux magnitude in the range of 10-35% between surfaces. This tendency has appeared for values of the Bi number between 0.05 and 0.08.

Keywords: Industrial quenching, quench probes, inverse heat transfer, extensive search algorithm, Hermite polynomials

Nomenclature

a_i, b_i , c_i, d_i	Coefficients of Hermite polynomials
CP_i	Control point
c	Specific heat, J/kg K
$E_{max,min}$	Error between test and simulation results
k	Thermal conductivity, W/m K
L	Probe length, mm
$q^{"}$	Heat flux, W/m^2
$RMSE$	Root mean square error, °C
s_i	Segment size, s
T	Temperature, °C
t	Time, s
W	Probe width, mm
x	Spacial variable in x-direction

Greek symbols

Γ	Distance off surface, mm
γ	Grid spacing, mm
δ	Probe thickness, mm
ε	Surface emissivity
ρ	Density, kg/m^3
σ	Stefan Boltzmann constant, W/(m^2 K^4)

Subscripts

HP	Values obtained from Hermite polynomials
inc	Time increment
lim	Limit value of a variable

m, n	Number of observations
rad	Radiation
raw, test	Raw test data
sim	Values obtained from simulation
start, init	Starting, initial condition
step	Step increment of a variable
surf	Surface value
surr	Surrounding
trial	Trial value to test

Abbreviations

BC	Boundary Condition
CP	Control Point
FD	Finite Differences
FE	Finite Element
HP	Hermite Polynomial
HT	Heat Treatment
HTC	Heat Transfer Coefficient
INBD	Inbound (direction or location)
MID	Mid thickness (location)
OTBD	Outbound (direction or location)
PPA, B or C	Plate Probe A, B or C
PPS	Probe Positioning System
RMSE	Root Mean Square Error
SS	Stainless Steel

5.1 Introduction

The manufacturing processes of a wide range of steel components require heat treatment steps to achieve the required mechanical properties of the material. In the case of low alloy martensitic steels, used for aircraft landing gears, the heat treatment cycle involves heating the steel up to the austenite phase followed by a rapid cooling stage commonly referred as quenching, which produces the very hard martensitic phase.

Obtaining accurate and representative heat transfer coefficients (HTC) for industrial quenching processes presents a mighty challenge due to the transient nature of the phenomena, the starting condition of the heat-treated load, fluid properties, geometry, agitation levels, surface condition (Liscic, 2016; Liscic & Singer, 2013; MacKenzie & Banka, 2009). Moreover, certain industrial systems, such as pit furnaces, require an air transfer step before quenching that cannot be avoided.

The influence of the air transfer step is entirely outside the scope of any standard testing procedure (ASTM D6200-21; ISO09950:1995, 1995) as they instruct immediate immersion. However, any exposure to air before immersion is expected to decrease the start temperature (T_{start}) of the specimen. Lower T_{start} diminishes the maximum heat flux (Babu & Prasanna, 2010; Hernandez-Morales et al., 2012), destabilizes the film boiling while shifting the maximum cooling rates towards lower temperatures (Babu & Prasanna, 2010; Li et al., 2007; Maniruzzuman et al., 2012). Only a few studies openly mention the appearance of a thermal gradient inside a body before quenching due to a transferring step (Ferguson et al., 2012, 2013; Salazar, Lemyre-Baron, Jahazi, Champliaud & Tahan, 2023, 2024). Hence, the degree to which a simplified analysis (i.e., lumped bodies) could be acceptable and the influence of the environment (i.e., industrial tooling) during the air transfer step remains as open questions.

This study is centered within this context, thus focusing on the identification of the boundary conditions (BC) during the air transfer step of an industrial quenching process. Quench probes made of 304 stainless steel, 304SS, with three different thicknesses were designed, manufactured and tested with multiple in-body sensors for two air transfer setups. The inverse heat transfer problem is solved by reconstructing the surface temperature from internal measurements using a sequential Hermite polynomials (HP) fitting approach. The method using HP ensures 1st derivative continuity, bounds the solution domain and reduces the number of variables to only two on a segment-by-segment basis. The penalty function in the form of RMSE is minimized while the accuracy of the predictions is verified against mid-body temperature measurements.

The surface boundary conditions are then presented as reactive heat fluxes for specimens that could qualify for lumped capacitance analysis ($Bi<0.1$), yet the influence of the environment requires a local BC per surface to properly predict the thermal distribution by the end of the air transfer.

5.2 Experimental Methods

5.2.1 Quench Probes

The work herein considers three large plate probes made of 304SS with equal length (L) and width (W) measuring 304.8 mm. Their thicknesses (δ) are: 50.8 mm, 41.28 mm and 28.58 mm, labelled as PPA, PPB, and PPC respectively. The resulting length over thickness (L/δ) ratios (6, 7.4 and 10.7 respectively) fulfill the prerequisite to ensure a 1D condition ($L/\delta>4$) (Liscic & Singer, 2013).

The probes were instrumented with three thermocouples placed parallel to the main surfaces: two subsurface thermocouples labelled as either INBD or OTBD, depending on the surface orientation, and one in the geometrical center of the probe labelled as MID, as shown in schematic in Figure 5.1. The subsurface thermocouples are positioned at the same distance (Γ = 4.8 mm) under the surface. The wells of the thermocouples were drilled to the mid-length (L/2) of the probe. The wells may disturb the local thermal field (Caron et al., 2006, Li & Wells, 2005; Luebben et al., 2009); this is greatly diminished by placing the sensors parallel to the main surface of exchange (Luebben et al., 2009). Additional details of the instrumentation strategy can be found in previous work by the authors (Salazar et al., 2023, 2024)

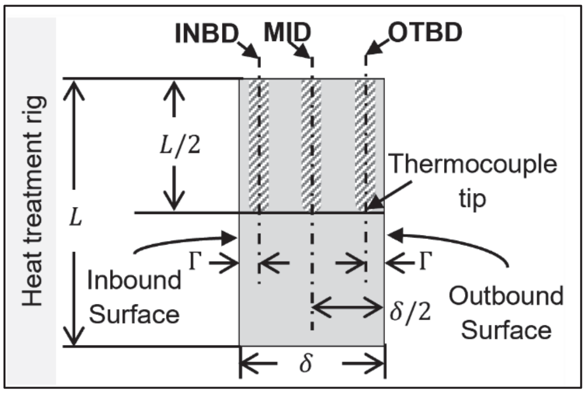

Figure 5.1 Schematic of plate probes and thermocouple locations

5.2.2 Data Acquisition Uncertainties

The test data was recorded using the Phoenix TM PTM1220 data logger. The logger was calibrated and passed as a field test instrument per AMS 2750. It has an accuracy of ±0.3°C with a level of confidence of 95%. The resolution of the logger (0.1°C) complies with the readability requirements as per AMS 2750. The maximum acquisition frequency is 5 Hz which is used for every experiment presented herein.

All the mineral insulated, metal sheathed, type K thermocouples were calibrated as per ASTM E220. The thermocouples meet the special limits (±1.1°C or 0.4%) as per specification up to 1250°C, covering the temperature range of interest (≤900°C).

5.2.3 Test Setup

The test campaign was carried out under comparable conditions to the typical heat treatment and quenching cycle under industrialized facilities. This includes using a typical Heat

Treatment rig (HT-rig), and considering the air transfer step from the austenitizing furnace to the quench bath, which can take up to 120 s. The air transfer can be subdivided into multiple steps starting with the opening of the furnace (1) to lock up the Heat Treatment rig (HT-rig) for its extraction (2). The lateral movement (3) clears the envelope of the furnace (4) until it is placed on top of the quench bath (5). Then, it descends towards the bath as the immersion process begins (6) as depicted in Figure 5.2. The identification of these steps plays a key role for the sequential approach in the proposed surface identification strategy as explained in the computational methods section.

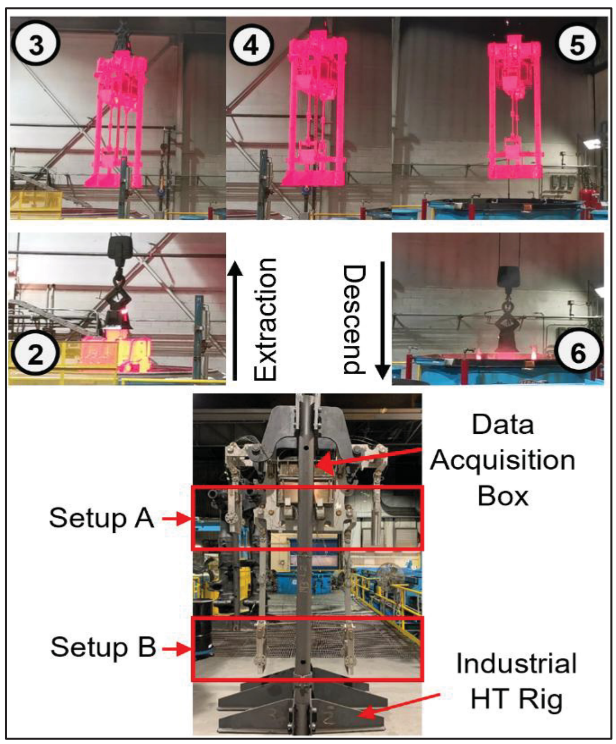

Figure 5.2 Typical steps during air transfer (top)
and experimental setup (bottom)

The transition through air was investigated using two setups: A and B, whose cumulative timing is shown in Table 5-1. The list of study cases is presented in Table 5-2 considering the multiple probes (x3) and setup (x2). Additional test runs were carried out for case I and IV to confirm the repeatability of the experimental data (Salazar et al., 2023).

Table 5-1 Cumulative time (s) per test setup

Step	**1**	**2**	**3**	**4**	**5**	**6**
Setup A	0	45	59	79	101	120
Setup B	0	58	65	85	107	120

Table 5-2 Experimental matrix (probes and air transfer setup)

Case	**Probe**	**Setup**	**Reps**
I	PPA	Case A	4
II	PPB		1
III	PPC		1
IV	PPA	Case B	2
V	PPB		1
VI	PPC		1

5.3 Computational Methods

The methodology to identify the unknown boundary conditions starts by converting the subsurface thermocouple experimental data into a mathematical expression based on the parametric identification of HPs. The resulting polynomial parameters, considered as near-solution values, become the input for the solver that identifies the surface boundary condition (BC). The solver is based on an extensive search and bracketing algorithm that minimizes a penalty function in the form of the Root Mean Square Errors (RMSE) at the sensors' locations against the experimental data. Lastly, the resulting temperature profiles obtained as BC are used as input to obtain the reactive heat flux at both INBD and OTBD surfaces of a given probe.

5.3.1 Test Data Parametrization

The thermal history of the subsurface thermocouples is converted using multiple connected third-degree HP assuring first derivative continuity at the junction points, also referred as control points (CP), and enabling to compute $T(t)$ and $\dot{T}(t)$ at any desired time.

The CPs during the air transfer step were chosen according to the timing of each movement through air as shown in Figure 5.2. These CPs are depicted in Figure 5.3 along the evolution of the typical cooling curve and cooling rate curve. The CPs may coincide with the peaks and transition of the cooling rate curve as drawn in Figure 5.3.

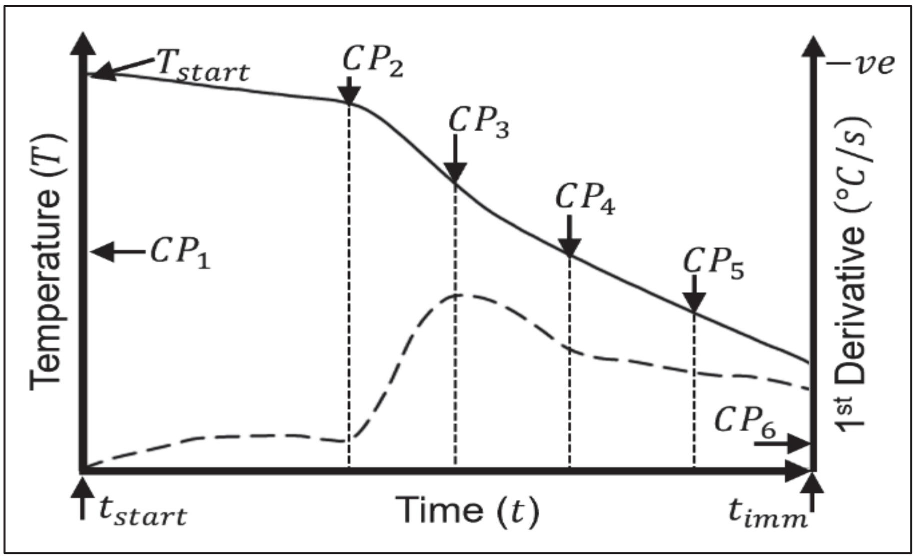

Figure 5.3 Typical cooling curve (continuous line), cooling rate curve (dashed line) and control points (vertical dotted lines) during the air transfer

The third-degree HP used to compute the analytical curve over a given time segment with size s_i given by (Jan & MacKenzie, 2021) with $(t - t_i) \in [0, s_i]$ is defined as:

$$T_i(t - t_i) = a_i + b_i(t - t_i) + c_i(t - t_i)^2 + d_i(t - t_i)^3 \tag{5.1}$$

The multiple HPs have continuous end points (T_i) and 1st order derivatives (U_i) at the CPs. Hence, the polynomial coefficients are computed as follows:

$$a_i = T_i \tag{5.2}$$

$$b_i = U_i \tag{5.3}$$

$$c_i = 3\frac{(T_{i+1} - T_i)}{s_i^2} - 2\frac{U_i}{s_i} - \frac{U_{i+1}}{s_i} \tag{5.4}$$

$$d_i = 2\frac{(T_i - T_{i+1})}{s_i^3} + \frac{U_i}{s_i^2} + \frac{U_{i+1}}{s_i^2} \tag{5.5}$$

Note that the 1st derivative of the experimental data must be computed prior to solving for coefficients c_i and d_i as shown in Eq. (5.4) and Eq. (5.5). The experimental raw data was smoothed using a rectangular filter (moving average) (Jan & MacKenzie, 2019, 2021) a priori to aid the algorithm to identify the max and the min values of the derivatives. For the case herein, the 1st derivatives were computed using a 2-point central finite difference (FD) scheme (Chapra & Canale, 2010).

The goodness of fit of the parametric curve based on the HPs $\left(T_{i_{HP}}\right)$ is evaluated against the raw data $\left(T_{i_{raw}}\right)$ by means of the RMSE as well as the max (E_{max}) and min (E_{min}) error as given by Eq. (5.6) and Eq. (5.7). Notably, the qualitative identification of the CPs produces RMSE ≤ 1°C and peak errors ± 1.6°C. As comparison, the threshold value given for the thermocouple uncertainty as per the calibration certificate of the sensors is ± 1.85°C. Hence, there is no need to implement a minimization algorithm to complete this step of the methodology.

$$RMSE = \sqrt{\frac{1}{n}\sum_{i=1}^{n}\left(T_{i_{raw}} - T_{i_{HP}}\right)^2} \tag{5.6}$$

$$\begin{gathered} E_{max} = \max\left(T_{i_{HP}} - T_{i_{raw}}\right); \\ E_{min} = \min\left(T_{i_{HP}} - T_{i_{raw}}\right) \end{gathered} \tag{5.7}$$

5.3.2 Surface Boundary Condition Identification

The identification of the unknown boundary condition requires solving the inverse heat conduction problem based on the response of the body (i.e., temperature history). Multiple strategies are available in the literature, including the function specification method, regularization methods, and gradient-based methods (Beck et al., 1996; Beck & Woodbury, 2016; Myrick, Keyhani & Frankel, 2016; Samadi, Woodbury & Beck, 2018). Different optimization strategies have estimated HTCs as polynomial functions (Colaço, Orlande & Dulikravich, 2006; Felde, 2012). Recent works integrate commercially available software with optimization algorithms (Behrem & Hrnjica, 2018; Duda & Konieczny, 2022) and implement neural networks to solve inverse problems (Bazgir & Zhang, 2024, Bouissa et al., 2019, Zhu, Chen & Han, 2022). Alternative strategies solve the direct problem in an enclosed region, followed by an inverse technique or optimization approach for the external region of the geometry (Cebula, Taler & Oclon, 2018, Li, Huang, Li, Wu & Yan, 2017, Sanchez-Sarmiento & Cavaliere, 2021).

In the present work, the identification of the unknown boundary conditions is carried out through an iterative technique solving the direct problem multiple times using different trial thermal profiles at both surfaces of the quench probe. It is assumed that the BCs follow a behavior comparable to the subsurface measurements. Thus, the already identified CPs and their resulting polynomials provide a starting shape function and bound the solution domain. The trials consist of the previously identified piecewise HP whose coefficients (a_i and b_i) are adjusted within a range defined by a bounding algorithm. Then, on a segment-by-segment basis, the trial coefficients yielding the lowest value of the penalty function are selected using exhaustive search (Colaço & Dulikravich, 2011). The penalty function is in the form of RMSE between the temperature test data and simulated cases (Fan et al., 2022; Hernandez-Morales et al., 2019). The flowchart depicted in Figure 5.4 details the different steps of the identification strategy.

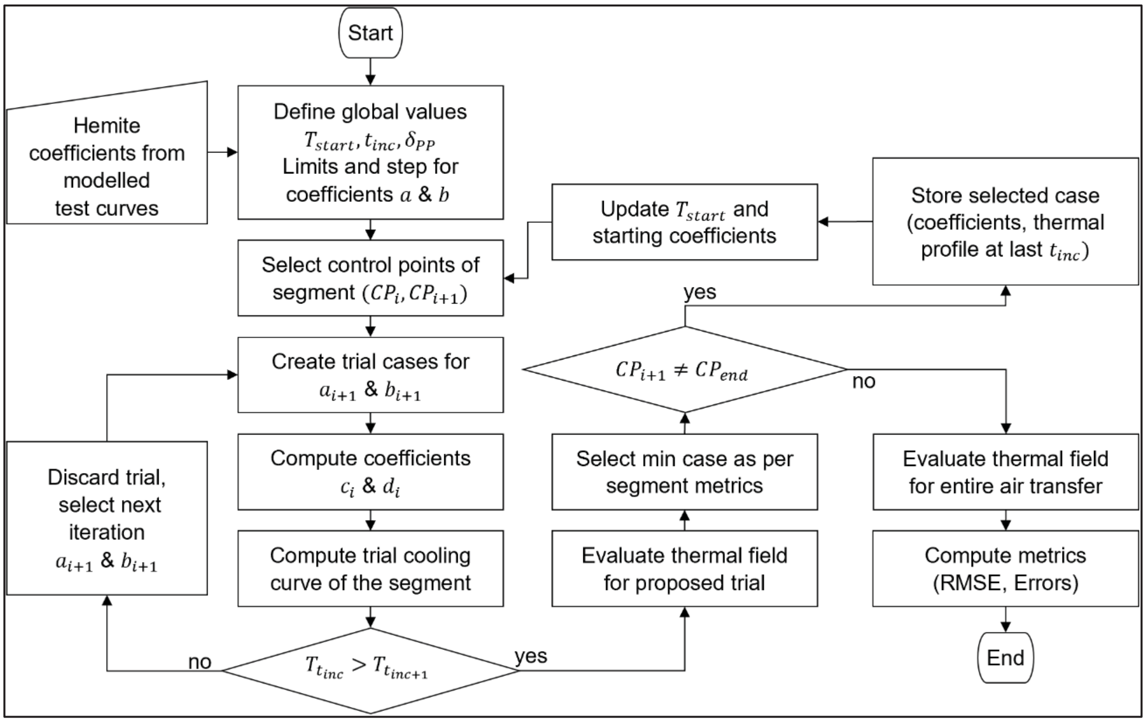

Figure 5.4 Surface identification strategy flowchart

For every trial of the BCs, the transient heat transfer through the quench probe thickness is governed by the general form of the heat diffusion equation as shown in Eq. 5.8, for a one-dimensional case without heat generation, as no phase transformation takes place in the material, but with temperature dependent material properties.

$$\frac{\partial}{\partial x}\left(k\frac{\partial T}{\partial x}\right) = \rho c\frac{\partial T}{\partial t} \tag{5.8}$$

For the case herein, the initial condition is known and can be written as:

$$T(x, t = 0) = T_{start} = 871°C \tag{5.9}$$

While the thermal history at the different sensor's location $x_0 \in [\Gamma, \delta/2\,, \delta - \Gamma]$ is known:

$$T(x_0, t) = T_{test}(t) \tag{5.10}$$

Where Γ is the distance off the surface where the sensors are located and δ is the thickness of the plate probe as shown schematically in Figure 5.5.

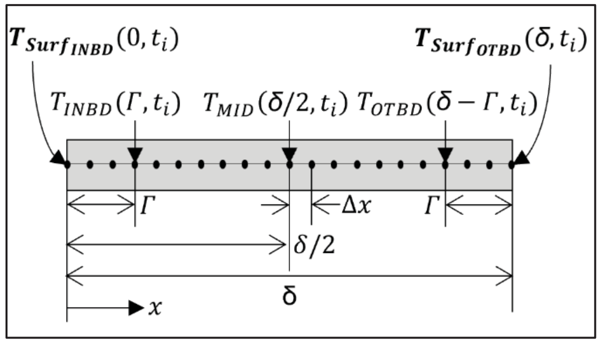

Figure 5.5 Schematic of 1D direct problem

The governing equation (Eq. (5.8)) is solved for each of the trials of the unknown thermal profiles. The direct solution of Eq. 5.8 is accomplished using the implicit form of the FD method, which is unconditionally stable (Bergman et al., 2011; Ozisik & Orlande, 2000). Temperature dependent physical properties of 304SS were considered by adjusting their values for (t_i) based on the mean temperature at the known time increment (t_{i-1}). The geometry was discretized into an equally spaced 1D nodal network (see Figure 5.5). The grid size (Δx) for each quench probe as well as the time increment (Δt) are given in Table 5-3.

Table 5-3 Grid size and time increment for the implicit FD method

Parameter	**PPA**	**PPB**	**PPC**
Grid size (Δx) [mm]	0.508	0.413	0.286
Time increment (Δt) [s]		1	

Given the sequential nature of the proposed strategy, the HP as per Eq. (5.1) representing a trial BC is evaluated by using the coefficients defined by (Eq. (5.2) to Eq. (5.5) for a pair of consecutive CPs, namely CP_i and CP_{i+1}, thus becoming the BCs to solve Eq. 5.8. Notably, the strategy requires only two unknown variables (a_{i+1}, b_{i+1}) to be identified per segment, which is advantageous as any other high order polynomials (i.e., quadratic, or cubic) require a higher number of variables to be found. The cost function (see Eq. (5.6)) is evaluated for the time intervals within CP_i and CP_{i+1}. The resulting constants of CP_{i+1} become the input for the subsequent segment. Once the solution is found for all the segments, a verification case is run using the newly found constants through the entire air transfer and evaluating the cost function versus the core readings to produce a global RMSE.

Additional constraints were implemented to redirect the search algorithm and bound the solution domain ensuring the unidirectional behavior of coefficients a_{i+1} and b_{i+1} as per (Eq. (5.11) and Eq. (5.12) respectively, and a decrease in temperature at any time increment (t_{inc}) in Eq. (5.13).

$$a_{init_{i+1}} \geq a_{trial_{i+1}} \quad \text{for} \quad a_{trial_{i+1}} \in \left[a_{init_{i+1}}: -a_{step}: a_{init_{i+1}} - a_{lim}\right] \tag{5.11}$$

$$b_{init_{i+1}} \geq b_{trial_{i+1}} \quad \text{for} \quad b_{trial_{i+1}} \in \left[b_{init_{i+1}} - b_{lim}: -b_{step}: b_{init_{i+1}}\right] \tag{5.12}$$

$$T_{t_{inc}} > T_{t_{inc+1}} \tag{5.13}$$

5.3.3 Surface Heat Flux Computation

The last step involves solving the direct problem one last time for the complete air transfer step using the identified thermal profiles $T_{Surf_{OTBD}}$ and $T_{Surf_{INBD}}$ as the BCs. The commercially available FE package Abaqus was used to solve a FE model made of 4-node linear elements (DC2D4) while considering variable material properties. The model mesh was adjusted for each probe as per their thickness while maintaining an element size ≈0.1 mm. Simulation results at nodal positions as per the in-body sensors were used to compute the final metrics (i.e., RMSE) considering all the sensors at once. Providing the results were within a 5% relative difference between simulation and test data, the time-dependent reaction heat fluxes at both surfaces INBD and OTBD were extracted by post-processing the FE simulation results.

5.4 Results and Discussion

The experimental results of the test campaign as outlined in
Table 5-2 are discussed first, followed by the numerical results from the parametrization of the test data and the identification of the surface boundary conditions.

5.4.1 Experimental Results

5.4.1.1 Test Data Repeatability

The repeatability of the test configuration was investigated for case I and case IV (see
Table 5-2). The variability of the experimental measurements remains within an envelope of ≈4°C as shown in Figure 5.6. Such value is consistent with the variation in experimental temperature readings obtained for a test plate cooled by air at comparable high temperatures (Malinowski et al., 2022). Thus, concluding that the experimental readings are repeatable during the air transfer. An average curve per thermocouple location was computed for both cases I and IV to maintain a single temperature profile per sensor.

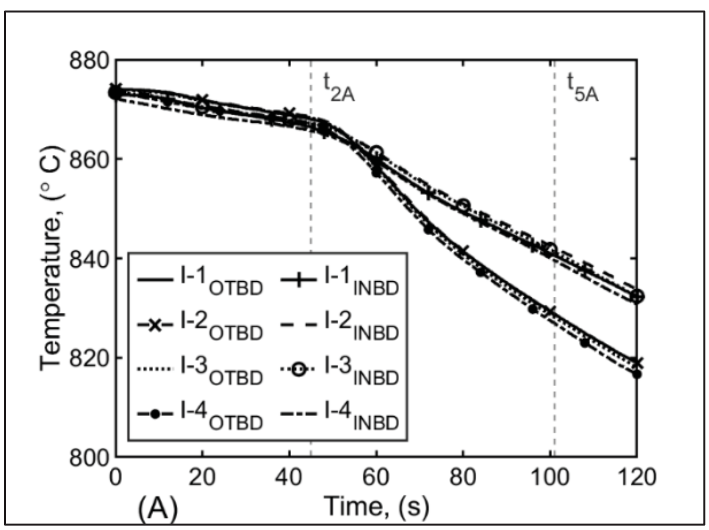

Figure 5.6 Experimental measurements:
Repeatability for case I

5.4.1.2 Temperature Evolution during Air Transfer

The cooling curves of the three probes: PPA, PPB, and PPC, during the air transfer step are shown in Figure 5.7B for setup A and Figure 5.7C for setup B as per the test cases labeling. Notably, the decrease in temperature follows an unsymmetrical profile across the ruling section of the probes regardless of the setup. This is mainly caused by the influence of mutually radiating surfaces as the mid plane components (i.e., tooling, acquisition box) remain at higher temperatures which slows down the cooling rate on the INBD surface.

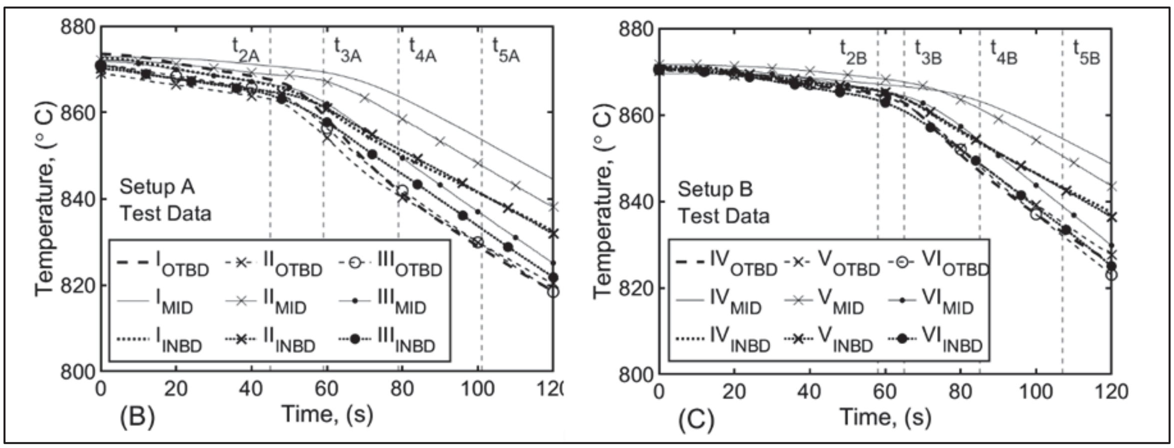

Figure 5.7 Experimental measurements
(B) Test data for cases I to III, and (C) cases IV to VI

The max temperature delta, computed by the difference between MID and OTBD readings, was reported for test case I at ≈26°C (Figure 5.7B). The temperature gradient becomes more evident once the probes have passed t_2. The thinner probe PPC has the least heterogenous condition compared to the thicker PPA and PPB.

These observations are relevant to the application in the industrial process given that the actual temperature profile before immersion is unknown and will differ depending on the thickness of the heat-treated load. Moreover, the final temperature was different depending on the setup, mainly attributed to the timing of the system movements.

5.4.2 Computational Results

The computational results can be subdivided into three stages: 1) test data parametrization based on HPs, 2) surface temperature reconstruction, and 3) verification of surface heat flux with FE. Notably, the resulting metrics at the different steps in the form of RMSE always remain < 2°C, while the peak (max/min) errors remain < 3.5°C, and relative errors ≈1%, well within the initial threshold < 5%. Based on the above findings, it can be concluded that there is no drastic decline in the accuracy levels for the explored cases.

5.4.2.1 Test Data Parametrization

Among all the parametrized cases, test case VI PPC-INBD had its highest peak error (≈1.6°C) as drawn in Figure 5.8, which was deemed acceptable given the uncertainty of the thermocouple at such high temperatures. Notably, the resulting time-dependent cooling curve $T(t)$ and cooling rate curve $\dot{T}(t)$ were adequately represented. Both curves indicate great similarities between test data and the resulting HP curve (see Figure 5.8), thus demonstrating the benefits of using a third-degree Hermite polynomial. The largest offset between both raw data and HPs series appeared before the t_2 mark, an instance where the tooling is being extracted from the furnace (between CP1 and CP2). The same condition was observed for all the cases. Nevertheless, the peak values are still acceptable (max 1.6°C, min -0.1°C), as well as the RMSE thus no additional control points are needed for the air transfer.

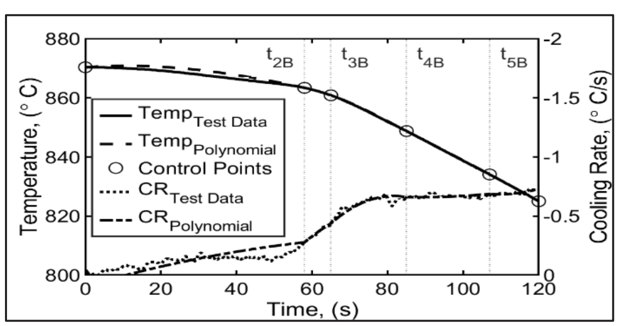

Figure 5.8 Cooling curve and cooling rate curve for test data parametrization case VI

5.4.2.2 Surface Temperature Reconstruction

Time increment sensitivity: The influence of the time increment was assessed for the first three cases listed in Table 5-2. The resulting RMSE at the subsurface sensors for multiple time increments used in the solver (12 s, 10 s, 8 s, 5 s, 2 s, 1 s) are shown in Figure 5.9. Results indicate RMSE values <2°C for the tested time increments. If computation time was a constraint, the time increment could be increased easily up to 5 s without compromising in the accuracy of the results as the RMSE barely improves for the more refined values. Further results were obtained with a time increment of 1 s as computation time was not a constraint.

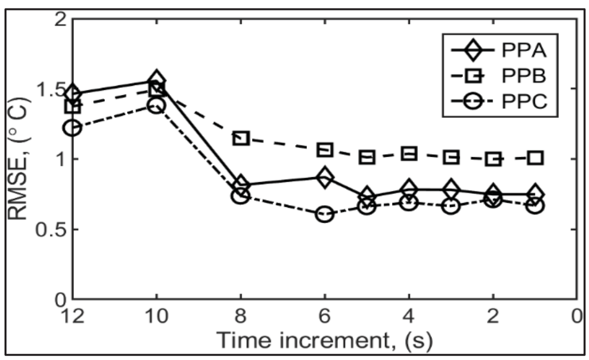

Figure 5.9 Time increment sensitivity: $RMSE$ for subsurface sensors for cases I to III

Metrics from surface temperature reconstruction: Test case II was identified as the worst case, it had the largest RMSE for any MID sensor (≈1.7°C) as well as the largest peak error computed at -3.3°C. The temperature evolution for the three sensors and its corresponding error (delta between simulated and test data) is depicted in Fig. 9. The largest errors appeared at the beginning of the thermal history for the subsurface sensors, always within the t_1 to t_2 timeframe, as the starting temperature of the experimental dataset differs from the "predefined" value. On the other hand, the largest error ("min") for the MID sensor appears near the 60 s mark, almost overlapping the t_3 mark. Given the high temperatures at which these readings are obtained, the resulting thermal profile and metrics (RMSE, max/min errors) are deemed acceptable.

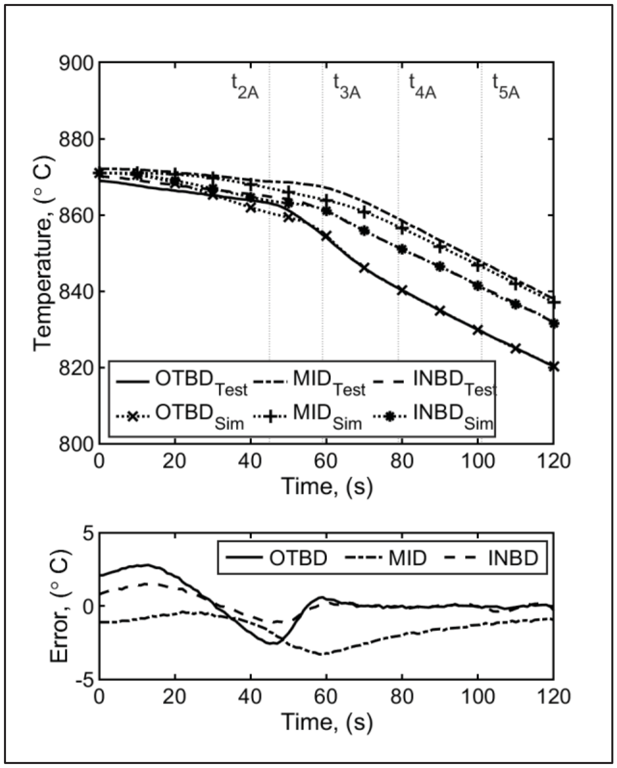

Figure 5.10 Results for “worst” case II PPB. Simulated temperature and test data (top). Error as difference between simulation and test data (bottom)

5.4.2.3 Surface Heat Flux

The heat flux during the air transfer was obtained by solving the direct problem using the reconstructed surface temperature profiles on a FE model. At this stage, the RMSE values considered the three sensors (OTBD, MID, and INBD) at once, resulting in values ≤ 2°C. Similarly, the max relative difference was always below 5% for all cases confirming the accuracy of the simulation.

The resulting reactive heat fluxes drawn in Figure 5.11 and Figure 5.12 are presented as a function of the Biot (Bi) number (Eq. 5.14) and the evolution in the time scale in its dimensionless form as the Fourier number (Eq. 5.15):

$$Bi = \frac{h_r L_c}{k} \tag{5.14}$$

$$Fo = \frac{\alpha t}{L_c^2} \tag{5.15}$$

Where L_c^2 is the characteristic length given by half the plate thickness (δ/2), k and α are the material thermal conductivity and diffusivity, and h_r the radiative HTC whose value was obtained using the relation given by (Bergman et al., 2011) as:

$$h_r = \varepsilon\sigma(T_{surf} + T_{surr})(T_{surf}^2 + T_{surr}^2) \tag{5.16}$$

Where σ is the Stefan Boltzmann constant $5.67 \times 10^{-8}\, W/(m^2K^4)$), ε is the surface emissivity for heavily oxidized stainless steel (Bergman et al., 2011), and T_{surf} and T_{surr} represent the surface and surrounding temperatures respectively. The values considered in Eq. 5.14 to Eq. 5.16 are shown in Table 5-4.

Table 5-4 Parameters used to calculate Bi and Fo numbers

Parameter	**Value**
Thermal conductivity[a] (k) [W/m K]	27.4
Thermal diffusivity[a] (α) [m^2/s]	5.74E-06
HTC (h_r) [W/m^2 K]	87.8
Surrounding temp (T_{surr}) [K]	313.15
Surface temp (T_{surf}) [K]	1143.15

[a] Thermal properties obtained for 870°C (Bergman et al., 2011)

Notably, the resulting Bi number for the three quench probes, 0.08, 0.07 and 0.05 for PPA, PPB and PPC respectively, fulfils the criteria of a lumped body ($Bi \leq 0.1$) as per classic textbooks (Bergman et al., 2011). This is one of the reasons why the air transfer step is widely simplified. Such simplification neglects the thermal distribution inside the body at the end of the air transfer caused by the heterogenous condition in the environment and thus disregarding its impact on the remaining cooling once immersion occurs.

Figure 5.11 presents the surface fluxes for case I PPA, clearly drawing the difference in heat flux magnitude between OTBD vs. INBD surfaces for $Bi = 0.08$. The different BCs are clearly noticeable once t_2 is passed, reaching its peak around t_4. In fact, the OTBD heat flux is ≈35% higher than INBD heat flux from t_4 onwards. The theoretical net rate of heat flux per unit area as per (Bergman et al., 2011), also included in Figure 5.11, is given by:

$$q''_{rad} = \varepsilon\sigma(T_{surf}^4 - T_{surr}^4) \tag{5.17}$$

Equation 5.17 was evaluated at the predicted surface temperature (T_{surf}) at discrete times from t_3 onwards. Direct comparison between the theoretical values and the identified fluxes leads to a 16% difference. Such differences can be attributed to the variable condition (transition steps) of the system, with additional influences on the OTBD due to the combination of convective and irradiative effects of the tooling in the INBD surface.

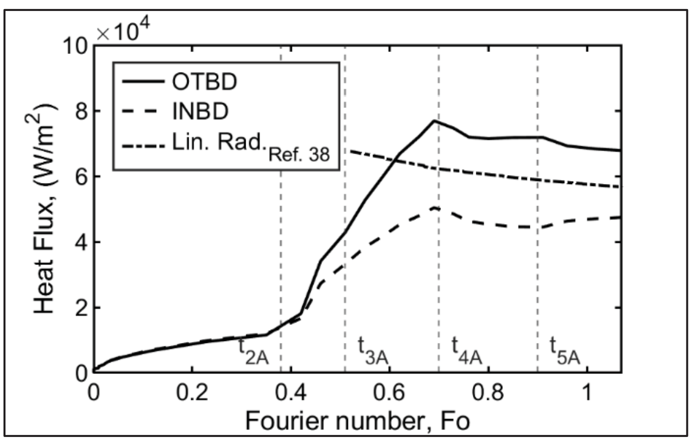

Figure 5.11 Comparison of reactive surface heat flux for case I, Bi=0.08. Linearized radiation heat flux rate as per Eq. 5.17 as per Bergman et al. (2011, p. 10)

The resulting heat fluxes profiles are segregated per air transfer setup in Figure 5.12. Note that the Fo number is different for the three probes as L_c varies. As Fo increases, the fluxes reach a plateau after their summit. On the OTBD surfaces (continuous lines, Figure 5.12), the max heat fluxes vary in the range of 50-80 kW/m^2 whereas on the INBD surface (dashed lines, Figure 5.12) oscillate between 30-50 kW/m^2.

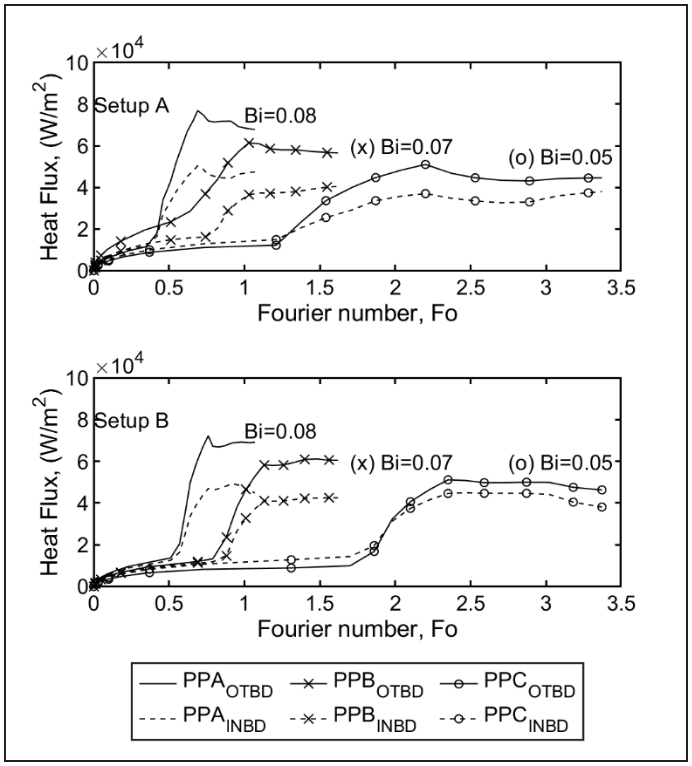

Figure 5.12 Surface heat flux using setup A (top) and B (lower) as a function of Bi and Fo numbers. Results for OTBD surfaces (continuous lines) and INBD surfaces (dashed lines)

Overall, the surfaces fluxes are higher on the OTBD surface compared against the INBD surfaces. This becomes more noticeable as the Bi number increases regardless of the test setup (see Figure 5.12), even the smaller Bi (0.05) has a difference of ≈10% between both surface fluxes. Based on these findings, specimens with $Bi \geq 0.05$, should consider the radiative effects of the tooling as their boundary conditions are non-homogeneous during the air transfer step.

5.4.3 Conclusions

The thermal boundary conditions during the air transfer step of large quench probes under an industrial environment were determined in the present study. Based on the experimental and computational results, the following conclusions were drawn:

- The heterogeneity, due to the in-situ conditions, produces an uneven thermal gradient across the probe thickness. The thermal gradient becomes more noticeable as the Biot (Bi) number increases.
- The parametrization of the test data using HPs is accurate enough (within the thermocouple uncertainty) thus no minimization algorithm is required.
- The proposed methodology to identify the boundary condition produces accurate results as per the metrics in the form of RMSE (< 2°C), peak errors (< 3.5°C) and relative errors (< 5%).
- The comparison between theoretical model (linearized heat flux) and reactive heat fluxes from this study indicates a variation of 16% which highlights the need to characterize industrial environments.
- Specimens with $Bi \geq 0.05$ should consider a local definition of their BCs to account for the heterogeneity of the system.

CHAPTER 6

ANALYSIS OF COOLING REGIMES AS A FUNCTION OF BIOT NUMBER DURING QUENCHING BY IMMERSION

Gamaliel Salazar[a], Jean-Sebastien Lemyre-Baron[b], Mohammad Jahazi[a], Henri Champliaud[a], Antoine Tahan[a]

[a] Department of Mechanical Engineering, École de technologie supérieure, 1100 Rue Notre-Dame Ouest, Montreal, QC, Canada
[b] Product Improvement Engineering, Safran Landing Systems Canada,13000 Rue du Parc, Mirabel, Quebec, Canada, J7J 0W6

Paper published in *Heat Transfer*, November 2025

Abstract: This paper analyzes the transition temperature and duration of the cooling regimes (film boiling, transition boiling, nucleate boiling and convection) during quenching by immersion of specimens covering a range of Biot numbers (Bi) from 0.70 to 1.32. Test data was acquired under an industrial environment, thus capturing the in situ conditions, an information that is rarely available in the literature. The experimentally acquired cooling curves were processed to determine characteristic points, in the form of time, temperature and cooling rate, representing the transition between cooling regimes. These points were precisely identified as per the inflection points and peak of the cooling curve. The results show that transition temperatures tend to decrease with the Bi number following a linear behavior. Correlation models between the duration of each regime and the Bi number were developed following the non-linear behavior of the regimes. The duration of boiling phases and convection evolve inversely; the former prevails as the Bi number decreases while the latter drives the cooling time for larger Bi numbers. The models provide reference points for time and temperature that constitute the basis for a more comprehensive thermal modeling of immersion quenching.

Keywords: Industrial quenching, Biot number, cooling regimes, film boiling, nucleate boiling, convection, cooling curve

Nomenclature

Bi	Biot number
c	Specific heat, J/kg K
$C.I.$	Confidence interval
CP	Characteristic point
CR	Cooling rate, °C/s
CR_{max}	Maximum cooling rate, °C/s
ΔT_e	Excess temperature, °C
ΔT_{max}	Maximum temperature diference, °C
E_{rel_i}	Relative margin of error
Fo	Fourier number
FT	Transition from Film boiling to Transition boiling
h_{av}	Average heat transfer coefficient, W/m^2 K
HT	Heat treatment
HTC	Heat transfer coefficient, W/m^2 K
$INBD$	Inbound direction, location
k	Thermal conductivity, W/m K
L	Length, mm
MID	Mid location
M_s	Martersitic transformation temperature
NC	Transition from Nucleate boiling to Convection
n	Sample size
$OTBD$	Outbound direction, location
$PP\ (A,B,C)$	Plate probe (A, B or C)
PPS	Probe positioning system
$q_s^{"}$	Surface heat flux, W/m^2
Q_{CHF}	Critical heat flux, W/m^2
Q_{MHF}	Minimum heat flux, W/m^2
R^2	Coefficient of determination
S_s	Sample variance

t	Time, s
t_{rel}	Relative time extent, %
t_{tot}	Total cooling time, s
T	Temperature, °C
T_{bath}	Bath temperature, °C
$T_{CR_{max}}$	Temperature at max CR, °C
T_{end}	End temperature, °C
T_{FP}	Flash point temperature, °C
T_{imm}	Immersion temperature, °C
T_s	Surface temperature, °C
T_{start}	Start temperature, °C
T_{T_i}	Transition temperature, °C
TC	Thermocouple
TN	Transition from transition boiling to Nucleate boiling
U	Experimental uncertainty
x^*	Non-dimensional space coordinate

Greek symbols

α	Diffusivity, m^2/s
Γ	Distance off surface, mm
δ	Thickness, mm
θ^*	Non-dimensional temperature
ρ	Density, kg/m^3
τ	Student's t-value
ω	Wall dimension, mm

6.1 Introduction

Quenching by immersion is a process commonly used to attain the mechanical properties of the material for its intended application. It involves a combination of multiple fields: thermal-metallurgical-mechanical, from which the thermal field is considered as the triggering factor for the other two fields (MacKenzie & Banka, 2009). Accurate prediction of the thermal field gives the opportunity of a better understanding of the thermal stresses caused by uneven thermal shrinkage and temperature gradients in quenched component. Moreover, prediction of quenched-induced distortion can be improved by a more realistic definition of the thermal boundary conditions during immersion quenching, yet it presents many challenges due to the non-linearity and transient nature of the process (Samuel & Prabhu, 2022b).

Characterization of the cooling characteristics of the quenchant typically relies on standard procedures such as ISO 9950, ASTM D6200, JIS K2242; the first two use a cylindrical Inconel 600 probe (Ø12.5 mm x 60 mm) while the latter uses a silver probe (Ø 10 mm x 30 mm). Because of their dimensions, the specimens are considered as lumped bodies ($Bi \leq 0.1$) thus neglecting any thermal gradient and any temperature dependency of the thermo-physical properties of the material across the specimen's thickness (Barrena-Rodriguez, Acosta-Gonzalez & Tellez-Rosas, 2021). Moreover, utilization of standard specimens, which are of smaller size than industry-oriented probes (Kobasko & Liscic, 2017; Liscic, 2016), often leads to the appearance of film boiling that larger specimens might not develop (Liscic et al., 2011; Salazar et al., 2023). Certainly, a strategy to deal with such differences is by utilizing larger probes, closer to industry size components, to truly capture the cooling dynamics and phenomena occurring during quenching (Kobasko & Liscic, 2017; Prasanna Kumar et al., 2014).

Studies on the influence of the specimen size indicate that the maximum cooling rate ($CR_{\max}$) increases as the ruling section decreases as per measurements at the center and subsurface locations when quenching in oil (Monroe & Bates, 1983; Nayak & Prabhu, 2018). Moreover, the temperature at which $CR_{\max}$ occurs may decrease as the probe thickness increases (Nayak

& Prabhu, 2018). Even the critical heat flux (Q_{CHF}) magnitude is affected by the size of the specimen (Fernandes & Prabhu, 2007). Furthermore, the driving factors of heat exchange and magnitude of the surface fluxes and heat transfer coefficients (HTC) widely vary depending on the cooling regime (Canale et al., 2009; Kobasko & Liscic, 2017). For instance, when quenching in water, the HTC values vary from $100 - 250\ W/m^2K$ during film boiling to $10 - 20\ kW/m^2K$ during nucleate boiling (Canale et al., 2009). The duration of each cooling regime also depends on the size of the specimen as demonstrated (Bourouga & Gilles, 2010). They reported that for the mean Biot number ($Bi_m > 0.5$) the duration of the boiling phase decreases non-linearly as Bi_m increases. These findings, in conjunction with the potential case where film boiling is null, as mentioned above, are critical when analyzing the quench immersion of large size components as the applicability of standard testing results becomes questionable.

The work herein is defined within this context, thereby assessing the influence of the specimen's size for a range of Biot number 0.70<Bi <1.32. This range inheritably presents thermal gradients across the specimen during quenching by immersion. Experimental work was carried out under conditions that represent, as much as possible, actual industrial configurations aiming to obtain reliable and accurate cooling curves that capture the heterogenous conditions due to the environment. These conditions, which cannot be reproduced following standard procedures, influence the extent and severity of each of the physical phenomena, the thermal boundary conditions, and as a result, the quench induced distortion of industrial size parts.

In this study, transition temperatures and duration of the cooling regimes, namely film boiling, transition boiling, nucleate boiling, and convection, were identified systematically based on the first derivative of the cooling curves. The total cooling time, duration of each cooling regime and transition temperatures, all affected by the specimen's thickness, are studied for the selected range of Bi number. This approach provides the foundations for a comprehensive modeling of the thermal boundary condition, transition points and regime duration as a function of Bi number applicable to quenching of large-size components.

6.2 The Biot Number

It is widely accepted that the non-dimensional Biot number (Bi) represents the ratio between the conduction inside the body against the heat extraction at the surface (Bergman et al., 2011). The mean Biot number (Bi_m) for a plate of thickness (δ) is defined as:

$$Bi_m = \frac{h_{av}\delta}{2k} \tag{6.1}$$

Where k represents the material conductivity in $(W/m)K$, and h_{av} the average heat transfer coefficient, which is computed as follows:

$$h_{av} = \frac{1}{(T_{Imm} - T_{end})} \int_{T_{imm}}^{T_{end}} h(T_S) dT_S \tag{6.2}$$

The temperature limits in Eq. 6.2 correspond to the surface temperature (T_S) at the beginning of immersion (T_{Imm}) and at the end of the cooling stage(T_{end}). In this study, T_{end} was assigned to the quenchant flash point temperature$T_{end} = T_{FP}$). h_{av} was computed from values previously published by the authors for a thick plate (δ=50.8mm) (Salazar et al., 2023), acquired under comparable conditions as the ones investigated in this study. As reported in (Salazar et al., 2023), the two main surfaces of exchange (i.e., Inbound and Outbound) experience different conditions leading to a $h(T_S)$ per surface. The identified $h(T_S)$ through the entire quenching process is shown in Figure 6.1. They were obtained by solving the inverse heat transfer using a Newton solver algorithm that minimises the sum of square residuals between simulation and internal measurements while considering temperature dependent physical properties. The identification strategy relies on reconstructing the surface temperature by iteratively optimizing linear piecewise temperature evolutions. The resulting surface temperature curves are then imposed as boundary conditions on a FE thermal field model. The surface heat flux is post-processed from the simulation and $h(T_S)$ is derived following the well-known Newton's Law of cooling. A more detail description of the strategy and methodology to solve the inverse problem can be found in (Lemyre-Baron, 2025; Salazar et al., 2023).

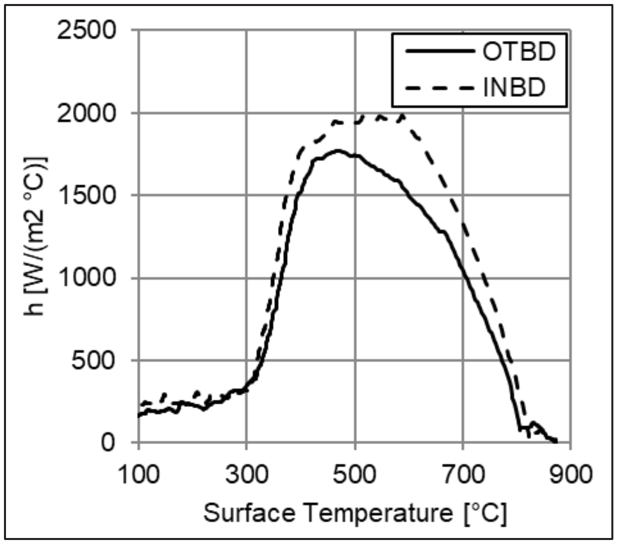

Figure 6.1 Identified heat transfer coefficient
for probe δ=50.8mm
Redraw from Salazar et al. (2023, p. 112)

In this study, Eq. 6.2 was evaluated for each curve shown in Figure 6.1, hence computing h_{av} per surface. Multiple specimens with different δ were tested under the postulate that the h_{av} per surface remains unchanged for the different specimens. Thereby, using Bi_m as independent variable by evaluating Eq. 6.1 allows for considering the influence of both specimen size, by the means of δ, and the h_{av} per surface, which represents the local interaction between internal conduction and external heat exchange at the given surface.

Classic textbooks (Bergman et al., 2011; Cengel, 2005) define $Bi_m \leq 0.1$ as criteria to ensure a lumped condition resulting in a quasi-uniform temperature distribution inside the body. Fulfilling such criteria requires a considerable large L/δ ratio (see Figure 6.2) with a thin body that most probably will cool before the end of immersion. Considering the variables in Eq. 6.1, this study covers specimens within a range $0.70 < Bi_m < 1.32$. These values are large enough to contain a temperature gradient during its transient cooling, and cannot be solely simplified as lump bodies, which is closer to realistic industrial conditions. Furthermore, the selected range of Bi_m fulfill the criteria ($Bi_m > 0.5$) considering a non-linear evolution of the duration of the cooling regimes (Bourouga & Gilles, 2010), which is yet to be confirmed under industrial conditions.

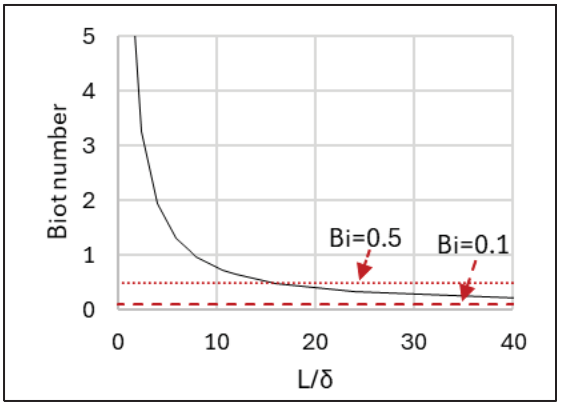

Figure 6.2 Evolution of Biot number vs L/δ
for L = 304.8 mm and $h_{av_{OTBD}}$

6.3 Experimental Means

The study herein considers three squared plate quench probes of thickness (δ): 50.8 mm, 41.28 mm and 28.58 mm, with a fixed length (L) of 304.8 mm, and made of 304SS. The selected values of δ cover the range of interest of Biot numbers mentioned above. The resulting length over thickness ratios (L/δ) are 6, 7.4 and 10.7 respectively. Such ratio is typically used as criteria ($L/\delta > 4$) to avoid end-cooling effects and considered as pre-requisite to ensure a 1D condition (Liscic & Singer, 2013; Matijevic, Liscic, Totten & Canale, 2017). The plate probes (PP) were labelled as PPA, PPB and PPC respectively.

Each probe was instrumented with three K-type thermocouples: two subsurface thermocouples placed at the same distance (Γ = 4.8 mm) under the surface, and one in the geometrical center of the probe. The labeling of the subsurface thermocouples depends upon the surface direction, either facing towards the tooling (INBD for Inbound) or opposite to it (OTBD for Outbound), while the thermocouple at the geometrical center is referred to as MID. This convention is maintained regardless of the assembly point of the probe on the Heat Treatment rig (HT-rig) as shown in Figure 6.3. The wells of the thermocouples were drilled parallel to the main surfaces of heat exchange, diminishing the perturbations produced by the drilling (Luebben et al., 2009), thus placing the thermocouple tip at the mid-length (L/2) of the probe. Further details regarding the instrumentation strategy can be found in recent publications by the authors (Salazar et al., 2023, 2024).

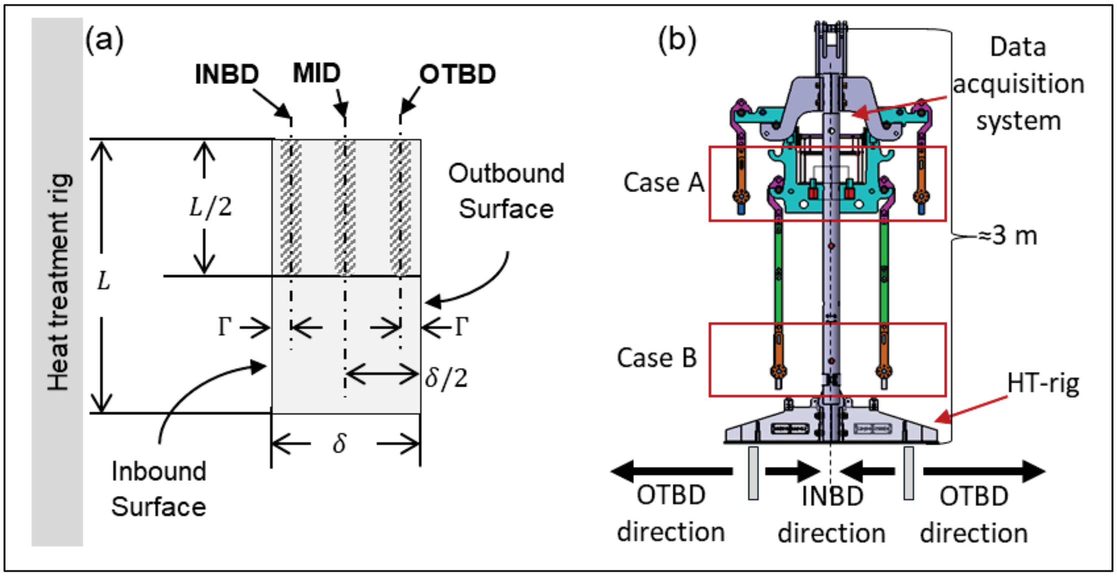

Figure 6.3 Test equipment schematics: (a) quench probe and thermocouples labeling, and (b) probe positioning system on HT-rig

In order to simulate actual industrial conditions, an air transfer step from the austenitizing furnace to the quench bath was also considered in the present study. It must be emphasized that such conditions are rarely considered in laboratory size samples, even in the ASTM D6200 testing protocol immediate immersion is encouraged. Similarly, due to the size of the heat-treated load (≈3 m height) and quench bath, the immersion step takes several seconds until the HT-rig is fully immersed.

A probe positioning system (PPS) was designed to allocate the data acquisition system and multiple quench probes on the HT-rig (see Figure 6.3b) to fully capture the particularities of the test environment. Using the PPS, it was possible to position the probes at different heights and sides of the HT-rig. The test setup with specimens at the top of the HT-rig is referred as case A, while specimens at the bottom station is referred as case B. A data logger (Phoenix TM PTM1220) was embedded at the top compartment preventing undesired perturbations of the oil flow during the quench process.

A typical test setup is shown in Figure 6.4, presenting the start of the test protocol (Figure 6.4a) and the condition of the load before immersion (Figure 6.4b). Multiple test cases with the three probes (PPA, PPB, and PPC) were carried out using the same quenching conditions with regards to bath temperature, agitation levels and transferring times.

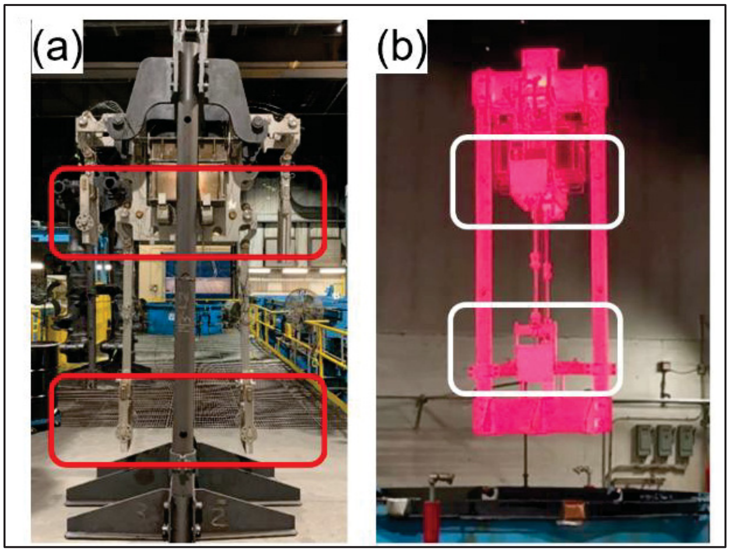

Figure 6.4 Typical test setup on HT-rig: (a) before test and (b) before immersion on top of quench bath. Stations with probes circled in both pictures

6.3.1 Data Acquisition Uncertainties

The Phoenix TM PTM1220 data logger was calibrated and passed as a field test instrument as per AMS 2750. It has an accuracy of ±0.3°C with a level of confidence of 95%. The resolution of the logger (0.1°C) complies with readability requirements as per AMS 2750. The logger was setup with an acquisition rate of 5 Hz for every test run. The type K thermocouples were calibrated as per ASTM E220, they meet the special limits (±1.1°C or 0.4%) up to 1250°C thus covering the complete temperature range of interest in this study (≤900°C). The data logger did consider the correction factors for the thermocouples and logger itself, thus data extracted after a test run considered the corrected readings. Thus, bias errors due to measurement instrument fault were minimized by utilizing calibrated instruments (Kumar & Chakraborty, 2021).

Each quench probe was instrumented using the same techniques. The position of the thermocouples was secured mechanically at the top end of the quench probes (Bohlooli Arkhazloo, Bazdidi-Tehrani, Jadidi, Morin & Jahazi, 2022; Bohlooli Arkhazloo et al., 2019). The thermocouples bore depth, which by design is 152.4 mm, were measured with a digital depth gauge whose resulting measurements did not exceed ±0.5°mm from the design value. Hence, it is assumed that all test measurements were taken at comparable positions in the quench probes geometry.

6.4 Cooling Regimes Identification

Multiple methods and strategies to analyze experimentally acquired cooling curves are available in the literature, the main studies are condensed in Table 6-1. Typically, characteristic points (CP) are identified along the experimental cooling curves for different purposes and significance. Table 6-1 presents the association, if any, between CPs and the transition between cooling regimes: film boiling to transient boiling (FT), transient boiling to nucleate boiling (TN), and nucleate boiling to convection (NC). The CPs can be in the form of time (t), temperature (T) or cooling rate (CR).

It must be noted that most studies prioritize CPs that are not necessarily related to the physical phenomena (i.e., cooling regimes), although reference temperatures are often used given their relevancy for metallurgical purposes (i.e., phase transformation temperature). For instance, ASTM D6200 provides six CPs, only two of them: CR_{max} and $T_{CR_{max}}$, can be associated to the transition from Transition boiling to Nucleate boiling. A typical value of martensitic transformation temperature (Ms, 300°C) is considered as reference in ASTM D6200. These CPs, although useful in practice, do not consider the evolution and transition of the cooling regimes.

Table 6-1 Identification of characteristic points on cooling curve

Reference	Quenchant	T_{start} (°C)	FT [a]	TN [a]	NC [a]	Additional points
ASTM D6200	Oil	850	--	T, CR	--	$t_{600C,400C,200C}$; CR_{300C}
(Jan & Mackenzie, 2020, 2024)	Water/Oil	500/ 850	t, T, CR	t, T, CR	t, T, CR	T_{Sat}; $\ddot{T}(t)_{min,max}$
(Matijevic et. al., 2017, 2019)	Oil	850	t	t, T	--	$\Delta T_{10s,100s,max}$; h_{max}
(Ramesh and Prabhu, 2016)	Oil	850	t, T	CR	--	$CR_{705C,550C,300C,200}$ $t_{730C-260C}$
(Canale et al., 2009)	Oil	850	t, T	--	t, T	$CR_{500C-600C}$
(Simencio Otero et al., 2018)	Oil	850	t, T, CR	T, CR	--	$CR_{700C,300C,200C}$; $t_{300C,200C}$

[a] FT - Film to Transition boiling; TN – Transition to Nucleate boiling; NC – Nucleate boiling to Convection

Few studies have purposely identified CPs according to the transition of the different cooling regimes (Jan & MacKenzie, 2020, 2024). Their CPs were identified on the assumption that on a typical boiling curve, the two reference points commonly named: minimum heat flux (Q_{MHF}) and critical heat flux (Q_{CHF}), can be associated with the peaks and valleys of the cooling rate curve $\dot{T}(t)$ (Jan & MacKenzie, 2024) as drawn in Figure 6.5. The former represents the minimum flux density required to maintain film boiling and appears at the frontier between film boiling and transition boiling (CP_{FT}). The latter is associated to the highest amount of energy extracted from the quenched body and can be identified at the peak of the boiling curve between transition boiling and nucleate boiling (CP_{TN}).

Utilizing the typical boiling curve, presented as surface heat flux ($q_s^{"}$) as a function of excess temperature (ΔT_e) in Figure 6.5a, to identify the transition regimes requires the determination of $q_s^{"}$. In the absence of $q_s^{"}$., the direct analogy between surface fluxes and cooling rates, as discussed above, can be used to determine the boundaries between cooling regimes. In this study, the CPs were identified based on the peaks of the first derivative of the cooling curve with respect to time, the cooling rate curve $\dot{T}(t)$, and the behavior of the second derivative $\ddot{T}(t)$. Each transition between cooling regimes ($CP_{FT,TN,NC}$) was determined along the time scale (see Figure 6.5b). A time value was associated to each CP and used to retrieve the corresponding transition temperature from the cooling curve. Thereby, each CP can be reported as a function of time, temperature and cooling rate.

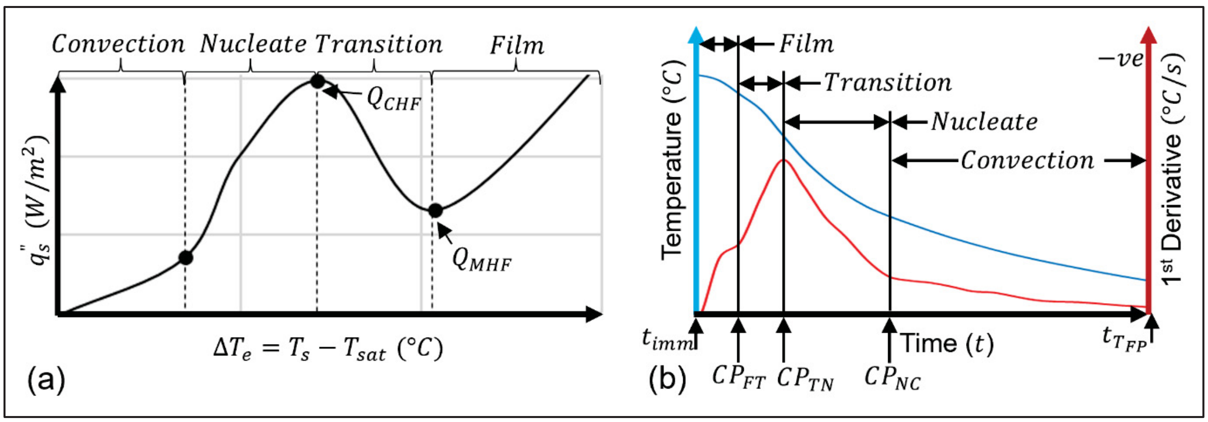

Figure 6.5 Cooling regimes identification on (a) typical boiling curve, and (b) cooling curve and cooling rate curve during quenching

6.4.1 Characteristic Points Identification

CP_{TN} is defined as the maximum value of the first derivative $\dot{T}(t)$ (Eq. 6.3). Given that CP_{TN} is a peak value of the curve, it occurs when the second derivative $\ddot{T}(t)$ is zero (Eq. 6.4).

$$CP_{TN} = \max(\dot{T}(t)) \tag{6.3}$$

$$CP_{TN} = \dot{T}(t)\big|_{\ddot{T}(t)=0} \tag{6.4}$$

The mathematical definition of CP_{TN} is consistent with previous works using temperature-time curves and its derivatives to identify the characteristic points (Jan & MacKenzie, 2024), graphically presented in Figure 6.6.

The next CP to identify is CP_{FT}, its position on the time scale has been associated with the local minimum before CP_{TN} (Eq. 6.5) as shown in Figure 6.6b, thus located at the valley before the rapid increase towards CP_{TN}. CP_{FT} is always smaller in magnitude and time than CP_{TN}.

$$CP_{FT} = \min\left(\dot{T}(t)\right) \quad t_{CP_{FT}} \in [t_{imm}: t_{CP_{TN}}] \tag{6.5}$$

Interestingly, CP_{FT} is not considered in the standard procedure ASTM D6200. Although, it is often identified in the literature (Canale et al., 2009; Simencio Otero et al., 2018), and even obtained through optimization algorithms (Jan & MacKenzie, 2024).

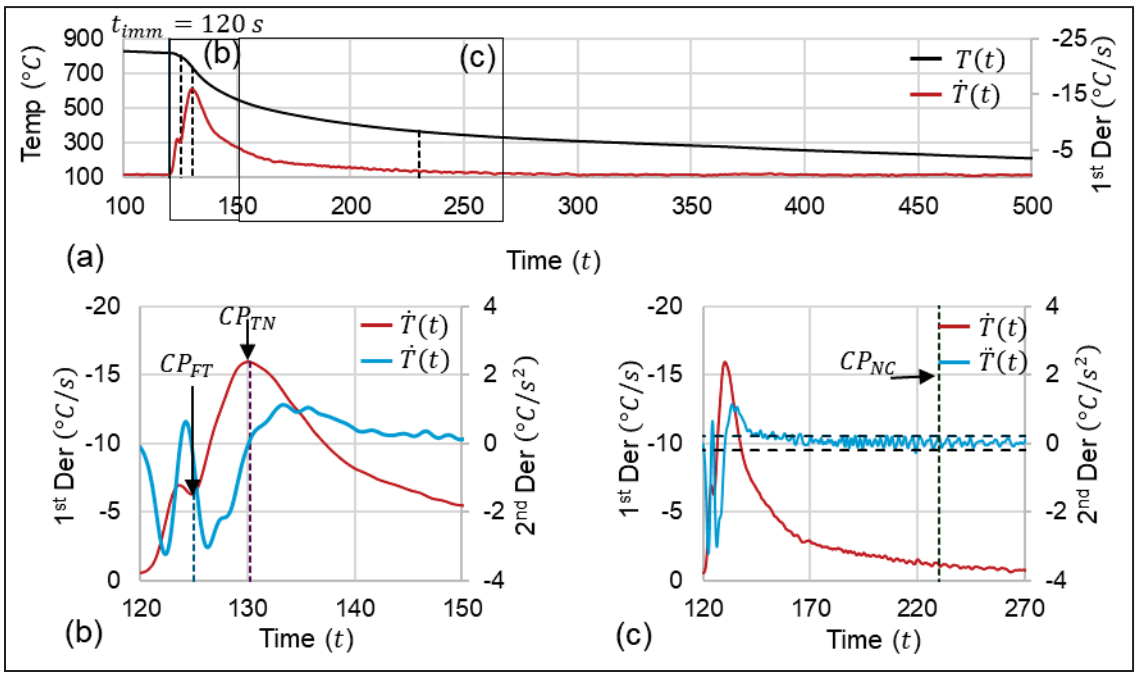

Figure 6.6 CP identification on (a) complete typical cooling curve,
(b) initial 30 s after immersion, and (c) transition from nucleate to convection

The last CP is CP_{NC}, which represents the instance when nucleate boiling ends and convection starts. As the body cools down after CP_{TN}, the heat extraction is driven by vapor columns, then isolated bubbles until the treated body is barely capable to sustain bubble formation. This last instance is typically referred as the onset of nucleate boiling (Bergman et al., 2011) while the remaining cooling regime is convection. Given that the convection stage can be modeled as an almost linear portion of the typical boiling curve (Figure 6.5a), this would be represented in the $\dot{T}(t)$ curve as a quasi-linear portion of the curve. Mathematically speaking, given that $\dot{T}(t)$ is almost linear from that point onwards in time, the oscillations of the second derivative $\ddot{T}(t)$ tend to zero, as shown in Eq. 6.6. This is shown schematically in Figure 6.6c, CP_{NC} and the evolution of $\dot{T}(t)$ and $\ddot{T}(t)$.

$$CP_{NC} = \dot{T}(t)\big|_{\ddot{T}(t)\to 0} \quad t_{CP_{NC}} \in \left[t_{CP_{TN}}: t_{CP_{FP}}\right] \tag{6.6}$$

One must note that most of the works that identify characteristic points on cooling curves (see Table 6-1) does not consider CP_{NC}. Partly because their interest is placed on predetermined temperature values instead of the evolution of the actual cooling regimes. Although optimization algorithms have been used to identify CP_{NC} (Jan & MacKenzie, 2024).

Since the identification of the CP requires of computing $\dot{T}(t)$ and $\ddot{T}(t)$, the experimental raw data were smoothed using a rectangular filter (moving average) (Jan & MacKenzie, 2020, 2024) aiding to identify maximum and the minimum values of the derivatives.

6.4.2 Calculation of Duration of Cooling Regimes

The experimental work did consider an air transfer step from the austenitizing furnace to the quench bath. Hence, the computation of the total cooling time after immersion (t_{tot}) is defined as the difference between the time required for the surface to reach the quenchant flash point temperature ($t_{T_{FP}}$) minus the immersion time, as shown in Eq. 6.7.

$$t_{tot} = t_{T_{FP}} - t_{imm} \tag{6.7}$$

Then, the duration of each of the cooling regimes is computed as the time between the transition points between regimes, for each regime (film, transition, nucleate, and convection), their time extent is given as:

$$t_F = t_{CP_{FT}} - t_{imm} \tag{6.8}$$

$$t_T = t_{CP_{TN}} - t_{CP_{FT}} \tag{6.9}$$

$$t_N = t_{CP_{NC}} - t_{CP_{TN}} \tag{6.10}$$

$$t_C = t_{T_{FP}} - t_{CP_{NC}} \tag{6.11}$$

The *relative extent* of each of the cooling regimes is computed as the ratio between the duration of each regime over the total cooling time, as shown in:

$$t_{rel} = t_j / t_{tot} \tag{6.12}$$

Note that the influence of the moving front (rewetting) is not considered given that the test specimens have the same length and all test measurements were taken at the same depth (mid-length), thus comparable among them.

The evolution of the relative extent of each cooling regime was analyzed as percentages in the results section. The computed cooling time (Eq. 6.7) and the relative extent (Eq. 6.12) were used to produce regression models as a function of the Bi_m. Such models were obtained by a nonlinear least squares method using the Matlab® toolbox. The goodness of fit was assessed using the coefficient of determination (R^2). These models are the main subject of the results section as they address the influence of the Bi_m on the duration of the cooling regime.

6.5 Results and Discussion

6.5.1 Experimental Results

6.5.1.1 Test Data Repeatability

The repeatability of the experimental results was investigated using PPA - case A (see Figure 6.3) as the reference case. Results from five test runs using such setup were considered to compute a mean cooling curve for each of the three thermocouples locations (OTBD, MID, and OTBD). All the test datasets were harmonised at t_{imm}, which allows for direct comparison of the temperature readings of the multiple tests along the entire cooling curve. Then. the relative margin of error (E_{rel}) was computed at every discrete value of the cooling curve as per Eq. 6.13

$$E_{rel} = (\tau_{n-1}\sqrt{(S_s/n)})/n \tag{6.13}$$

Where τ_{n-1} is the critical t-value for $(n-1)$ degrees of freedom for a confidence level of 95%, n is the sample size, and S_s is the variance of the sample.

The resulting mean cooling curve and its corresponding E_{rel} for the most penalising case are represented in Figure 6.7a. Note that E_{rel} evolves nonlinearly as temperature decrease yet always remain <3%. Conservatively, it is assumed that $E_{rel_T} = 3\%$ for the complete cooling curve when temperature (T) is the variable of interest.

An alternative study was conducted now considering time (t) as the variable of interest, hence comparing the required time to reach a target temperature using intervals of 20°C. The resulting mean time to reach a target temperature and its corresponding E_{rel} are shown in Figure 6.7b.

Despite the nonlinear behavior, E_{rel_t} always remain <4%. In further sections, E_{rel_T} and E_{rel_t} are used to compute the uncertainty of either temperature or time values under the postulate that the experimental uncertainty is represented by twice the computed margin of error.

$$U_i = \pm E_{rel_i} \tag{6.14}$$

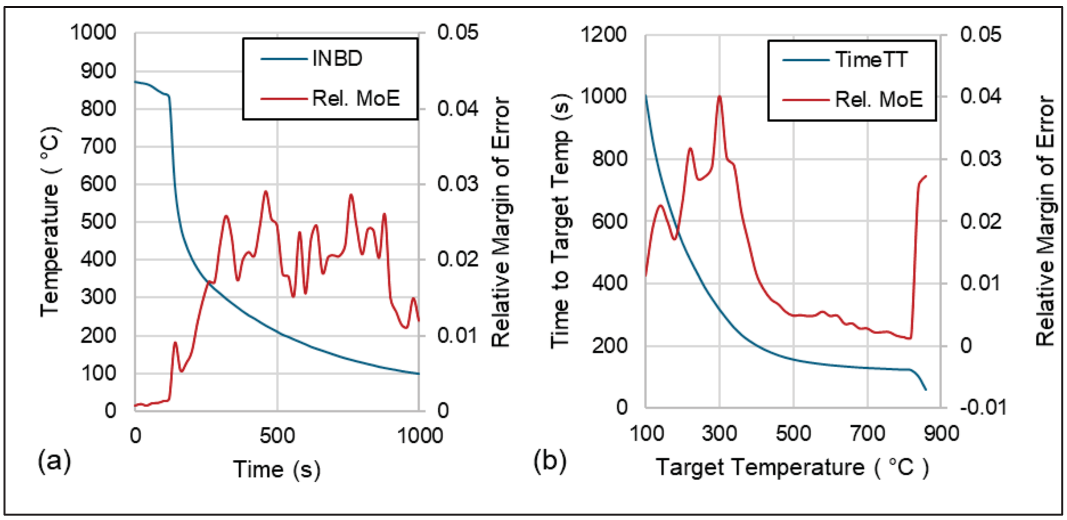

Figure 6.7 Margin of error based on experimental results: (a) cooling temperature as function of time, and (b) time to reach a target temperature

6.5.1.2 Cooling Curves Comparison

Experimentally acquired cooling curves at the three thermocouples locations (i.e., OTBD, MID and INBD, see Figure 6.3) for quench probes PPA, PPB and PPC are shown in Figure 6.8. The specimen's core (i.e., MID) remains at a higher temperature than the subsurface locations (i.e., INBD, OTBD) producing non-homogeneous cooling through the complete quench process. Note that the temperature gradient becomes more significant through PPA and PPB, due to their increased thickness compared to PPC. The test values correspond to a test setup with the probes placed at the top station in the HT-rig, case A, as per Figure 6.3. The curves depict the complete cooling process, including the exit from the furnace, air transfer, and immersion until the probe's temperature reaches 100°C.

The influence of probe size is evident when observing the overall cooling time. This can be quantified by computing the required time to reach a reference temperature such as the quenchant flash point (FP, 170°C). As the thickness (δ) increases, the time delay between subsurface reading and core readings to reach a reference temperature (i.e., FP) becomes larger as shown in Table 6-2. Similarly, the maximum temperature difference (ΔT_{max}) between subsurface and core readings becomes more pronounced as thickness increases. One must note that ΔT_{max} consistently occurs at temperatures >500°C. This is mainly due to the abrupt heat extraction rate during the boiling phase that cools down the surface of the quenched body while the core remains at higher temperatures.

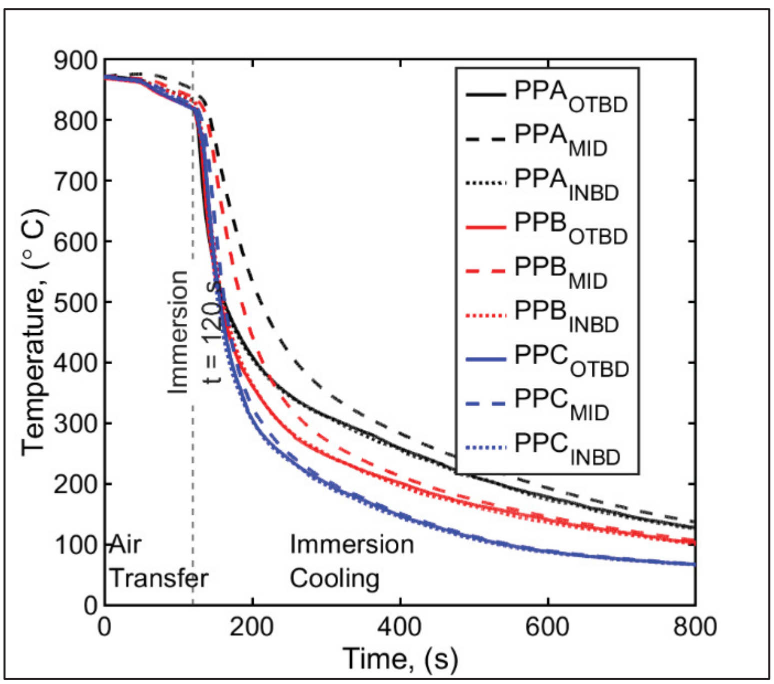

Figure 6.8 Complete thermal history for PPA, PPB and PPC. Thermal gradient clearly noticeable between MID readings (dashed line) and near-surface values (continuous lines).

The cooling rate curves $T'(t)$ for OTBD sensors as per Figure 6.8 are plotted in Figure 6.9. The cooling rates reach an initial plateau due to the existence of a vapor film upon immersion. This film needs to collapse in order to transition from film boiling into nucleate boiling (Arai & Furuya, 2011). One can observe that the duration of the film boiling regime is different for each specimen. The thinner PPC ($Bi_m = 0.70$), with the smallest Bi_m, presents the more stable and prolonged film boiling. On the other hand, PPA ($Bi_m = 1.24$) has a very short, almost null film blanket thus transitioning towards the maximum cooling rates rapidly upon immersion. These results are in agreement with the findings reported by (Liscic et al., 2011) who found that the film blanket appears was diminished for the larger cylinder probe. Thus the maximum heat extraction was attained directly upon immersion when film boiling was absent (Liscic et al., 2011). To further validate these observations, the following sections address the results of both case A and case B by discussing transition temperatures between regimes and its duration.

Table 6-2 Time delays and maximum temperature difference

Probe	δ, [mm]	Δt_{FP} [a], $[s]$	ΔT_{max}, $[°C]$
PPA	50.8	49.8	213
PPB	41.3	31.4	180
PPC	28.6	10.8	95

[a] Time delays Δt_{FP} between core and subsurface measurements

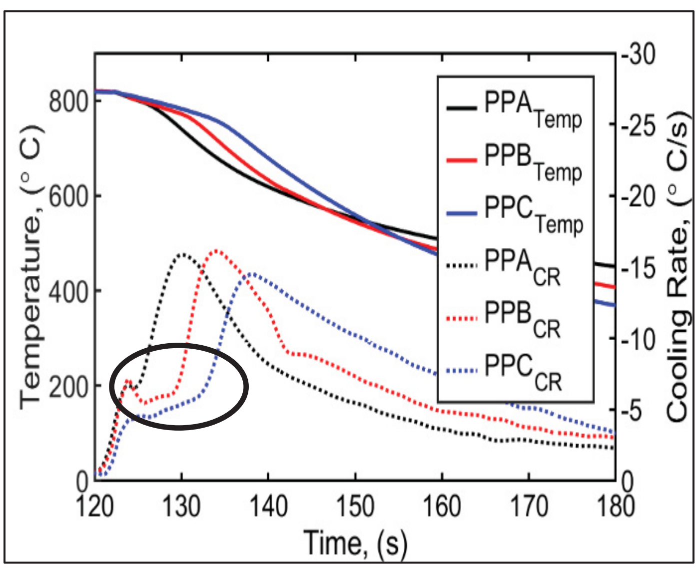

Figure 6.9 Cooling curves and cooling rate curves at OTBD right after immersion Duration of film boiling (circled) varies depending on the probe size

6.5.2 Transition Temperatures

Although the influence of probe size on the cooling regimes has been acknowledged in previous studies (Kobasko & Liscic, 2017; Liscic et al., 2011; Liscic & Singer, 2014), no further details are given with regards to the transition temperatures (T_{T_i}) between regimes. Given that the film boiling duration is different per probe size as shown in Figure 6.9, the temperature at which it collapses will probably be affected. Hence, the transition points between regimes might be delayed and occur at lower temperatures depending on the probe size. The resulting T_{T_i} between regimes are plotted against their corresponding Bi_m number in Figure 6.10 based on test results for case A, previously shown in Figure 6.8 and Figure 6.9 from which the initial observations were made, and case B that represents a different position on the HT-rig.

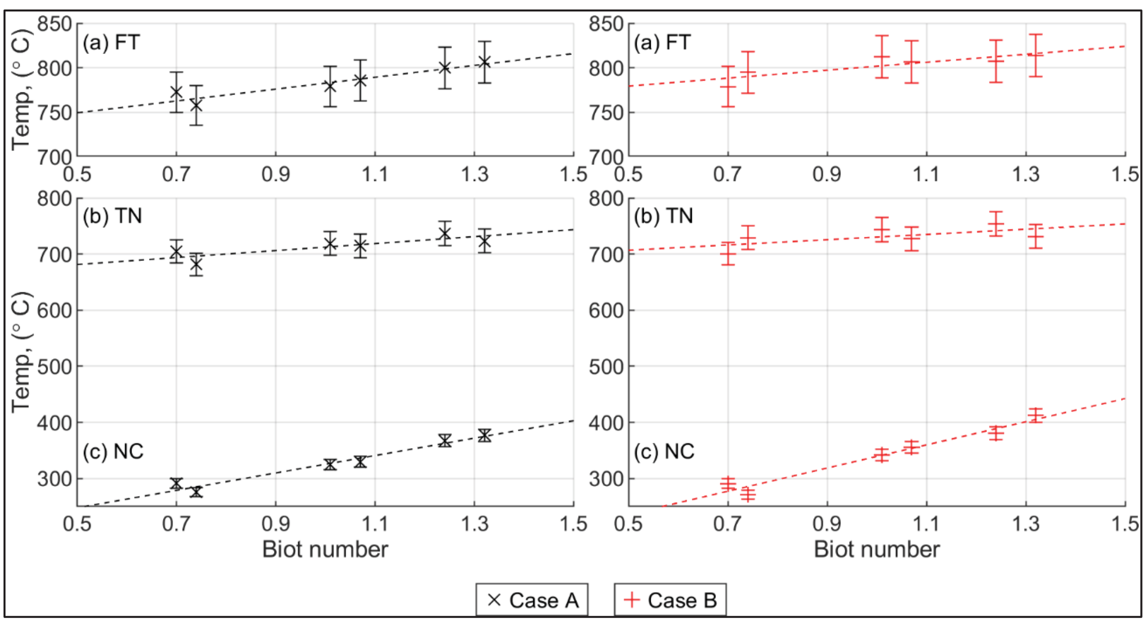

Figure 6.10 Evolution of transition temperatures for Case A and Case B as Biot number decreases. Curves: (a) Film to Transient boiling, (b) Transient to Nucleate boiling, and (c) Nucleate boiling to Convection. Error bars consider $\pm E_{rel_T}$

The transition temperature between film boiling and transient boiling (Figure 6.10, curve (a) FT) tends to drop as Bi_m decreases, this is caused by the prolonged film boiling that last longer for smaller Bi_m. Such condition appears for both cases A and B (see Figure 6.10). Note that the transition temperatures are on average $\approx 18°C$ higher for case B than case A. This is expected as the specimens were located at a position that dives first, more influenced by the agitation system (bottom of the HT-rig), which enhances fluid flow around the specimen thus influencing the transition between regimes. Regardless of the test setup, a decrease in Bi_m leads to lower transition temperatures FT.

The subsequent transition temperatures, transient boiling to nucleate boiling (Figure 6.10, curve (b) TN) and nucleate boiling to convection (Figure 6.10, curve (c) NC), present similar tendencies of lower values for smaller Bi_m. One must note that case B still presents higher values than case A, while the slopes shown in Figure 6.10 also illustrate both the difference between setups and the evolution of the transition temperatures. These tendencies might be related to the ability of the solid to supply heat to the liquid, as quenching conditions are the same, and the limited amount of heat that can be transferred from the inside towards the liquid (Monde et al., 2006). Given that the tendencies outlined in Figure 6.10 were captured at different stations of the tooling, even on a position more sensitive to agitation effects for case B, it can be confirmed that the transition temperatures decrease as Bi_m decreases for the tested conditions.

The data points presented in Figure 6.10 reveal an almost linear relationship between the transition temperatures and Bi_m. This is consistent with the linear dependency between the end temperature of the nucleate boiling process and the diameter of the specimens (Kobasko, 2017), thus confirming the overall behavior of the results presented herein. Given the dependency of the film boiling on the Bi_m as per Figure 6.10, a linear model was fitted to the test data for case A and B as shown in Figure 6.11. The confidence interval (C. I.) for the regression model is included in Figure 6.11 for a confidence level of 95%. The goodness of fit (R^2) is computed at $> 80\%$ for both models. One must note that there are multiple parameters that might affect the transition temperatures. To the knowledge of the authors, no relation has been provided to estimate the transition temperature at the end of the film boiling regime as a function of Bi_m during immersion quenching.

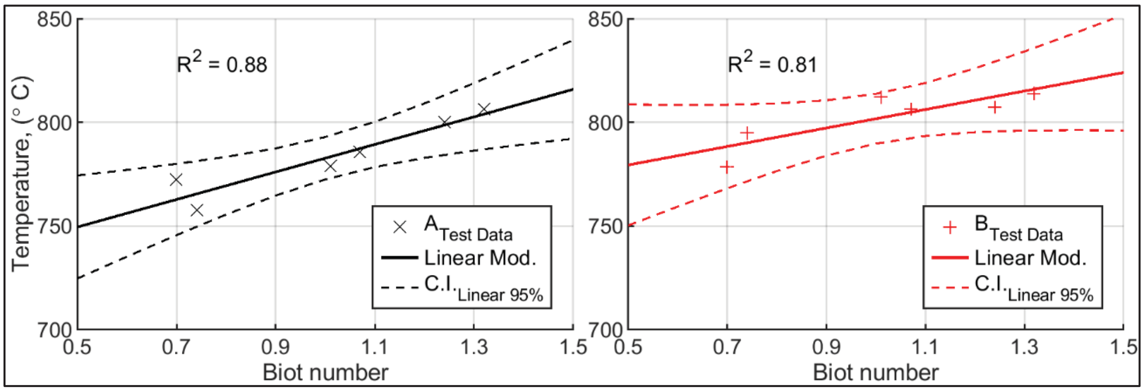

Figure 6.11 Linear regression model for transition temperature from film boiling to transition boiling showing the strong dependency on Bi_m

6.5.3 Total Cooling Time

The analysis of the total cooling time is presented herein while considering both cases A and B separately. The cooling time progressively increases as Bi_m grows as shown in Figure 6.12a, thus presenting the relationship between total cooling time (t_{tot}, Eq. 6.7) and the Bi_m number. Note that such increase in cooling time exist for both test setup, although case B clearly shows lower cooling times (Figure 6.12a), which has a more effective cooling mainly caused by its position on the HT-rig.

Figure 6.12 also includes a power-like model obtained through non-linear least squares regression for each case A and case B. The C. I. for both regression models are plotted in Figure 6.12b for a confidence level of 95%. The R^2 for both models is computed $\geq 90\%$ suggesting a strong correlation. The coefficients of the power-like model are included in Table 6.3 as they correspond to the same type of equation model for each of the cooling regimes as will be shown in the following section.

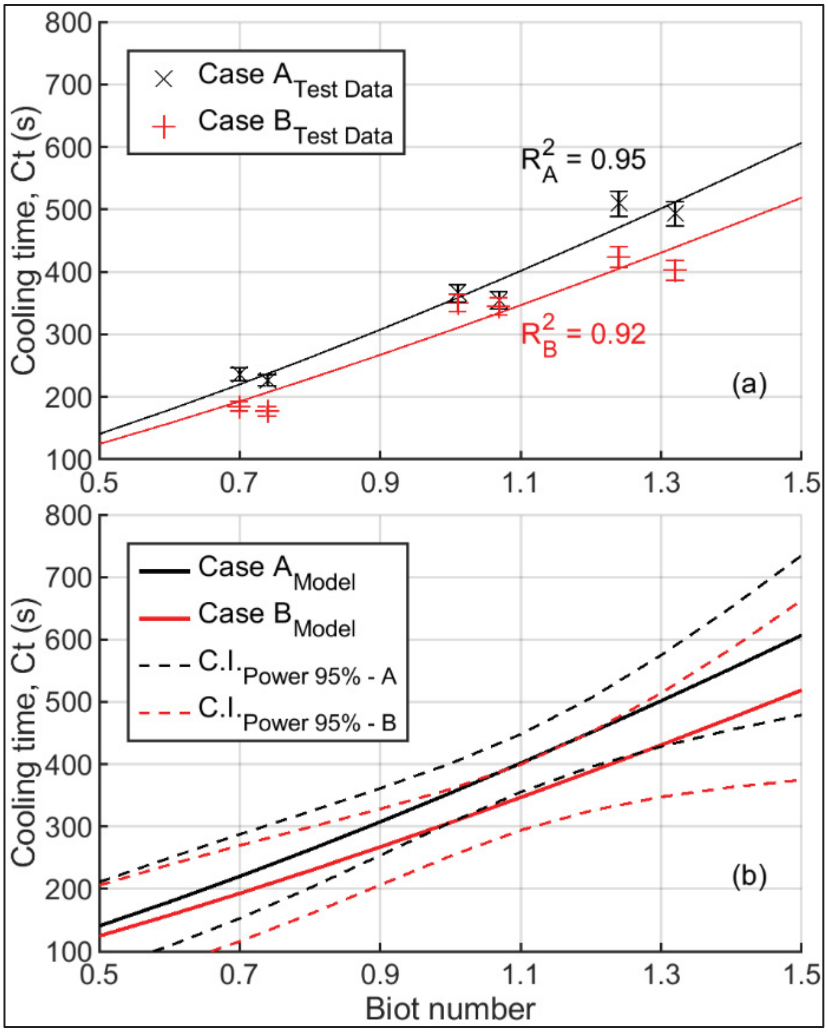

Figure 6.12 Total cooling time (t_{tot}) as a function of Bi number.
(a) Regression models based on power-like equation,
and (b) confidence intervals for each model.
Error bars consider $\pm E_{rel_t}$.

The dependency of cooling time with regards to the Biot number is further revealed by the analytical formulation of the first-term approximate solution for a plane wall one-dimensional case (Bergman et al., 2011). Based on such formulation, the time required to reach a target temperature is obtained as follows:

$$t = ln\left(\frac{\theta^*}{C_1 \cos(\zeta_1 x^*)}\right)\left(\frac{\omega^2}{-\zeta_1^2 \alpha}\right) \tag{6.15}$$

Given the definition of Eq. 6.15, the equivalent position of the temperature sensors is accounted for in the non-dimensional space coordinate x^*. Thus, the wall dimension ω is increased until the range of Biot numbers of interest is fully covered. Details about the derivation of Eq. 6.15 can be found in ANNEX 6. The resulting curve as per Eq. 6.15 is depicted in Figure 6.13 (dashed line) and plotted with the regression curves of each case (see Figure 6.12)

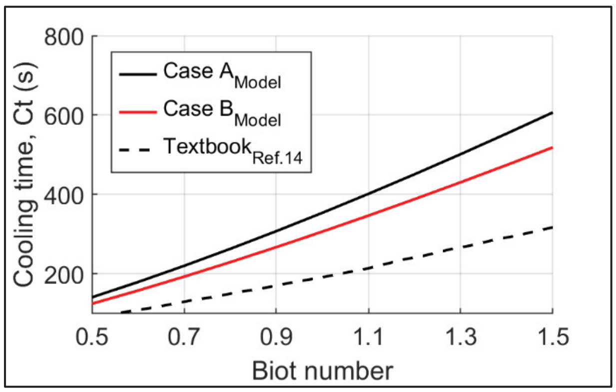

Figure 6.13 Comparison between models and textbook total cooling time vs Bi number

Experimental results and textbook calculations indicate a consistent rise in cooling time as Biot increases (Figure 6.13). Results are in good agreement for small Biot numbers, although always reflecting faster cooling times for textbook calculations than the experimental data. However, the discrepancy between the textbook calculations (Eq. 6.15) and test data becomes evident as Bi number grows. The difference is attributed to utilizing one singular value of the HTC (as with the analytical calculation from the textbook), neglecting the actual cooling behavior during and therefore an oversimplification is taking place. This has been discussed by (Jan & MacKenzie, 2018, 2020) with regards to quench severity values such as Grossman number which fails to represent the cooling dynamics of quenching by immersion. Nevertheless, the main intend in this study is to analyze the relative duration of each cooling regime, whose time duration does not evolve linearly and cannot be predicted analytically, as is presented in the next section.

6.5.4 Evolution of Cooling Regimes

Upon establishing the relationship between t_{tot} and Bi_m, the relative extent of each of the regimes with regards to the total cooling time was computed as per Eq. 6.8 to Eq. 6.12. The resulting values are shown in Figure 6.14 plotting each cooling regime as a function of the Bi_m number for both cases A and B separately. The influence of test setup (A or B) can be appreciated by the spread of nucleate boiling (triangle markers) and convection (cross markers) data points (see Figure 6.14); they spread over a wider range for case B than for case A. This is attributed to the location of setup B, more susceptible to the convective effects as it is placed at the bottom of the HT-rig, which is reflected on the cooling regimes that are more easily enhanced by forced convection. Clearly, certain patterns can be observed, specially for nucleate and convection which evolve inversely. Nucleate boiling increases as Bi_m decreases whereas convection has an opposite tendency, becoming more dominant as Bi_m increases. These patterns can be observed regardless of the test setup.

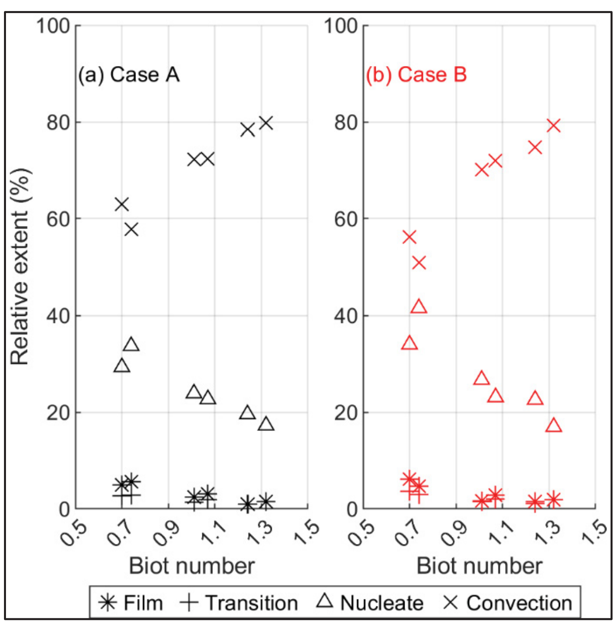

Figure 6.14 Relative extent of cooling regimes vs Bi number. Each regime follows a non-linear behavior

When quenching large specimens, most of the cooling would occur under the convective stage (Liscic & Singer, 2013). This is the case for the specimens in this study as the relative extent of convection cooling (Figure 6.14) remains >50% regardless of the test setup. Overall, convection varies widely as it can represent up to ≈80% for the larger Bi_m but only ≈52% for smaller Bi_m. The decrease in convection cooling as the quenched bodies become thinner, represented by a decrement in Bi_m, is caused by the increase in the duration of the boiling regimes. Specially film boiling and nucleate boiling as they become more evident for smaller Bi_m reducing the duration of the convective stage (see Figure 6.14).

Among the boiling regimes (film, transition, and nucleate), nucleate boiling is the one that varies the most, reaching up to ≈40% for smaller Bi_m but only around 10% for larger Bi_m (triangle markers, Figure 6.14). Such behavior follows the understanding that the duration of boiling is proportional to the part thickness and inversely proportional to the material's diffusivity (Liscic & Singer, 2014). Film boiling and transition boiling are the regimes lesser in magnitude as both remain <10% (start and plus markers, Figure 6.14). Their impact, particularly of film boiling at the beginning of immersion, cannot be neglected as it delays the subsequent transitions influencing the relative extent of each regime.

6.5.5 Regression Models per Cooling Regime

Based on the values per regime shown in Figure 6.14, regression models were fitted for each regime individually. The resulting prediction curves and corresponding $CI_{95\%}$ are reported in Figure 6.15 for film boiling and transition boiling, and Figure 6.16 for nucleate boiling and convection. These figures present the models for both case A and case B separately, thus accounting for the influence of the test setup.

The models can be used to estimate the duration of the cooling regimes for Biot numbers covered in this study, which then can be used to adjust the boundary conditions for a more comprehensive heat transfer modeling during quenching. The regression models obey a power form equation (Eq. 6.16) for each regime producing an $R^2 > 80\%$. The coefficients of the regression models per cooling regime and its corresponding R^2 values are shown in Table 6-3.

Table 6-3 Regression models coefficients

HT Mode	a_A	b_A	R_A^2	a_B	b_B	R_B^2
Cooling time	353.8	1.330	0.95	306.4	1.298	0.92
Film	0.026	-2.073	0.89	0.025	-.2.234	0.91
Transition	0.017	-1.353	0.86	0.020	-1.475	0.82
Nucleate	0.235	-0.874	0.90	0.261	-1.090	0.85
Convection	0.706	0.459	0.93	0.671	0.623	0.93

$$f(x) = a\,x^b \tag{6.16}$$

The results of multiple tests indicate that the film boiling at the larger Bi_m numbers is considerably short (see Figure 6.15a,b) regardless of the test setup. Hence, under the quenching conditions of this study, the dimensions at which film boiling would briefly appear are near the limits of the studied Bi_m range. The film boiling stage always remain <10% (see Figure 6.15a,b), which aligns with the results reported in (Bourouga & Gilles, 2010) where the film boiling relative duration also decreases ≈10%. The resulting R^2 of the regression models for the film boiling were computed at 0.89 and 0.91 for case A and case B respectively, indicating the strong correlation between Bi_m and the duration of film boiling.

Note that the lowest coefficient of determination was obtained for the Transition boiling regime (see Figure 6.15d). It is worth mentioning that Transition boiling is the regime with the least variation. It evolves between 1% to 4% (Figure 6.15c,d) regardless of the test setup, which is considerably less than the other cooling regimes. This is consistent with results reported for transition boiling in (Bourouga & Gilles, 2010) as such regime almost remain unchanged through a wider range of Biot numbers.

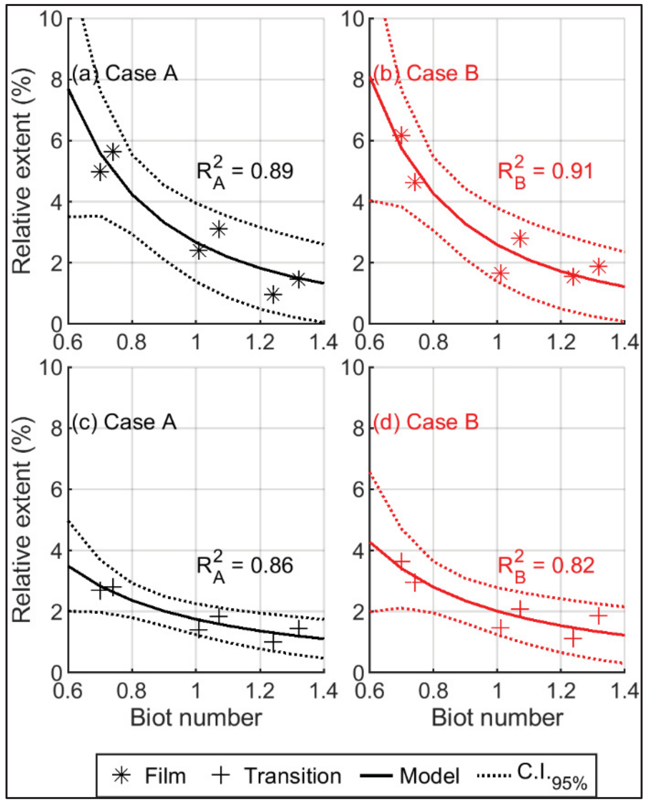

Figure 6.15 Regression models for Case A (black) and B (red). (a, b) film boiling and (c, d) transition boiling. Models follow a power-like equation (Eq. 6.16 and Table 6.3)

The most dominant regimes, nucleate boiling and convection, are shown in Figure 6.16. The former covers a window of 30% (from 10% to 40%, see Figure 6.16a,b) for either test setup. The range is comparable to reported values expanding from 35% to 55% (Bourouga & Gilles, 2010) for the range of Bi_m explored herein. The differences can be attributed to the quenching conditions between the two studies and the quenchant itself being mineral oil herein, as opposed to water in the comparison case.

The dependence of convection with regards to Bi_m is shown in Figure 6.16c and Figure 6.16d for case A and case B respectively. Convection is the only cooling regime that is less dominant as Bi_m decreases. Different quenching conditions would require adjusting factors, specially with regards to flow velocity as more turbulent flows would certainly influence the convective conditions. Nevertheless, the power-like model adequately represents the influence of Bi_m and the duration of the convective stage (see Figure 6.16c, d) supported by R^2 values of 0.93 for both test case A and B.

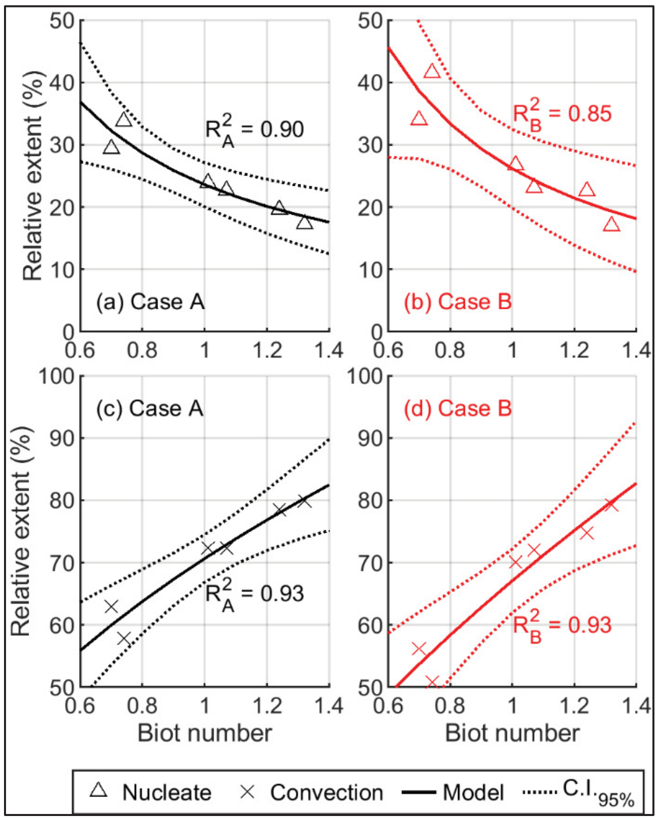

Figure 6.16 Regression models for Case A (black) and B (red). (a, b) nucleate boiling and (c, d) convection. Models follow a power-like equation (Eq. 6.16 and Table 6.3)

The regression models presented in this section are consistent with the physics of immersion quenching processes. They represent industrial conditions that leads to different h_{av} as well as typical ruling sections (δ) commonly encountered in workpieces, both variables captured by computing Bi_m. This avoids the limitations encountered when utilizing standardized test samples. In fact, the combination of transition temperatures and duration of cooling regimes might provide the basis for a more comprehensive thermal modeling during immersion quenching. Thereby, it would be possible to accurately determine the range (time and temperature) of a given cooling regime aiding to adjust the boundary condition depending on the cooling regime as a function of Bi_m.

6.6 Conclusions

The study presented herein demonstrates the non-uniform condition of quench bodies covering a range of Biot numbers 0.70<Bi_m <1.32. The following conclusions were drawn based on the results and discussions:

- The temperature delta across the ruling section (thickness) becomes more evident as Bi_m increases. The largest delta always appears at high temperatures >500°C.
- The appearance of the film boiling regime impacts the transition temperatures and duration of the subsequent cooling regimes (transition boiling, nucleate boiling and convection). The former decreases linearly for smaller Bi_m numbers while regression models for each of the cooling regimes have been developed.
- Nucleate boiling and convection evolve inversely. The former becomes more dominant for smaller Biot numbers (up to 40%) while the latter prevails for larger Biot numbers (up to 86%).
- The proposed models for transition temperatures and duration of cooling regimes provide the basis for defining a more comprehensive modeling of the thermal boundary conditions that considers the influence of the ruling section by means of the Biot number.

CHAPTER 7

MATHEMATICAL MODELING OF THE THERMAL BOUNDARY CONDITIONS DURING INDUSTRIAL QUENCHING (AIR TRANSFER AND IMMERSION)

Gamaliel Salazar[a], Jean-Sebastien Lemyre-Baron[b], Mohammad Jahazi[a], Henri Champliaud[a], Antoine Tahan[a]

[a] Department of Mechanical Engineering, École de technologie supérieure, 1100 Rue Notre-Dame Ouest, Montreal, QC, Canada
[b] Product Improvement Engineering, Safran Landing Systems Canada,13000 Rue du Parc, Mirabel, Quebec, Canada, J7J 0W6

Content of this chapter submitted for publication in *Transactions of the Canadian Society for Mechanical Engineering*, April 2026

Abstract: This study develops mathematical models of the thermal boundary conditions of quench probes during an industrial quenching process that requires an air transfer step from the furnace to the quench bath, followed by an immersion into oil. Both steps were modeled separately while accounting for the influence of quench probe size by defining characteristic points as a function of the Biot number. During the air transfer step, temperature dependent heat transfer coefficients are modeled as per characteristic points given by the process. During immersion, the models adjust the surface heat flux instead, whose characteristic points represent the boundaries between cooling regimes (film boiling, transition boiling, nucleate boiling and convection), thus associated to the physical phenomena. Nonetheless, the models were validated against experimental measurements from an independent test specimen, providing an acceptable degree of accuracy in the form of relative error below 8%, a clear improvement from a relative error of 30% obtained with a baseline HTC, without accounting for the influence of the specimen's size. Thereby, the proposed strategy directly challenges the understating of the HTC as an intensive property, a common practice in the heat-treating industry.

Keywords: Industrial quenching, HTC, surface heat flux, Biot number, film boiling, nucleate boiling, convection

7.1 Introduction

In this project, Chapter 4 demonstrated that accurate HTC identification could be achieved in a large heat treatment facility and that isothermal initial conditions should not be considered with large industrial equipment. Chapter 5 evidenced the advantages of analyzing the characteristics points of the cooling curve to outline heat transfer regimes. The same points may then serve as control points of an Hermite polynomial that can remodel a cooling curve elegantly with few values, providing the means to carry out inverse identification with great efficiency. Further on, the observation of the characteristics points, should it be temperature or rate, allow to derive correlations between the heat transfer parameters and some metrics of the systems, during immersion quenching, as presented in Chapter 6. Now, in this section, the full potential of this approach is developed into a geometry and temperature dependent HTC model that allows for predictive calculations of heat transfer in quench media.

This chapter provides the resulting mathematical models to determine the boundary conditions of the quench plate probes, PPA, PPB and PPC (see Chapter 3, 4 and 5 for details), during the industrial quenching process under study. The solutions given by the inverse methods, in the form of temperature dependent HTCs, are verified first for both air transfer and immersion steps confirming the accuracy of the inverse results on different specimens. Upon such verification, the temperature dependent HTC and temperature dependent surface heat flux are used as input to develop the mathematical models for each step respectively.

The air transfer step is addressed first; the strategy considers three segments of the air transfer driven by the process requirements thus producing semiempirical models for each segment. The immersion step follows afterwards; its modeling approach is based upon the evolution of characteristic points, delimiting the boundaries between cooling regimes during immersion. These points are often given in the form of flux densities (i.e., MHF, CHF), thus being the reason for using surface heat flux instead for the modeling of the immersion step. Both steps make use of the Biot number, as a dependent variable, to correlate the characteristic points with the size of the probes. Lastly, a verification step is carried out for each step (i.e., air transfer and immersion) confirming the accuracy of the proposed models.

Also, in this chapter, the postulate of HTC being an intensity property is tested and debunked for the industrial application. A sensitivity study referred as “cross-over” can be found in ANNEX V. Such analysis presents the results of utilizing the identified boundary condition from a given plate probe (i.e., PPA) onto a different probe geometry (i.e., PPC) under the postulate that the heat transfer coefficient could be considered an intensive property for a given surface-fluid combination. As the results demonstrate, following such a path strongly decreases the accuracy of the simulations, leading to an increase in the relative error up to 30% (see ANNEX V).

Therefore, this chapter provides the final user with accurate and flexible mathematical models to adjust their boundary conditions, in the form of HTCs, when processing plate-like geometries. The data and results in this chapter use the test setup Case A (specimens in the top station of the HT-rig). The corresponding models and results for setup Case B (bottom station on the HT-rig) can be found in ANNEX VI for the air transfer step, and ANNEX VII for the immersion step.

7.2 Inverse Results Verification for Air Transfer and Immersion Steps

7.2.1 Inverse Results Verification During Air Transfer

In CHAPTER 5, the quench probes PPA, PPB and PPC were used to identify the HTC during the air transfer step. Herein, each PP was simulated using its corresponding HTC from the inverse results as BC. Simulation results indicate a good level of accuracy with RMSE $\leq 3°C$ and relative error $<1\%$ for all the PPs. The worst case is presented in Figure 7.1 for PPB. Thereby, verifying the accuracy when predicting the thermal field evolution during the air transfer, as well as the end condition of the specimen before immersion.

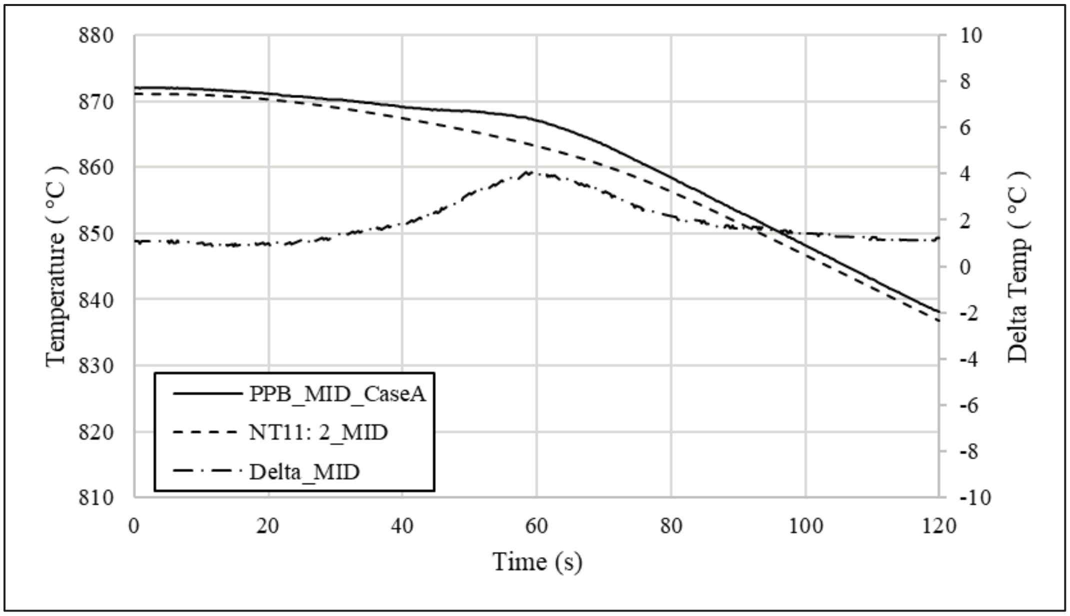

Figure 7.1 Cooling curve and error plots for PPB MID sensor. Delta temperature computed as the difference between test (continuous line) and simulation (dash line)

7.2.2 Inverse Results Verification During Immersion

The inverse identification strategy outlined in CHAPTER 4 was applied to PPA and PPC. The resulting temperature dependent surface fluxes for PPA and PPC are presented in Figure 7.2. Note that the given solutions present certain characteristics, such as the clear appearance of the film boiling for the thinner PPC. Findings with regards to transition temperatures between cooling regimes and the duration of the cooling regimes based on the cooling curves have been discussed in detail in CHAPTER 6. Hence, the differences in the BC for PPA and PPC are expected and representative of the different phenomena occurring at the surface-fluid interface.

Based on the surface heat flux (see Figure 7.2), local HTCs were derived and then used as a boundary condition in a FE simulation as verification. The accuracy of such simulations is presented herein in the form of error plots: temperature differences between test data and simulation, and relative errors, for PPA and PPC in Figure 7.3 and Figure 7.4, respectively. The results are deemed acceptable, as the error never exceeded 20°C, even at high temperatures, and the relative error always remains ±5% thus confirming the applicability of the inverse method to different specimen sizes and the accuracy of the identified HTC. Upon verifying the accuracy of the found HTCs, the mathematical models for immersion described in further subsections consider the inverse method results as their input.

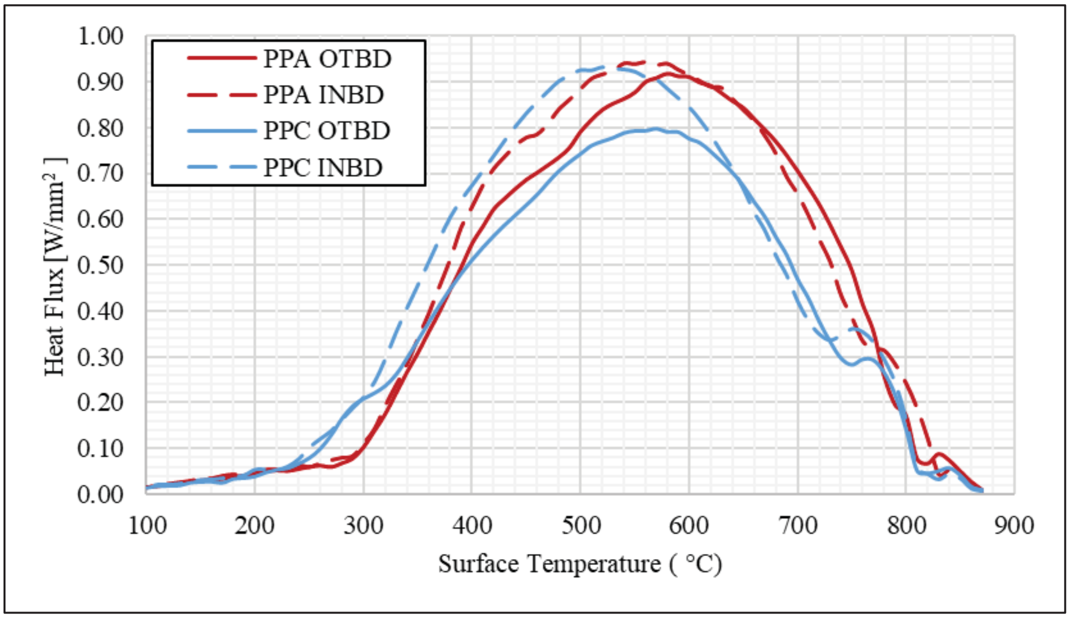

Figure 7.2 Surface heat flux obtained by inverse method. PPA (red) and PPC (blue) correspond to Case A test setup

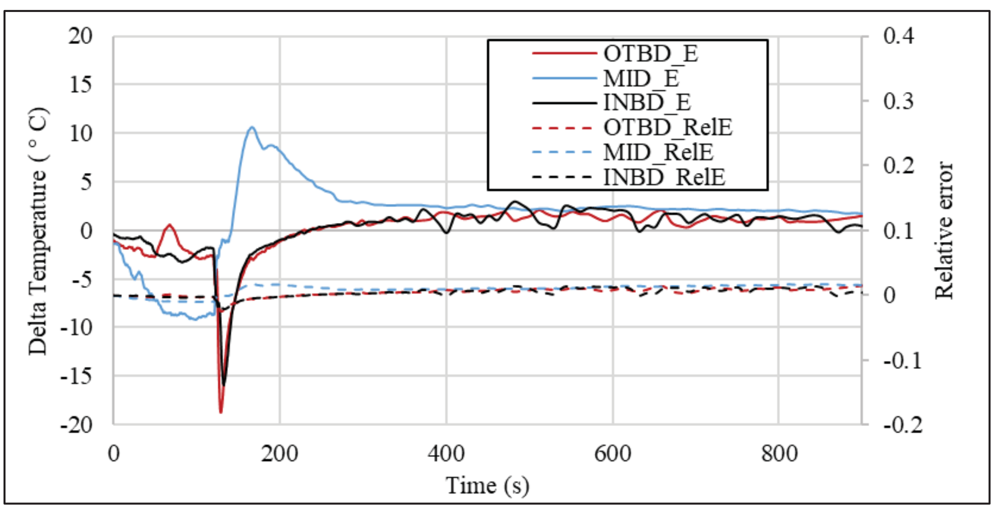

Figure 7.3 PPA error plots at the three sensor’s locations. Simulation values obtained with HTC from Inverse Results for PPA

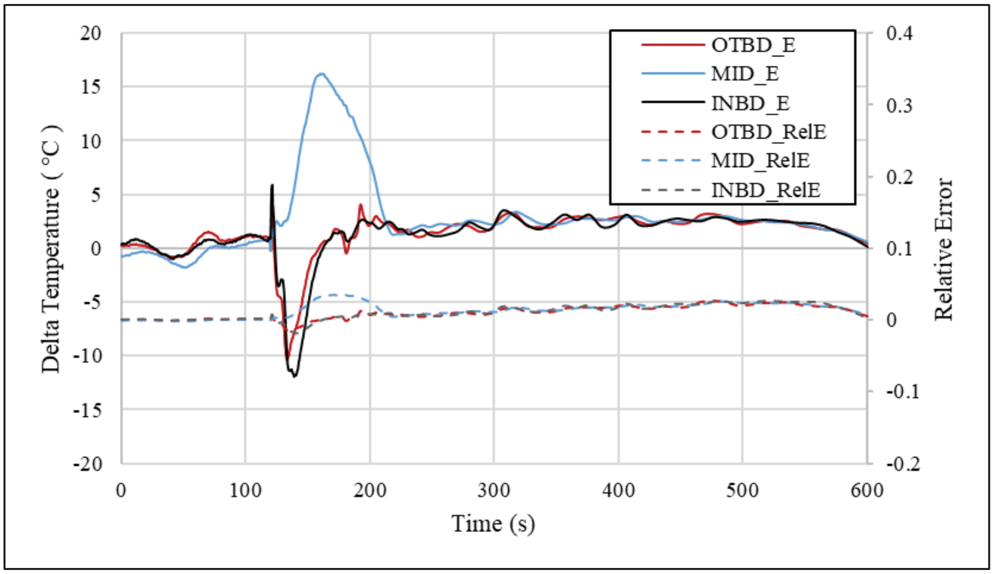

Figure 7.4 PPC error plots at the three sensor's locations. Simulation values obtained with HTC from Inverse Results for PPC

7.3 Air Transfer Modeling

The proposed modeling strategy for the air transfer step comprises three main segments: Air 1 – Furnace, Air 2 – Extraction, and Air 3 – Open Air Transfer, as shown in Figure 7.5. Each segment can be associated with specific instances of the trajectory of the heat-treated load thus dictated by the system movements. Such approach follows on the strategy implemented in CHAPTER 5 to identify control points, as per the system movement, which proved effective to identify the thermal BC of different probes.

The modeling strategy for the first segment follows a generalized average linear HTC; this is the only size independent segment. The model for the second segment is based on the exponential behavior of the identified HTCs (see Figure 7.5). The third segment is modeled by adjusting the linearized radiative HTC, as per theoretical correlations from classic textbooks. The influence of the probe's size is accounted from the second segment onwards, as explained in further subsections, this is achieved by considering the correlation between the peak HTC during the air step and the Biot number.

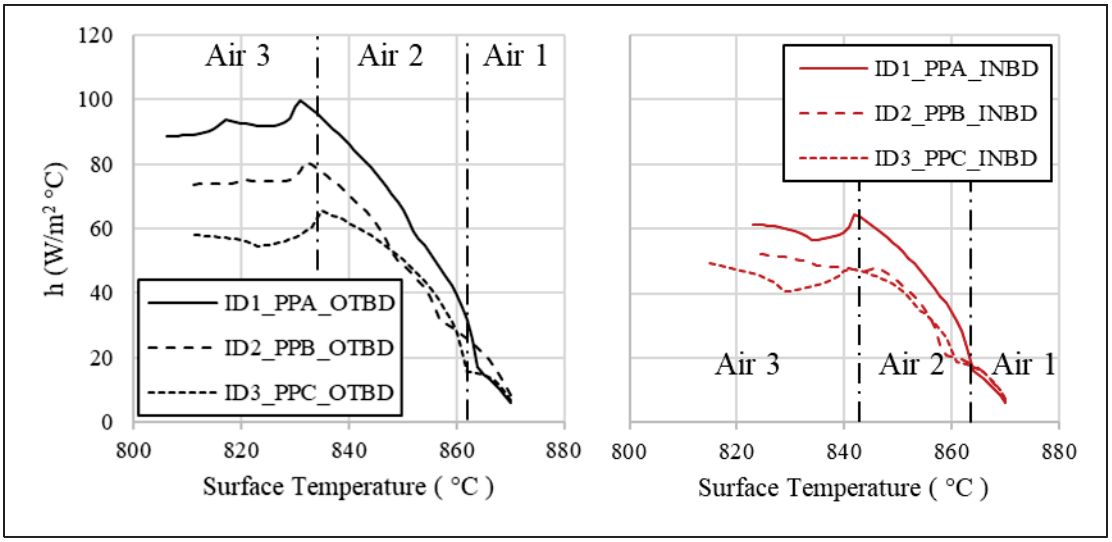

Figure 7.5 Temperature dependent HTC during air transfer for OTBD (left) and INBD (right) surfaces

7.3.1 Air 1 - Furnace

The HTC for first segment of the air transfer step (h_{A1}) is modeled as an average value that evolves linearly as temperature decreases. At the beginning of cooling, while the specimens remain inside the furnace, the radiative effects of the furnace walls dominate the heat exchange, almost reducing cooling to a minimal. This is clearly observed in the Air-1 portion of the curves in Figure 7.5, the magnitude of the HTC is considerably smaller during this segment when compared to the instances afterwards. Thus, the range of temperatures covered by h_{A1} starts at the beginning of the process (T_{start}) until $h(T)$ presents a rapid increase and the values spread out according to Figure 7.5. Hence, the lower temperature limit for h_{A1} is $863°C$. The spread of the $h(T)$ was verified by computing the standard deviation of $h(T)$, whose values almost doubled (from 2.7 to 4.4) between 863°C to 862°C. The averaged $h(T)$ curve is depicted in Figure 7.6, as well as two additional curves representing the Case A (Top) and Case B (bottom) averaged curves. The differences are disregarded given their closeness in magnitude.

Thus, h_{A1} follows a linear model for all the cases, test setup (A or B), and surfaces (INBD and OTBD). Thereby, this is the only segment that is independent of the size of the specimen and surface orientation. The average curve was computed considering all the cases and modeled with a linear equation (m=1.48, b=1299.5) in the form:

$$h_{A1}(T_i) = mT_i + b \tag{7.1}$$

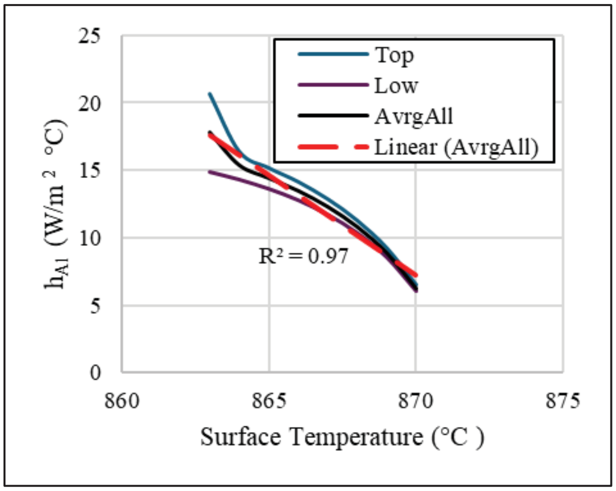

Figure 7.6 Temperature dependent HTC for Air 1 - Furnace

7.3.2 Air 2 - Extraction

The second segment of the air transfer step comprises the extraction of the load from the furnace, labelled as Air-2 in Figure 7.5. The HTC during this segment (h_{A2}) evolves exponentially over the range of temperature starting by the end of h_{A1} and the temperature when the peak HTC (h_{Amax}) occurs, which corresponds to the peak, once the furnace envelope has been cleared off. Such reference temperature is referred herein as $T_{h_{Amax}}$. The influence of the probe's size becomes noticeable from this point onwards, shown by the increase in magnitude of the HTC for the different curves in Figure 7.5. However, $T_{h_{Amax}}$ is not sensitive to the effects of size, as h_{Amax} appears around the same temperature, but should be adjusted depending on the surface orientation (either INBD or OTBD), as shown in Figure 7.5.

The HTC model h_{A2} is the product of $h(T_n)$, a non-dimensional curve (h_n, T_n) built upon the identified boundary conditions, and $h_{Amax}(Bi)$, thus h_{A2} is computed as follows:

$$h_{A2}(T_i) = h(T_n) * h_{Amax}(Bi) \qquad (7.2)$$

From this segment onwards, the influence of the size of the specimen is accounted for during the air transfer by considering the dependence of h_{Amax} with regards to the Biot number. The h_{Amax} values, shown in Figure 7.7, correspond to the peaks once the tooling is outside the envelope of the furnace. It includes data for both INBD and OTBD surfaces, allowing for a more generalized model dependent upon case setup (A or B) only.

Thus, the exponential relation describing h_{Amax} as a function of the Biot number, as shown in Figure 7.7, obeys the following relation:

$$h_{Amax}(Bi) = ae^{bBi} \qquad (7.3)$$

Where the constants of the model are given as $a = 29.793$, and $b = 14.557$, with a goodness of fit of $R^2 = 0.95$.

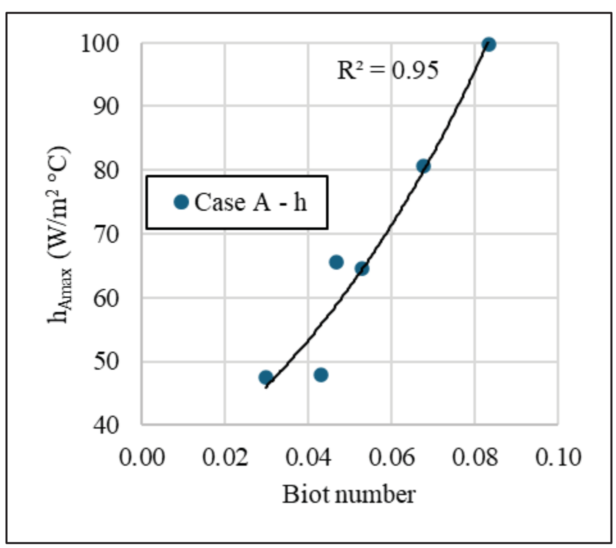

Figure 7.7 Evolution of h_{Amax}

The non-dimensional curve $h(T_n)$ in Eq. 7.2 is built upon the inverse identification results from CHAPTER 5. Thus, data from the different plates (PPA, PPB, PPC) and surfaces (INBD and OTBD) were processed. Hence, six different non-dimensional data series were used to develop a general model of the non-dimensional curve $h(T_n)$ which follows the form:

$$h(T_n) = a - \frac{(T_n + b)^2}{c} \tag{7.4}$$

For which the constants are given as $a = 1.123, b = -0.697, c = 0.769$, with a goodness of fit of $R^2 = 0.99$. The data and model are shown in Figure 7.8 for the non-dimensional datasets for Air 2. The proposed model in Eq. 7.4 applies to Case A only, data and model for Case B can be found in ANNEX VI.

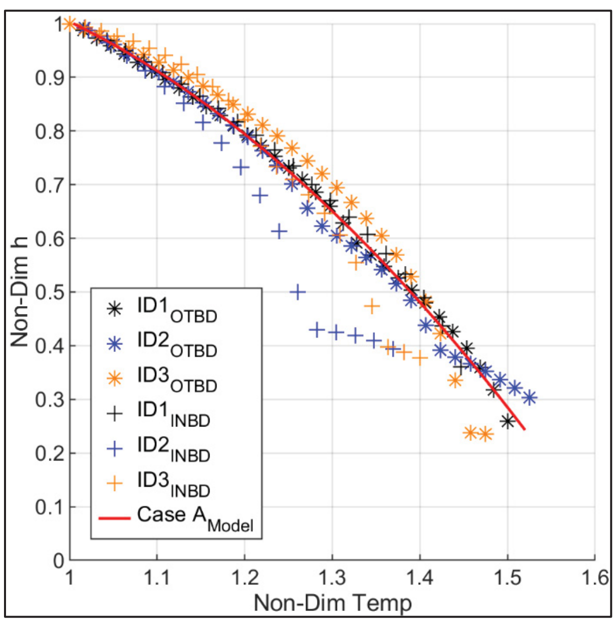

Figure 7.8 Non-dimensional h during Air 2

Each of the non-dimensional curves $h(T_n)$, shown in Figure 7.8, are based on the identified HTCs, which were transformed into non-dimensional values by the ratio:

$$h_{n_i} = \frac{h_i}{h_{MaxT}} \tag{7.5}$$

Where h_{MaxT} represents the peak HTC once the tooling is outside the envelope of the furnace for a given case, just before the h curve progressively decreases, and h_i represents every discrete value for a given surface. The resulting non-dimensional h_n values represent the y-axis in the non-dimensional curve (see Figure 7.8).

Then, the temperature values (x-axis) were converted to non-dimensional values as follows:

$$T_n = 1 + \frac{T_i - T_{h_{MaxT}}}{T_{range}} \tag{7.6}$$

Where T_i is the discrete values from the boundary condition identification results, $T_{h_{MaxT}}$ is the temperature when h_{MaxT} occurs based on the inverse results, and T_{range} is the temperature range per case, which is given as follows:

$$T_{range} = T_{start} - T_{t_{120}} \tag{7.7}$$

Where T_{start} is the starting condition in the furnace and $T_{t_{120}}$ is the temperature at the end of the air transfer (before immersion). Note that $T_{t_{120}}$ changes on a case-by-case basis, hence each curve has its own T_{range}. The resulting non-dimensional temperature values were assigned to the x-axis (see Figure 7.8).

The values for $T_{t_{120}}$ can be obtained graphically on a case-by-case basis following the trendlines plotted in Figure 7.9. Care should be taken as INBD and OTBD surfaces behave differently, the OTBD surfaces cool down faster, leading to lower temperatures than INBD surfaces by the end of the air transfer.

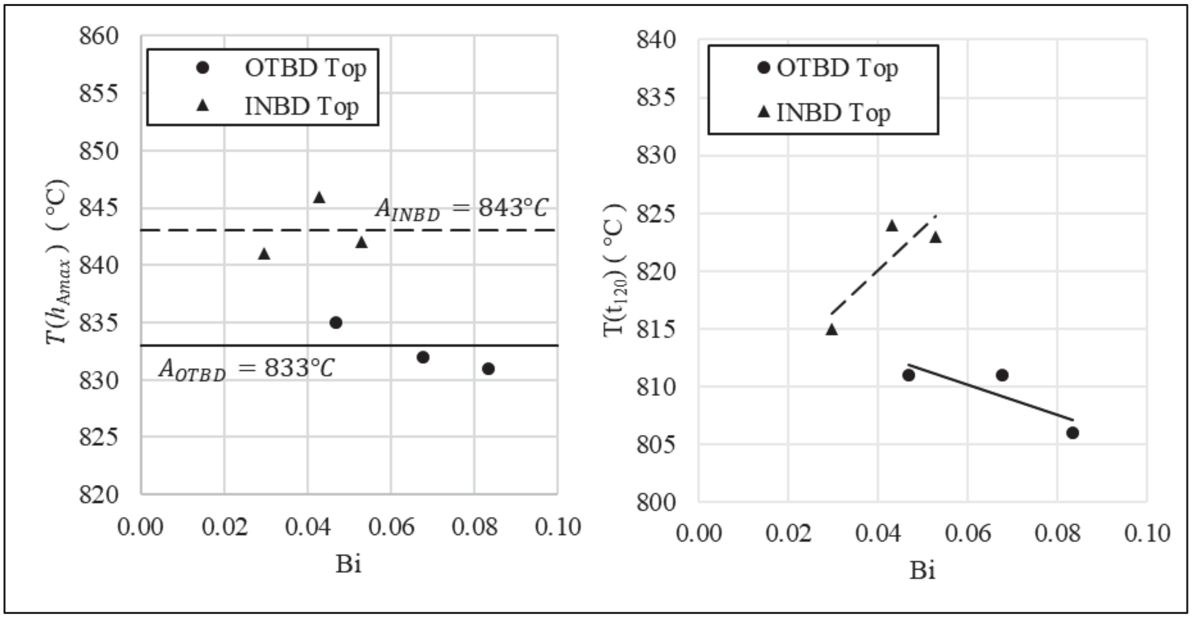

Figure 7.9 Reference temperature $T_{h_{Amax}}$ (left) and $T_{t_{120}}$ (right) during Air 2

At the beginning of this subsection, it is mentioned that h_{Amax} appears around the same temperature, depending on the surface orientation only (see Figure 7.5). On that basis, $T_{h_{Amax}}$ which marks the end of the $h_{A2}(T)$ model, is also independent of the probe size but must be adjusted for a given surface. $T_{h_{Amax}}$ data for OTBD and INBD surfaces (see Figure 7.9) indicate a variation between 4°C-6°C between the different probes, deemed acceptable for the purposes of a more generalized model. Thus, an average value of $T_{h_{Amax}}$ per surface can be considered. As a reminder, INBD temperatures are always higher than their equivalent OTBD for a given test setup.

7.3.2.1 Air 2 Model Evaluation and Considerations

The main steps to evaluate the model $h_{A2}(T)$ are described in the flowchart shown in Figure 7.10. In summary, $h_{A2}(T)$ as per Eq. 7.2 is obtained by evaluating Eq. 7.4, then factored by $h_{Amax}(Bi)$, which obeys the relation as per Eq. 7.3 depicted in Figure 7.7. The non-dimensional temperature values are then adjusted by solving for T_i from Eq. 7.6 to obtain the actual temperature values encompassed in this segment. The reference temperatures $T_{h_{Amax}}$

and $T_{t_{120}}$ can be obtained graphically from Figure 7.9. Details about the computation of the Biot number for the air transfer step are included in Chapter 5. The model provides curves that account for the difference between cases (A or B), surface (INBD or ORBD) and size (by different Bi numbers).

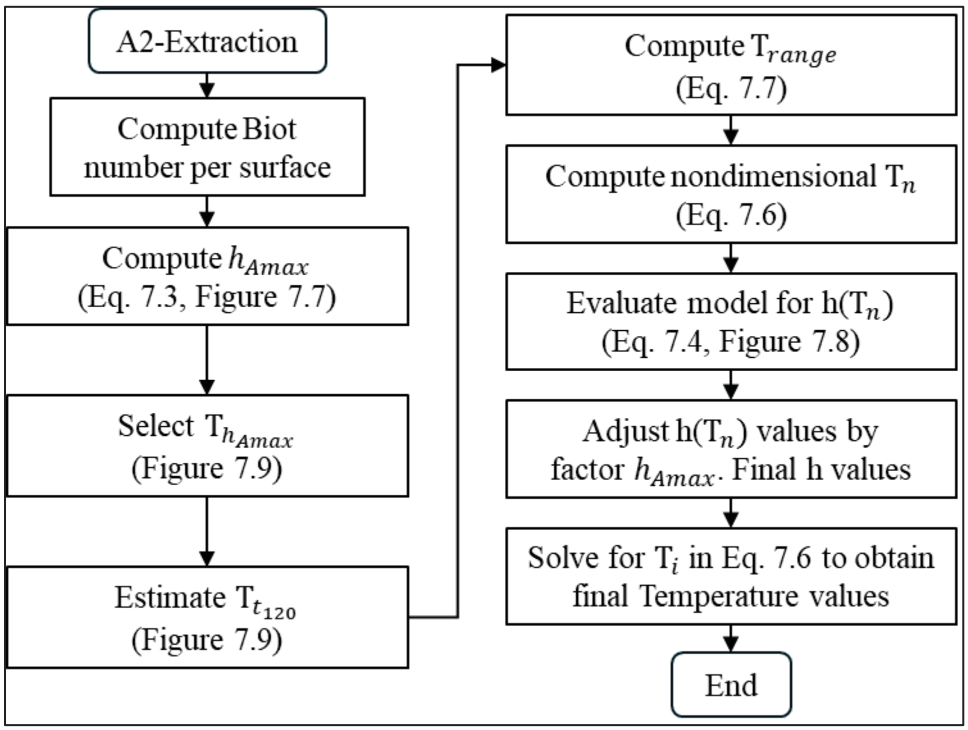

Figure 7.10 Model evaluation and considerations during Air 2

The resulting curves after evaluating the proposed model for Case A are shown in Figure 7.11. The influence of size is shown by the difference in magnitude of the HTC associated to their corresponding Biot number. Similarly, the influence of the orientation of the probe in the system, OTBD (black lines) and INBD (red lines), is properly captured. The lower temperature limit of the model $h_{A2}(T)$ depends on the surface: 833°C for OTBD, and 843°C for INBD, driven by the selection of the reference temperature $T_{h_{Amax}}$ but independent of the probe's size.

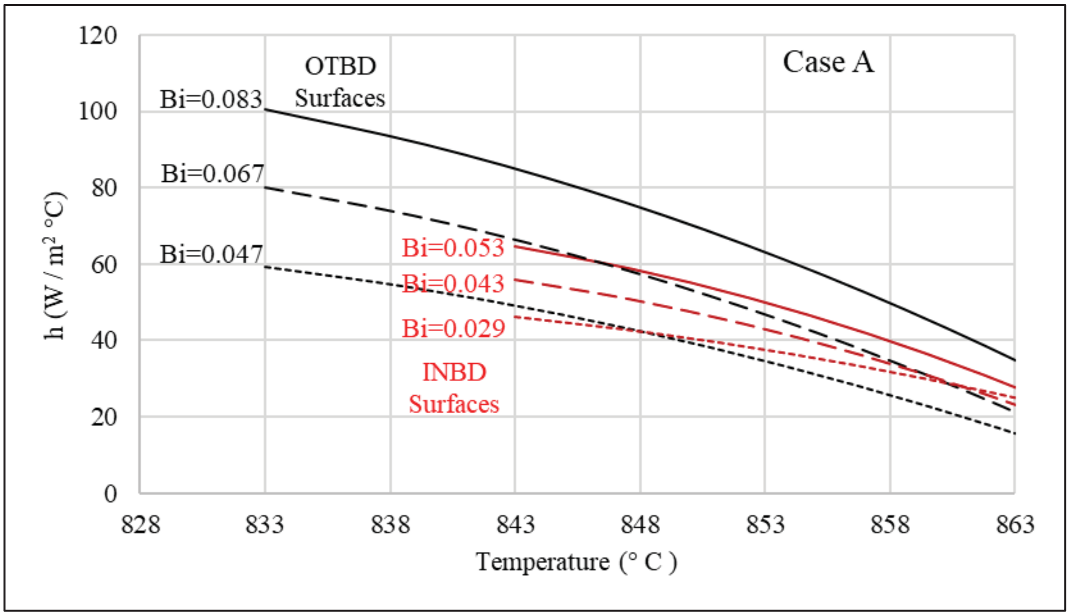

Figure 7.11 Model for INBD and OTBD surfaces during Air 2

7.3.3 Air 3 – Open Air Transfer

The third segment of the air transfer step encompasses the open-air transfer, once the load is outside the furnace envelope and moving towards the quench bath. Thus, the HTC model for this segment (h_{A3}) starts right at the end of h_{A2}, which was given by the reference temperature $T_{h_{Amax}}$, until immersion occurs. The influence of the probe's size is also noticeable during this segment (see Figure 7.5). The available linearized radiative HTC (h_r) correlations, as per classic textbooks (Bergman et al., 2011), do not account for the influence of size. Yet, those theoretical correlations can be used to produce a semi empirical model, where h_r is simply multiplied by a factor h_{Arat} as follows:

$$h_{A3}(T_i) = h_r(T_i) * h_{Arat} \tag{7.8}$$

For $T_i \in \left[T_{t_{120}} < T_i < T_{h_{Amax}}\right]$, where $h_r(T_i)$ is given in the form (see also Eq. 5.16):

$$h_r = \epsilon\sigma_r(T_{surf} + T_{surr})(T_{surf}^2 + T_{surr}^2) \tag{7.9}$$

Where σ_r is the Stefan Boltzmann constant $5.67 \times 10^{-8}\ W/(m^2K^4)$), ϵ is the surface emissivity for heavily oxidized stainless steel (Bergman et al., 2011), and T_{surf} and T_{surr} represent the surface and surrounding temperatures, respectively.

In Eq. 7.8, h_{Arat} is given by the following relation:

$$h_{Arat} = h_{Amax}/h_{r_{TAmax}} \tag{7.10}$$

Where h_{Amax} has been defined previously as a function of the Bi number (Figure 7.7), and $h_{r_{TAmax}}$ is the corresponding theoretical radiative heat transfer coefficient at the same reference temperature where h_{Amax} occurs, and thus can be evaluated with Eq. 7.9 at the reference temperature $T_{h_{Amax}}$.

The resulting temperature dependent $h_{A3}(T_i)$ per surface can be obtained for the different plate probes as shown in Figure 7.12. Note that the plotted values cover until 800°C, although the body temperatures just before immersion are likely to stay above such threshold.

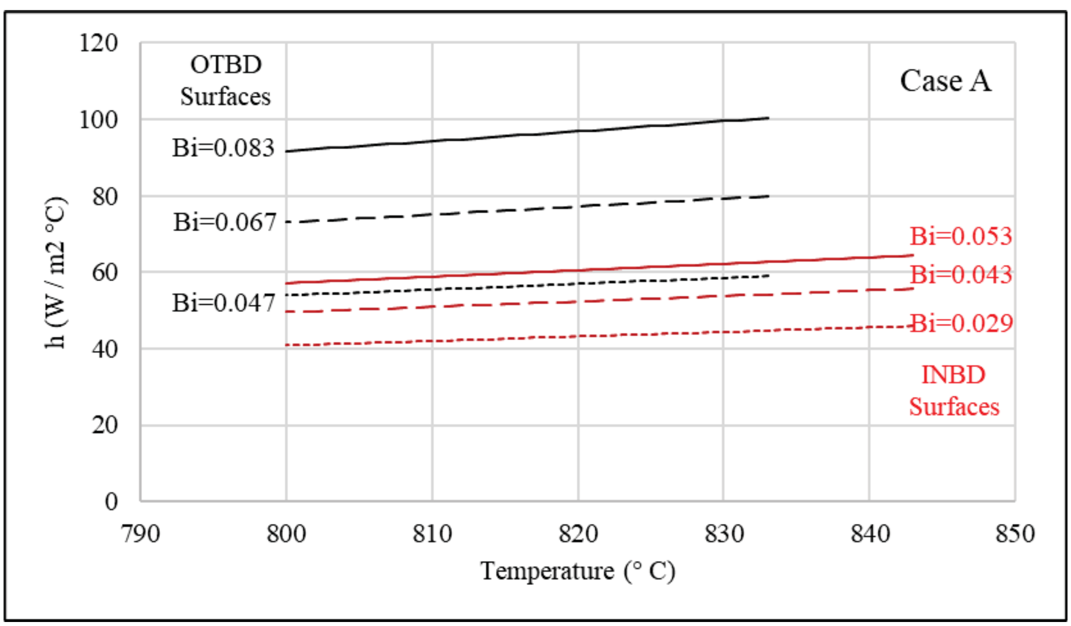

Figure 7.12 Model for INBD and OTBD surfaces during Air 3

7.3.4 Air Transfer Model Verification

Using the proposed models for the three stages of air transfer, the BC on a given surface can be represented as function of surface temperature. The resulting models for the sizes herein are shown in Figure 7.13. The three stages are also marked on the figure to indicate the start and end of each stage.

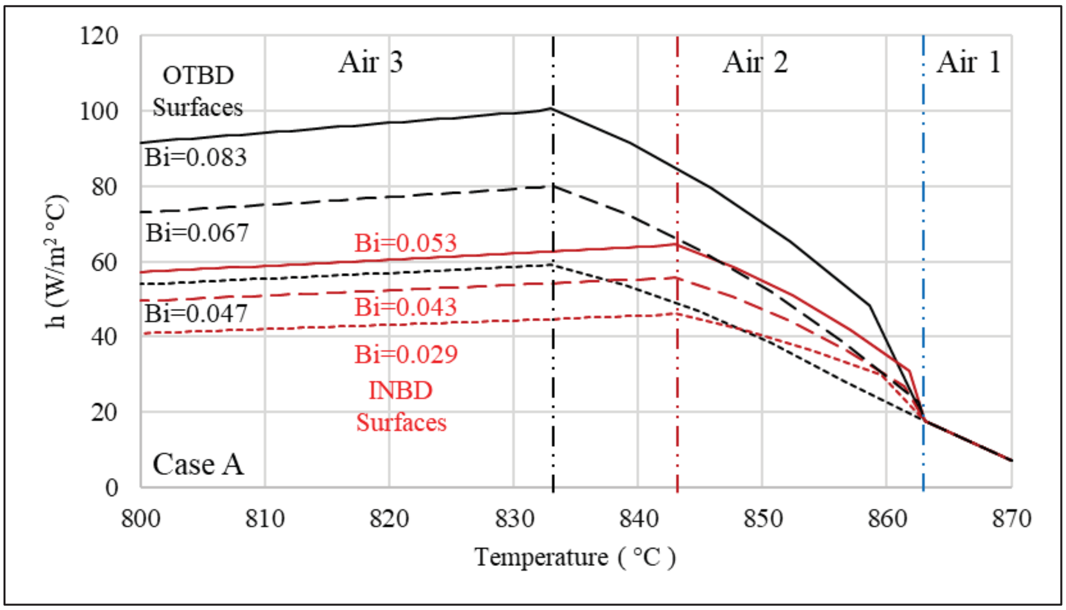

Figure 7.13 Model for INBD and OTBD surfaces during the complete air transfer

The model was assessed by using the curves from Figure 7.13 as BC in a FE simulation and then evaluated against the experimental temperature recordings. The FE simulation was carried out for the 120 s of the expected air transfer step only. Results indicate that all the cases produce a relative error <1.2%, while RMSE never exceeded 3.2°C. Note that the largest temperature difference between test and simulation by the end of the air transfer was <4°C, which was deemed acceptable. Figure 7.14 presents the worst case for PPB-MID sensor, indicating good agreement between simulation and test data.

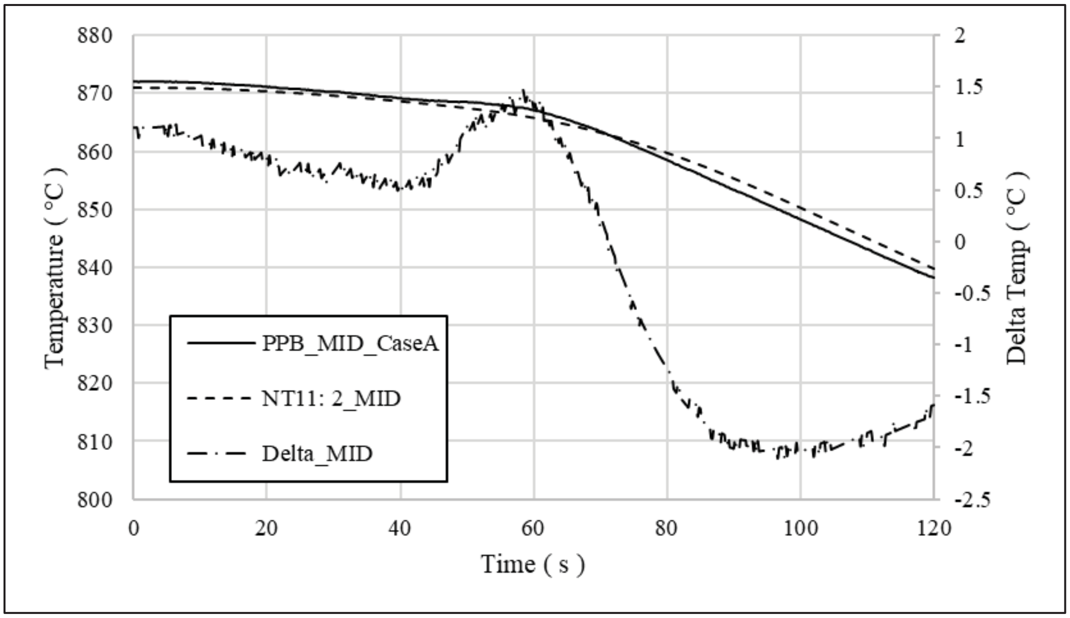

Figure 7.14 Cooling curves of PPB-MID from test data (continuous line) and simulation (dashed line) results as per model BC; delta temperature computed as the difference between test and simulation values

7.4 Immersion Modeling

The proposed mathematical models for the immersion step rely on the identified surface heat fluxes for the different specimens. The models follow the behavior of a typical curve for each of the cooling regimes (see Figure 7.15). The surface fluxes for each cooling regime, bounded as per the characteristic points (CPs) shown in Figure 7.15, are converted into a dimensionless curve. The non-dimensional curves, which model a given cooling regime, are adjusted as per correlations of the characteristic points that evolve as a function of the Biot number.

The models developed for the immersion step represent the surface heat flux instead of the HTC (as done for the air transfer step). The rationale is founded on the CPs of the boiling curve (see Figure 7.15), which are typically given as flux densities in the literature (i.e., CHF, MHF). These CPs can be associated with the physical phenomena occurring during immersion. In Figure 7.15, Q_{MHF} represents the end of film boiling and beginning of transition boiling, Q_{CHF} illustrates the beginning of nucleate boiling upon the end of transition boiling, and Q_{conv} corresponds to the beginning of a convection driven regime. These CPs might be different in magnitude and appear at different temperatures for PPA & PPC, as shown in Figure 7.2. On this basis and following up on the findings presented in detail in CHAPTER 6 for the evolution of the cooling regimes during immersion, the strategy herein postulates that the BCs must be adjusted as per the evolution of the CPs of a $q(T)$ curve.

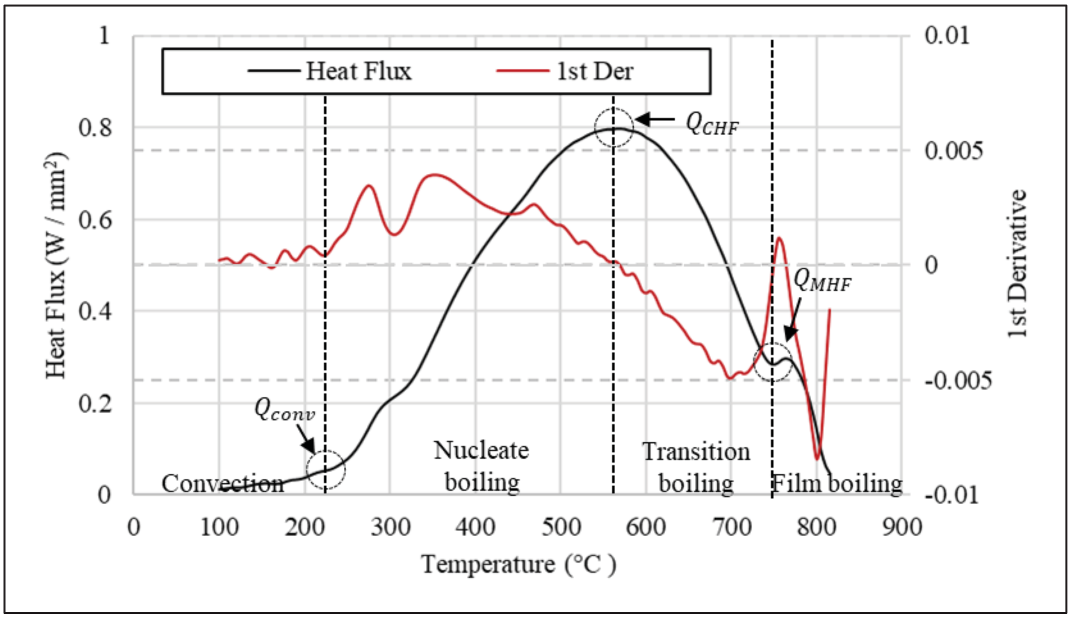

Figure 7.15 Typical surface heat flux curve during immersion

This section discusses first the built up of the models, starting by discussing the evolution of the CPs during immersion. It is followed by describing the procedure to obtain the dimensionless curves of the surface fluxes. Then, the proposed models for each of the cooling regimes are introduced before concluding with their evaluation and verification. Nonetheless, the resulting heat flux models as per the strategy herein are then converted into temperature dependent HTC for the verification and validation step. The accuracy of the models is evaluated by computing the temperature difference and relative error between test data and results as per the models.

7.4.1 Model Build Up

This section presents the evolution of the CPs, followed by the conversion of inverse results into dimensionless values, and presenting the model fitting per cooling regime. Note that several of the relations presented herein make use of the non-dimensional Bi number as described in Section 6.2.

7.4.1.1 Evolution of Characteristic Points

Minimum Heat Flux – Q_{MHF} has special significance as it represents the end of the film boiling regime. It is easily located on the typical heat flux curve at the valley before the rapid increase in magnitude of the flux as shown in Figure 7.15. By averaging the inverse results, it was determined that its magnitude can be approximated as 297 kW/m^2, as shown in Figure 7.16. However, inverse results indicate that the smaller the specimen, and thus the Bi number, the lower T_{MHF}, which represents the temperature at which Q_{MHF} appears. Figure 7.16 includes a linear tendency and the expression that can be used to compute T_{MHF}. Thus, the present strategy considers T_{MHF} to be dependent on Bi with a constant magnitude of Q_{MHF}.

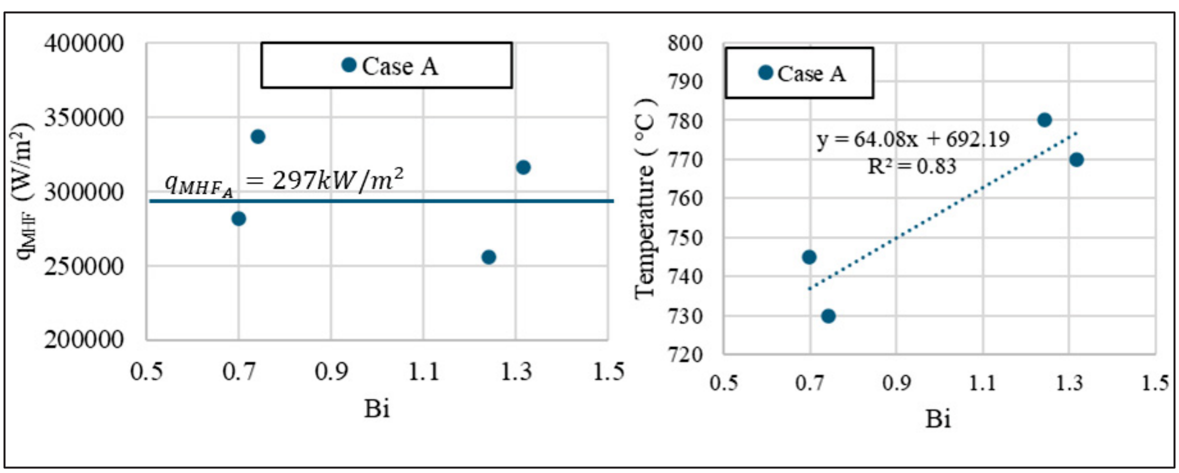

Figure 7.16 Minimum heat flux: magnitude (left) and temperature evolution (right)

Critical Heat Flux - Q_{CHF} represents the peak surface heat flux during immersion. Its evolution on both INBD and OTBD surfaces can be seen in Figure 7.17. Note that the values on the INBD surface were almost identical and, averaged at 940 kW/m^2. The Q_{CHF} on OTBD surfaces are lower in magnitude with a tendency to decrease as the body size decreases. Hence, a ratio between INBD to OTBD values is proposed and shown in Figure 7.17. This approach leads to adjusting the magnitude of Q_{CHF} based on probe size.

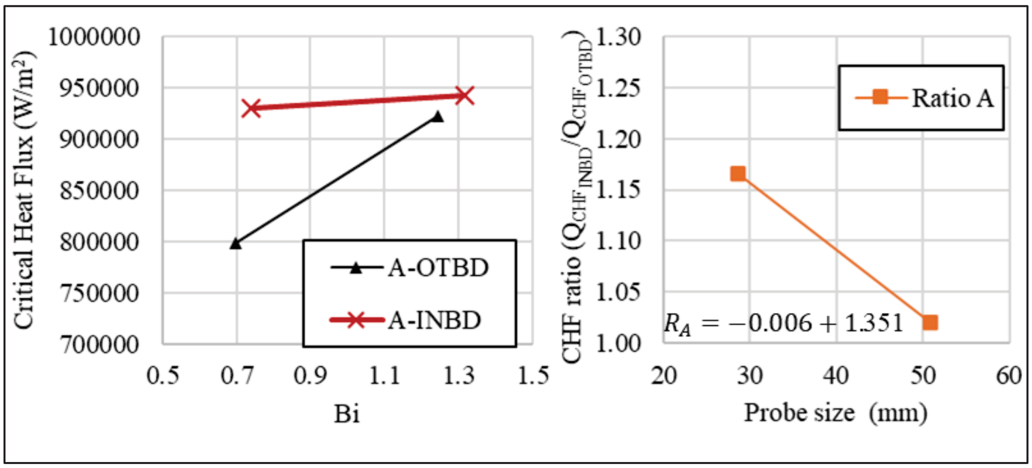

Figure 7.17 CHF: magnitude (left) and Q ratio INBD/OTBD (right)

The temperature at which Q_{CHF} occurs, also referred as T_{CHF}, has a consistent behavior with T_{MHF} as it tends to decrease for the smaller specimens (see Figure 7.18). However, the predicted T_{CHF}, values for INBD surface are almost identical (triangle markers, Figure 7.18, whose variations can be considered neglectable whereas OTBD surfaces (cross markers) have a wider range of temperatures. For modeling purposes, it was decided to consider an average T_{CHF} depending on the surface whose values are shown in Figure 7.18. Data shown in Figure 7.17 and Figure 7.18 correspond to Case A (top of HT-rig), further details for Case B are given in ANNEX VII following the same rationale.

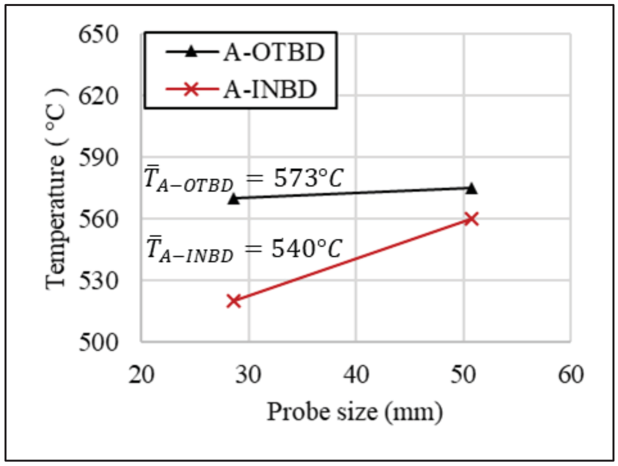

Figure 7.18 Evolution of T_{CHF} per surface

Onset of Boiling - Q_{conv} is the last CP of the typical surface heat flux curve in Figure 7.15. It marks the end of the nucleate boiling, and signals that, from that point onwards, heat exchange is mainly driven by convection. Hence, the flux curve follows an almost linear behavior whose derivative with regards to temperature tends to 0, as shown in the schematic in Figure 7.15. Such criteria were used to identify Q_{conv} and T_{conv} on the inverse result curves. The evolution of Q_{conv} and T_{conv} are shown in Figure 7.19. In both instances, there is a linear relation that describes their behavior with regards to the Bi number. Both variables indicate that the smaller specimens have lower Q_{conv} and T_{conv}. The strategy presented herein considers both Q_{conv} and T_{conv} as a function of Bi.

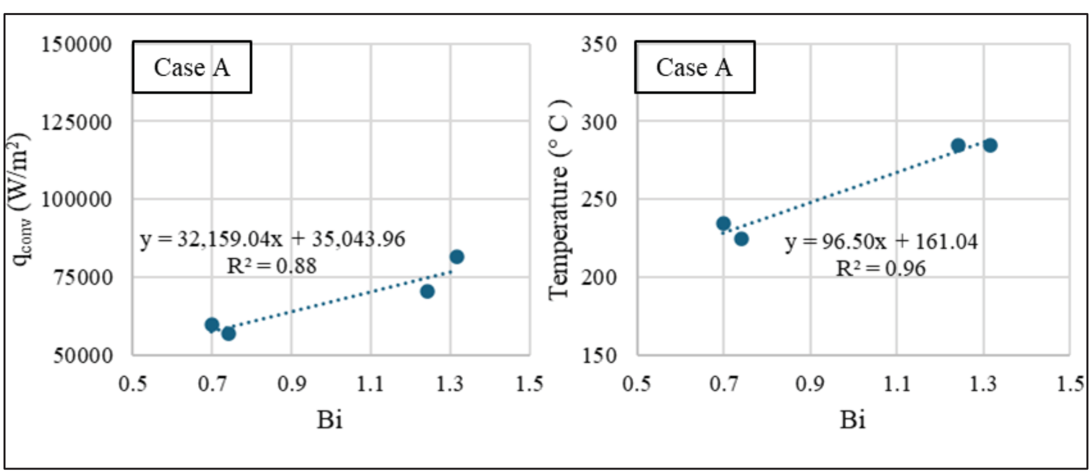

Figure 7.19 Onset of boiling: magnitude (left) and temperature evolution (right)

7.4.1.2 Dimensionless Boundary Conditions

The identified boundary conditions for PPA and PPC, in the form of $q(T)$, were transformed into non-dimensional curves for each of the cooling regimes: film boiling, transition boiling, nucleate boiling, and convection (see Figure 7.15). These curves became the input data for the regression models to represent the exponential nature of the fluxes during each regime.

The cooling regimes are bounded as per the CPs limiting each regime (see Figure 7.15). Thus, the surface flux from immersion until the end of film boiling (FB) were normalized as per Eq. 7.11 as a function of a dimensionless temperature parameter given in Eq. 7.12:

$$q_{0_{FB}} = \frac{q_{surf}}{q_{MHF}} \tag{7.11}$$

$$T_{0_{FB}} = \frac{T_{imm} - T_{surf}}{T_{imm} - T_{MHF}} \tag{7.12}$$

The temperature and flux during transition boiling (TB), which are encompassed within the CPs labelled as Q_{MHF} and Q_{CHF}, were transformed into non-dimensional values as per Eq. 7.13 and Eq. 7.14:

$$q_{0_{TB}} = \frac{q_{surf} - q_{MHF}}{q_{CHF} - q_{MHF}} \tag{7.13}$$

$$T_{0_{TB}} = \frac{T_{MHF} - T_{surf}}{T_{MHF} - T_{CHF}} \tag{7.14}$$

Data during nucleate boiling (NB), which appears from Q_{CHF} until Q_{conv}, were converted as dimensionless parameters using the relations described in Eq. 7.15 and Eq. 7.16:

$$q_{0_{NB}} = \frac{q_{conv} - q_{surf}}{q_{conv} - q_{CHF}} \tag{7.15}$$

$$T_{0_{TB}} = \frac{T_{CHF} - T_{surf}}{T_{CHF} - T_{conv}} \tag{7.16}$$

Lastly, fluxes values during convection, which correspond to the last portion of the heat flux curve, were converted as dimensionless parameters given by Eq. 7.17 and Eq. 7.18:

$$q_{0_{conv}} = \frac{q_{end} - q_{surf}}{q_{end} - q_{conv}} \tag{7.17}$$

$$T_{0_{conv}} = \frac{T_{conv} - T_{surf}}{T_{conv} - T_{end}} \tag{7.18}$$

The end temperature was assumed to be 100°C, hence q_{end} was obtained for that reference temperature to complete the dimensionless procedure as outlined herein.

7.4.1.3 Model Fitting per Regime

Using the non-dimensional data obtained using Eq. 7.11 to Eq. 7.18, a regression model was fitted onto each of the cooling regimes curves. Thereby, each cooling regime has its own mathematical formulation, while the connection between each regime is given by the values and evolution of the characteristic points.

The non-dimensional model for film boiling (FB) and transition boiling (TB) follows an equation of the form:

$$q_{0_{FB,TB}} = \frac{a}{1 + e^{(-b(T_0 - c))}} \tag{7.19}$$

The nucleate boiling (NB) model obeys the form as per Eq. 7.20, while convection is described by Eq. 7.21.

$$q_{0_{NB}} = d + (a - d)e^{(-e^{(-b(T_0 - c))})} \tag{7.20}$$

$$q_{0_{conv}} = ae^{(bT_{non})} + ce^{(dT_0)} \tag{7.21}$$

The coefficients as per Eq. 7.19 to Eq. 7.21 are included in Table 7-1 for Case A. Figure 7.20 includes the dimensionless data per cooling regime. Note that proposed models were fitted while considering multiple data series for PPA and PPC, represented as ID1 & ID3 respectively, as well as both surfaces INBD and OTBD of the specimens Despite the variations observed, the proposed models indicate a goodness of fit $R^2 > 90\%$, which was deemed acceptable.

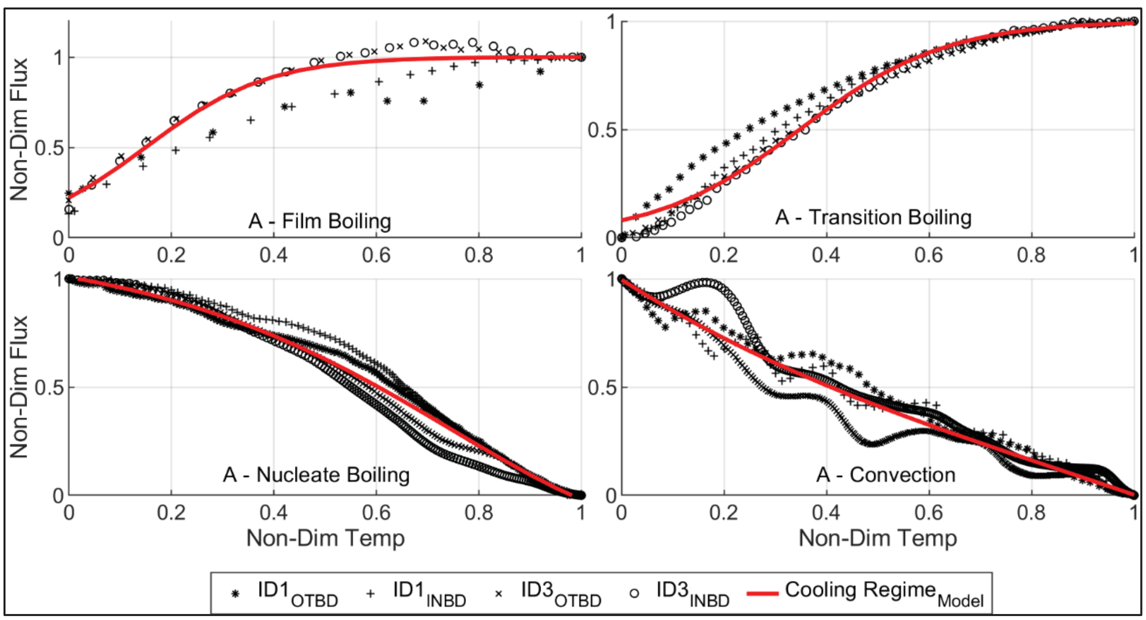

Figure 7.20 Dimensionless data (markers) per cooling regime during immersion with their corresponding model (red line)

Table 7-1 Regression models coefficients for dimensionless surface flux

Cooling Regime	a	b	c	d	R^2
Film	1.002	8.396	0.149	--	0.90
Transition	1.001	7.026	0.347	--	0.99
Nucleate	1.165	-2.803	0.747	-0.199	0.98
Convection	-0.045	1.736	1.040	-1.382	0.99

7.4.2 Immersion Model Evaluation

The main steps to evaluate the models for the immersion step are described in the flowchart depicted in Figure 7.21. In essence, the exponential models per cooling regime, built upon their corresponding non-dimensional curves, should be evaluated and then expanded, based on the evolution of the characteristic points. Thus, the strategy herein produces surface heat flux curves per cooling regime whose magnitude and temperatures are driven by the dependency of the characteristic points with respect to the Biot number, as presented in previous subsections.

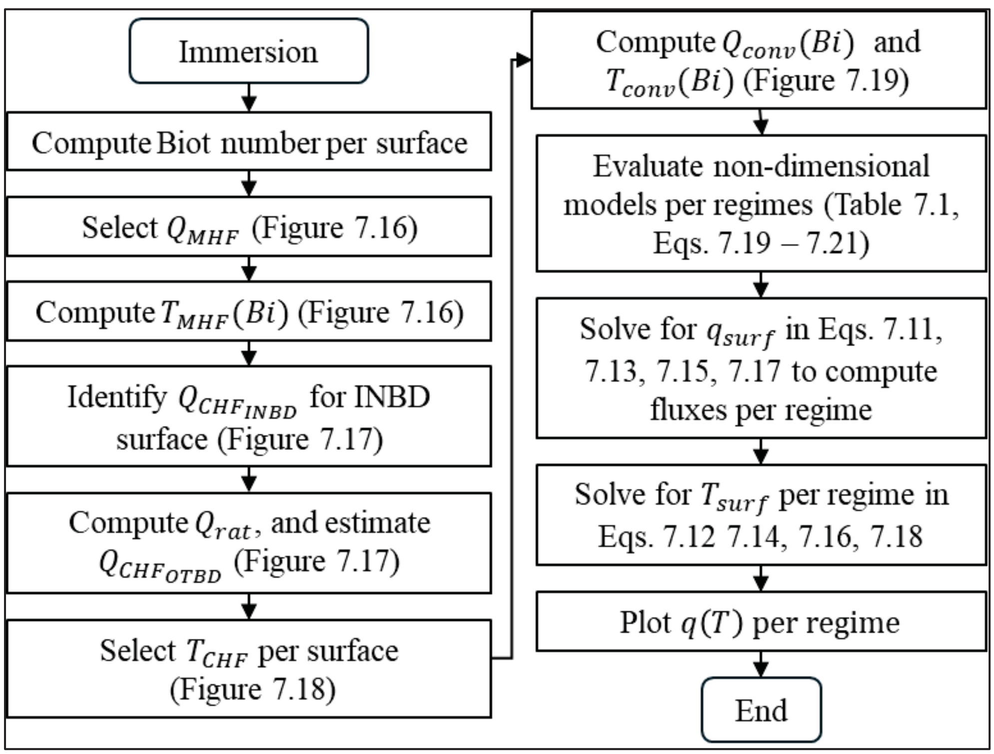

Figure 7.21 Model evaluation and considerations for immersion step

The resulting surface heat flux of plate probes PPA and PPC following the methodology outline herein is depicted in Figure 7.22 and Figure 7.23 respectively. The boundaries of the models per regime are their corresponding CPs, as shown schematically in the figures. The generated fluxes show good agreement with the results of the inverse procedure shown in Figure 7.2. Verification and validation of the models is discussed in the next section.

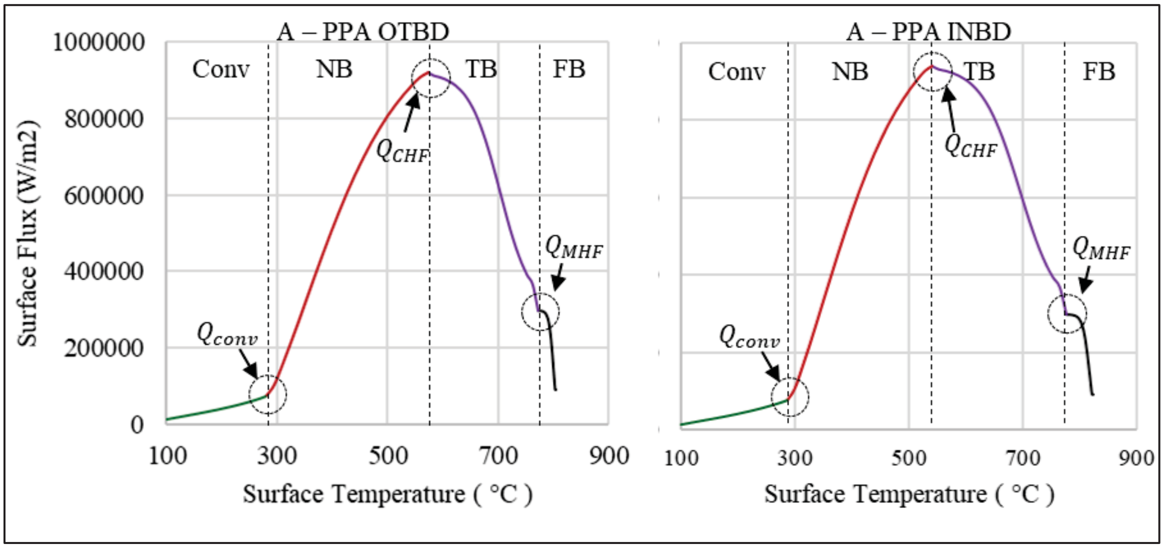

Figure 7.22 PPA adjustable BC: OTBD (left) and INBD (right) surface heat flux

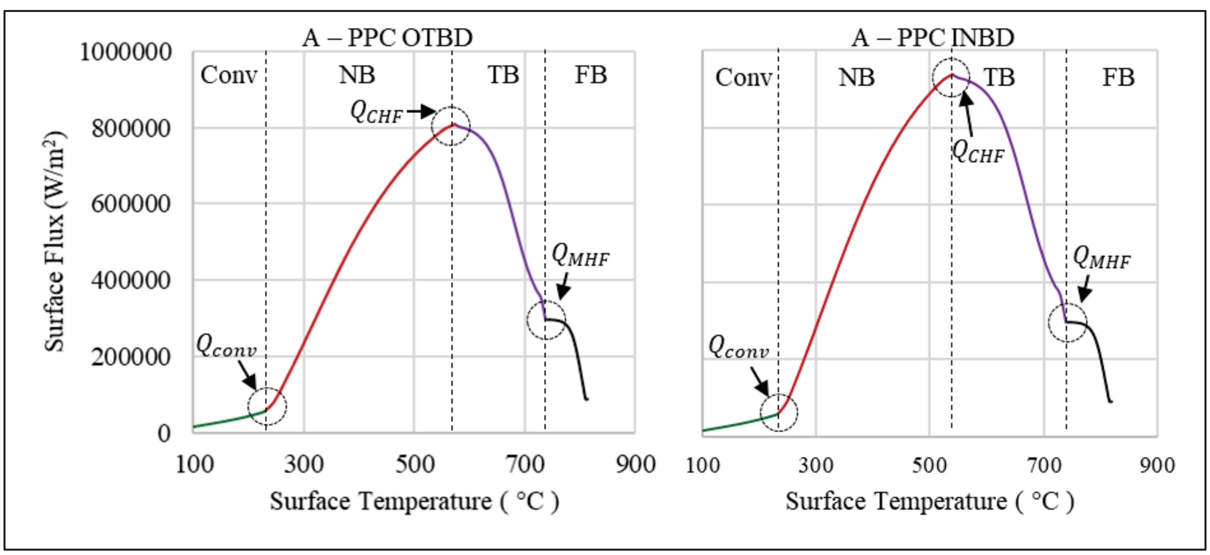

Figure 7.23 PPC adjustable BC: OTBD (left) and INBD (right) surface heat flux

7.4.3 Model Verification & Validation

The actual verification of the proposed models was done against the experimentally acquired cooling curves, thus assessed with regards to temperature values. The resulting surface fluxes plotted in Figure 7.22 and Figure 7.23 were converted into temperature dependent HTCs as per the well-known Newton's law of cooling in order to use them as BCs on a FE model. The resulting HTC curves are depicted in Figure 7.24 for both PPA and PPC.

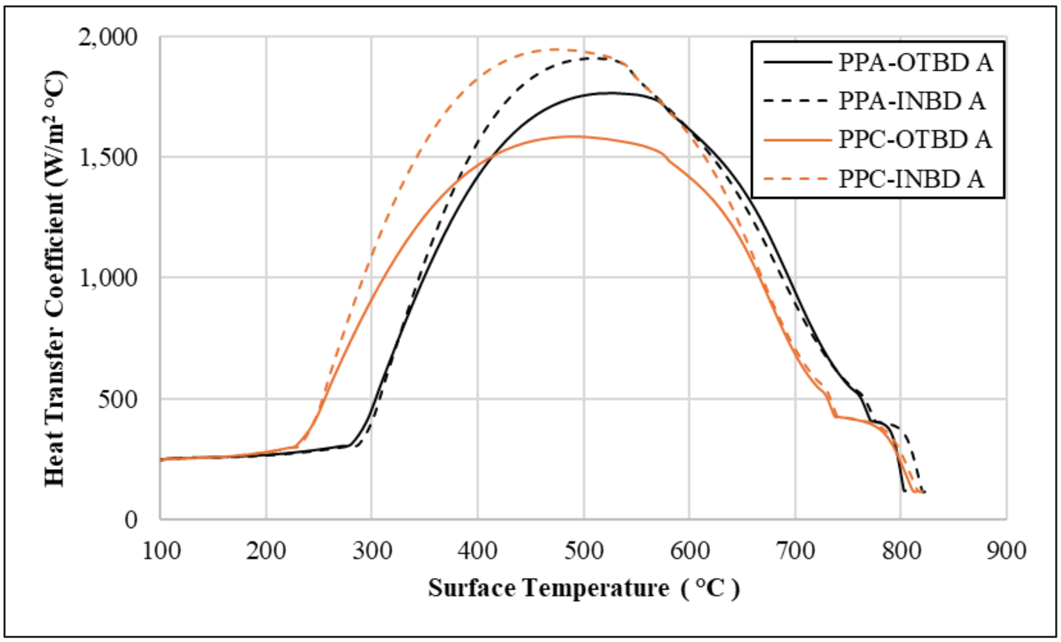

Figure 7.24 Heat transfer coefficients for PPA and PPC as per proposed models

Simulation results indicate good agreement between experimental data and simulation results, as shown in Figure 7.25 and Figure 7.26 for PPA and PPC respectively. The temperature delta between simulation and test data is slightly higher than those obtained from the inverse results (see Figure 7.3 and Figure 7.4), leading to an increase in relative error, yet always remaining <8%, which was deemed acceptable. These results are deemed acceptable for verification purposes of the proposed modeling strategy.

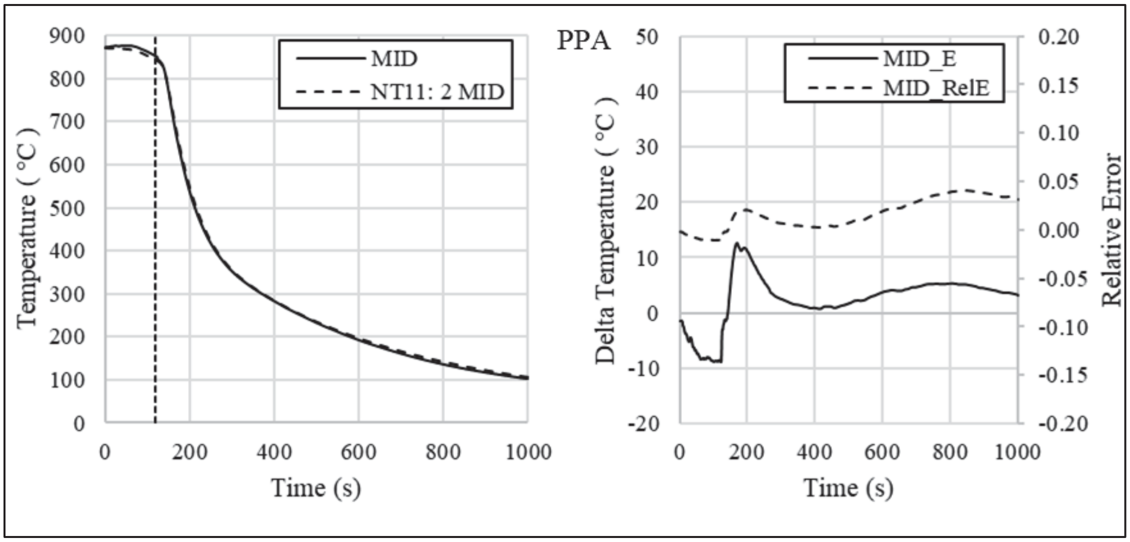

Figure 7.25 Model verification for PPA: cooling curves (left) and error plots (right)

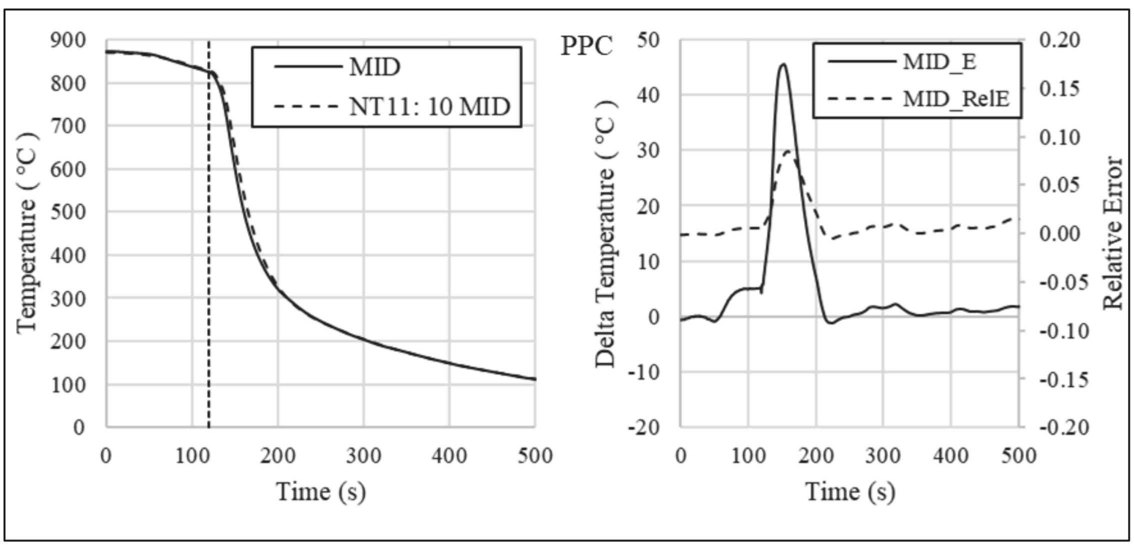

Figure 7.26 Model verification for PPC: cooling curves (left) and error plots (right)

The validation step was carried out using a third geometry, PPB whose size (thickness of 41.28 mm) falls within PPA and PPC range. This specimen was quenched under the comparable conditions to the reference probes but was not considered in the build-up of the mathematical model for the immersion step. A model of the BCs was built for PPB following the methodology outlined in this chapter. The resulting HTC curve for the OTBD and INBD surfaces of PPB is shown in Figure 7.27. A FE simulation was carried out using the modeled

BCs of PPB and compared against test data. The resulting cooling curves and error plots for the MID sensor of PPB are shown in Figure 7.28. The results indicate good agreement between cooling curves, while showing error values comparable to those obtained during the verification step. It can be concluded that the proposed model successfully adjusts the boundary conditions for plate-like geometries.

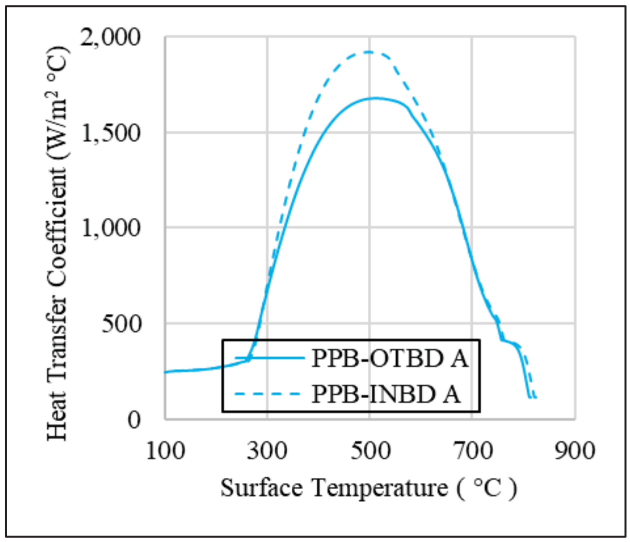

Figure 7.27 PPB HTC as per the proposed model

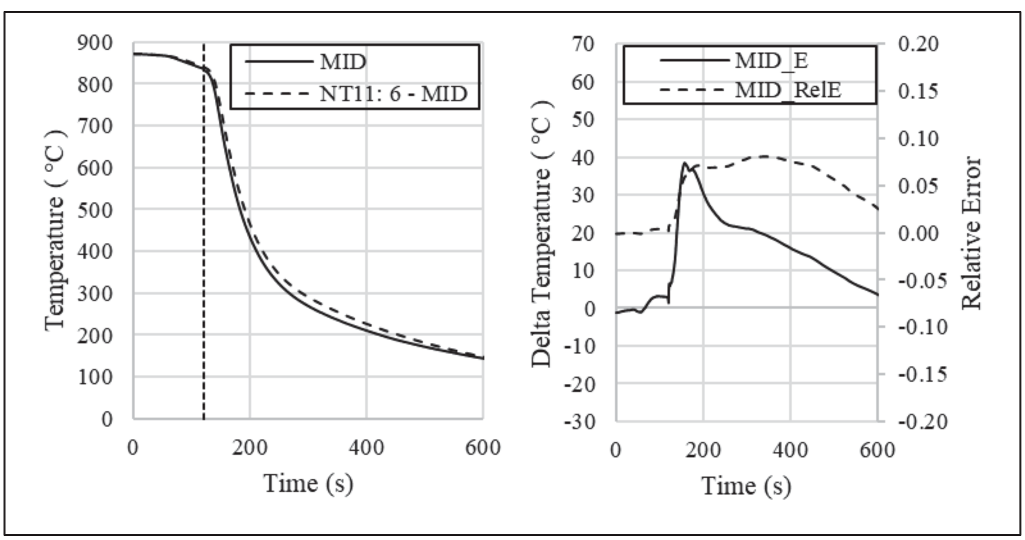

Figure 7.28 Model validation PPB: cooling curves (left) and error plots (right)

GENERAL CONCLUSIONS

This thesis presents the methods and means to characterize and model the thermal boundary conditions during quenching by immersion. The characterization was successfully carried out by utilizing multiple quench probes, in the form of plate-like and hollow-cylinder geometries, that provided the data to identify the thermal boundary conditions along the process. Such data was then implemented on a mathematical modeling strategy of the boiling curve. Based on such works, the following conclusions are drawn:

1. The pioneering work on industrial scale characterization has confirmed the existing differences between laboratory-based and industrial scale testing. It is therefore necessary to develop industry-oriented experimental means to truly capture the conditions under industrial environments.

2. The numerical tools used to estimate the boundary conditions provide the required accuracy (relative error <5%). Two different techniques were used for the identification of the boundary conditions, one an iterative algorithm based on the characteristic points of the process and the other using a Newton-based solver, both fulfilling the accuracy criteria.

3. The developed database of cooling curves and thermal boundary conditions has confirmed the influence of the variables of interest. Thereby, it has been demonstrated that specimen's orientation, position on HT-rig, probe size and probe geometry affect the HTC, and must be accounted for when defining temperature dependent HTCs.

4. Heterogenous conditions on the heat-treated load appear even before immersion due to the air transfer step. Therefore, it is necessary to characterize and account for the evolution of the local boundary conditions before immersion. A step never accounted for as per standard specifications.

5. Specimens that qualify as lumped bodies under classic heat transfer textbook require the identification of the local heat transfer coefficients depending on the direction of the surface of exchange due to the local heterogeneities for the air transfer step. Avoiding such consideration will reduce the accuracy of the estimated starting condition before immersion.

6. During immersion, this study shows that the local HTC must be defined as per the surface orientation as the local conditions produce different cooling performances. This must be carried out for both plate-like geometries and hollow-cylinders, the latter requires further refinement along the circumferential direction.

7. The variation on local conditions and specimen size led to unexpected phenomena during immersion. It was found that the cooling regimes are affected by the specimen's size under the tested conditions. Film boiling tends to vanish as the specimen increase in size thus affecting all the boiling regimes, such phenomena appear on the external surfaces of both types of probes. On the contrary, convection becomes more dominant as the specimens become bigger.

8. The probe size increases the transition temperatures along the cooling regimes; larger probes have higher transition temperatures. Such behavior has not been clearly reported in the literature and requires further studies. Nevertheless, the test data gathered at different locations on the HT-rig confirmed such tendencies.

9. The proposed mathematical modeling strategy proved to be accurate at the verification stage (relative error <5%). Although validation with an independent test increased the peak relative error to <8% for the reference configuration. Such values are deemed acceptable as it is comparable to error levels from inverse identification strategies in the literature.

10. The current definition of the modeling strategy relies on characteristic points of physical significance (transition between cooling regimes). Such approach provides the flexibility to adjust the BC (HTC or flux) as per the evolution of those characteristic points. Therefore, the modeling strategy can easily be expanded to different quenchants (or even variables) provided the values of the reference characteristic points are known.

Scientific dissemination:

The work herein has been published (or submitted for publication) as follows:

1. Salazar, G., Lemyre-Baron, J.-S., Jahazi, M., Champliaud, H., & Tahan, A. (2026). Mathematical Modeling of the Thermal Boundary Conditions during Industrial Quenching (Air Transfer and Immersion). *Transactions of the Canadian Society for Mechanical Engineering, (submitted for publication)*
2. Salazar, G., Lemyre-Baron, J.-S., Jahazi, M., Champliaud, H., & Tahan, A. (2025). Analysis of Cooling Regimes as a Function of Biot Number During Quenching by Immersion. *Heat Transfer, 55 (2*), 930-943. DOI: 10.1002/htj.70114
3. Salazar, G., Lemyre-Baron, J.-S., Jahazi, M., Champliaud, H., & Tahan, A. (2025). Determination of Thermal Boundary Conditions Using Piecewise Hermite Polynomials During the Air Transfer Step of an Industrial Quenching Process. ASME. *Journal of Thermal Science and Engineering Applications*, *17(9):* 094503. DOI: 10.1115/1.4068867
4. Salazar, G., Lemyre-Baron, J.-S., Jahazi, M., Champliaud, H., & Tahan, A. (2025). Analysis of Geometry Orientation in the Calculation of Transient Heat Fluxes During Immersion Quenching of Hollow Cylinder. In *QDE 2025: Proceedings of the 29th International Federation for Heat Treatment and Surface Engineering World Congress September, May 6–7, 2025* (pp. 133 – 140). Vancouver, BC, Canada. ASM International. DOI:10.31399/asm.cp.qde2025p0133
5. Salazar, G., Lemyre-Baron, J.-S., Jahazi, M., Champliaud, H., & Tahan, A. (2024). Identification of Thermal Boundary Conditions during Industrial Quenching (Air Transfer + Mineralized Oil Immersion) of a Hollow Cylinder. In *IFHTSE 2024: Proceedings of the 29th International Federation for Heat Treatment and Surface*

Engineering World Congress September, Sep 30–Oct 3, 2024 (pp. 152–159). Cleveland, OH, USA. ASM International. DOI: 10.31399/asm.cp.ifhtse2024p0152

6. Salazar, G., Lemyre-Baron, J.-S., Jahazi, M., Champliaud, H., & Tahan, A. (2023). Analysis of Industrial Quenching (Air Transfer + Oil Immersion) and the Cooling Regimes after Immersion. In *Heat Treat 2023: Proceedings of the 32nd ASM Heat Treating Society Conference, October 17–19, 2023* (pp. 106–113). Detroit, MI, USA. ASM International. DOI: 10.31399/asm.cp.ht2023p0106
7. Salazar, G., Lemyre-Baron, J.-S., Jahazi, M., Champliaud, H., & Tahan, A. (2023). Experimental Characterisation of Heat Flux during Industrial Quenching Processes for Accurate Estimation of the Heat Transfer Coefficient. In *Proceedings of the Canadian Society for Mechanical Engineering International Congress, May 28-31, 2023,* Sherbrooke, QC, Canada. DOI: 10.17118/11143/20998

RECOMMENDATIONS

Based on the findings reported in this thesis, the following future investigations are suggested:

1. Although it is practically impossible to test all geometry configurations, additional specimens should be tested to account for the influence of specimen size. It is suggested to investigate a range of dimensions that would be, at least, comparable to standard specimens.

2. The influence of specimen's orientation was captured with the plate-like probes, yet further refinement is required for angular orientations (for plates and hollow cylinders) below 45deg with regards to the oil flow during immersion.

3. Although it was not part of the scope of this project and might not be plausible to apply on the case of study, the influence of surface condition (roughness) is vastly addressed in the literature and may provide the industrial partner with further information on the boiling phenomena occurring during immersion. A similar argument can be made for the following variables: immersion speed, quenchant flow velocity, and bath temperature.

4. It is suggested to carry further work on analyzing the dependency of the characteristic points during immersion quenching to variables such as flow speed. This will provide the ability to expand the modeling strategy and adjust the boundary conditions as required.

5. The developed database can be used to adjust and calibrate CFD models. Both cooling curves and surface BC can be easily introduced in the development of multiphase models for immersion quenching.

ANNEX I

QUENCH PROBES

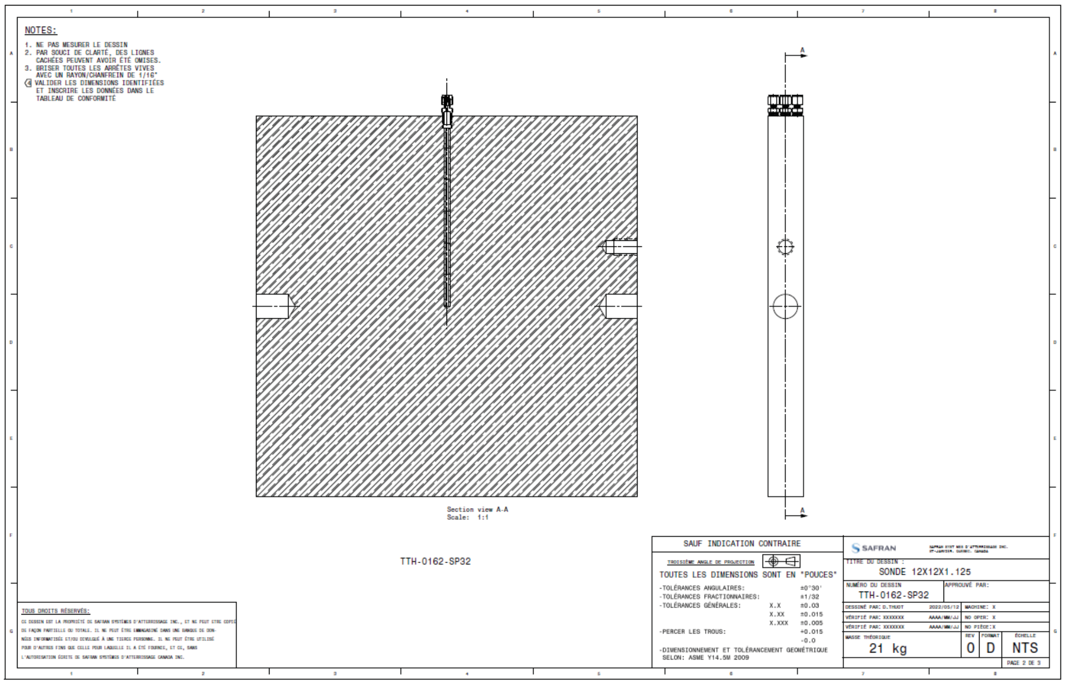

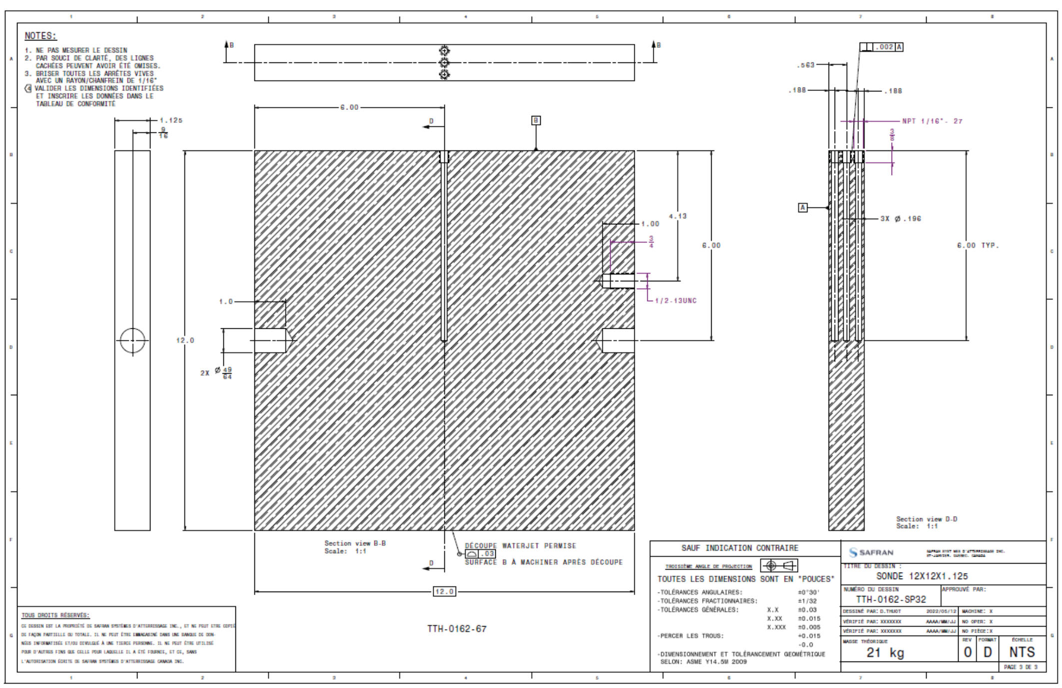

Figure A I-1 Quench probe TTH-0169-SP32 Section A-A (top) and B-B (bottom)

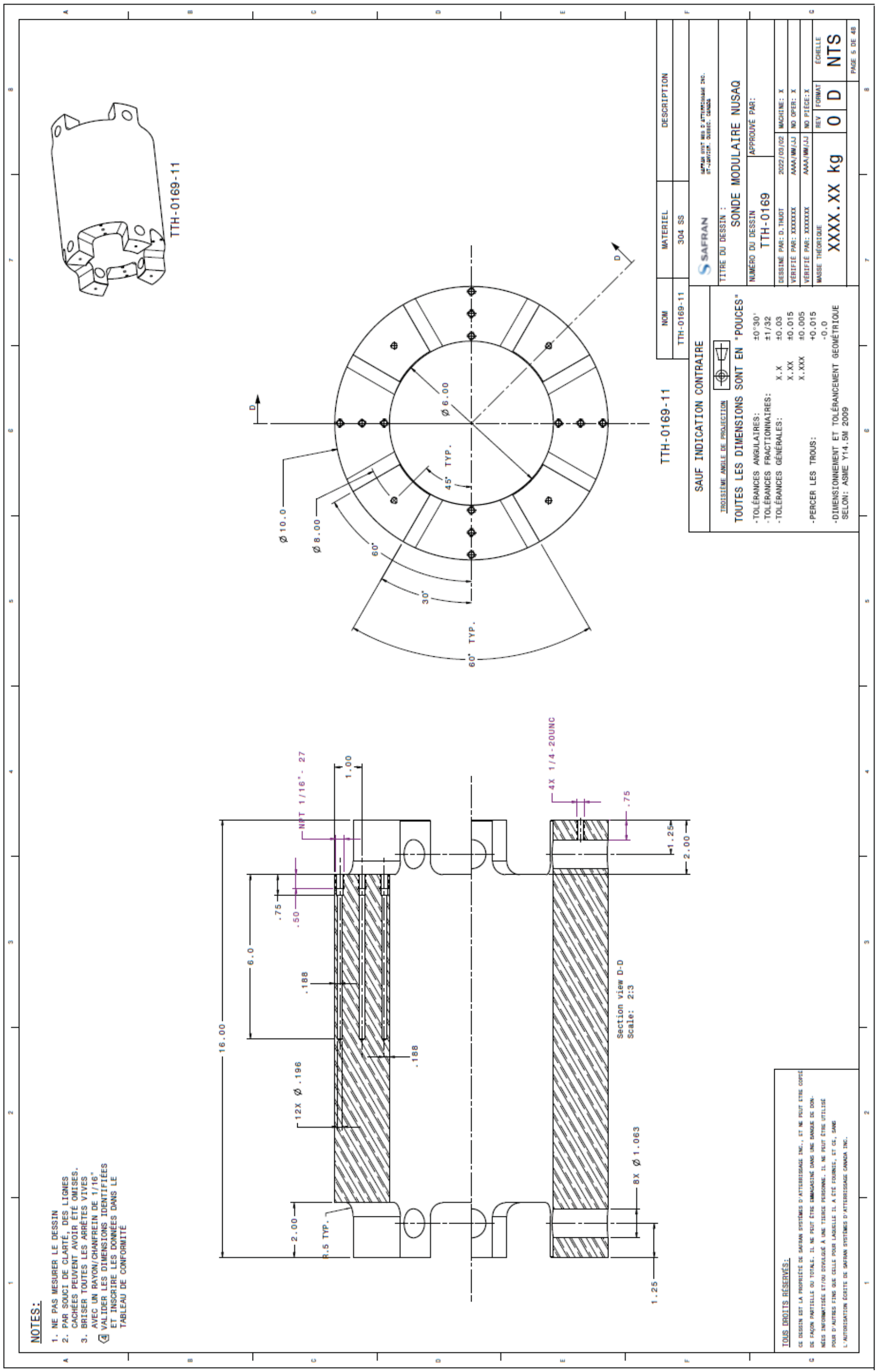

Figure A I-2 Hollow cylinder quench probe TTH-0169-11

ANNEX II

INFLUENCE OF QUENCH PROBE ORIENTATION ON THERMAL BOUNDARY CONDITION

The influence of orientation of the quench probe while quenching is discussed on Section 4.3.3 as per experimental data obtained for a quench probe with thickness of 50.8 mm, referred herein as PPA. Test data considers three orientations: 0 deg, 45 deg and 90 deg with regards to the immersion direction. As the specimen has two main surfaces of exchange, as shown in Figure A II-1, the discussion can be centered on the evolution per surface, labelled as Surf1 and Surf2. Using the methodology outlined in CHAPTER 4, the thermal boundary conditions were inverse identified for the three orientations, thus temperature dependent heat transfer coefficients (HTC) were obtained for each surface.

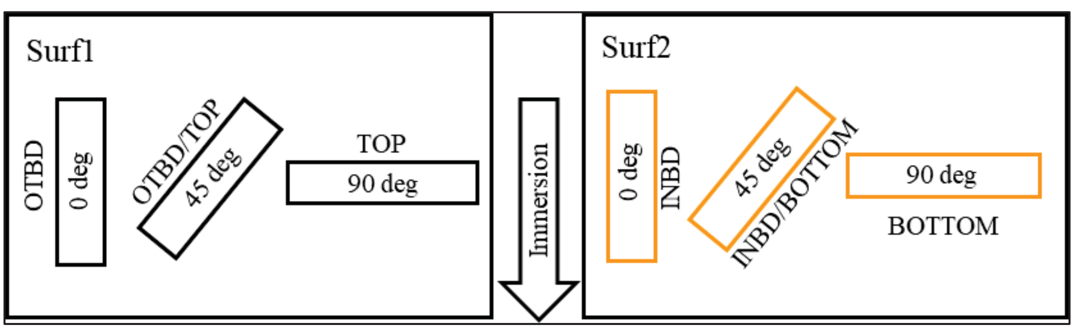

Figure A II-1 Schematic of probe orientation for each surface

The resulting HTC are plotted in Figure A II-2 and Figure A II-3 for each surface. On Surf1, there is an increase of HTC peaks as the body becomes horizontal. This is expected as such surface would experience more turbulence aiding the heat exchange. On the other hand, Surf2 has the opposite behavior, as the HTC decreases, especially for the horizontal setup (90deg) whose peak is just around 55% of the max value when vertical (0deg). Such evolutions can be appreciated in Figure A II-4 when the HTCs for both surfaces are plotted on a case-by-case basis. It must be noted however that the variations between the inclined (45deg) and horizontal (90deg) for Surf1 are not as evident, in fact, their HTC often overlaps along the temperature range of interest.

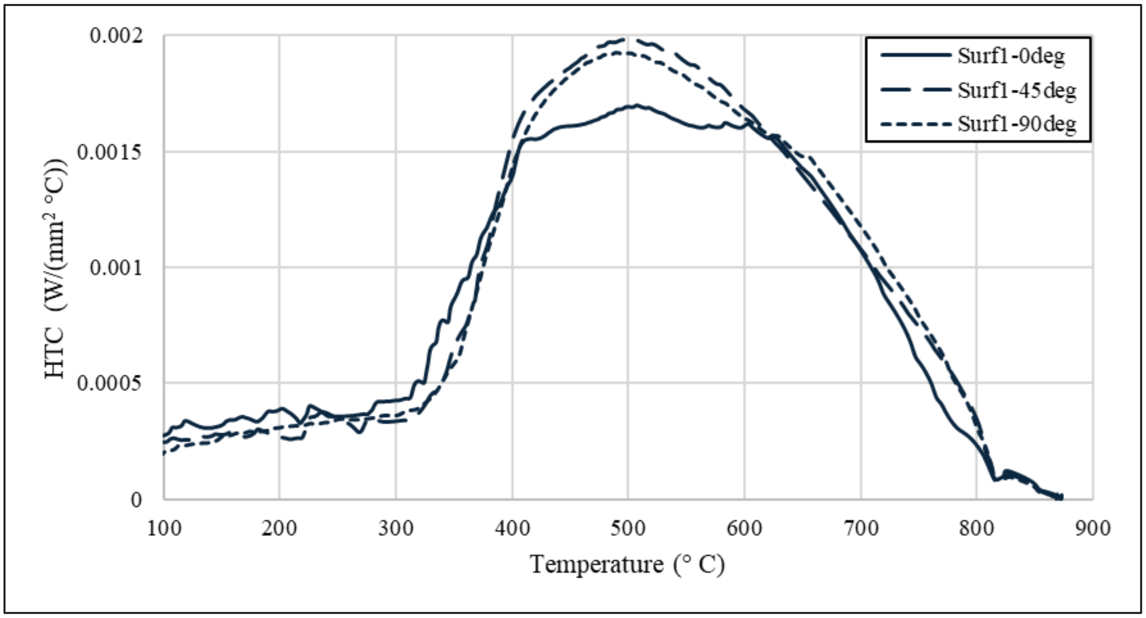

Figure A II-2 Influence of probe orientation on HTC at Surf1 PPA

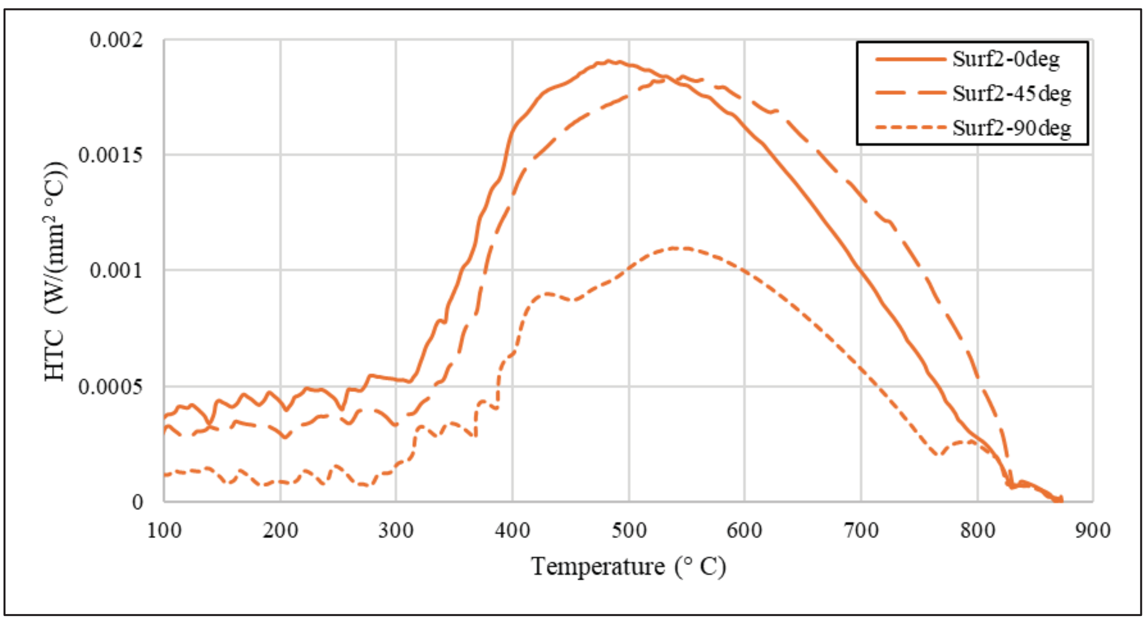

Figure A II-3 Influence of probe orientation on HTC at Surf2 PPA

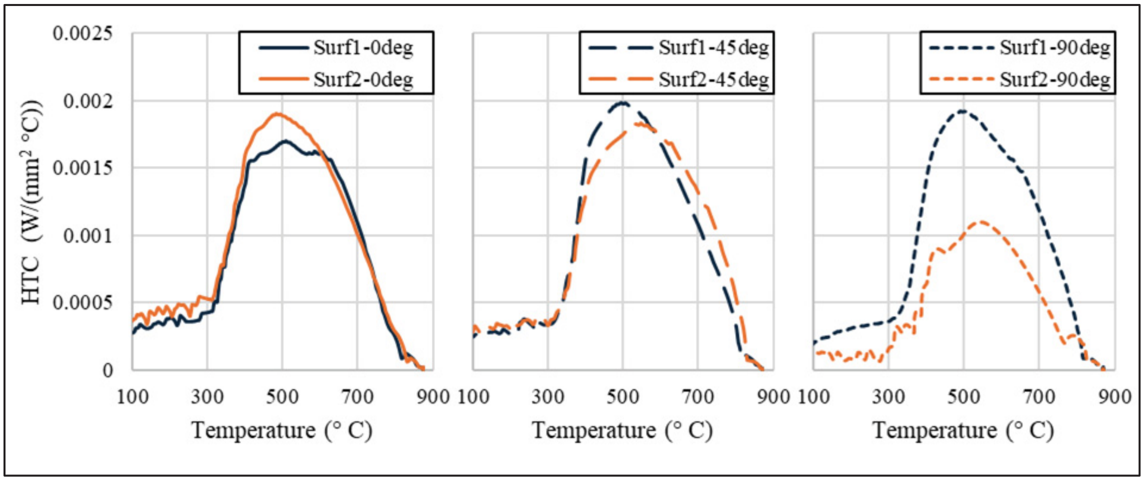

Figure A II-4 Influence of probe orientation on HTC for PPA both surfaces

To further explore the subject while considering the combined effects due to size of the quench probe, a similar analysis for a specimen with thickness 28.58 mm, referred herein as PPC, was carried out. It is important to mention that size has proved to influence the thermal history, and boundary conditions as discussed in CHAPTER 5 to CHAPTER 7. For the study herein, the specimen was quench under comparable conditions as PPA while the same inverse identification strategy was applied to obtain the surface thermal boundary conditions.

The resulting HTCs are plotted in Figure A II-5 for the three orientations. The HTC on Surf1 follows a similar behavior of increasing peaks as the body rotates towards an horizontal (90deg) orientation, while the HTC peaks on Surf2 appears to decrease as the body rotates, both tendencies are consistent with findings for PPA. However, there are clear differences in the magnitude of the HTCs, for both Surf1 and Surf2, when comparing PPA and PPC. Furthermore, the identified HTC for PPA at 90deg clearly shows a large difference in the magnitude of the HTC whereas the same configuration (90deg) has very similar HTCs for PPC. Such condition was initially attributed to the sensitivity of the specimen to the local forced flow, this is especially important as the specimens were tested at the lowest station on the HT-rig, as PPC is thinner than PPA, then the agitation system might be more effective on the heat removal at the local surface.

Thus, the combined effects of position and orientation for PPC was explored for an horizontal configuration (90deg). The specimens were tested at three different heights, referred herein as Levels 3, 4 and 5. The latter being the reference position as it is at the bottom of the HT-rig and the other two upwards on the tooling. The resulting HTCs for these cases are shown in Figure A II-6, it is shown the difference on HTC between Surf1 and Surf2 becomes more evident as the specimen is placed upwards, at positions where Surf2 is less sensitive to the forced flow and producing a decrease on the local HTC.

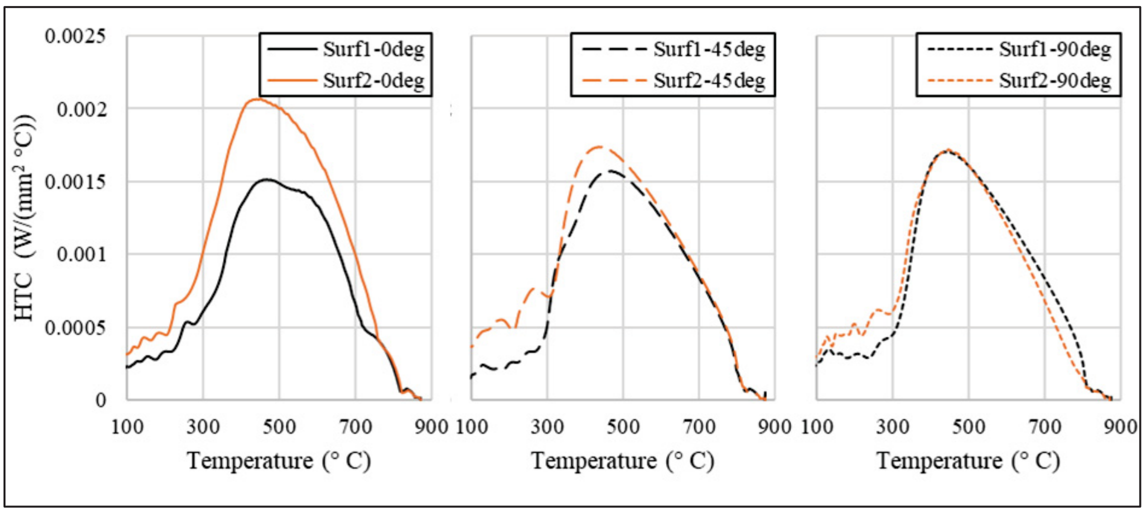

Figure A II-5 Influence of probe orientation on HTC for PPC both surfaces

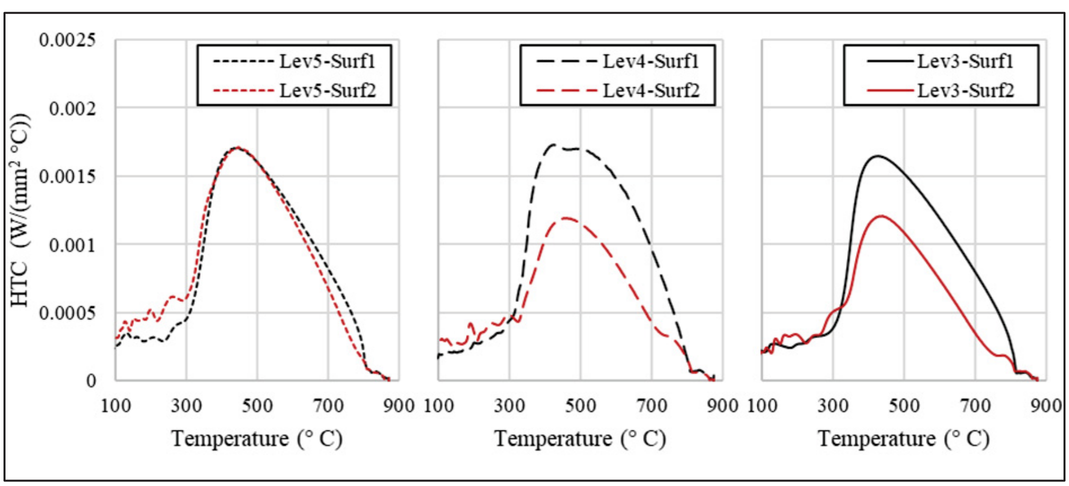

Figure A II-6 Combined effect of probe orientation and position in assembly on HTC for PPC both surfaces

The evolution of the HTC on Surf2 while the specimen is quenched at different heights is shown in Figure A II-7. Once can notice that the HTC values appear to reach a plateau at Level 3, which is considerably further away from the base of the HT-rig. Thus, verifying the postulate that the local position on the HT-rig influence the thermal boundary condition on an horizontally quench specimen.

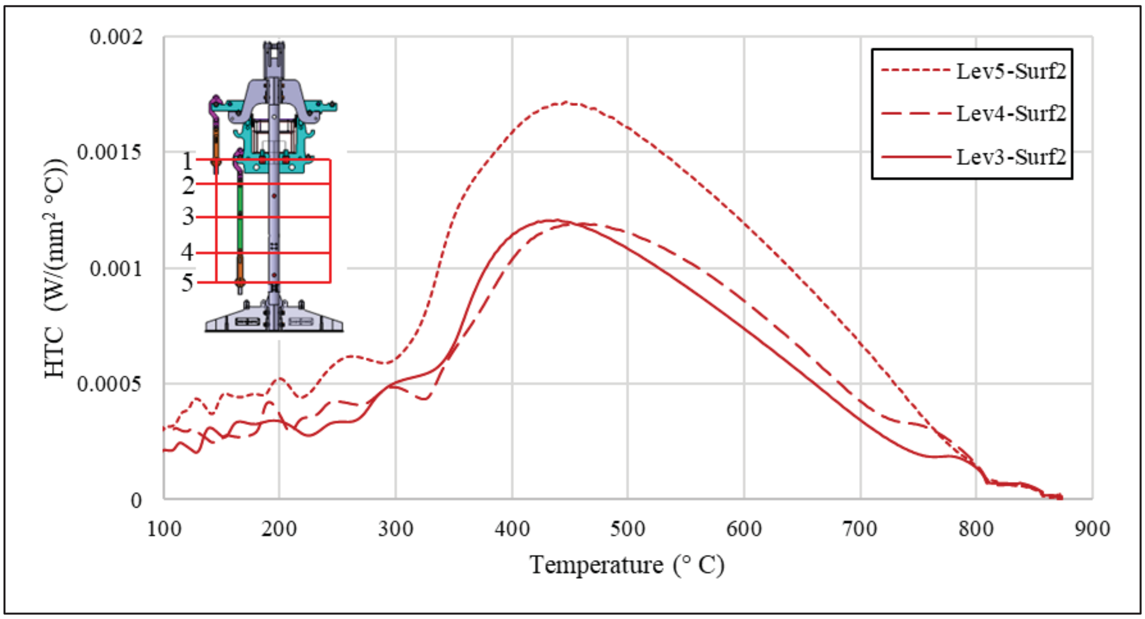

Figure A II-7 Combined effect of probe orientation and position in assembly on HTC for PPC Surf 2

ANNEX III

IDENTIFICATION OF THERMAL BOUNDARY CONDITIONS DURING INDUSTRIAL QUENCHING (AIR TRANSFER + MINERALIZED OIL IMMERSION) OF A HOLLOW CYLINDER

Gamaliel Salazar[a], Jean-Sebastien Lemyre-Baron[a], Mohammad Jahazi[a], Henri Champliaud[a], Antoine Tahan[a]

[a] Department of Mechanical Engineering, École de technologie supérieure, 1100 Rue Notre-Dame Ouest, Montreal, QC, Canada

Paper published in *IFHTSE 2024: Proceedings of the 29th International Federation for Heat Treatment and Surface Engineering World Congress*, October 2024

Abstract: Previous studies have pointed out the need to properly characterize industrial quenching processes to account for the inherent heterogeneities of the process. This study focuses on the identification of thermal boundary conditions of a hollow cylinder quenched by immersion in mineralized oil previously subjected to a predefined air transfer step. The test specimen is instrumented with in-body thermocouples at multiple locations along the radial and azimuthal direction thus mapping the outer and inner surfaces of the hollow cylinder. Based on the experimentally acquired datasets, characteristic points of physical significance during the cooling regimes after immersion are identified to produce time dependent analytical cooling curves. An inverse identification method is applied to estimate heat flux and temperature dependent heat transfer coefficients at locations of interest in both inner bore and outer surfaces. Results demonstrate the non-homogeneous cooling of the specimen during the quenching process before immersion (air transfer) and after immersion in the quenchant, hence confirming the importance of accounting for the influence of the industrial environment. The results are also compared with previous characterization data obtained with a plate probe for the same facilities thus capturing the influence of probe geometry on the identification of thermal boundary conditions

Introduction

Heat treatment steps are typically part of the manufacturing process of steel made components in order to enhance the mechanical properties. In the case of low alloy martensitic steels, the heat treatment cycle involves heating up the material to its austenitic phase and then cooling it down very rapidly, a process known as quenching. Mineral oils are commonly used as quenchants as they are versatile and adjustable allowing to obtain the desired microstructure and material properties.

The available standard test methods (ASTM D6200-21, 2021; ASTM D6482-21, 2021; ASTM D6549-06, 2021; ISO 9950:1995, 1995) assess the performance of a quenchant by cooling curve analysis. These standards aim for almost immediate immersion of cylindrical samples (12.5mm x 60mm) made of Inconel 600 with one thermocouple at the center of the sample. These methods are highly useful to compare different quenchants. However, the conditions of industrial environment, the size and shape of the components, materials and process requirements strongly influence the thermal history of the heat-treated load during quenching.

Moreover, small probes tend to generate a stable film blanket due to higher initial flux densities after immersion (Kobasko & Liscic, 2017) which might not be the case for industrialized components. The probe diameter also influences the heat transfer coefficient (HTC) diminishing the film boiling stage (Liscic et al., 2011).

In this study, the experimental work is carried out at the facilities of the industrial partner SAFRAN Landing Systems Montreal. The heat treatment and quenching system comprises an austenitizing furnace and a four-meter-high quench tank with a capacity of +55k liters of oil. A special rig is used to treat their massive and complex components (Salazar et al., 2023). The industrial partner assesses the quenchant condition as per ASTM D6200. The typical cooling curve (see Figure A III-1) depicts the main cooling stages: film boiling whose vapor blanket collapses around 700°C, transition boiling towards the maximum cooling at approximately 600°C followed by full nucleate boiling until reaching its convective stage around 350°C. It was pointed out by the authors (Salazar et al., 2023) that the system heterogeneities strongly influence the cooling performance of the quenchant. Initial results did demonstrate that characterizing this type of facility using a massive plate probe made of 304SS produces an almost null film boiling stage.

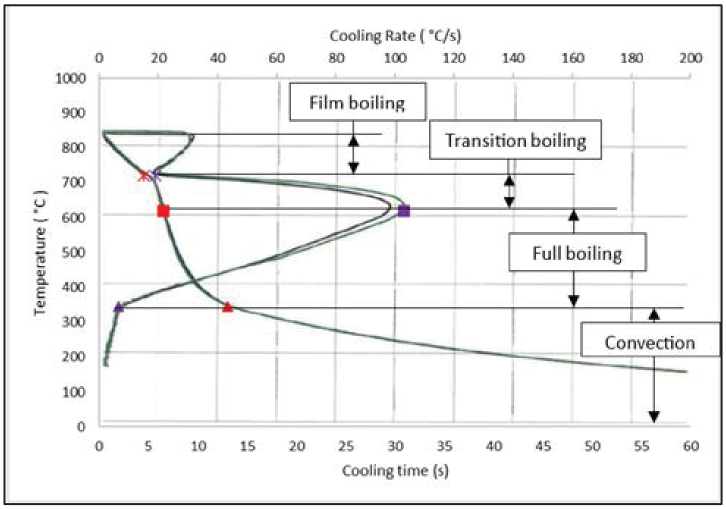

Figure A III-1 Typical cooling curve
Courtesy of SLS

This study presents the results of the boundary condition identification using a hollow cylinder quench probe, which is somehow closer to the tube-like geometries found in multiple components of the industrial partner (Salazar et al., 2023). The hollow cylinder allows for studying both internal flow in the bore of the cylinder as well as the external cooling in the outer surface around the body. The effect of the air transfer and evolution of the cooling performance after immersion along the azimuthal and radial direction is discussed in this paper aiming to provide an insightful characterization of the industrial process.

Methodology

Quench Probe: Hollow Cylinder

The quench probe geometry for this study is a concentric hollow cylinder made of 304SS with an estimated weight of 85 kg. The geometrical characteristics and probe schematic are included in Table A III-1. Previous work by the authors (Salazar et al., 2023) did confirm that a 50.8mm thick plate, also made of 304SS, was suitable to characterize the facilities under study. The plate dimensions were adequate to retain surface temperature above 800°C during the air travel from the austenitizing oven to the oil quench tank, thus excessive cooling during air travelling was no longer a concern.

Table A III-1 Quench probe characteristics

Hollow Cylinder Probe			
Length	Thickness	Inner radius	Material
L	δ	r_{bore}	---
304.8 mm	50.8 mm	76.2 mm	304ss
Stations	Orientation	No. Sensors	TC-locations
A	Inbound	3	Bore/Mid/OutSurf
C	Side	2	Mid/OutSurf
D	Outbound	3	Bore/Mid/OutSurf

The strategy to instrument the hollow cylinder considers the thermocouple wells parallel to the main surfaces (both bore and outer surface) with a depth similar to the mid-length of the hollow cylinder. It is known that the thermocouple wells may cause disturbances in the temperature field, rendering inaccurate measurements (Caron et al., 2006; Li & Wells, 2005; Wells & Daun, 2009). Although thermocouples parallel to the main surface of heat exchange produce almost negligible effects on the temperature field (Luebben et al., 2009).

For the case herein, three main stations labelled as Station A, C & D are defined in the hollow cylinder (see Figure A III-2). Each of the stations has one sub-surface thermocouple close to the outer surface of the cylinder. Each station has a mid-thickness thermocouple. Lastly, only Station A and D have a thermocouple in the sub-surface positions towards the bore of the hollow cylinder.

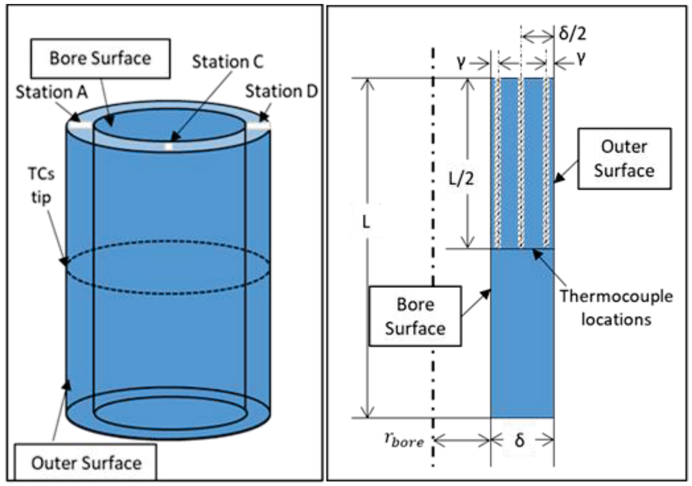

Figure A III-2 Schematic of the hollow cylinder (left) and typical arrangement per station (right).

The experimental data is converted into time dependent analytical curves as per the methodology proposed by (Jan & MacKenzie, 2021) and adapted in the initial studies for a similar industrial application in (Salazar et al., 2023). The polynomial relies on the identification of characteristic points of physical (boiling phases, critical heat flux at max heat flux, minimum heat flux, transition to convection) and mathematical significance (1st and 2nd derivatives). The polynomial between control points over a given width s_i is given by (Jan & MacKenzie, 2021):

$$T_i(t-t_i) = a_i + b_i(t-t_i) + c_i(t-t_i)^2 + d_i(t-t_i)^3$$
$$(t-t_1) \in [0, s_i] \tag{A III-1}$$

While the polynomial constants are defined as follows:

$$a_i = T_i \tag{A III-2}$$

$$b_i = \dot{T}(t) \tag{A III-3}$$

$$c_i = 3\frac{(T_{i+1}-T_i)}{s_i^2} - 2\frac{q_i}{s_i} - \frac{q_{i+1}}{s_i} \tag{A III-4}$$

$$d_i = 2\frac{(T_i - T_{i+1})}{s_i^3} + \frac{q_i}{s_i^2} + \frac{q_{i+1}}{s_i^2} \tag{A III-5}$$

Inverse Identification Strategy

The inverse identification strategy is founded on previous successful work as outlined in (Bourouga & Gilles, 2010; Ramesh & Prabhu, 2014a) focusing on 1D or 2D heat transfer and using in-body measurements. The objective is to produce temperature dependent heat transfer coefficients (HTC) at the predefined stations of the hollow cylinder, the main steps are depicted in Figure A III-3. First, the surface temperature is reconstructed using a direct FEM heat transfer solution (Huiping et al., 2006; Li, 2003) of the temperature field coupled with a damped Newton solver algorithm (Chapra & Canale, 2010). The sum of square residuals between simulation and internal measurements is minimized by optimizing linear piecewise surface temperature evolutions using sequential time intervals. The Hessian matrix and the gradient vector of the Newton solver equation are approximated using numerical differentiation from sensitivity simulations of the modeled temperature field while considering temperature dependent physical properties. Numerical instability may become an issue due to small time intervals while longer time intervals, useful to stabilize the results (Beck, 1970), may misrepresent steep transitions.

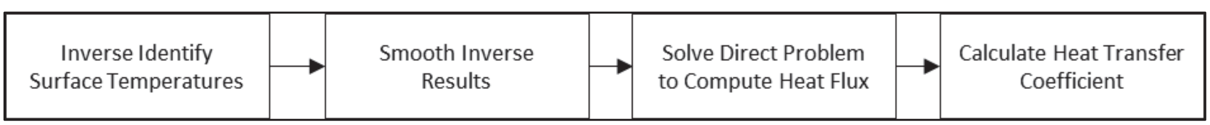

Figure A III-3 Main steps of inverse identification strategy as per Salazar et al. (2023, p. 108)

The reconstructed surface temperature curves may present a characteristic «saw teeth». Thus, the curves are smoothed out using a Least Squares B-Spline Regression, inspired from a point distance minimization algorithm (Flory, 2009). The resulting smoothed curves are defined as boundary conditions on the FE thermal field model. Then, the temperature dependent HTC is derived as per the well-known Newton’s Law of cooling based on the post-processed heat flux.

Experimental Means

The experimental work is carried out at the industrial partner’s facilities following the typical quenching process. The schematic in Figure A III-4 depicts the main steps of a typical quenching process: once the typical HT-rig is locked up (0), the heat-treated load is extracted vertically using an overhead crane (1), it continues its vertical movement until reaching a pre-defined height to clear the furnace (2), then it travels through air laterally (3) until reaching the top of the quench bath (4); the system descends before being immersed into the quenchant (5) and continues all the way down in the tank where it completes its cooling (6). The work presented herein uses an instrumented hollow cylinder, thus the temperature profile in the outer surface and the bore surface are expected to be different during the air transfer (1 to 5). The outer surface starts to cool down once the system is out of the furnace (1), yet immersion (5) occurs at the same time as the sensors are located at the same depth inside the hollow cylinder.

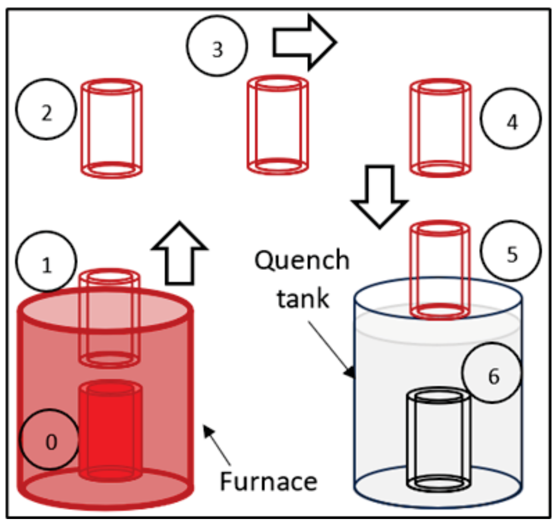

Figure A III-4 Schematic of the quenching process at the industrial partner site

The hollow cylinder probe is mounted on a typical production rig as depicted in Figure A III-5. The test set up includes a data acquisition system Phoenix TM PTM1220 embedded in an insulated compartment at the top of the tooling. The data logger has an accuracy of 0.3°C & a resolution of 0.1°C with a max capacity of 20 thermocouples. For the case herein, 8-sensors are installed in the hollow cylinder spread in the three stations as depicted in Figure A III-5. The quench probe is instrumented with type K thermocouples calibrated as per AMS 2750. The sampling rate is set to 5 Hz.

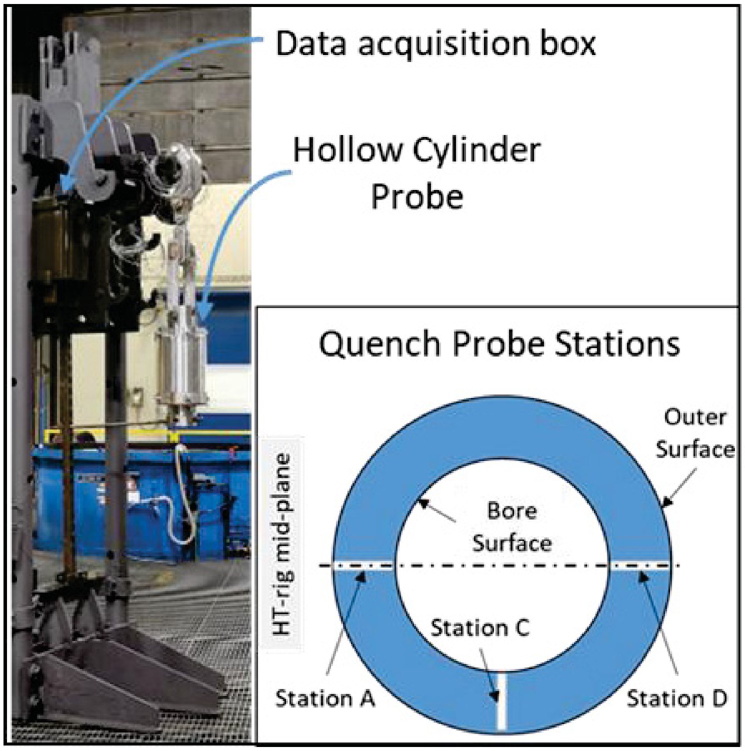

Figure A III-5 Assembly of hollow cylinder in the HT-rig

Experimental Results

Experimental Results: Air Transfer

For the results herein, the transfer from furnace to quench bath is addressed first as it produces a non-uniform drop in temperature in the hollow cylinder. The entire load is extracted from the furnace at 870°C. At the end of the air transfer step, Station A (facing towards the tooling) indicates a temperature of 830.1°C whereas Station D (opposite to the tooling) ends the air transfer step at 823.9°C (see Table A III-2). The outer surface on Station C (side) registered a temperature of 826.6°C. The variation in the temperature profile is mainly cause by the radiation emitted by the tooling towards Station A. On the other hand, the inner bore surface barely cools during the entire air transfer. Experimental readings indicate a temperature of 860°C in the sub-surface sensors in Station A & C. This is mainly produced by the radiation exchange between the inner faces of the hollow cylinder and the null-to-no air circulation inside the bore as the body moves laterally for most of the air transfer.

Table A III-2 Experimental temperature at the different stations before immersion (t=120s)

Temperature before immersion (°C)			
Station	Bore	Mid	Outer Surf
A	860.9	854.3	830.1
C	---	853.5	826.6
D	860.0	853.6	823.9

Interestingly, the readings at the mid-thickness of the three stations have a lower temperature (≈853°C) than the sub-surface sensors towards the bore. The thermal history during the entire air transfer is shown in Figure A III-6. Such representation aids to visualize the thermal profile in the azimuthal and radial direction of the hollow cylinder by the end of the air transfer. Similarly, the experimental data provides evidence of an increase in the cooling of the outer surface once the hollow cylinder is entirely out of the furnace (blue dotted line) and starts its travel through air.

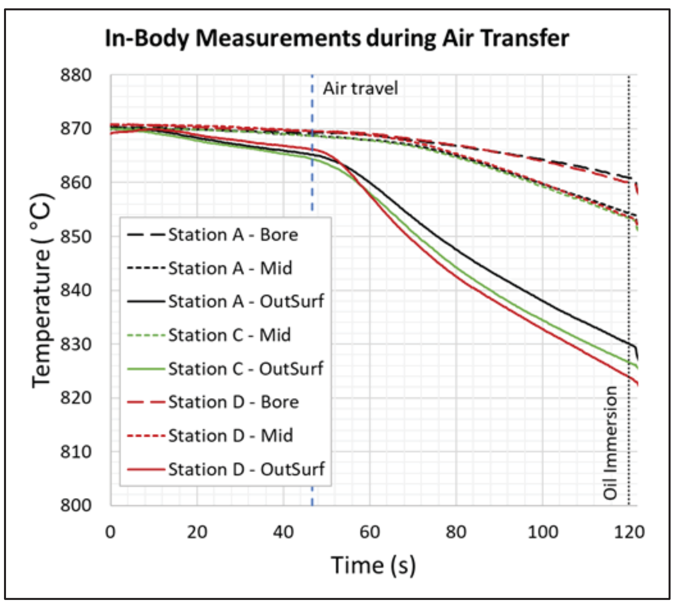

Figure A III-6 Temperature measurements during air transfer

Immersion Quenching

The discussion in this subsection is centered on Station A and Station D as they are apposite to each facing towards INBD and OTBD direction respectively. The complete thermal history of the three sensors for each station is included in Figure A III-7.

After immersion in the quenchant, the outer surfaces (solid lines) cool down faster than the bore (dash lines) while the mid-thickness sensors cool down even slower clearly depicting the thermal gradient across the ruling section. This condition delays the time required to reach transformation temperature (Ms, 300°C) in the bore surface. For Station A, it takes approximately 30 seconds more to reach Ms in the bore sensor than the outer surface sensor, Similarly, the mid-thickness sensor takes around 65 seconds more to cool down to Ms. Data from the thermocouples in Station D indicate delays of 24s and 54s for sub-surface and core readings to reach Ms temperature when compared with the outer surface. It shall be noted that the hollow cylinder is entirely open in both ends, yet oil circulation is less effective inside the bore thus reducing the cooling performance of the quenchant on top of the higher starting temperature of the bore at immersion.

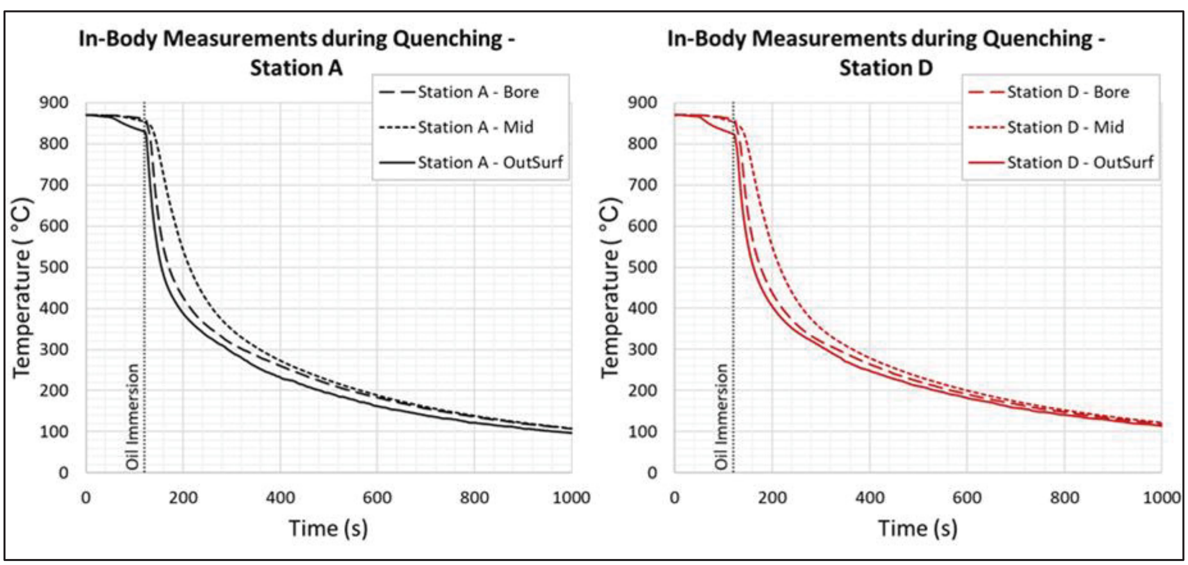

Figure A III-7 Temperature measurements for station A (left) and Station D (right). Outer surface (solid line), bore (dash line) and mid-thickness (dotted line)

The cooling rates (CR) plots for the initial 200 s of the process (80 s after immersion) are shown in Figure A III-8. These plots aid to identify the cooling stages after immersion. The sensors near the outer surface have a very short (or even null) film stage, which is consistent with the findings of the authors in previous studies using a plate quench probe of thickness 50.8mm. However, the readings near the inner bore surface indicate a stable film boiling after immersion lasting 10 s-12 s as per the experimental data, clearly differing from the readings in the outer surface. This phenomenon is attributed to the higher temperature at immersion and the poor oil circulation inside the bore.

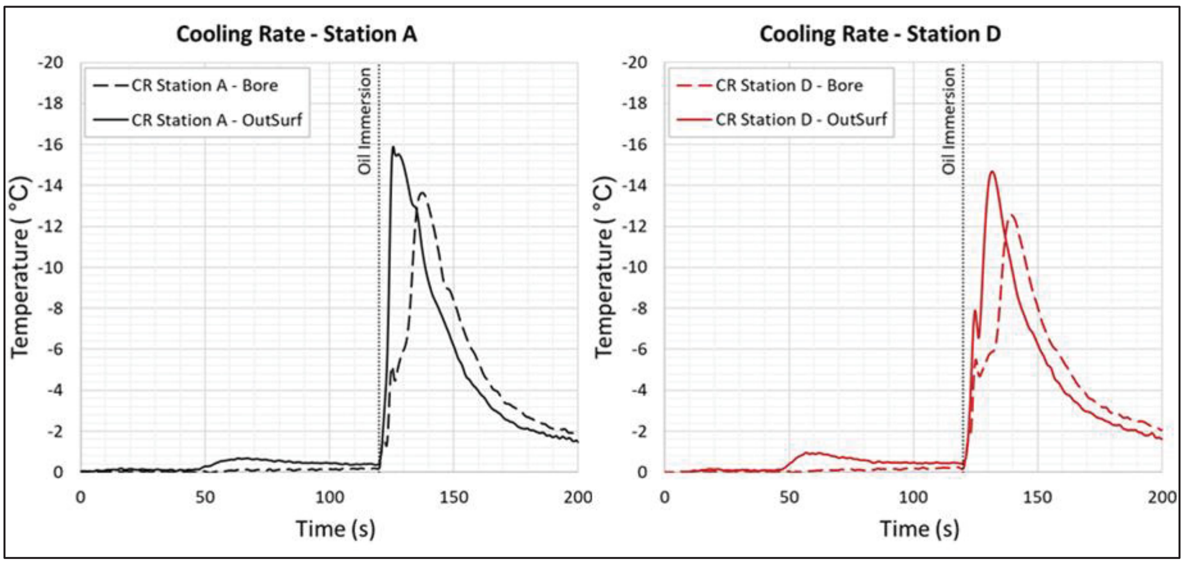

Figure A III-8 Cooling rates for Station A (right) and Station D (left). Outer surface (solid line) and bore surface (dash)

Table A III-3 Maximum cooling rates based on experimental data

Cooling rates (°C/s)		
Station	Bore Surface	Outer Surface
A	13.6	15.9
C	---	14.4
D	12.6	14.7

Due to the appearance of the film boiling in the bore surface, the CR_{max} is delayed in time and lesser in magnitude when compared with the cooling rates in the outer surface. Station A has a CR_{max} of 15.9°C/s for the outer surface compared to 13.6°C/s in its bore surface. Similarly, Station D registers CR_{max} of 14.7°C/s and 12.7°C/s respectively (see Table A III-3). Hence, the experimental data confirms that cooling in locations closer to the mid-plane of the tooling (Inbound) is more effective than positions facing outwards.

Inverse Identification Results

Surface Temperature Reconstruction

The experimentally acquired measurements are used to reconstruct the surface temperature as outlined in the methodology subsection. The estimated surface temperature for both Station A and Station D are plotted in Figure A III-9. The plots include the experimental sub-surface readings for each station. The secondary vertical axis in both figures plots the relative difference (%) between simulated temperatures at the thermocouple locations and the experimental values computed as:

$$T_i = \frac{(T_{i_{sim}} - T_{i_{test}})}{T_{i_{test}}} \qquad \text{A III-6}$$

The relative difference always remains below ±3% throughout the entire dataset for all the stations including air transfer and immersion quenching which are deemed acceptable.

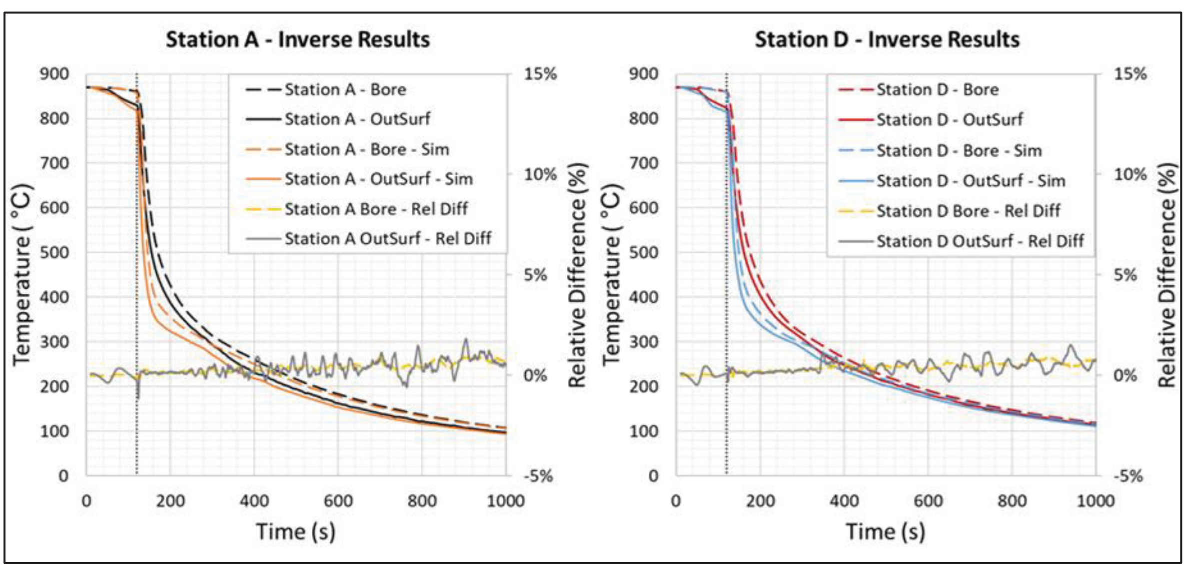

Figure A III-9 Surface temperature reconstruction – Station A (left) & Station D (right)

Heat Flux: Outer Surface & Inner Bore

The surface temperature at each station is used to extract the local surface heat flux by means of a FE direct simulation. Figure A III-10 presents the local heat flux for the outer surface stations and bore surface stations as a function of surface temperature. The heat flux plots allow the identification of the critical heat flux (Q_{CHF}) and minimum heat flux (Q_{MHF}). The former is estimated between 0.8-0.9 W/mm^2, while the latter, which only appears in the bore surface, is computed at around 0.27 W/mm^2.

Note that the amplitude of heat flux curves is different between Station A (INBD) and Station D (OTBD), the former being wider (higher flux magnitude) indicating a higher heat extraction rate in the inbound direction of the hollow cylinder. Interestingly, the heat flux at Station C (between A & D) is closer to the Station D curve at high temperatures after immersion before almost overlapping the Station A curve after passing the peak Q_{CHF}. The corresponding transition towards the convective stage occurs at approximately the same temperature along the three stations in the outer surface. The bore heat flux curves (Stations A & D) present similar shape almost overlapping in the film stage and convective stage, the main differences occur along the nucleate stage (transition and full) indicating higher values for Station A than Station D.

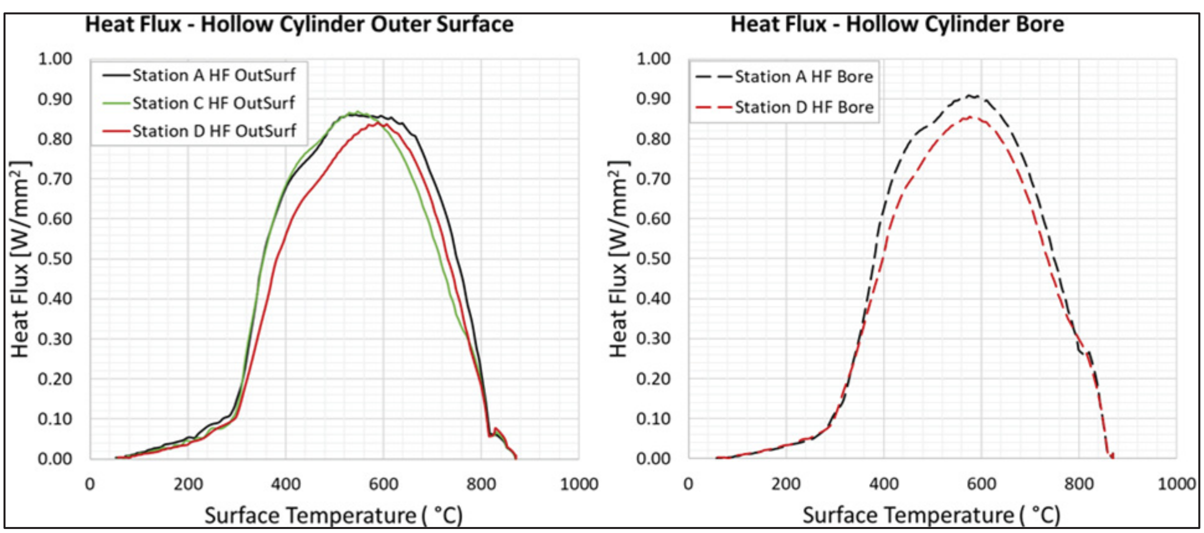

Figure A III-10 Heat flux as a function of surface temperature
Outer surface (right) & bore surface (left)

Hollow Cylinder Heat Transfer Coefficient

The heat flux curves are used to compute the local heat transfer coefficients (HTC) at the corresponding stations. Figure A III-11 presents the HTCs of the hollow cylinder. The curves for Station A (black lines) and Station D (red lines) indicate a higher local HTC for the inbound Station A. The plot covers the entirety of the quenching process; thus, the outer surface curves include the air transfer stage before immersion. Similarly, the bore surface curves cover the complete process, but as the plot is a temperature dependent curve, its values mainly correspond to the cooling after immersion of the hollow cylinder. These results are highly relevant for industrial application as they reveal the evolution of the local HTC depending on their position in the tooling, their orientation, and the stage of the process.

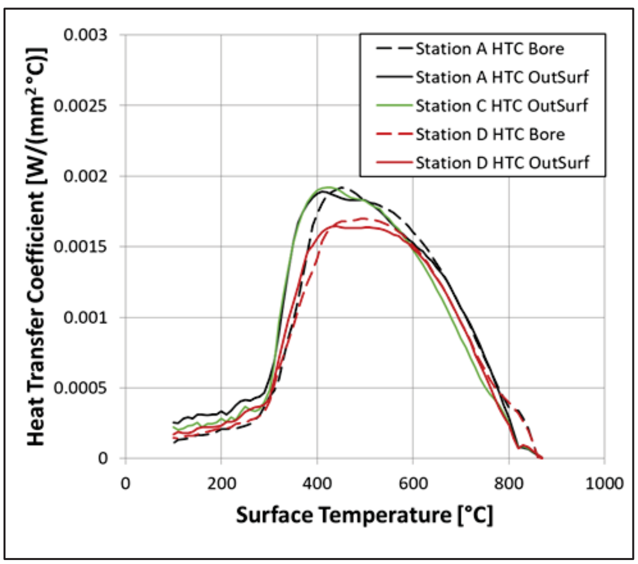

Figure A III-11 Heat transfer coefficients as a function of surface temperature

The differences between the HTC curves after immersion becomes more evident as the temperature decreases. This includes the full nucleate boiling stage and the convective stage as shown in Figure A III-12. Along the outer surface, the influence of the oil flow circulation is clear as Station A (Inbound) has higher HTC than the other two stations (C & D) during the convective stage. The bore surface however is more consistent in the HTC values during the convective stage and lower than the outer surface due to the less efficient oil circulation.

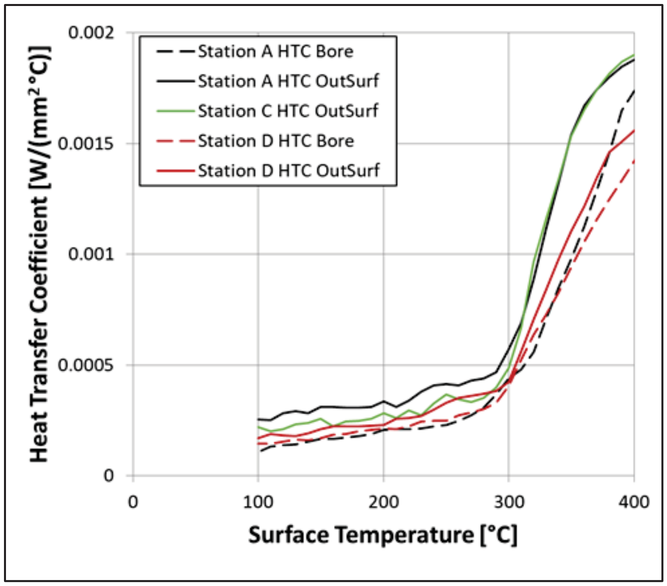

Figure A III-12 Heat transfer coefficients as a function of surface temperature at low temperatures

HTC Comparison with Plate Probe

The computed HTCs of the hollow cylinder are compared with the baseline HTC obtained in previous works by the authors (Salazar et al., 2023) using a plate probe with a thickness of 50.8 mm. The bore surface and outer surface HTCs are compared against the temperature dependent heat transfer coefficient (HTC) for the INBD and OTBD surfaces of a plate probe.

Local HTCs in the bore of the hollow cylinder are different at the beginning of the process since the plate probe starts to cool down during the transfer (see Figure A III-13). Following the collapse of the film blanket in the bore surface, the bore HTCs rapidly converge towards the INBD HTC of the plate probe. The outer surface HTCs almost overlap with the plate OTBD curve at high temperatures (see Figure A III-14).

Overall, the hollow cylinder curves are closer to the Plate OTBD, even the curves in Station A towards the inbound side of the tooling. Due to the massive size of the hollow cylinder, the overall cooling performance is less drastic than the plate probe despite the similar thickness (50.8mm) of the local section probes, yet it is necessary to consider the heterogeneous conditions inherent of the geometry and the process.

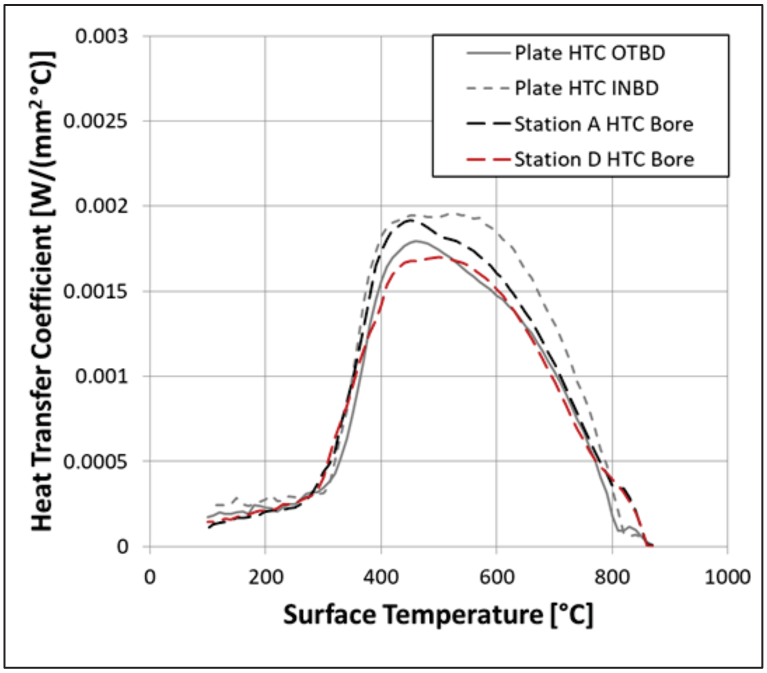

Figure A III-13 HTC comparison: hollow cylinder bore surface vs plate probe from Salazar et al. (2023, p. 112)

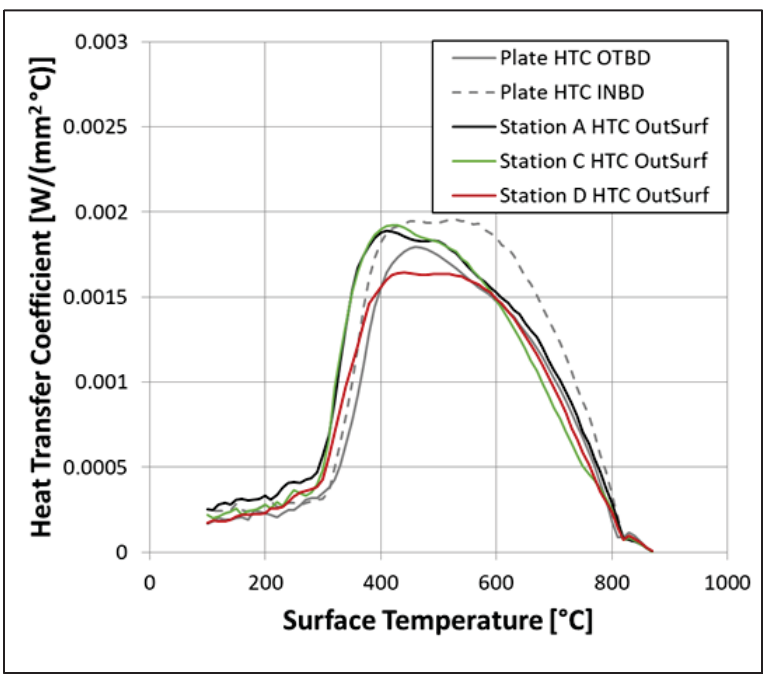

Figure A III-14 HTC comparison: hollow cylinder outer surface vs plate probe from Salazar et al. (2023, p. 112)

Conclusions

The quenching process of large steel components requires the utilization of special equipment to adequately account for the heterogeneities of the process. The proposed hollow cylinder probe provided insightful information during the air transfer and immersion quenching. Due to the nature of the geometry, a clear thermal gradient appears by the end of the air transfer. Such condition, on top of the flow circulation after immersion have a strong impact on the cooling regimes after immersion. While externally cooled surfaces confirm an almost null film blanket, internal surfaces (bore) present a stable film regime.

The results of this study allow for computation of critical heat flux (Q_{CHF}) and minimum heat flux (Q_{MHF}) representative of the solid-fluid interaction under the quenching environment. Further studies should consider the influence of orientation of the hollow cylinder as the obtained values are applicable for a vertical set up only.

ANNEX IV

ANALYSIS OF GEOMETRY ORIENTATION IN THE CALCULATION OF TRANSIENT HEAT FLUXES DURING IMMERSION QUENCHING OF HOLLOW CYLINDER

Gamaliel Salazar[a], Jean-Sebastien Lemyre-Baron[a], Mohammad Jahazi[a], Henri Champliaud[a], Antoine Tahan[a]

[a] Department of Mechanical Engineering, École de technologie supérieure, 1100 Rue Notre-Dame Ouest, Montreal, QC, Canada

Paper published in *QDE 2025: Proceedings of the 3rd International Conference on Quenching and Distortion Engineering*, May 2025

Abstract: Quenching of large and complex geometries often involves surfaces with different orientation with regards to the quench bath. Previous work by the authors includes the characterization of industrial quenching facilities with specially design quench probes. The study herein explores the influence of quenching a hollow cylinder in a horizontal set up as it replicates a condition frequently faced in the industrial application of interest where large tubular geometries are quenched in a similar orientation. The study considers the required air transfer step before immersion that produces non-homogeneous condition of the heat-treated load even before its immersion. The work in this study includes the analysis of experimentally acquired thermal history at different angular and azimuthal locations of a hollow cylinder. Then, the inverse heat transfer problem is solved to compute the transient surface heat fluxes around the outer surface and bore surface of the tested geometry. Findings capture the evolving condition on both surfaces, including the gradient before immersion due to the air transfer as per process constraints and the thermal gradient once the body is immersed demonstrating the uneven cooling of the test specimen. Results in the form of transient heat fluxes are compared with previous findings from fully horizontal plates as well as the hollow cylinder condition quenched on a vertical orientation.

Introduction

Modeling of quenching processes requires the coupling of multiple physical fields: thermal, metallurgical, and mechanical. It is widely perceived that the thermal boundary condition, typically in the form of heat transfer coefficients (HTC), is one of the most influential parameters in the modeling of heat treatment and quenching processes (Simsir, 2014) yet remains one of the biggest challenges. Accurate determination of the thermal evolution of the quenched body is crucial as the heat transfer triggers both the metallurgical and mechanical fields. For instance, the driving force for phase transformation is the transient temperature field. Similarly, thermal stresses due to uneven thermal shrinkage, even on transformation less cases, are caused by the temperature gradient across the thickness of the quenched body (Samuel & Prabhu, 2022b; Wallis, 2010).

Studies on the boiling conditions for horizontal tubes and surfaces can be traced back to the works of Zubber & Tribus (1958) and Bromley (1949). The former developed a correlation for boiling heat transfer, including a horizonal cylinder, and the latter focused on heat transfer during film boiling. Modern work on the determination and correlations for the critical heat flux (CHF) under pool boiling conditions have considered the influence of orientation (Howard & Mudawar, 1999), material and subcooling temperature (Pattanayak & Kothadia, 2022), while a review of CHF predictive models has been reported by (Liang & Mudawar, 2018). Similarly, the pool film boiling regime has been studied for different geometries and fluids (Ahmad et al., 2024). Notably, transient conditions, like the ones encountered during quenching by immersion under industrial environments, are barely addressed.

HTCs are often obtained for specific mediums and conditions (Wallis, 2010) which might differ or misrepresent the industrial environment which limits the applicability of boiling curves obtained under steady-state conditions. Previous studies have explored the influence of decreasing the starting temperature of the load finding out its impact on the film boiling stage while shifting the critical heat flux towards lower temperatures (Hernandez-Morales et al., 2012; Maniruzzaman et al., 2012). The influence of orientation during quenching has been reported to reduce the surface heat fluxes at the bottom of a horizontally quenched blade down to a range ≈15-25% when compared against the heat flux on the top surface (MacKenzie & Banka, 2009). For cylindrical geometries, the critical heat flux (CHF) presents a considerable variation around the surface when quenched horizontally under saturated and subcooled conditions (Thibault, 1978), it has been proposed that the outer surface of a cylinder should consider at least three different regions due to the variable conditions (Howard & Mudawar, 1999). Moreover, even vertically quenched standard quench probes might present non-uniform conditions in the axial and circumferential directions (Ramesh & Prabhu, 2014a).

The authors of this study have identified the boundary condition for vertically quenched plates (Salazar et al., 2023) and hollow cylinder (Salazar et al., 2024) under an industrial environment. In both studies a thermal gradient was reported by the end of the air transfer step, which influences the remaining cooling once immersion occurs. Contrary to standard procedures, the immersion movement (vertical descend in this study) might take several seconds to complete due to the dimensions of the load. The interaction between tooling and quenched load, as well as the agitation system, influences the quenchant flow leading to different boundary conditions on the quenched geometry.

The study herein presents the determination of the boundary condition for a horizontally quenched hollow cylinder under an industrial environment. The experimental results of the quenching process are included first, followed by the methodology used to identify the surface boundary conditions. A comparison with vertically quenched geometries (plate and hollow cylinder) is included to highlight the variable conditions on the bore and outer surface of the quenched body.

Methodology

Quench Probe & Experimental Means

In this study a concentric hollow cylinder made of 304SS was quenched in a horizontal orientation so the quenchant flows perpendicular to the body. The quench probe has a length (L) of 304 mm, a thickness (δ) of 50.8 mm and an inner radius (r_{bore}) of 76.2 mm. The stations around the cylinder are labelled as A, C & D as shown in the schematic in Figure A IV-1.

Station A is placed at the top of the cylinder, it is the first to exit the furnace but the last to enter the quenchant whereas Station D is the last to exit the furnace and first to enter the quenchant. These two stations are the main subject of interest in this study as they provide the most insightful results.

The instrumentation strategy considers K-type thermocouples inserted along the length of the body parallel to the main surfaces of the probe. Measurements are taken at mid-length of the quench probe. Each thermocouple is labelled according to their position: OutSurf & Bore are sub-surface thermocouples whose distance off the surface (γ) is 4.8 mm; the Mid thermocouple is placed at the mid-thickness of the body. A Phoenix TM PTM1220 data logger was used to record the thermal history during the test, it has an accuracy of 0.3°C & a resolution of 0.1°C. The test was carried out with a sampling rate of 5 Hz.

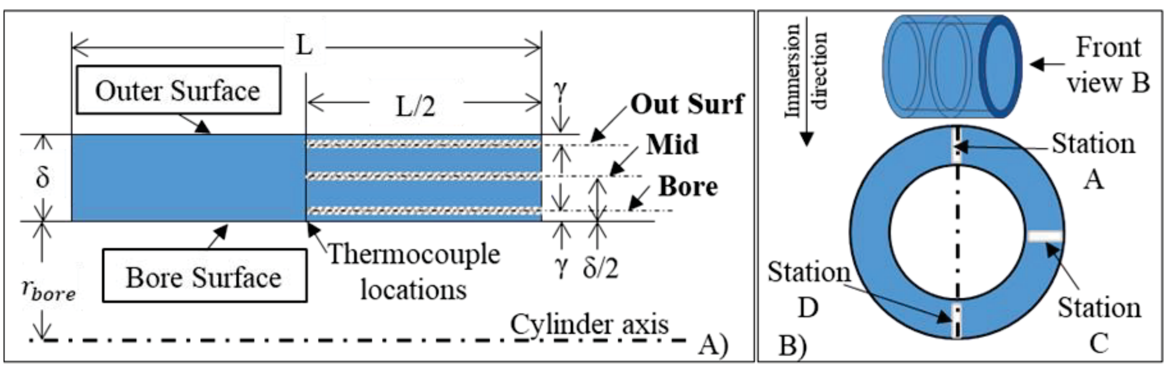

Figure A IV-1 A) Schematic of typical instrumentation per station & B) stations labeling

The testing was carried out at the industrial partner site, thus accounting for the heterogeneities of the process as well as the transferring through air form the furnace to the quench bath. The schematic in Figure A IV-2 depicts the typical movements of such transfer: extraction of the system from the furnace (1), lateral transition until the system is placed on top of the quench bath (2-4), descend step as immersion (5) occurs, the load remains in the bath to complete its cooling (6). The probe was mounted on an industrial heat treatment rig as shown in Figure A IV-2 while placed around the mid-height of the assembly. Both ends of the quench probe are open, thus the quenchant can flow in and out of the bore freely. Due to the orientation of the body, the outer surface of the hollow cylinder is subject to crossflow during immersion and the remaining cooling time in the bath. The quenchant flow in the bath is assumed to move upwards (contrary to the immersion direction) due to the agitation system. The comparison cases included in the results section were tested under similar bath conditions and parameters such as air transfer step, bath temperature and agitation.

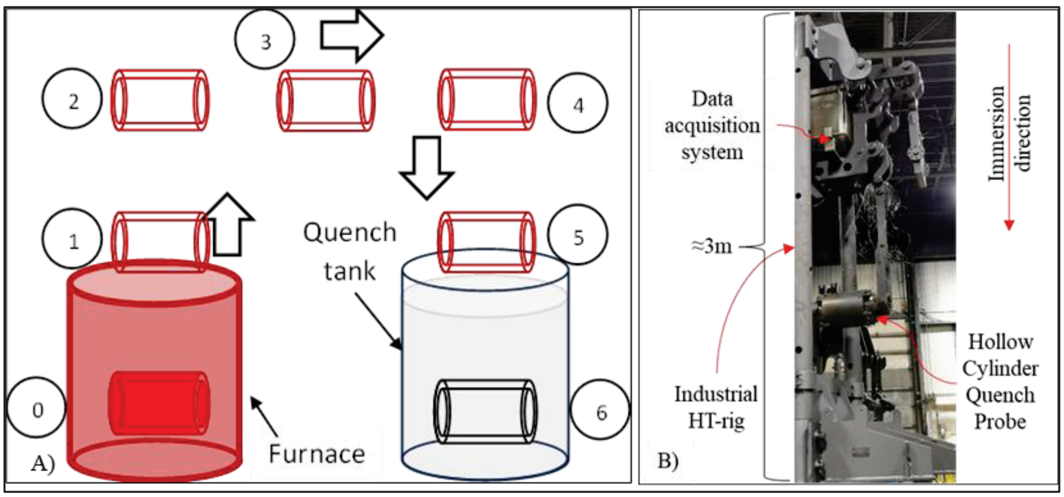

Figure A IV-2 A) Schematic of the quenching process at the industrial partner site and B) test setup on industrial HT-rig with the quench probe in a horizontal setup

Surface Boundary Condition Identification

The identification of the boundary condition requires solving the inverse heat transfer problem. Methods and strategies to solve the inverse problem are well documented in the literature (Beck & Woodbury, 2016; Samadi, Woodbury & Kowsary, 2021, Woodbury et al., 2023). Recent works combine commercially available software with optimization algorithms to identify the surface boundary conditions in the form of transient heat fluxes and HTCs varying in time and space (Behrem & Hrnjica, 2018; Duda & Konieczny, 2022). In this study, the boundary conditions are identified on a station-by-station basis, thus solving a 1D axisymmetric case. The solution is verified running the direct problem for a 2D case (half cylinder) using the identified BCs as input. Overall, the identification strategy follows the methodology applied on a plate probe (Salazar et al., 2023) and a vertically quenched hollow cylinder (Salazar et al., 2024).

The main steps of the methodology are shown in the schematic in Figure A IV-3. Firstly, the surface temperature profile is reconstructed using a damped Newton-Raphson algorithm (Chapra & Canale, 2010). The sum of square residuals between simulation and test data is optimized following a linear piecewise temperature evolution for sequential time intervals. Numerical differentiation based on sensitivity simulations of the thermal field using the FE method are used to build up the Hessian matrix and gradient vector. Temperature dependent thermophysical properties of the material are considered in the FE simulations using the commercially available FE package Abaqus. An axisymmetric FE model was employed with element type DCAX4, and element size of ≈ 1 mm.

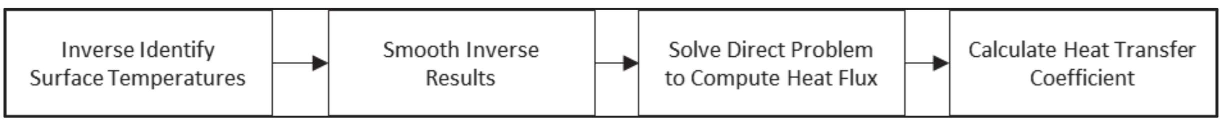

Figure A IV-3 Main steps of inverse identification strategy as per Salazar et al. (2023, p. 108)

The surface temperature profiles are smoothed out using a Least Squares B-Spline, inspired from a point distance minimization algorithm, to diminish the impact of the characteristic «saw teeth» (Beck, 1970). The smoothed thermal profiles are used as boundary condition in a FE simulation from which the reactive fluxes are extracted. This step uses a refined axisymmetric FE model with a refined size ≈ 0.1 mm and same element type (DCAX4). The results of this simulation can be used to compute the heat transfer coefficient following the well-known Newton's Law of cooling.

A verification simulation using the identified HTC as boundary condition was run for a 2D geometry (half cylinder, element type DC2D4). The bore and outer surfaces were split into sections to assign a local HTC per station and compared against test readings. The relative difference (%) between simulated temperatures and the experimental values is computed as:

$$T_{RelDiff} = \frac{(T_{i_{sim}} - T_{i_{test}})}{T_{i_{test}}} \qquad \text{A IV-1}$$

The relative difference always remained below ±5% throughout the entire dataset, including air transfer and immersion quenching, thus confirming that the identified boundary conditions adequately match the experimental readings. Note that the results section is centered on the temperature evolution and heat flux profiles per station though, the former due to the experimental nature of the values, and the latter due to the physical significance in terms of cooling regimes

Results and Discussions

This section presents the experimental data followed by the identified surface boundary condition. Most of the discussion is centered on Stations A & D as they present the most insightful results. Comparison with previous studies considering a plate and vertically quenched hollow cylinder (Salazar et al., 2023, 2024). The results from the comparison cases were obtained under similar conditions, thus comparison can be done directly.

Experimental Data

The complete thermal history of the different sensors is plotted in Figure A IV-4. The labeling of each sensor follows the convention outlined in Figure A IV-1. The temperature evolution during the air transfer is also included in Figure A IV-4 (right plot). The experimental readings indicate that the bore surface enters the oil at ≈863°C, barely decreasing from the starting temperature and even slightly higher than the readings at the MID position (854°C - 857°C). The high temperature in the bore is mainly attributed to the radiation exchange between the faces of the hollow cylinder. The outer surfaces enter the oil at temperatures in the range of 822°C to 830°C, with Station A being the coolest and Station D the hottest. These readings clearly demonstrate that there is a thermal gradient across the cross section of the body by the end of the air transfer.

The temperature evolution and cooling rates after immersion are shown in Figure A IV-5 for Stations A & D. The influence of the body orientation can be clearly appreciated in both plots. Station D is immersed first as it is placed in the lower side of the horizontally quenched body. The data shows that Station D outer surface cools down faster than its bore, yet considerably more similar than the readings for Station A which is placed on the upper side of the body. The outer surface at Station A cools down abruptly, even faster than Station D outer surface, down to the ≈400°C. This is attributed to the interaction between the fluid and body that enhances the cooling during the boiling regimes in the top side of the body (A – at top), when compared with the lower side (D – at bottom). However, when the influence of the convective stage becomes more evident (below 400°C), then the lower side (D-at bottom) has a better heat exchange than the top side as it is more susceptible to the oil flow coming from the agitation underneath. This is also influenced by the conditions in the bore surface at the top (D – bore), which has very low cooling rates during most of the process. During the boiling stages, this can be attributed to a combination of quenchant bubbles moving upwards (vertical) inside the bore, which functions as a prolongated vapor film in the upper station A, thus reducing the heat extraction in the bore surface in that station, and the flow stagnation that may occur due to the concave geometry itself in the top half of the body.

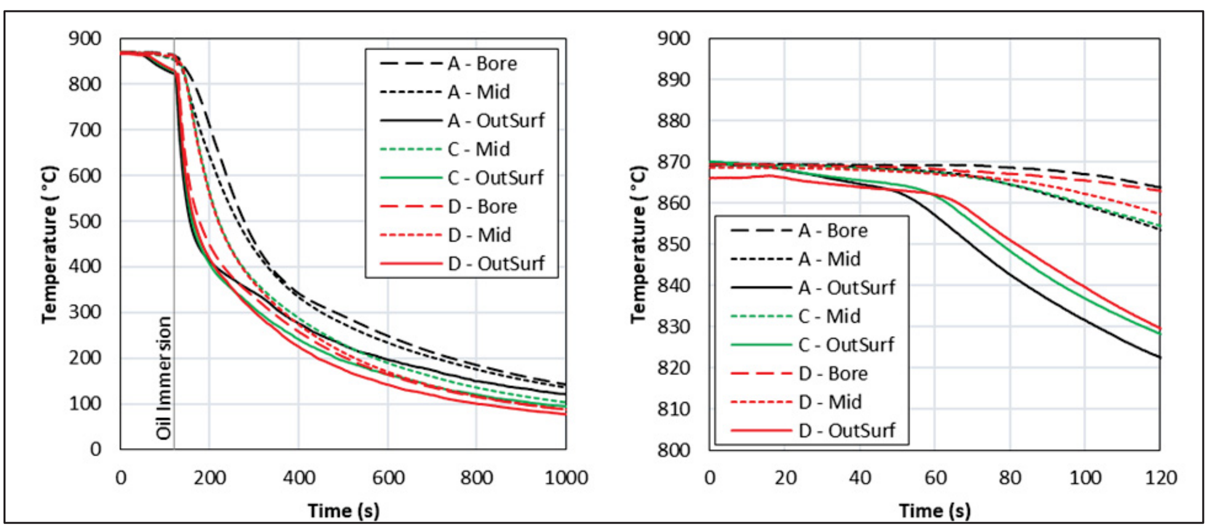

Figure A IV-4 Experimental data: complete thermal history (left) and air transfer only (right)

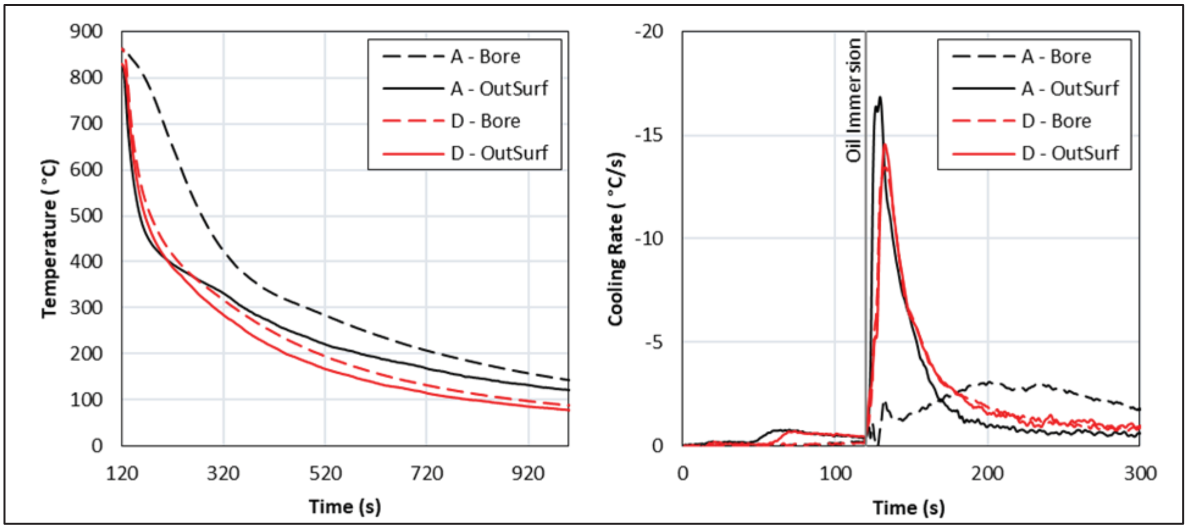

Figure A IV-5 Experimental data for Stations A & D: temperature evolution at sub-surface locations for immersion only (left) and cooling rates (right).

Surface Identification Results

The resulting surface temperature profiles for the entire cooling are shown in Figure A IV-6 for both stations A & D. Clearly, both stations present a thermal gradient but entirely different shape. At Station D, the temperature gradient, although more pronounced towards the outer surface, appears towards both surfaces as they cool down faster than the mid location. However, the temperature gradient in Station A has a clear shift towards the outer surface as the bore surface remains at high temperatures. In fact, the highest temperature gradient in Station A can be computed at a location ≈12 mm off the bore surface, not the mid thickness, as most of the heat is extracted through the outer surface thus the mid location cools faster than the reference location. The max temperature difference at Station A is computed at ≈445°C around the 38 s mark after immersion (t=158s). Conversely, in station D the max temperature difference is ≈25% less in magnitude (≈350°C) while both surfaces present a large gradient with regards to the mid body temperature.

Figure A IV-6 includes the estimated relative difference (secondary axis) that compares the simulation results at the sensors location. Every case remains within the ±5% relative difference during both the identification stage and the verification step, thus confirming the accuracy of the proposed methodology.

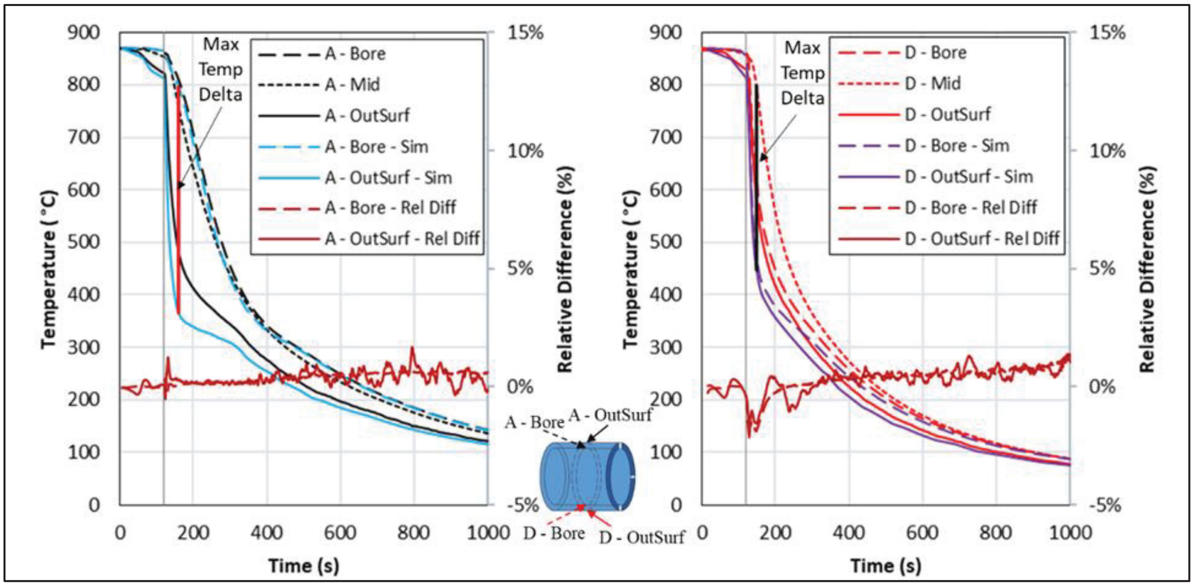

Figure A IV-6 Surface temperatures for Station A and Station D - surface temperature (main Y-axis) and relative error (secondary Y-axis). Evolution of thermal difference at max delta

Surface Heat Flux

The temperature dependent heat flux profiles are plotted in Figure A IV-7, bore (Figure A IV-7A) and outer (Figure A IV-7B) surfaces are presented separately. Figure A IV-7 also contains the surface fluxes for a vertically quenched hollow cylinder (Salazar et al., 2024), and the flux profile for the lower surface of horizontally quenched plate (Figure A IV-7A), based on the thermal profile previously reported (Salazar et al., 2023). The following lines address the current test setup (horizontal) first, followed by a comparison against the vertically quenched hollow cylinder and the horizontal plate during the different cooling stages.

Hollow cylinder - horizontal only

The resulting flux profiles at the bore (Figure A IV-7A, dashed lines) clearly depict the radically different conditions between D-Bore, which has higher flux rates, when compared with A-Bore, whose surface flux magnitude is only ≈18% of the fluxes at D-Bore. Once the convection stage is reached, the fluxes in the bore surface remain lower in magnitude than those in the outer surface (Figure A IV-7A vs Figure A IV-7B), which can be attributed to the poor flow circulation inside the bore.

The heat flux profiles along the outer surfaces (Figure A IV-7B, continuous lines) are more similar than those in the bore surface, yet they present clear differences in the temperature range between 800°C to 300°C, during the boiling stages. The external surface at the top (A-OutSurf) has a higher extraction rate than the lower side D-OutSurf until the convective stage appears below 300°C. The CHF varies around 10% between both locations, although the difference in magnitude is more evident in the full nucleate boiling towards the convective stage. Such condition is attributed to the interaction between liquid and vapor boundary layers flowing upwards next to the quenched body (Thibault, 1978).

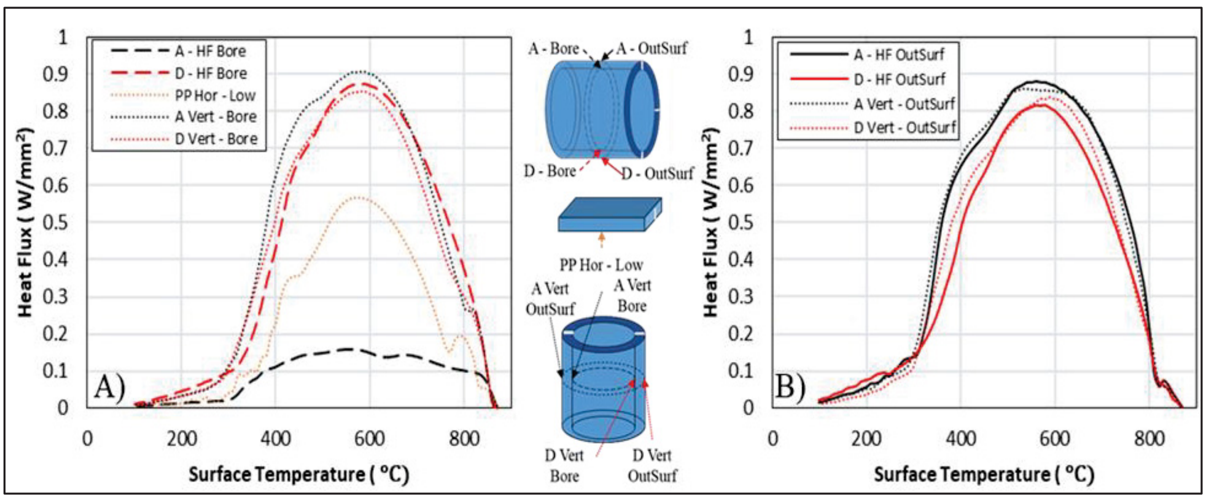

Figure A IV-7 Comparison of surface heat flux: A) Bore surface (horizontal & vertical) vs horizontal plate, B) Outer surface (horizontal & vertical). Geometry schematics for the three geometries shown between plots

Influence of orientation: horizontal vs vertical

Data corresponding to the vertically quenched body is shown as dotted lines in Figure A IV-7. Clearly, the body orientation has a strong effect on the location A-Bore (black dashed line, Figure A IV-7A). The profile shape and magnitude are entirely different from those for the vertical setup. Conversely, the D-Bore flux profile exhibits similar shape like the vertically quenched cases, its CHF is almost the same in magnitude (0.8-0.9 W/mm^2) and appears at similar temperatures (580-590°C). Although the heat extraction during the nucleate boiling at lower temperatures after the CHF is more effective for the vertical configuration (dotted lines,

Figure A IV-7A). Similarly, the transition to convection is more drastic for the vertical setup and begins at slightly lower temperatures than the horizontal setup.

The outer surfaces have similar flux profiles for both orientations (Figure A IV-7B). Peak heat fluxes (CHF) appear at slightly higher temperatures for the vertical setup although the magnitude remains almost the same. Once convection appears, the horizontal setup has higher fluxes (Figure A IV-7B) than the vertical configuration. This could be attributed to the interaction of the body with the oil flow as the horizontal setup is more sensitive to the oil flow.

Hollow cylinder horizontal vs horizontal plate

The lower surface heat flux profile of a horizontally quenched plate (orange dotted line, Figure A IV-7A) is around 60-65% lesser in magnitude than the D-Bore flux profile during transition and full nucleate boiling. Notably, the stagnant flow under the plate's surface, although reducing the heat extraction, is less insulating as previously reported for plate-like horizontal surfaces (MacKenzie & Banka, 2009). Notably, the horizontally quenched plate has a higher flux magnitude than the A–Bore, which is located at the top of the hollow cylinder. Such difference is attributed to the concave geometry that restrains any displacement of any bubbling coming from the bore surfaces thus decreasing the heat extraction more drastically. Conversely, once the convective stage begins, both plate and A-Bore have practically the same heat flux profile, which is still lower than the other profiles for the vertical case and D-Bore.

Conclusions

A hollow cylinder quenched horizontally under the industrial environment presents different boundary conditions for the bore and outer surface. Notably, the condition in the hollow cylinder bore varies drastically, the predicted boundary condition at Station A Bore is only ≈18% of the flux profiles for the other locations. The variable conditions caused by the quenched orientation create a non-symmetrical thermal gradient inside the thickness of the body. Such gradient is around 25% higher at the top station than the lower station. In fact, at the top station most of the heat is extracted through the outer surface, which causes the max thermal gradient at a different location other than the mid thickness.

The outer surface of the hollow cylinder has higher heat extraction rates at the top of the body compared with the lower side. This phenomenon is attributed to the interaction between flow and body that enhances the heat exchange at such location. The boiling regime is more effective when quenched vertically as the heat flux profiles are higher in magnitude than those for the horizontal configuration, yet differences remain within a range of 10-15%. Conversely, once convection starts, the horizontal setup is more efficient than the vertical setup along the outer surface. Findings confirm the influence of orientation and geometry that should be considered to adequately model a quenching process.

ANNEX V

BOUNDARY CONDITION CROSS-OVER

The content herein presents the results of a sensitivity analysis using the identified BC from a given plate (i.e., PPA) unto a different geometry (i.e., PPC). Such strategy aims to strengthen the case for adjustable boundary conditions that must consider the specimen size, as the accuracy of the prediction is greatly diminish when using a BC from a different geometry. Overall, this subsection challenges the typical understanding of the heat transfer coefficient being an intensive property for any given surface to fluid combination. Such postulate leads to utilize the same BC (in the form of heat transfer coefficient) regardless of the specimen size.

Air Transfer Cross-Over

Solving the inverse problem during the air transfer step produce accurate results as depicted in Figure A V-1. The simulation values in Figure A V-1 were obtained by using the identified HTC as per PPA data, one must note that error between simulation and test values always remains in a $\pm$4°C window, leading to an accurate prediction through the entire air transfer as well as the end condition before immersion.

In contrast, when the identified HTC from PPC is used as BC on a geometry like PPA, there is a clear increase in the error between simulation and test results as depicted in Figure A V-2. Results indicate a temperature difference of $\pm$15°C all the way to the end of the air transfer. Although the expected temperature gradients once immersion occurs are likely to be greater than the error during the air transfer, the global accuracy of the thermal field is influence by the starting condition of the specimen before immersion. Thereby, the prediction of the thermal field distribution before immersion must be carefully simulated by the proposed models.

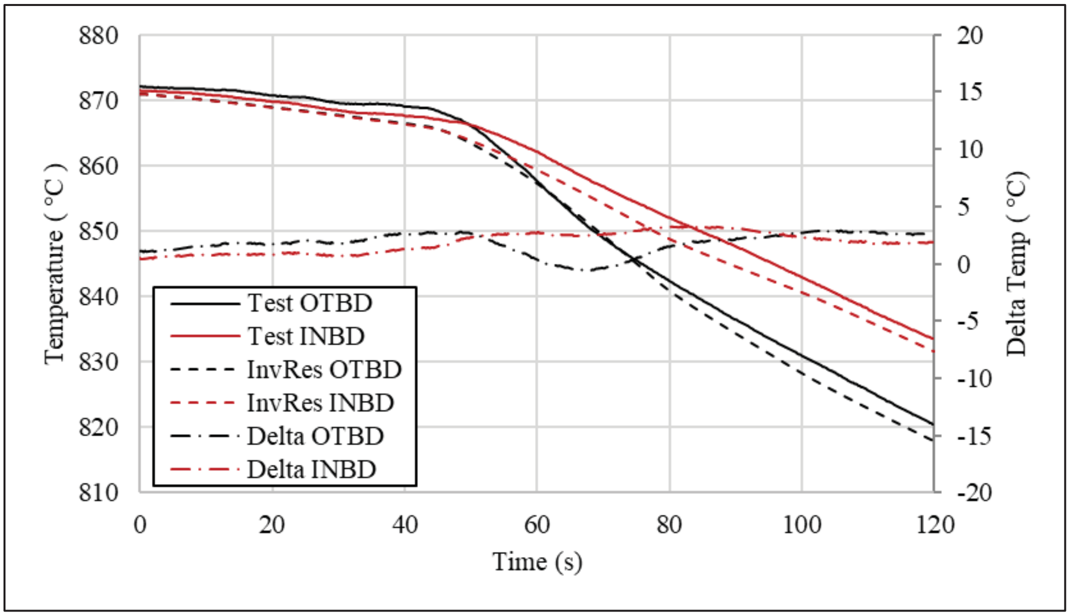

Figure A V-1 PPA air transfer results: comparison between test and simulation. Simulation considers BC from found solution as per inverse problem results indicating good agreement between test data and simulation

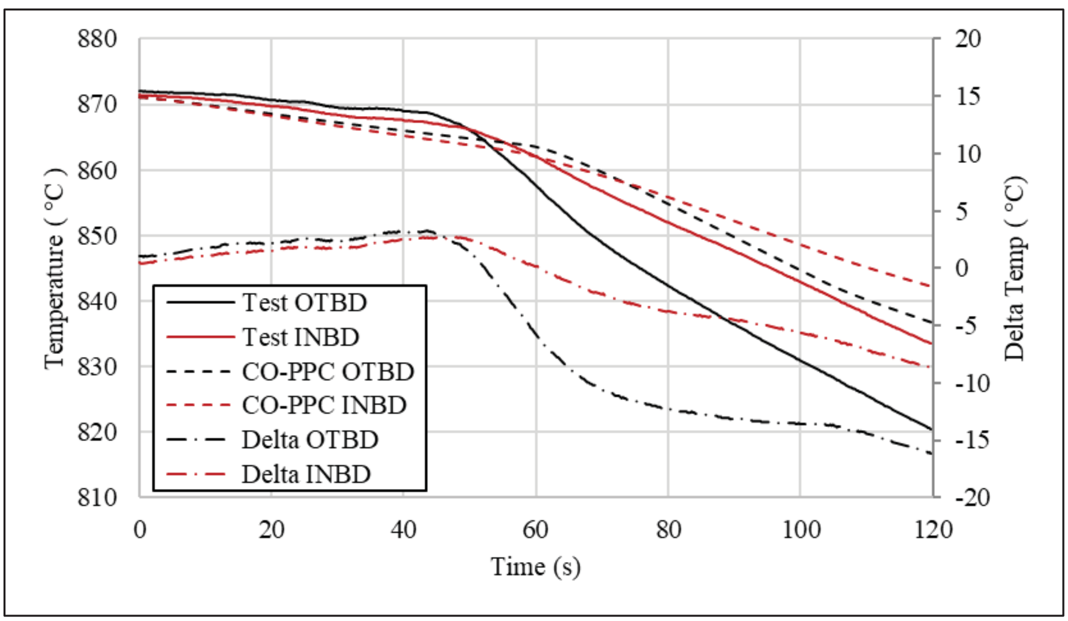

Figure A V-2 PPA air transfer results: comparison between test and simulation. Simulation considers BC obtained for PPC. Simulation (dotted) results clearly differ from test data (continuous lines)

Immersion Cross-Over

Similar sensitivity cases were carried out for the immersion stage, thus using the identified HTC from PPC on a geometry like PPA, and a secondary case following the inverse order (HTC from PPA on PPC like geometry). The results of these analyzes are presented in Figure A V-3 and Figure A V-4 respectively. The error and relative error curves at the three different locations were included on each plot. Clearly, employing the HTC from a different plate produces large errors up to 30%.

In Figure A V-3, the error in temperature (referred as delta temp) is positive while in Figure A V-4 such value is negative. This is caused by the relatively longer film boiling appearing when quenching PPC as can be seen in Figure 7.2. Thereby, when using the HTC from PPC on the PPA geometry, the simulation slows down the cooling at the begging of immersion while the test data cools down faster. The opposite phenomena are observed in the second case when using PPA-HTC on PPC, as the identified HTC would have no film boiling, thus proceeding to transition boiling almost immediately upon immersion leads to a faster cooling on the simulation results.

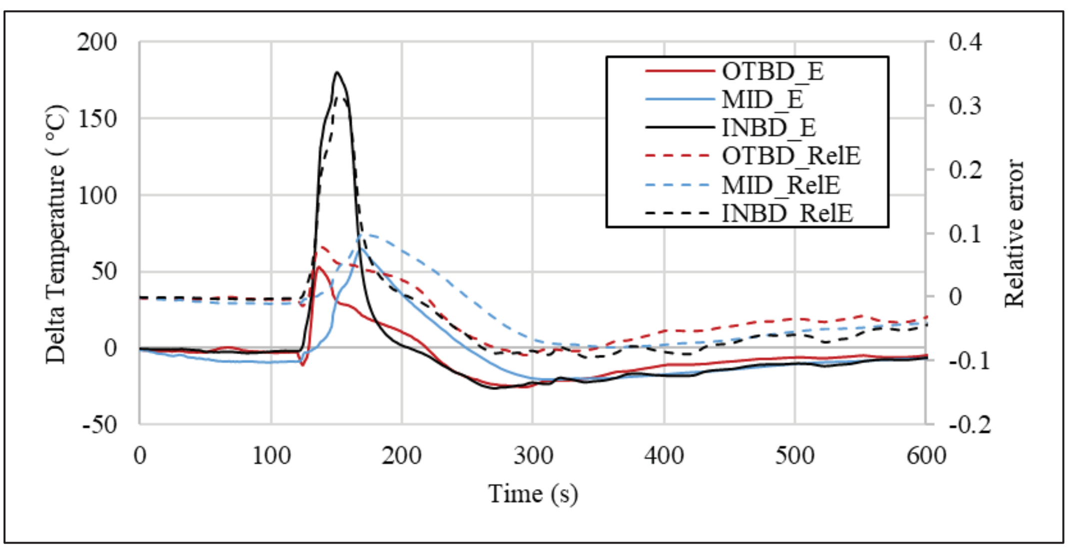

Figure A V-3 Error plots for PPA using HTC from PPC

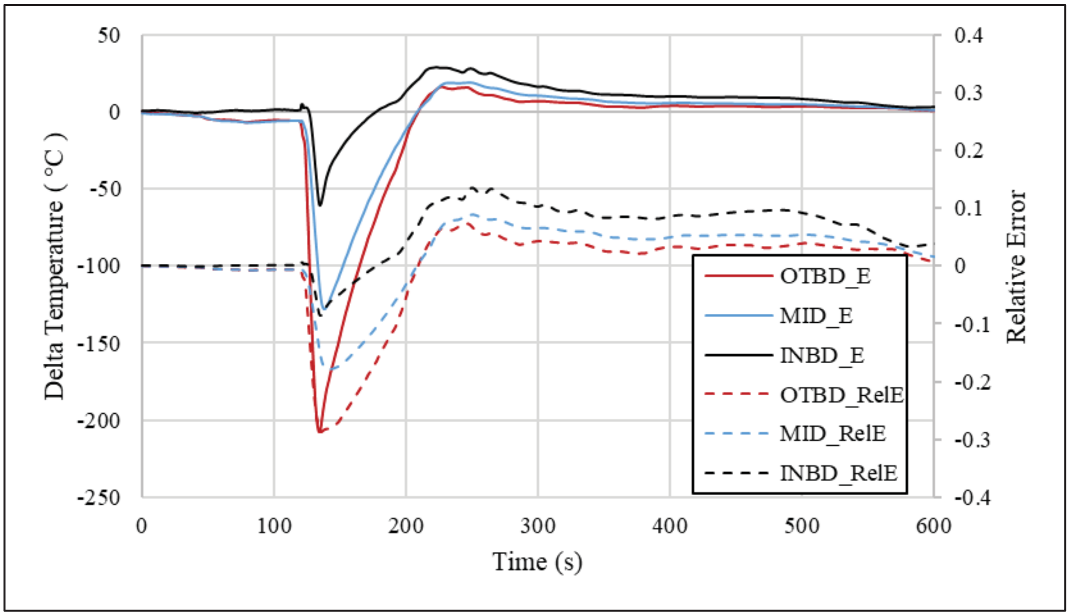

Figure A V-4 Error plots for PPC using HTC from PPA

ANNEX VI

AIR TRANSFER BOUNDARY CONDITION MODEL - CASE B

Section 7.3 presented the modeling strategy applicable to the test setup Case A (specimens at the top of the HT-rig). This annex presents the equivalent data and results applicable to Case B, when the specimens are allocated at the bottom of the HT-rig. Overall, the same strategy is applied to both cases, meaning that the complete air transfer is segregated into three segments: Air 1 – Furnace, Air 2 – Extraction, and Air 3 – Open Air Transfer.

Air 1 - Furnace

This segment is the only one that does not require any further information as the strategy considers a global linear model, see Section 7.3.1.

Air 2 - Extraction

This segment uses the same strategy of utilizing a non-dimensional curve factorized by a peak value $h_{Amax}(Bi)$, see Eq. 7.2 and Eq. 7.3. The coefficients modeling the $h_{Amax}(Bi)$ and the plot representing the data and such relation are shown in Table A VI-1 and Figure A VI-1. Data for both Case A and Case B is included just for comparison purposes, as it was deemed necessary to consider each case separately.

Table A VI-1 Coefficients for $h_{Amax}(Bi)$

Case	**a**	**b**	R^2
A	29.793	14.557	0.95
B	39.786	9.344	0.84

The obtained boundary conditions were nondimensionalized as per the methodology outlined in Section 7.3.2.1. The resulting non-dimensional curve and its corresponding coefficients for case B are shown in Figure A VI-2 and Table A VI-2.

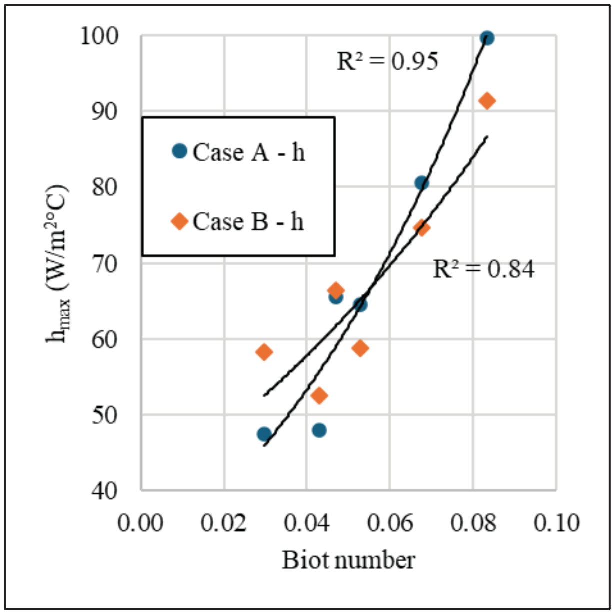

Figure A VI-1 Peak HTC during air transfer for case A and case B

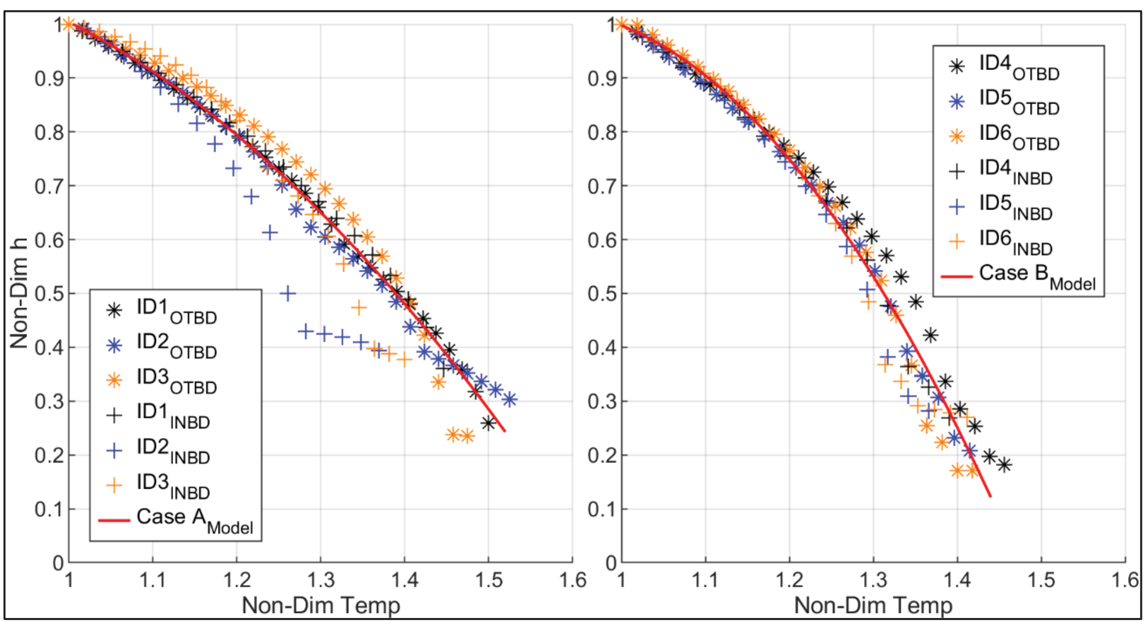

Figure A VI-2 Non-dimensional curves for Case A (left) and Case B (right) during Air 2

As for Case A, the process to evaluate the model for Air 2 Case B requires the selection of the reference temperature $T_{h_{Amax}}$ and $T_{t_{120}}$, which depend on the surface under consideration. Such values are shown in Figure A VI-3 and Figure A VI-4 respectively.

Table A VI-2 Coefficients for non-dimensional curve during Air 2

Case	a	b	c	R^2
A	1.123	-0.697	0.769	0.99
B	1.028	-0.901	0.320	0.99

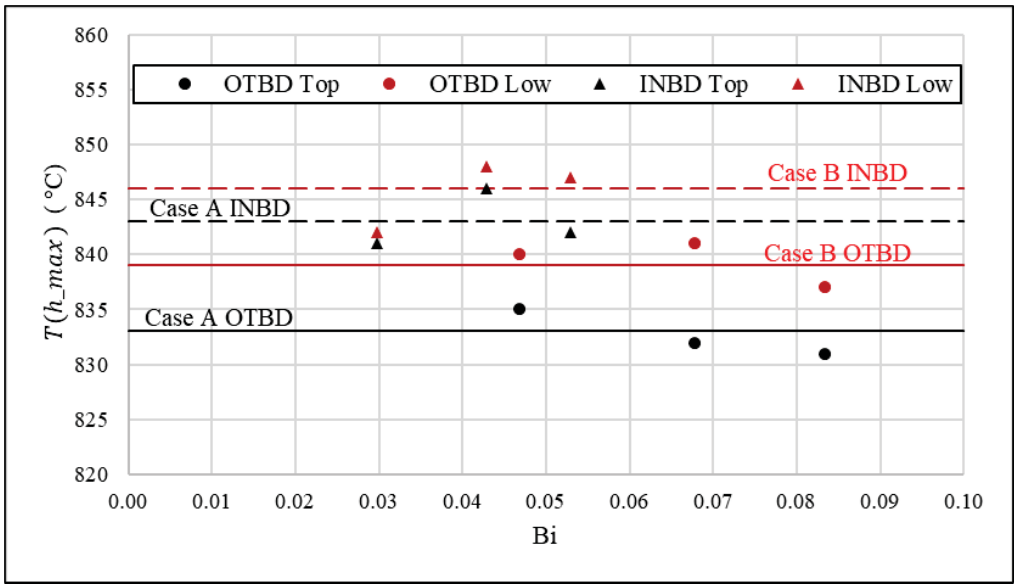

Figure A VI-3 Reference temperature $T_{h_{Amax}}$ per case and surface

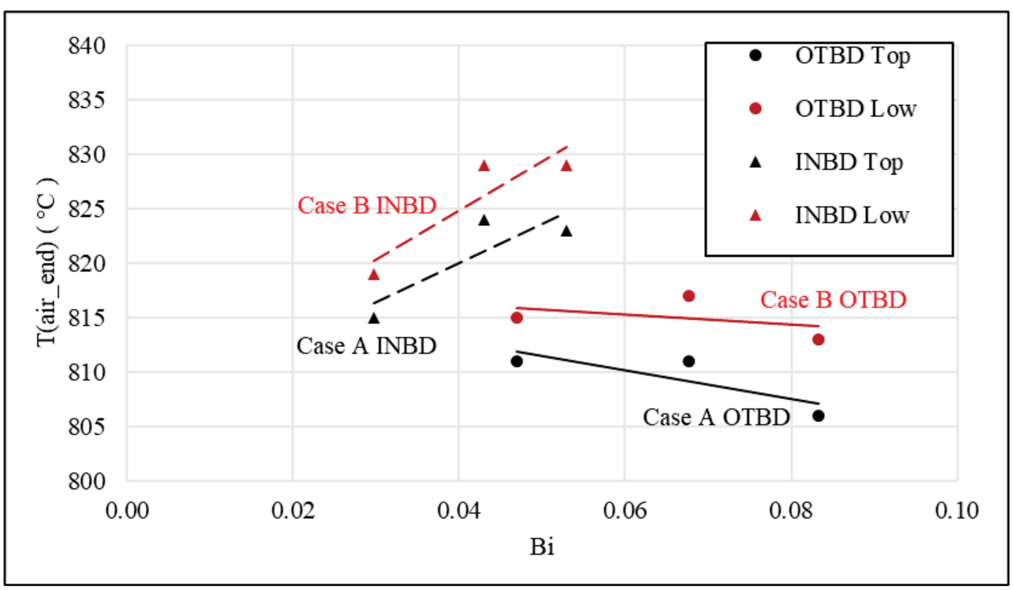

Figure A VI-4 Reference temperature $T_{t_{120}}$ per case and surface

Air 3 – Open Air

This segment follows the same principle as outline in Section 7.3.3, hence requires the calculation of the peak HTC as per Figure A VI-1 to factorize Eq. 7.8.

Model Evaluation and Verification

The air transfer HTC model for Case B is presented in Figure A VI-5. Such values could be compared with those in Figure 7.13 for Case A. Nevertheless, the verification step against test data indicates good agreement with experimentally acquired temperature readings. The worst case is presented in Figure A VI-6 which is deemed acceptable as relative error <1.2%.

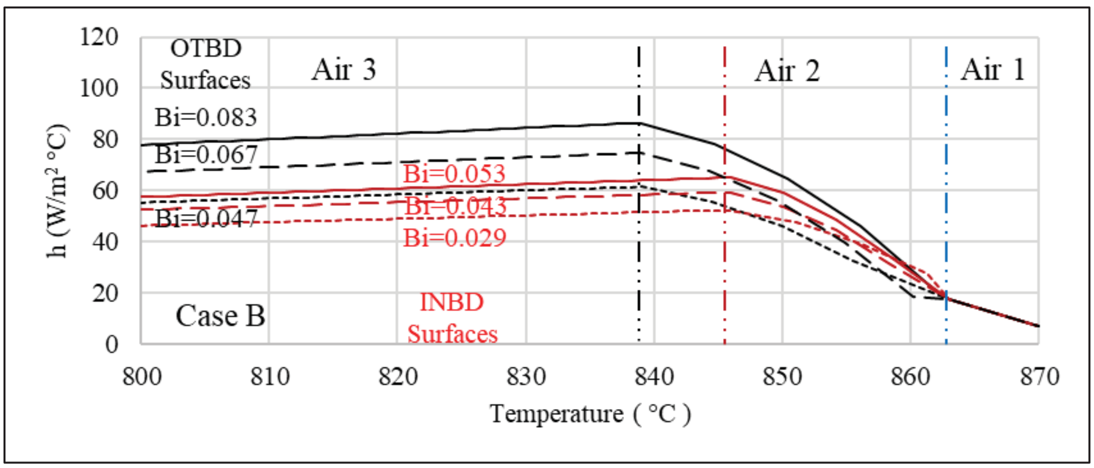

Figure A VI-5 Model air transfer HTC for Case B

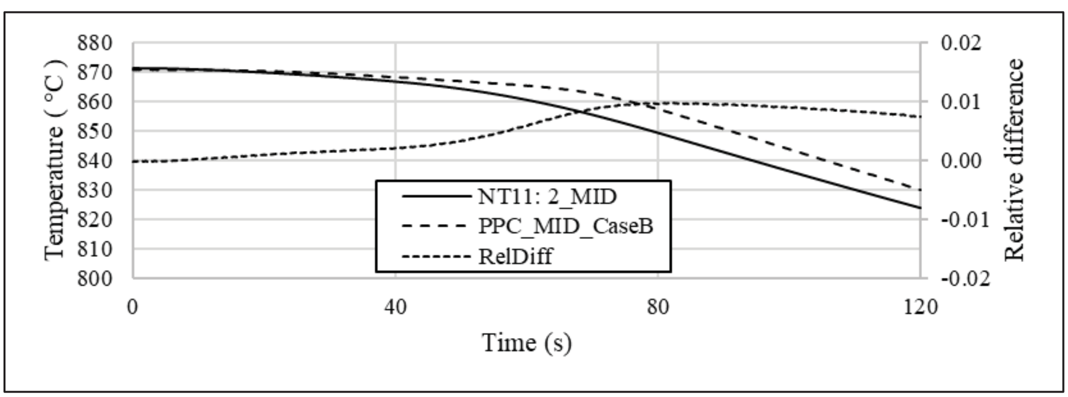

Figure A VI-6 Error plot for worst case B

ANNEX VII

IMMERSION BOUNDARY CONDITION MODEL – CASE B

Section 7.4 presented the modeling strategy applicable to the immersion step for test setup Case A (specimens at the top of the HT-rig). This annex presents the equivalent data and results applicable to Case B, when the specimens are allocated at the bottom of the HT-rig.

Evolution of Characteristic Points

The same characteristic points $Q_{MHF}, Q_{CHF}, Q_{conv}$, were identified for Case B. While Q_{MHF} is considered to be 297 kW/m^2 for case A, the averaged values for case B led to estimate Q_{MHF} at 276 kW/m^2. Figure A VII-1 presents the different values of Q_{MHF} for both cases, A and B, for comparison purposes. Similarly, the evolution of T_{MHF} was registered for Case B as shown in Figure A VII-2. The same behavior is observed in both cases, T_{MHF} decreases as Bi becomes smaller. Despite the similarities, it was decided to maintain Q_{MHF} and T_{MHF} per case, thus Case B has its own evolution of this characteristic point.

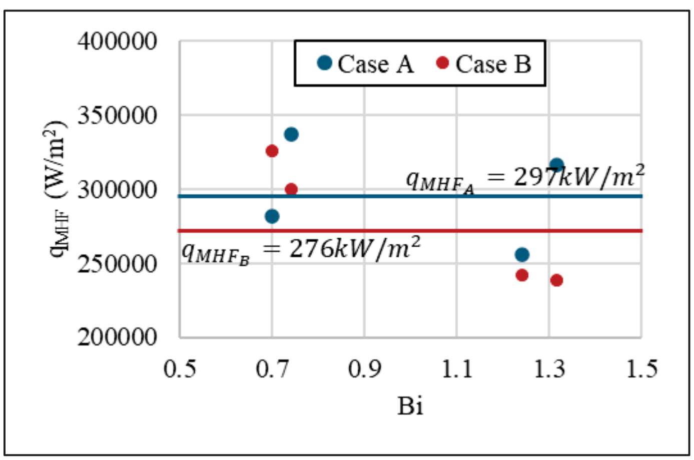

Figure A VII-1 Minimum heat flux

The evolution of Q_{CHF} is shown in Figure A VII-3, which includes the values for Case A for comparison purposes. Overall, the same approach was taken, thus averaging the values for the INBD surface and applying a ratio between INBD and OTBD to estimate Q_{CHF} at the OTBD surface based on the specimen's size. Notably, such ratio is more pronounced for Case B than Case A, which is attributed solely to the local conditions at the bottom of the HT-rig.

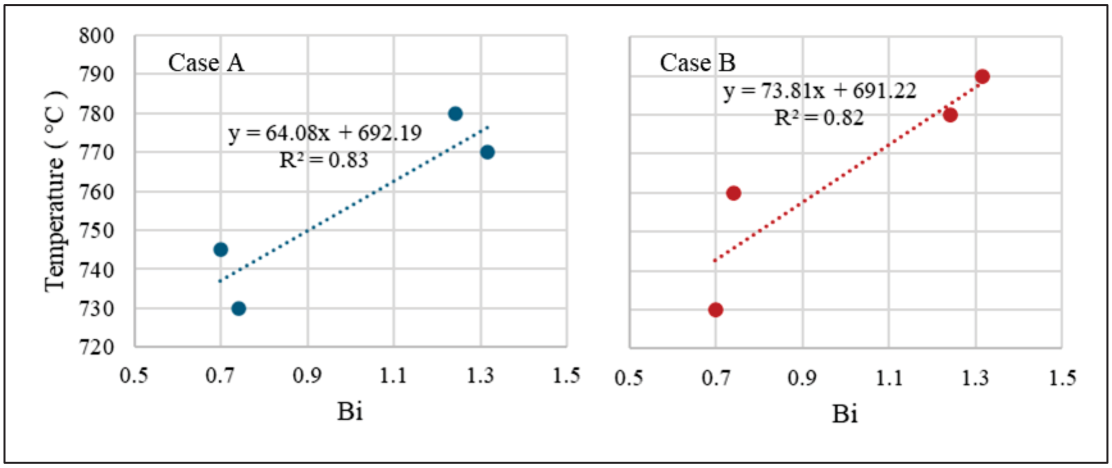

Figure A VII-2 Temperature at minimum heat flux

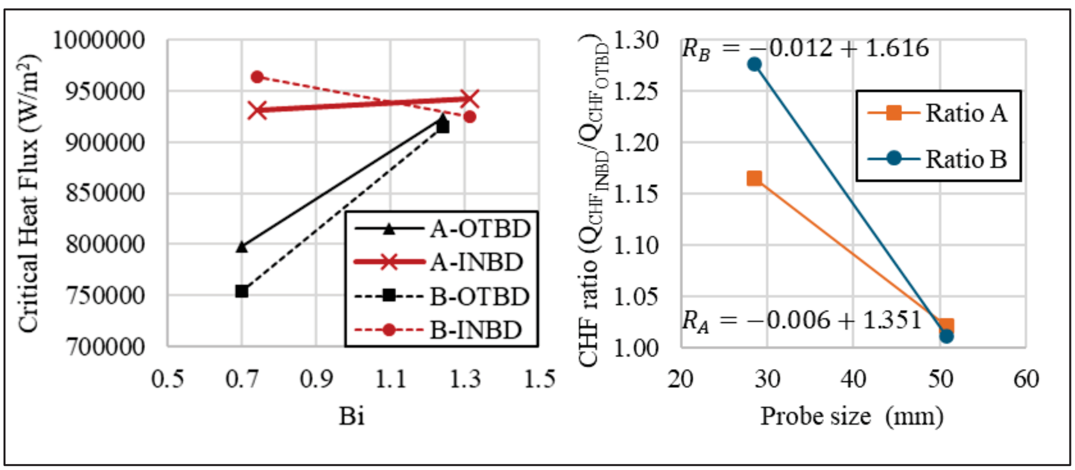

Figure A VII-3 Critical heat flux: magnitude (left) and ratio between surface (right) for both Case A and Case B

The next parameter to determine is T_{CHF}, whose averaged values per surface and case are shown in Figure A VII-4. Interestingly, the temperature on a given surface for Case A are lower than Case B, meaning that case B peaks are achieved first (at higher temperature), than for case A. This could be due to the positioning in the tooling as Case B always enters first the bath and is more influenced by the fluid forced near the base of the tooling.

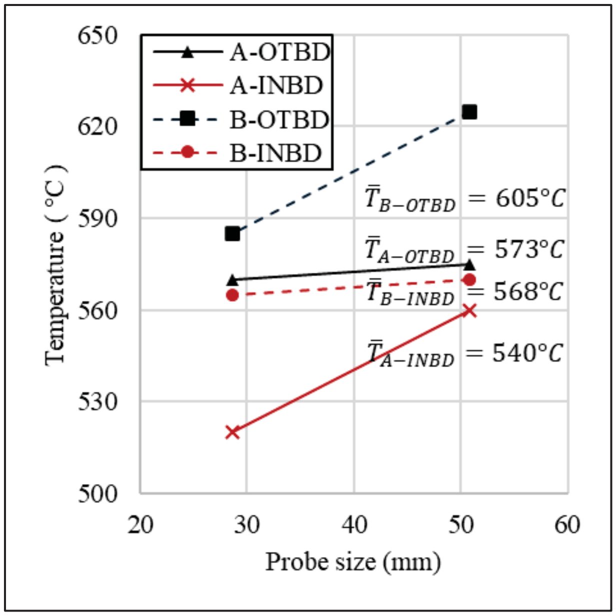

Figure A VII-4 Evolution of T_{CHF} per surface and case. Averaged values shown

The last characteristic point, Q_{conv}, clearly shows the most differences between Case A and Case B, the evolution of Q_{conv} and T_{conv} are shown in Figure A VII-5 and Figure A VII-6 respectively. Notably, the magnitude of Q_{conv} varies over a wider range for Case B than for Case A. This enhances the need to adjust the BCs as required per case setup.

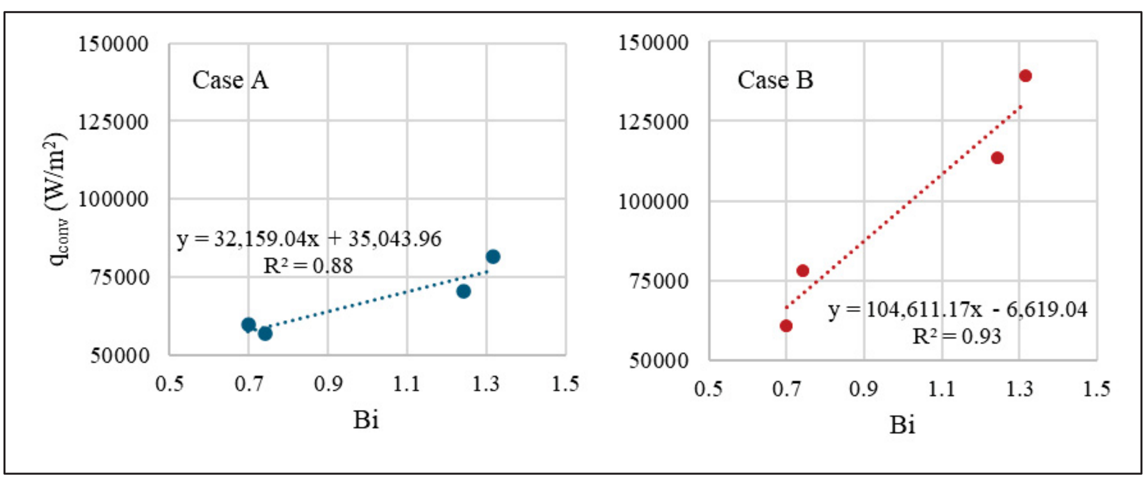

Figure A VII-5 Evolution of Q_{conv} per case

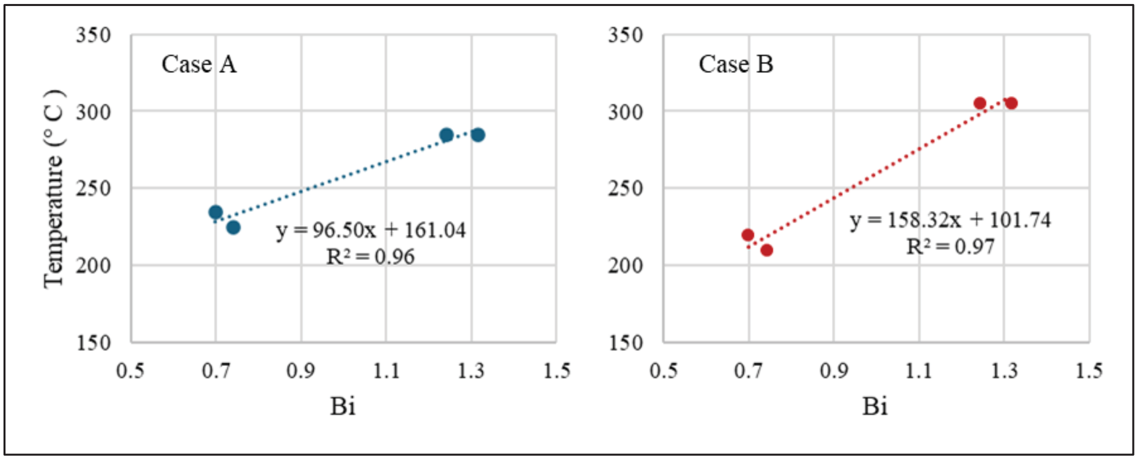

Figure A VII-6 Evolution of T_{conv} per case

Model Fitting per Regime

As outlined in Section 7.4.1.3, the non-dimensional curves of each of the cooling regimes has been model as per Eq. 7.19 to Eq. 7.21. The corresponding coefficients for Case B are included in Table A VII-1 while Figure A VII-7 presents the data and model plots. Note that the process to nondimensionalize the data for Case B follows the same strategy as for Case A as outlined in Section 7.4.1.2.

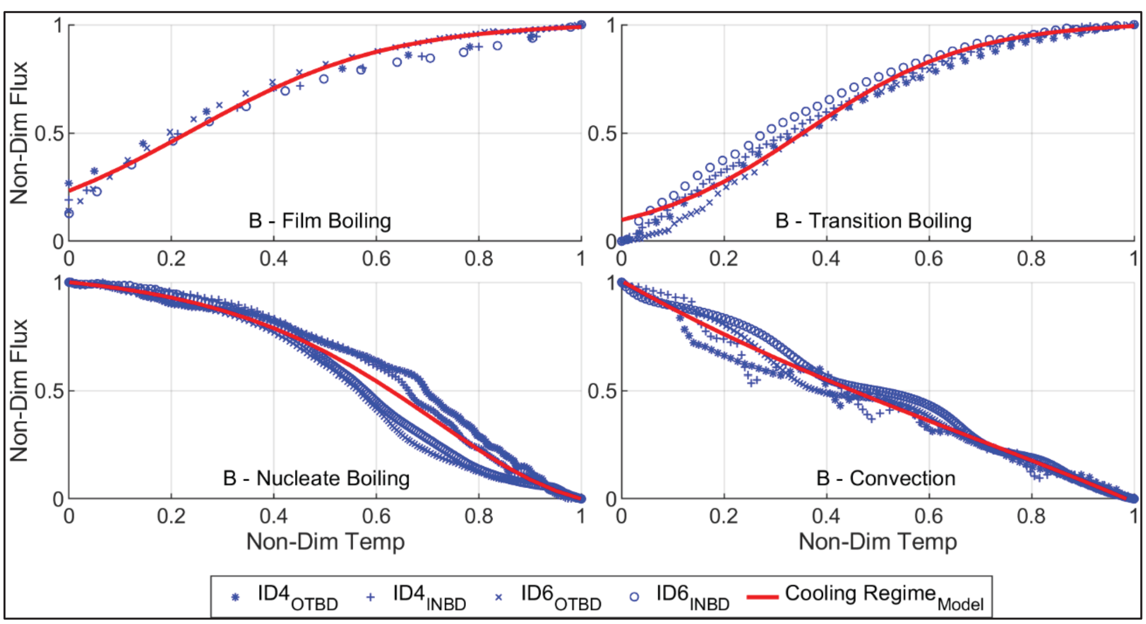

Figure A VII-7 Dimensionless data (markers) per cooling regime during immersion with their corresponding model (red line)

Table A VII-1 Coefficients for model per regime during immersion for Case B

Case	Regime	a	b	c	d	R^2
B	Film	1.009	5.133	0.234	--	0.98
	Transition	1.011	6.236	0.357	--	0.97
	Nucleate	1.062	-3.976	0.716	-0.051	0.96
	Convection	-0.055	1.827	1.061	-1.171	0.98

Model Verification and Validation

The proposed models for Case B were first verified using the predicted HTC as BC in a FE simulation. The modeled HTC are shown in Figure A VII-8. The comparison between model and test data is shown in Figure A VII-9 and Figure A VII-10 for PPA and PPC respectively. The results are deemed acceptable as the relative error always remaining <8%, which is in the same range as the results obtained from the verification step for Case A, see Section 7.4.3.

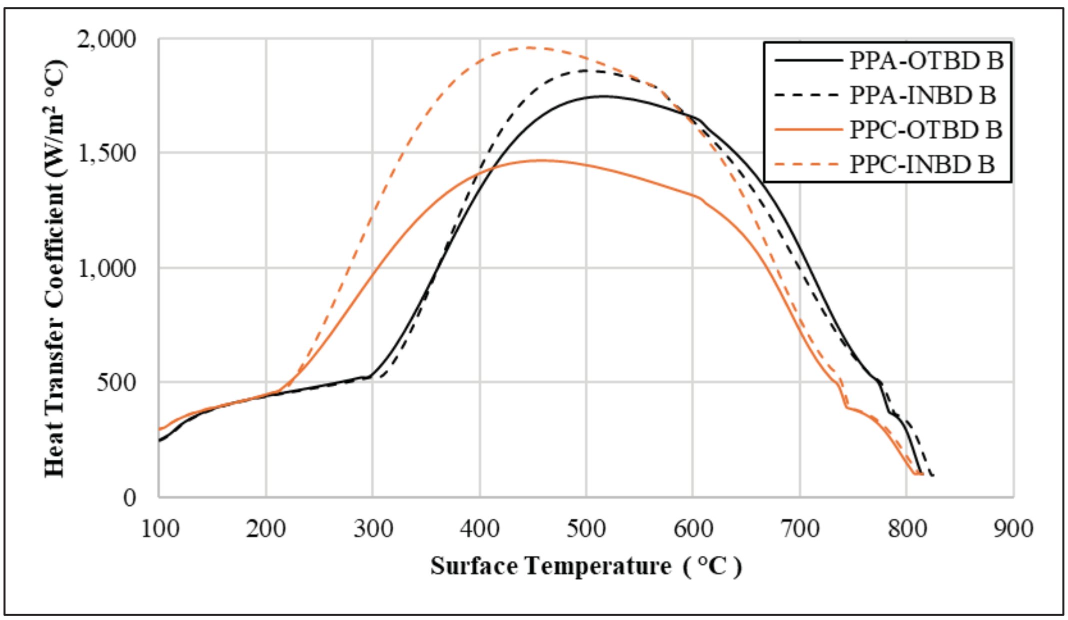

Figure A VII-8 Model HTC for Case B

The last step corresponds to the evaluation of PPB-HTC and comparison with its test data. Such data are included in Figure A VII-11 and Figure A VII-12 respectively. The results are deemed acceptable given the good agreement between the cooling curves as shown in Figure A VII-12. Note that the relative error increases up to 12%. However, such value occurs at lower temperatures by the end of the cooling time while at high temperatures (>400°C) remains within <9%, which is deemed acceptable as its comparable to the verification results.

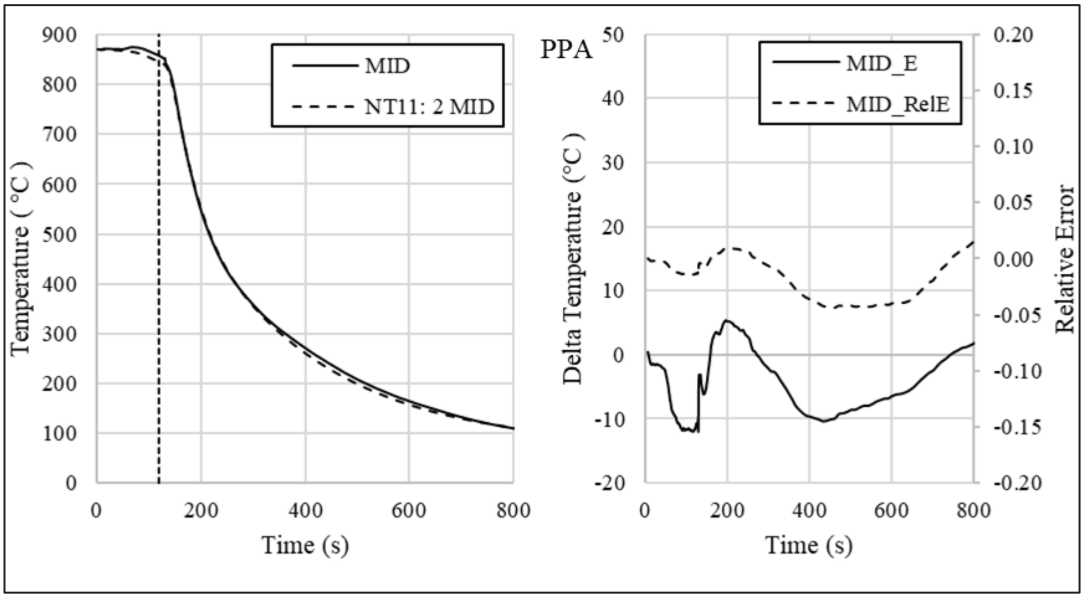

Figure A VII-9 Model verification for PPA-Case B: cooling curves (left) and error plots (right)

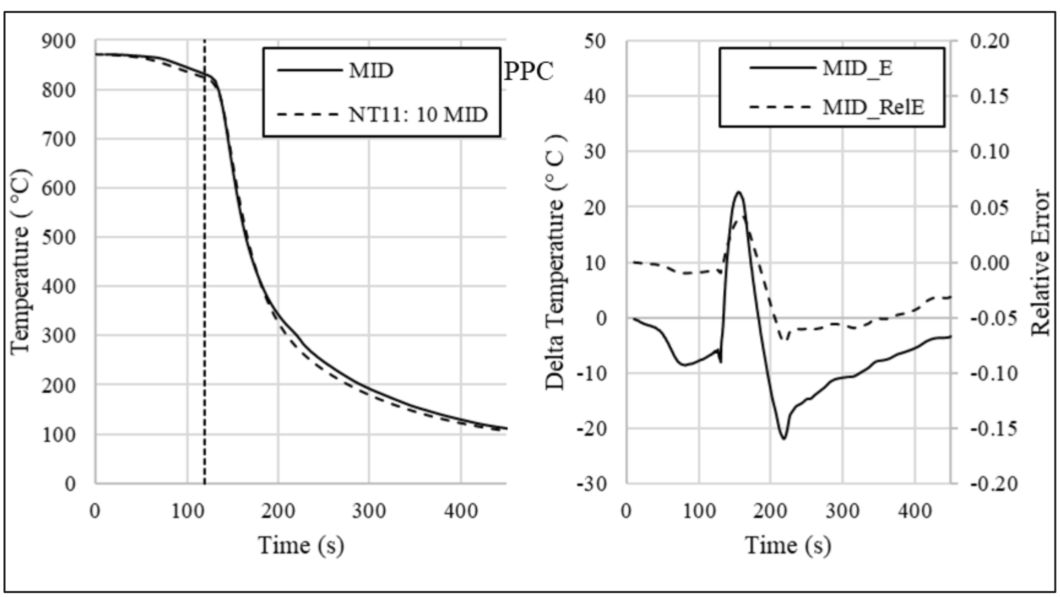

Figure A VII-10 Model verification for PPC-Case B: cooling curves (left) and error plots (right)

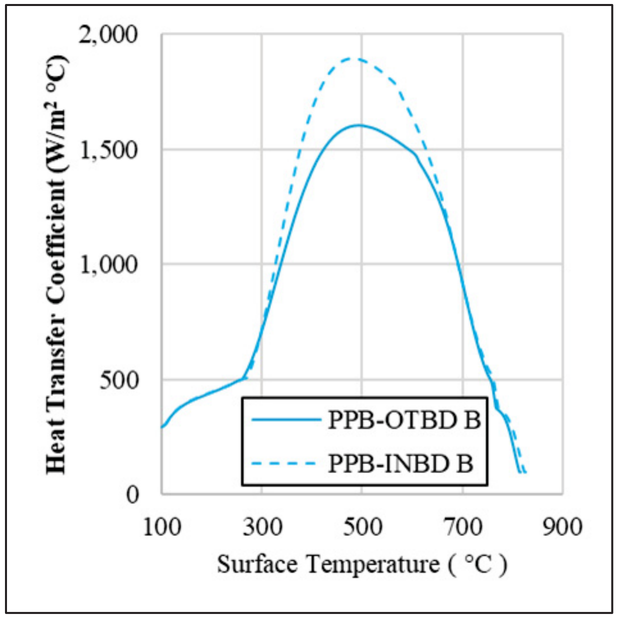

Figure A VII-11 HTC model for PPB-Case B

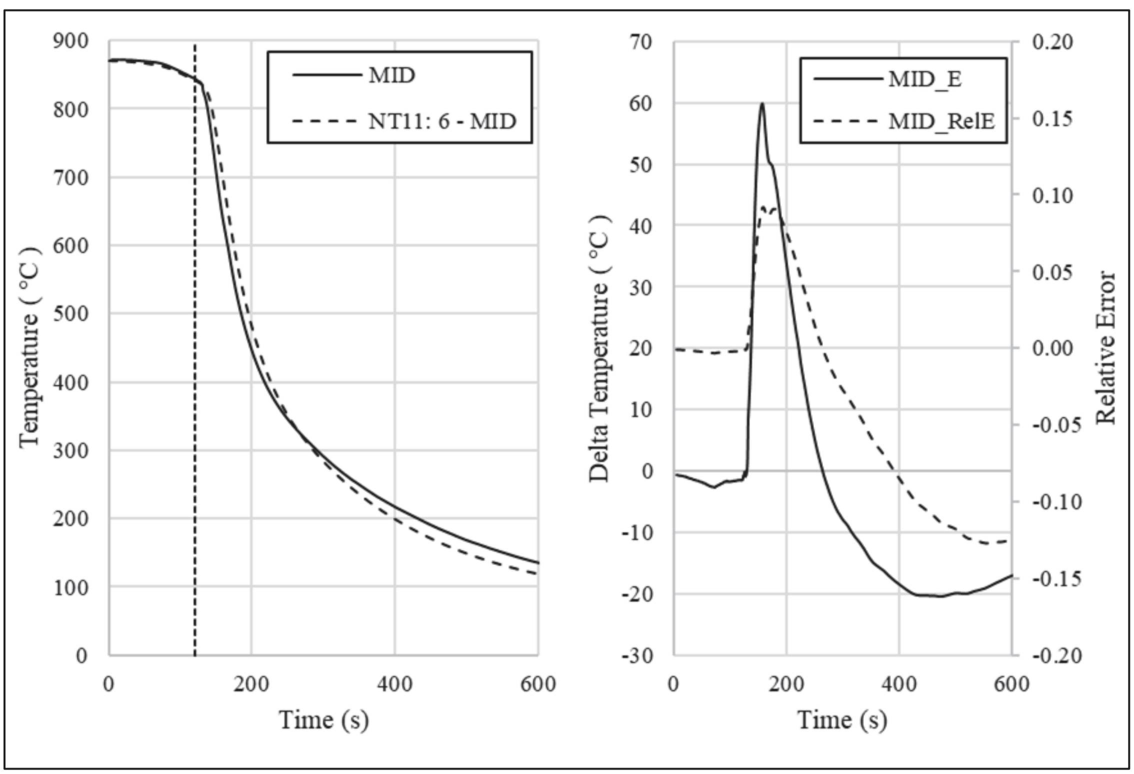

Figure A VII-12 PPB-Case B: cooling curves (left) and error plots (right)

ANNEX VIII

INFLUENCE OF OUTER DIAMETER ON THE BOUNDARY CONDITIONS OF A HOLLOW CYLINDER

The findings reported from Chapter 5 to Chapter 7 address the influence of the specimen size, in the form of thickness (δ), on the thermal BC for plate-like quench probes. Such findings were further discussed on Annex V where the identified BCs were interchanged for two plate-like geometries with different thicknesses. In summary, the common understanding of the HTC being an intensive property is challenged by such findings. To further explore the subject of the influence of probe size, this annex presents the identified boundary conditions for two hollow cylinders with different thicknesses. One referred as HC_A with δ=50.8 mm, and a thinner one labelled as HC_B with δ=30.2 mm, see Figure A VIII-1. A specimen similar to HC_A has been used in the studies presented in Annex III and Annex IV, the former considers a vertical setup while the latter analyzes a horizontal setup. This annex considers the vertical setup only, thus, HC_B was quenched in a comparable configuration, while the boundary conditions were obtained following a similar procedure as outlined in Annex III.

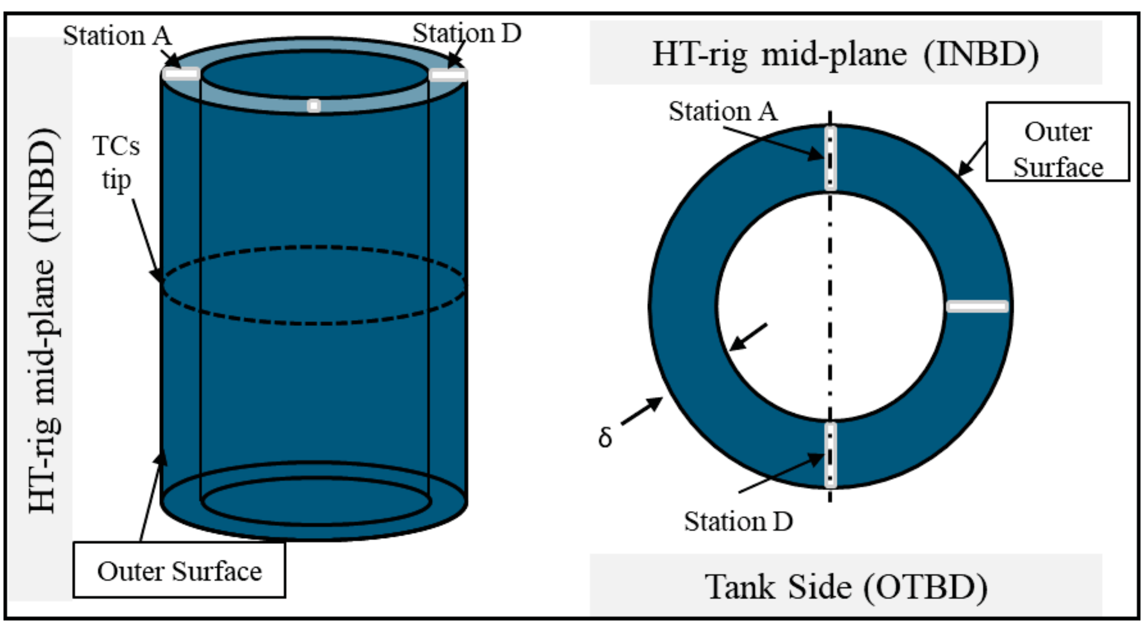

Figure A VIII-1 Schematic of hollow cylinder probe

The resulting boundary conditions in the form of surface heat flux are shown in Figure A VIII-2 for the outer surface of the specimens, at stations A and D. One must note that HC_A (thicker specimen) presents an almost null film boiling, thus the transition boiling cooling regime appears almost immediately upon immersion. On the contrary, HC_B has a very stable film boiling regime at both stations upon immersion that ends when the surface temperature is around the 715°C, such behavior was observed on the plate-like geometries as reported in Chapter 6 and Chapter 7.

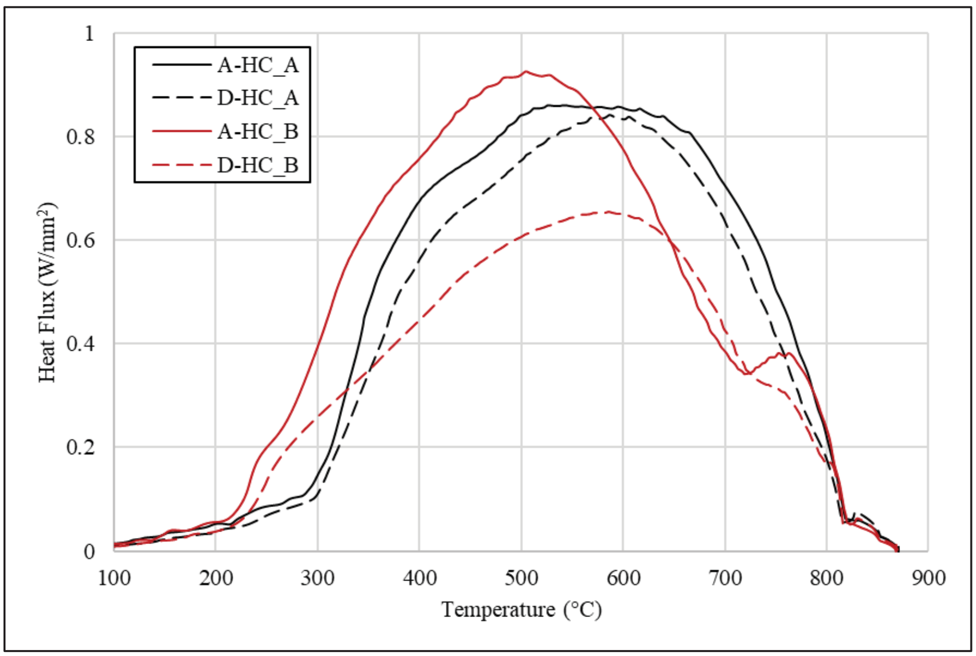

Figure A VIII-2 Surface Heat Flux on Outer Surface of Hollow Cylinder at Stations A and D. Thickness as δ_{HC_A}=50.8mm, δ_{HC_B}=30.2mm

The appearance of the film boiling on HT_B influences the remaining transition points between the cooling regimes, especially the temperature that delimits the boundary from one regime to the other. For instance, the peak of the boiling curve for HC_B appear at lower temperatures than HC_A, thus the fully nucleate boiling starts at a lower temperature for HC_B. Similarly, the end of nucleate boiling and beginning of convection is shifted for the thinner specimen. Thus, confirming the findings reported for plate-like geometries.

While plate-like geometries have two main surfaces of exchange, the utilization of a hollow cylinder also involves an evolution of the surface boundary condition along the circumferential direction. Once can notice that the fluxes for HC_A at station A and station C are close in magnitude, specially when compared with the differences between the same stations for HC_B. Such findings are also consistent with the plate-like geometries as the thinner bodies have a more drastic difference between surfaces. However, this behavior indicates that the boundary condition at the external surface of HC_B must be carefully considered for further modeling. The evolution of the surface fluxes at three stations is shown in Figure A VIII-3. Such results can be used as reference values for further modeling of the outer surface boundary condition.

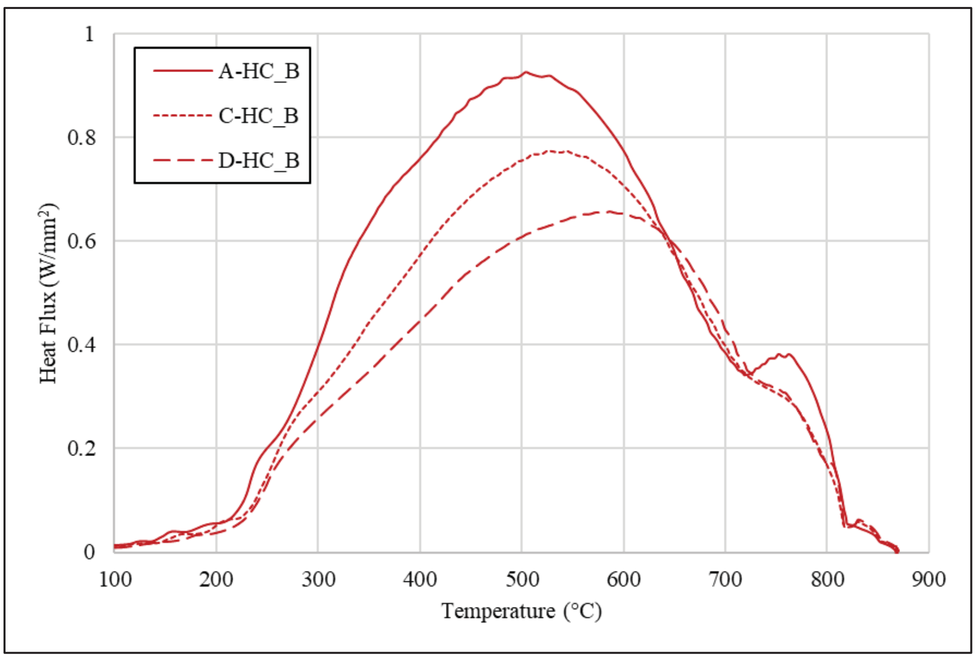

Figure A VIII-3 Evolution of Surface Heat Flux on Outer Surface
of Hollow Cylinder B

ANNEX IX

DERIVATION OF COOLING TIME

The first-term approximate solution of the dimensionless temperature distribution in a plane wall under with conduction along its x-axis (one-dimensional) is given by Eq. 5.42a in (Bergman et al., 2011), rewritten below as:

$$\theta^* = C_1 \exp(-\zeta_1^2 Fo)\, cos\, (\zeta_1 x^*) \qquad \text{A IX-1}$$

Where θ^* is the dimensionless temperature distribution and x^* represents non-dimensional space coordinate. C_1 and ζ_1 represent the first term constant and positive eigenvalues as per (Bergman et al., 2011). By the definition, the Fourier number (Fo) is given as:

$$Fo = \frac{\alpha t}{\omega^2} \qquad \text{A IX-2}$$

Where α is the thermal diffusivity of the material and ω is the half thickness of a wall with thickness 2ω. Hence, replacing Eq. A IX-2 in Eq. A IX-1 and rearranging to solve for time (t), the following relation is obtained:

$$t = ln\left(\frac{\theta^*}{C_1 \cos(\zeta_1 x^*)}\right)\left(\frac{\omega^2}{-\zeta_1^2 \alpha}\right) \qquad \text{A IX-3}$$

Considering that the bath temperature (T_{bath}), the treated part start temperature (T_{start}), and target temperature given by T_{FP} are known, the non-dimensional temperature θ^* is computed as follows:

$$\theta^* = \frac{T_{FP} - T_{bath}}{T_{start} - T_{bath}} \qquad \text{A IX-4}$$

While the non-dimensional space coordinate x^* is given by the position of the thermocouple (distance off the surface Γ known) and the value of ω. Thus, given by:

$$x^* = \frac{x}{\omega} = \frac{\omega - \Gamma}{\omega} \qquad \text{A IX-5}$$

The values of C_1 and ζ_1 given in Table 5.1 in (Bergman et al., 2011) are presented as a function of the Biot number (Bi), which have been included for reference purposes in Table A IX-1.

Table A IX-1 Constants values C_1, ζ_1, extracted from Table 5.1, in (Bergman et al., 2011)

Bi	C_1	ζ_1
0.3	0.5218	1.0450
0.4	0.5932	1.0580
0.5	0.6533	1.0701
0.6	0.7051	1.0814
0.7	0.7506	1.0919
0.8	0.7910	1.1016
0.9	0.8274	1.1107
1	0.8603	1.1191
2	1.0769	1.1785

Then, using Eq. A IX-1 it is possible to compute a range of Bi numbers for the range of interest as Bi depends on the wall thickness ($\delta,\ Eq.\ 6.1$). Therefore, the thickness values (ω, in this annex) have been varied to cover a range of $0.5 > Bi > 1.5$, consistent with the range of interest in the study presented in Chapter 6. Given the values of the heat transfer coefficient and thermal conductivity in Table A IX-2, the wall thickness is varied as 0.062 m>2ω > 0.02 m to cover the desired Bi range. The material properties have been maintained as constant values computed for the average temperature between T_{start}.and T_{bath}. A summary of the values used in the calculation in this annex are shown in Table A IX-2.

Table A IX-2 Summary of values used in the calculation of the cooling time

Variable	Symbol	Value
Heat transfer coefficient	h	$988\ W/(m^2°C)$
Flash point temperature	T_{FP}	$170°C$
Start temperature	T_{start}	$870°C$
Bath temperature	T_{bath}	$40°C$
Conductivity	k	$20.2\ (W/m)K$
Diffusivity	α	$4.79E-06\ (m^2/s)$
Constants	C_1, ζ_1	Table A-II-1
Wall thickness range	2ω	$0.062\text{m} > 2\omega > 0.02\text{m}$
Bi range	Bi	$0.5 > Bi > 1.5$
Distance off surface	Γ	$4.8\ mm$

The resulting cooling time (t) as per Eq. A IX-3 is shown in Figure A IX-1 at three locations: wall surface ($x^* = 1$), mid plane ($x^* = 0$) and thermocouple (TC) location for which x^* is computed on a case-by-case basis which is the curve included in Figure 6.13. All the curves represent the time to reach the target temperature FP. The spacing between curves represents the additional time required to reach the target temperature for an in-body position versus the surface. Clearly, when $x^* = 0$, or the mid plane of a wall, the cooling time is higher when compared to the other two locations.

The regression model developed in the main body of Chapter 6 (Figure 6.13) has been included for comparison purposes in Figure A IX-1. The observations from the test data, and the subsequent regression model correlating cooling time to the Biot number, are consistent with the tendencies appreciated when solving the first-term approximation as the cooling time does depend on the Biot number.

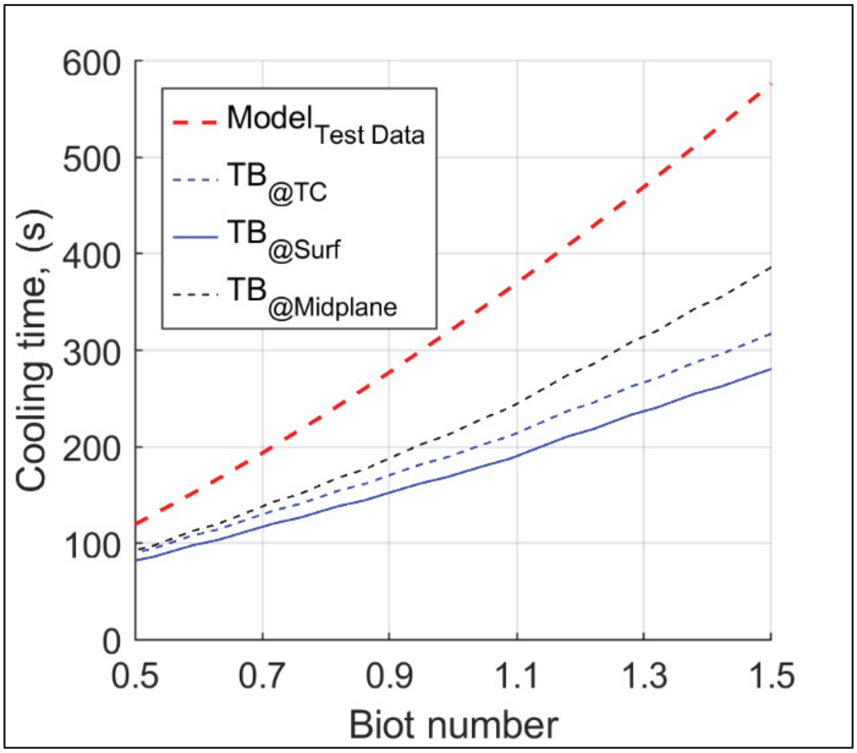

Figure A IX-1 Cooling time: first-term approximation at TC locations (dashed blue line), surface (blue line) and mid plane of a wall (dashed black line)
Regression model from test data (dashed red line) included for comparison

LIST OF BIBLIOGRAPHICAL REFERENCES

Ahmad, F., Meyer, M., Hartwig, J., Mudawar, I., Ave, K., & Lafayette, W. (2024). Saturated Pool Film Boiling of Cryogenic Fluids: Review of Databases, Assessment of Existing Models and Correlations, and Development of New Universal Correlation. *International Journal of Heat and Mass Transfer, 235*, 126190. DOI: 10.1016/j.ijheatmasstransfer.2024.126190

Arai, T., & Furuya, M. (2011). Effect of Salt Additives on Film Boiling Heat Transfer and Mechanism of Quenching Temperature Rise. *Heat Transfer - Asian Research, 40*(2), 101–113. DOI: 10.1002/htj.20327

ASTM International (2021). *Standard Test Method for Determination of Cooling Characteristics of Quench Oils by Cooling Curve Analysis*. ASTM D6200-21. DOI: 10.1520/D6200-21.2

ASTM International (2021). *Standard Test Method for Determination of Cooling Characteristics of Aqueous Polymer Quenchants by Cooling Curve Analysis with Agitation (Tensi Method)*. ASTM D6482-21. DOI: 10.1520/D6482-21.2

ASTM International (2021). *Standard Test Method for Determination of Cooling Characteristics of Quenchants by Cooling Curve Analysis with Agitation (Drayton Unit)*. ASTM D6549-06. DOI: 10.1520/D6549-06R21.2

Atkins, M. (1980). *Atlas of Continuous Cooling Transformation Diagrams for Engineering Steels*. Metals Park, Ohio. American Society for Metals

Babu, K., & Prasanna, T. S. (2010). Mathematical Modeling of Surface Heat Flux During Quenching. *Metallurgical and Materials Transactions B, 41*, 214–224. DOI: 10.1007/s11663-009-9319-y

Banka, A. L., Ferguson, B. L., & Mackenzie, D. S. (2013). Evaluation of Flow Fields and Orientation Effects Around Ring Geometries During Quenching. *Journal of Materials Engineering and Performance, 22*(7), 1816–1825. DOI: 10.1007/s11665-013-0509-z

Barrena-Rodriguez, M., Acosta-Gonzalez, F., & Tellez-Rosas, M. M. (2021). A Review of the Boiling Curve with Reference to Steel Quenching. Metals, *Metals, 11*(6), 974. DOI: 10.3390/met11060974

Bazgir, A., & Zhang, Y. (2024). Harnessing Deep Learning to Solve Inverse Transient Heat Transfer With Periodic Boundary Condition. *Journal of Thermal Science and Engineering Applications, 16*(12), 122001. DOI: 10.1115/1.4066451

Beck, J. V. (1968). Surface Heat Flux Determination using an Integral Method. *Nuclear Engineering and Design, 7*(2)*,* 170–178. DOI: 10.1016/0029-5493(68)90058-7

Beck, J. V. (1970). Non-linear Estimation Applied to the Non-linear Inverse Heat Conduction Problem. *International Journal of Heat and Mass Transfer, 13*(4), 703–716. DOI: 10.1016/0017-9310(70)90044-X

Beck, J. V., Blackwell, B., & Haji-Sheikh, A. (1996). Comparison of Some Inverse Heat Conduction Methods using Experimental Data. *International Journal of Heat and Mass Transfer, 39*(17), 3649–3657. DOI: 10.1016/0017-9310(96)00034-8

Beck, J. V., & Woodbury, K. A. (2016). Inverse Heat Conduction Problem: Sensitivity Coefficient Insights, Filter Coefficients, and Intrinsic Verification. *International Journal of Heat and Mass Transfer, 97*, 578–588. DOI: 10.1016/j.ijheatmasstransfer.2016.02.034

Beckermann, C., & Carlson, K. (2011). Simulation of Distortion and Residual Stress Development During Heat Treatment of Steel Castings (OSTI ID 1022073). Retrieved from: https://www.osti.gov/biblio/1022073

Behrem, S., & Hrnjica, B. (2018). Estimation of Heat Transfer Coefficient during Quenching in Water. *Transactions of FAMENA XLII, 42*(SI-1), 61–73. DOI: 10.21278/TOF.42Si106

Behrem, S., & Hrnjica, B. (2021). Results of Heat Transfer Coefficient Estimation during the Quenching of Cylindrical Samples in Aqueous Solutions. *Transactions of FAMENA XLV, 45*(SI-1), 49–58. DOI: 10.21278/TOF.45Si1008421

Berenson, P. J. (1960). *Transition Boiling Heat Transfer from a Horizontal Surface.* (Report No. 17). Cambridge, Massachusetts: Division of Sponsored Research MIT.

Berenson, P. J. (1961). Film-Boiling Heat Transfer from a Horizontal Surface. *Journal of Heat Transfer, 83(3)*, 351–356. DOI: 10.1115/1.3882280

Bergman, T. L., Lavine, A. S., Incropera, F. P., & Dewitt, D. P. (2011). Fundamentals of Heat and Mass Transfer. (7th ed). John Wiley & Sons.

Bohlooli Arkhazloo, N., Bazdidi-Tehrani, F., Jadidi, M., Morin, J. B., & Jahazi, M. (2022). Determination of Temperature Distribution during Heat Treatment of Forgings: Simulation and Experiment. *Heat Transfer Engineering, 43*(12), 1041–1064. DOI: 10.1080/01457632.2021.1932039

Bohlooli Arkhazloo, N., Bouissa, Y., Bazdidi-Tehrani, F., Jadidi, M., Morin, J. B., & Jahazi, M. (2019). Experimental and Unsteady CFD Analyzes of the Heating Process of Large Size Forgings in a Gas-Fired Furnace. *Case Studies in Thermal Engineering, 14*, 100428. DOI: 10.1016/j.csite.2019.100428

Bouissa, Y., Shahriari, D., Champliaud, H., & Jahazi, M. (2019). Prediction of Heat Transfer Coefficient During Quenching of Large Size Forged Blocks Using Modeling and Experimental Validation. *Case Studies in Thermal Engineering, 13,* 100379. DOI: 10.1016/j.csite.2018.100379

Bourouga, B., & Gilles, J. (2010). Roles of Heat Transfer Modes on Transient Cooling by Quenching Process. *International Journal of Material Forming, 3*, 77–88. https://doi.org/10.1007/s12289-009-0645-z

Breen B. P., & Westwater, J. W. (1962). Effect of Diameter of Horizontal Tubes on Film Boiling Heat Transfer. Chem. Eng. Progress Series, Vol. 58, pp. 67-72

Bromley, L. A. (1949). *Heat Transfer in Stable Film Boiling*. (Report No. UCRL-122) Berkeley, California: Radiation Laboratory University of California.

Buczek, A., & Telejko, T. (2013). Investigation of Heat Transfer Coefficient during Quenching in Various Cooling Agents. *International Journal of Heat and Fluid Flow, 44,* 358–364. DOI: 10.1016/j.ijheatfluidflow.2013.07.004

Cai, C., Mudawar, I., & Liu, H. (2020). Mechanistic Method to Predicting Minimum Heat Flux Point Wall Temperature in Saturated Pool Boiling. *International Journal of Heat and Mass Transfer, 156*. DOI: 10.1016/j.ijheatmasstransfer.2020.119854

Canale, L. C. F., Luo, X., Yao, X., & Totten, G. E. (2009). Quenchant Characterization by Cooling Curve Analysis. *J. ASTM Int, 6*(2), 1-29. DOI: 10.1520/stp49188s

Caron, E., Wells, M. A., & Li, D. (2006). A Compensation Method for the Disturbance in the Temperature Field Caused by Subsurface Thermocouples. *Metallurgical and Material Transactions B, 37*, 475–483. DOI: 10.1007/s11663-006-0031-x

Cebula, A., Taler, J., & Oclon, P. (2018). Heat Flux and Temperature Determination in a Cylindrical Element with the Use of Finite Volume Finite Element Method. *International Journal of Thermal Sciences, 127*, 142–157. DOI: 10.1016/j.ijthermalsci.2018.01.022

Cengel, Y. A. (2005). Heat Transfer: A Practical Approach. McGraw-Hill.

Chapra, S. C., & Canale, R. P. (2010). *Numerical Methods for Engineers* (6th ed). McGraw-Hill.

Churchill, S. W., & Chu, H. H. S. (1975). Correlating Equations for Laminar and Turbulent Free Convection from a Vertical Plate. *International Journal of Heat and Mass Transfer, 18*(11), 1323–1329. DOI: 10.1016/0017-9310(75)90243-4

Colaço, M. J., & Dulikravich, G. S. (2011). A Survey of Basic Deterministic, Heuristic, and Hybrid Methods for Single-Objective Optimization and Response Surface Generation. In H. Orlande, O. Fudym, D. Maillet, & R. Cotta (Eds.), *Thermal Measurements and Inverse Techniques.* Taylor & Francis Group.

Colaço, M. J., Orlande, H., & Dulikravich, G. S. (2006). Inverse and Optimization Problems in Heat Transfer. *J. of the Braz. Soc. of Mech. Sci. & Eng, 28*(1), 1–24. DOI: 10.1590/S1678-58782006000100001

Cruces-Resendez, R., Hernandez-Morales, B., & Guzman, J. (2021). Flow Effects on the Transient Behavior of Vapor Film and Bubbles During Forced- Convective Quenching Experiments. *Proceedings of the 31st ASM Heat Treating Society Conference, September 14-16, 2021*, (293–301). St. Louis, Missouri, USA. ASM International. DOI: 10.31399/asm.cp.ht2021p0293

da Silva, A., Pedrosa, T., Gonzalez-Mendez, J., Xiaohui, J., Cetlin, P., & Altan, T. (2012.). Distortion in Quenching an AISI 4140 steel C-Ring Predictions and Experiments. *Materials & Design*, *41*, 55-61. DOI: 10.1016/j.matdes.2012.05.031

Danev, I., Gospodinov, D., Radev, R., & Ilieva, M. (2020). Influence of Heat Transfer Coefficient on Quenching Processes Simulation. *Metal*. DOI: 10.37904/metal.2020.3510

DANTE Solutions Inc. (2019). *Case study 1: Distortion Analysis of Landing Gear during Oil Quench*. Retrieved from: https://img1.wsimg.com/blobby/go/e793bb6d-7bc3-472a-a860-2edb78c47e2b/downloads/Landing_Gear_Case_Study_Presentation.pdf?ver=1678891302701 (Accessed: 31 May 2023)

Darr, S. R., Dong, J., Glikin, N., Hartwig, J. W., & Chung, J. N. (2019). Rewet Temperature Correlations for Liquid Nitrogen Boiling Pipe Flows Across Varying Flow Conditions and Orientations. *Journal of Thermal Science and Engineering Applications, 11*(October), 1–12. DOI: 10.1115/1.4042857

Duda, P., & Konieczny, M. (2019). A New Algorithm for Solving an Inverse Transient Heat Conduction Problem by Dividing a Complex Domain into Parts. *International Journal of Heat and Mass Transfer, 128*, 865-874. DOI: 10.1016/j.ijheatmasstransfer.2018.09.064

Duda, P., & Konieczny, M. (2022). An Iterative Algorithm for the Estimation of Thermal Boundary Conditions Varying in Both Time and Space. *Energies, 15* (7), 2686. DOI: 10.3390/en15072686

Ebner, G., Lubben, T., & Surm, H. (2025). Shaft Distortion as a Result of Local Flow Inhomogeneities during Oil Quenching in an Industrial Quench Tank. In *QDE 2025: Proceedings of the 3rd International Conference on Quenching and Distortion Engineering, May 6-7, 2025* (pp. 92–95). Vancouver, Canada. ASM International. DOI: 10.31399/asm.cp.qde2025p0092

Elkassabgi, Y., & Lienhard, J. H. (1988). Influences of Subcooling on Burnout of Horizontal Cylindrical Heaters. *Journal of Heat Transfer, 110*(2), 479–486. DOI: 10.1115/1.3250511

Faghri, A., & Zhang, Y. (2020). *Fundamentals of Multiphase Heat Transfer and Flow* (2nd ed). Springer Cham. DOI: 10.1007/978-3-030-22137-9.

Fan, N., Xiong, B., Li, Z., Li, Y., Li, X., Zhang, Y., Wen, K., & Yan, H. (2022). Heat Transfer Behavior During Water Spray Quenching of 7xxx Aluminum Alloy Plates. *Journal of Thermal Science and Engineering Applications, 14*(4), 041013. DOI: 10.1115/1.4051824

Fang, X., & Dong, A. (2017). A Comparative Study of Correlations of Critical Heat Flux of Pool Boiling. *Journal of Nuclear Science and Technology, 54*(1), 1–12. DOI: 10.1080/00223131.2016.1209138

Felde, I. (2012). Determination of Thermal Boundary Conditions during Immersion Quenching by Optimization Algorithms. *Materials Performance and Characterization, 1*(1), 1–11. DOI: 10.1520/MPC104417.

Ferguson, B. L., Freborg, A., & Li, Z. (2012). Probe Design to Characterize Heat Transfer during Quenching Process. In D. S. MacKenzie (Ed.), *Proceedings from the 6th International Quenching and Control of Distortion Conference. Including the 4th International Distortion Engineering Conference, Quenching Control and Distortion, September 9-13, 2012,* (pp. 792-801). Chicago, Illinois, USA. ASM International.

Ferguson, B. L., Li, Z., & Freborg, A. M. (2013). Characterizing Water Quenching Systems with a Quench Probe. In B.L. Ferguson (Ed), *Proceedings of the 27th ASM Heat Treating Society Conference, September 16-18, 2013,* (pp. 224–227). Indianapolis, IN, USA. ASM International.

Fernandes, P., & Prabhu, K. N. (2007). Effect of Section Size and Agitation on Heat Transfer during Quenching of AISI 1040 Steel. *Journal of Materials Processing Technology, 183*, 1–5. DOI: 10.1016/j.jmatprotec.2006.08.028

Flöry, S. (2009). Fitting curves and surfaces to point clouds in the presence of obstacles. *Computer Aided Geometric Design, 26*(2), 192–202. DOI: 10.1016/j.cagd.2008.04.003

Frerichs, F., & Luebben, T. (2009). The Influence of Surface Temperature on Rewetting Behavior During Immersion Quenching of Hollow and Solid Cylinders. *ASTM International, 6(1),* 1032-1051. DOI:10.1520/JAI101852

Gaertner, R. F. (1965). Photographic Study of Nucleate Pool Boiling on a Horizontal Surface. *Journal of Heat Transfer, 87*(1), 17–27. DOI: 10.1115/1.3689038

Galloway, J. E., & Mudawar, I. (1993). CHF Mechanism in Flow Boiling from a Short Heated Wall - I. Examination of Near-Wall Conditions with the Aid of Photomicrography and High-Speed Video Imaging. *International Journal of Heat and Mass Transfer, 36*(10), 2511–2526. DOI: 10.1016/S0017-9310(05)80190-5

Ghiaasiaan, S. M. (2017). Transition and Film Boiling. In F. A. Kulacki (Ed.), *Handbook of Thermal Science and Engineering.* (pp. 1695-1746). Springer. DOI: 10.1007/978-3-319-26695-4_42

Haramura, Y., & Katto, Y. (1983). A New Hydrodinamic Model of Critical Heat Flux, Applicable Widely to Both Pool and Forced Convection Boiling on Submerged Bodies in Saturated Liquids. *International Journal of Heat and Mass Transfer, 26*(3), 389–399. DOI: 10.1016/0017-9310(83)90043-1

Heming, C., Xieqing, H., & Jianbin, X. (2003). Comparison of Surface Heat-Transfer Coefficients between Various Diameter Cylinders during Rapid Cooling. *Journal of Materials Processing, 138*, 399–402. DOI: 10.1016/S0924-0136(03)00106-7

Henry, R. E. (1974). A Correlation for the Minimum Film Boiling Temperature. *AIChE Symp. Ser., 79*(138), 81–90.

Hepher, T. (2022). *Airbus diffère son objectif de remontée des cadences de production de la famille A320.* Retrieved from: https://www.usinenouvelle.com/article/airbus-differe-son-objectif-de-remontee-des-cadences-de-production-de-la-famille-a320.N2030202

Hernandez-Morales, B., Cruces-Resendez, R., & Duran-Garcia, E. I. (2025). Effect of Fluid-Probe Interaction on Heat Extraction in Laboratory-Scale Forced Convective Quench Tests. In *QDE 2025: Proceedings of the 3rd International Conference on Quenching and Distortion Engineering, May 6-7, 2025*, (pp. 147–156), Vancouver Canada. ASM International. DOI: 10.31399/asm.cp.qde2025p0147

Hernandez-Morales, B., Cruces-Resendez, R., & Tellez-Martinez, J. (2019). Revisiting the Temperature Gradient Method. *Materials Performance and Characterization, 8*(2), 170–187. DOI: 10.1520/MPC20180031

Hernandez-Morales, B., Lopez-Sosa, F., & Cabrera-Herrera, L. (2012). A New Methodology for Estimating Heat Transfer Boundary Conditions during Quenching of Steel Probes. In S. MacKenzie (ed). *Proceedings from the 6th International Quenching and Control of Distortion Conference. Including the 4th International Distortion Engineering Conference*, *September 9-13, 2012,* (pp. 81–92) Chicago, IL. ASM International

Howard, A. H., & Mudawar, I. (1999). Orientation Effects on Pool Boiling Critical Heat Fux (CHF) and Modeling of CHF for Near-Vertical Surfaces. *International Journal of Heat and Mass Transfer, 42*(9), 1665-1688. DOI: 10.1016/S0017-9310(98)00233-6

Hua, T. C., & Xu, J. J. (2000). Quenching Boiling in Subcooled Liquid Nitrogen for Solidification of Aqueous Materials. *Materials Science and Engineering, 292* (2), 169–172. DOI: 10.1016/S0921-5093(00)01004-2

Huiping, L., Guoqun, Z., Shanting, N., & Yiguo, L. (2006). Inverse Heat Conduction Analysis of Quenching Process using Finite-Element and Optimization Method. *Finite Elements in Analysis and Design, 42*(12), 1087–1096. DOI: 10.1016/j.finel.2006.04.002

International Organization for Standardization (1995). *Industrial Quenching Oils – Determination of Cooling Characteristics – Nickel-Alloy Probe Test Method*. ISO 9950:1995. Retrieved from: https://www.iso.org/obp/ui/#iso:std:iso:9950:ed-1:v1:en

Jahedi, M., Berntsson, F., Wren, J., & Moshfegh, B. (2018). Transient Inverse Heat Conduction Problem of Quenching a Hollow Cylinder by One Row of Water Jets. International *Journal of Heat and Mass Transfer, 117*, 748–756. DOI: 10.1016/j.ijheatmasstransfer.2017.10.048

Jan, J., & MacKenzie, D. S. (2018). On the Characterization of Heat Transfer Rate in Various Boiling Regimes Using Quenchometers and Its Application for Quenching Process Simulations. In L. Ferguson, L. Frame, R. Goldstein, D. Guisbert, D. Scott MacKenzie (eds), *Thermal Processing in Motion 2018—Conference Proceedings of the Thermal Processing in Motion, June 5-7, 2018* (pp. 112–123). Spartanburg, South Carolina, US. ASM International.

Jan, J., & MacKenzie, D. S. (2019). On the Development of Parametrical Water Quenching Heat Transfer Model Using Quenchometer and Its Validation for All Boiling Regimes. In Heat Treat 2019: Proceedings of the 30th ASM Heat Treating Society Conference October 15–17, 2019 (pp. 279-289). Detroit, Michigan, USA. ASM International. DOI: 10.31399/asm.cp.ht2019p0279

Jan, J., & MacKenzie, D. S. (2020). On the Development of Parametrical Water Quenching Heat Transfer Model Using Cooling Curves by ASTM D6200 Quenchometer. *Journal of Materials Engineering and Performance, 29*(6), 3612–3625. DOI: 10.1007/s11665-020-04803-z

Jan, J., & MacKenzie, D. S. (2021). On the Construction of Analytical Cooling Curves from ASTM D6200 Data Using Multi-Variable Gradient Descent Method. In *Heat Treat 2021: Proceedings from the 31st Heat Treating Society Conference and Exposition, September 14-16, 2021* (pp. 280–292), St. Louis, MI, USA. DOI: 10.31399/asm.cp.ht2021p0280

Jan, J., & MacKenzie, D. S. (2024). On the Construction of Analytical Cooling Curves from ASTM D6200 Data Using Multi-Variable Gradient Descent Method. *Journal of Materials Engineering and Performance, 33*(9), 4234–4252. DOI: 10.1007/s11665-023-09104-9

Jouhara, H., & Axcell, B. P. (2009). Film Boiling Heat Transfer and Vapour Film Collapse on Spheres, Cylinders and Plane Surfaces. *Nuclear Engineering and Design, 239*, 1885–1900. DOI: 10.1016/j.nucengdes.2009.04.008

Katto, Y. (1994). Critical Heat Flux. *International Journal of Multiphase Flow, 20*(1), 53–90. DOI: 10.1016/0301-9322(94)90070-1

Kim, H. K., & Oh, S. I. (2001). Evaluation of Heat Transfer Coefficient during Heat Treatment by Inverse Analysis. *Journal of Materials Processing Technology, 112*, 157–165. DOI: 10.1016/S0924-0136(00)00877-3

Kim, J., Jun, S., Laksnarain, R., & You, S. M. (2016). Effect of Surface Roughness on Pool Boiling Heat Transfer at a Heated Surface Having Moderate Wettability. *International Journal of Heat and Mass Transfer, 101*, 992–1002. DOI: 10.1016/j.ijheatmasstransfer.2016.05.067

Kim, K. M., Hurley, P., & Duarte, J. P. (2022). Physics-Informed Machine Learning-Aided Framework for Prediction of Minimum Film Boiling Temperature. *International Journal of Heat and Mass Transfer, 191*, 122839. DOI: 10.1016/j.ijheatmasstransfer.2022.122839

Kobasko, N. (2017). Investigation of Transient Nucleate Boiling Processes and their Practical Use in Heat Treating Industry. *EUREKA: Physics and Engineering, 5*. DOI: 10.21303/2461-4262.2017.00409

Kobasko, N., & Liscic, B. (2017). Liscic/Petrofer Probe to Investigate Real Industrial Hardening Processes and some Fundamentals During Quenching of Steel Parts in Liquid Media. *EUREKA: Physics and Engineering, 6(November),* 48–56. DOI: 10.21303/2461-4262.2017.00495

Kobasko, N., Moskalenko, A. A., Totten, G. E., & Webster, G. M. (1997). Experimental Determination of the First and Second Critical Heat Flux Densities and Quench Process Characterization. *Journal of Materials Engineering and Performance, 6*(February), 93–101. DOI: 10.1007/s11665-997-0037-9

Koistinen, D., & Marburger, R. (1959). A General Equation Prescribing the Extent of the Austenite-Martensite Transformation in Pure Iron-Carbon Alloys and Plain Carbon Steels. *Acta Metallurgica, 7*, 59–60. DOI: 10.1016/0001-6160(59)90170-1

Kolev, N. I. (2007). *Multiphase Flow Dynamics 2: Thermal and Mechanical Interactions* (3rd ed.). Berlin: Springer. DOI: 10.1007/3-540-69835-3

Kopun, R., Škerget, L., Hriberšek, M., Zhang, D., Stauder, B., & Greif, D. (2014). Numerical Simulation of Immersion Quenching Process for Cast Aluminium Part at Different Pool Temperatures. *Applied Thermal Engineering, 65*(1–2), 74–84. DOI: 10.1016/j.applthermaleng.2013.12.058

Kopun, R., Zhang, D., Edelbauer, W., Stauder, B., Basara, B., & Greif, D. (2014). Immersion Quenching Simulation of Realistic Cylinder Head Geometry. SAE Int. J. Mater. Manf, 7(3), 520–529. DOI: 10.4271/2014-01-0641

Kumar, P., & Chakraborty, S. (2021). Experimental Investigation of Hot AISI 304 Steel Plate with Very-High Mass-Flux Varying Water Temperature Spray. *Heat Transfer*, *51*(September), 1110–1137. DOI: 10.1002/htj.22344

Lemyre-Baron, J.-S. (2025). *Conception d'une sonde de trempe industrielle et identification du coefficient d'échange de chaleur* [Design of an Industrial Quench Probe and Identification of Heat Transfer Coefficient]. (Master Thesis. École de technologie superieure, Montreal, Canada)

Li, D. (2003). *Boiling Water Heat Transfer during Quenching of Steel Plates and Tubes*. (Doctoral thesis, University of British Columbia, Vancouver, Canada)

Li, D, & Wells, M. A. (2005). Effect of Subsurface Thermocouple Installation on the Discrepancy of the Measured Thermal History and Predicted Surface Heat Flux during a Quench Operation. Metallurgical and Material Transactions B, 36, (343–354). DOI: 10.1007/s11663-005-0064-6

Li, D, Wells, M. A., Cockcroft, S. L., & Caron, E. (2007). Effect of Sample Start Temperature during Transient Boiling Water Heat Transfer. *Metallurgical and Materials Transactions B, 38*, 901–910. DOI: 10.1007/s11663-007-9091-9

Li, R., Huang, Z., Li, G., Wu, X., & Yan, P. (2017). A Modified Space Marching Method Using Future Temperature Measurements for Transient Nonlinear Inverse Heat Conduction Problem. *International Journal of Heat and Mass Transfer, 106*, 1157–1163. DOI: 10.1016/j.ijheatmasstransfer.2016.10.095

Liang, G., & Mudawar, I. (2018). Pool Boiling Critical Heat Flux (CHF) – Part 1: Review of Mechanisms, Models, and Correlations. *International Journal of Heat and Mass Transfer, 117*, 1352–1367. DOI: 10.1016/j.ijheatmasstransfer.2017.09.134

Lienhard V, J. H., & Lienhard IV, J. H. (2024). *A Heat Transfer Textbook* (6th Ed.). Cambridge MA: Phlogiston Press.

Liscic, B. (2006). Steel Heat Treatment. In G. E. Totten (Ed.), *Steel Heat Treatment, Metallurgy and Technologies* (2nd ed. pp. 278–414). Taylor & Francis Group.

Liscic, B. (2009). Heat Transfer Control During Quenching. *Materials and Manufacturing Processes, 24*(7), 879–886. DOI: 10.1080/10426910902917694

Liscic, B. (2016). Measurement and Recording of Quenching Intensity in Workshop Conditions Based on Temperature Gradients. *Materials Performance and Characterization, 5(1)*, 202–219. DOI: 10.1520/MPC20160007

Liscic, B., & Singer, S. (2013). Large Probes for Characterization of Industrial Quenching Processes. In J. Dossett & G.E. Totten (Eds) *Steel Heat Treating Fundamentals and Processes* (Vol. 4A, pp. 176–191). ASM International. DOI: 10.31399/asm.hb.v04a.a0005789

Liscic, B., & Singer, S. (2014). Calculation of the Heat Transfer Coefficient Based on Experiments by the Liscic Probes. In Hasmhi, S., Ferreira Batalha, G., Van Tyne, C. J. & Yilbas, B. (Eds.), *Comprehensive Materials Processing* (Vol. 12, pp. 123-176). DOI: 10.1016/B978-0-08-096532-1.01205-X

Liscic, B., Singer, S., & Beitz, H. (2011). Dependence of Heat Transfer Coefficient at Quenching on Diameter of Cylindrical Workpieces. *International Heat Treatment and Surface Engineering, 5*(3), 101–105. DOI: 10.1179/174951411X13051201040910

Lopez-Garcia, R. D., Medina-Juarez, I., & Maldonado-Reyes, A. (2022). Effect of Quenching Parameters on Distortion Phenomena in AISI 4340 Steel. *Metals, 12*, 759. DOI: 10.3390/met12050759

Lu, J. F., Bourouga, B., & Ding, J. (2013). Transient Boiling Heat Transfer Performances of Subcooled Water during Quenching Process. *International Communications in Heat and Mass Transfer*, *48*, 15–21. DOI: 10.1016/j.icheatmasstransfer.2013.08.016

Luebben, T., Lohrmann, M., Segerberg, S., & Sommer, P. (2009). Formulation of a Guideline for the Determination of Heat Transfer Coefficient during Gas Quenching. *Journal of ASTM International, 6*(3), 63–83. DOI: 10.1520/JAI101781

MacKenzie, D. S., & Banka, A. L. (2009). Determination of Heat Transfer Coefficients for Thermal Modeling. In D.U. Furrer and S.L. Semiatin (Eds), *ASM Handbook: Fundamentals of Modeling for Metals Processing* (Vol. 22A, pp. 106–126). ASM International. DOI: 10.31399/asm.hb.22a.a0005436

Malinowski, Z., Hadała, B., & Cebo-Rudnicka, A. (2022). Inverse Solutions to a Vertical Plate Cooling in Air – A Comparative Study. *International Journal of Heat and Mass Transfer, 188,* 122636. DOI: 10.1016/j.ijheatmasstransfer.2022.122636

Maniruzzaman, M., Dai, X., & Sisson, R. (2012). Effect of Quench Start Temperature on Surface Heat Transfer Coefficients. In S. MacKenzie (ed). *Proceedings from the 6th International Quenching and Control of Distortion Conference. Including the 4th International Distortion Engineering Conference*, September 9-13, 2012, (pp. 57-68) Chicago, IL. ASM International

Matijevic, B., Canale, B. F., Liscic., B., & Totten, G.E. (2019). Using Thermal Gradient Measurements to Compare Bath Temperature and Agitation Effects on the Quenching Performance of Palm Oil, Canola Oil and a Conventional Petroleum Oil. *Materials Performance and Characterization, 8* (1), 223–248, DOI: 10.1520/MPC20180135

Matijevic, B., Liscic, B., Totten, G., & Canale, L. C. F. (2017). Comparative Measurement and Evaluation of the Quenching Intensity of Palm Oil, Canola Oil and a Conventional Petroleum Oil Quenchant Based on Temperature Gradient Measurements. *Materials Performance and Characterization, 6*(5), 757-776. DOI: 10.1520/MPC20170041

McHale, J. P., & Garimella, S. V. (2010). Bubble Nucleation Characteristics in Pool Boiling of a Wetting Liquid on Smooth and Rough Surfaces. *International Journal of Multiphase Flow, 36*, 249–260. DOI: 10.1016/j.ijmultiphaseflow.2009.12.004

Mohanty, R. L., & Das, M. K. (2017). A Critical Review on Bubble Dynamics Parameters Influencing Boiling Heat Transfer. *Renewable and Sustainable Energy Reviews, 78*, 466–494. DOI: 10.1016/j.rser.2017.04.092

Monde, M., Liu, W., Mitsutake, Y., & Zin, K. (2006). Characteristics of Boiling Curve in Transition Region between Nucleate Boiling and Film Boiling. *Heat Transfer - Asian Research, 35*(1), 20-43. DOI:10.1002/htj.20097

Monesh Kumhar, K., Rahul, B., Sathyaseelan, S., & Babu, K. (2023). Estimation and Analysis of Surface Heat Flux during Gas Quenching through IHC method. *Materials Today: Proceedings: Part 4, 72*, 2174–2180. DOI: 10.1016/j.matpr.2022.08.458

Monroe, R. W., & Bates, C. E. (1983). Evaluating Quenchants and Facilities for Hardening Steel. J. Heat Treating, 3(2), 83–99. DOI: 10.1007/BF02833078

Myrick, J. A., Keyhani, M., & Frankel, J. I. (2016). Inverse Prediction of Temperature Through Time Rescaling of High-Temperature Experimental Data. *Journal of Thermal Science and Engineering Applications, 8*(4), 041005. DOI: 10.1115/1.4034093

Narazaki, M., & Totten, G. E. (2007). Distortion of Heat-Treated Components. In G. E. Totten (Ed.), *Steel Heat Treatment, Metallurgy and Technologies* (2nd ed. pp. 607–650). Taylor & Francis Group.

Narazaki, M, Kogawara, M., Shirayori, A., Kim, S. Y., & Kubota, S. (2012). Experimental and Simulation Studies on Asymmetrical Quench Distortion of Long Thin Steel Parts. In D. S. MacKenzie (Ed.), *Proceedings from the 6th International Quenching and Control of Distortion Conference. Including the 4th International Distortion Engineering Conference, Quenching Control and Distortion, September 9-13, 2012,* (pp. 457–464). Chicago, Illinois, USA. ASM International.

Nayak, U. V, & Prabhu, K. N. (2018). Effect of Section Thickness on Heat Transfer during Quenching in Vegetable Oils. *Materials Performance and Characterization, 7*(1), 384–396. DOI: 10.1520/MPC20180084

Nelson, R. A., & Pasamehmetoglu, K. O. (1992). Quenching Phenomena. In G. F. Hewitt, J. M. Delhaye, & N. Zuber (Eds.), *Post-Dryout Heat Transfer* (1st Ed, pp. 39–183). CRC Press.

Ozisik, M., & Orlande, H. (2000). *Inverse Heat Transfer Fundamentals and Applications.* (1st ed). New York NY: Taylor & Francis Group.

Pati, A. R., Bhatt, N. H., Das, L., Teja, S., Nayak, S., Kumar, A., Sahoo, A., Munshi, A., Behera, A., Sutar, H., & Mohapatra, S. S. (2019). The Discrepancy in the Prediction of Surface Temperatures by Inverse Heat Conduction Models for Different Quenching Processes from Very high Initial Surface Temperature. *Inverse Problems in Science and Engineering, 27*(6), 808–835. DOI: 10.1080/17415977.2018.1501369

Pattanayak, B., & Kothadia, H. (2022). Experimental Study of Critical Heat Flux During Pool Boiling on Mini Tubes: Effect of Subcooling, Orientation, and Dimensions. *Heat Transfer Engineering, 43*(11), 896–921. DOI: 10.1080/01457632.2021.1919971

Peterson, L. J., & Bajorek, S. M. (2002). Experimental Investigation of Minimum Film Boiling Temperature for Vertical Cylinder at Elevated Pressure. *Proceedings of the ICONE10 10th International Conference on Nuclear Engineering, April 14-28, 2002,* (pp. 1–10). Arlington, VA. USA. ASME.

Prasanna Kumar, T. S., Hernandez-Morales, B., & Totten, G. (2014). "Reference Quench Probe" - An Alternative Probe Design for In-Situ Estimation of Cooling Rates, Heat Flux, and Hardenability during Immersion Quenching of Hardenable Steels. *Materials Performance and Characterization, 3(4)*. DOI: 10.1520/MPC20140003

Ramesh, G., & Prabhu, K. N. (2012). Effect of Boundary Heat Transfer Coefficient and Probe Section Size on Cooling Curves during Quenching. *Materials Performance and Characterization, 1*(1). DOI : 10.1520/MPC104365

Ramesh, G., & Prabhu, K. N. (2014a). Wetting Kinetics, Kinematics and Heat Transfer Characteristics of Pongamia Pinnata Vegetable Oil for Industrial Heat Treatment. *Applied Thermal Engineering, 65*, 433–446. DOI: 10.1016/j.applthermaleng.2014.01.011

Ramesh, G., & Prabhu, K. N. (2014b). Assessment of Axial and Radial Heat Transfer during Immersion Quenching of Inconel 600 Probe. *Experimental Thermal and Fluid Science, 54*, 158–170. DOI: 10.1016/j.expthermflusci.2014.01.016

Ramesh, G., & Prabhu, K. N. (2016). Wetting and Cooling Performance of Vegetable Oils during Quench Hardening. *Heat Transfer - Asian Research, 45*(4), 342–357. DOI: 10.1002/htj.21165

Rohsenow, W. M. (1952). A Method of Correlating Heat-Transfer Data for Surface Boiling of Liquids. *Transactions of the ASME, 74*(6), 969-975. DOI: 10.1115/1.4015984

Rohsenow, W. M., & Griffith, P. (1955). *Correlation of Maximum Heat Flux Data for Boiling of Saturated Liquids* (Report No. 6627). Cambridge, Massachusetts: MIT Division of Industrial Operation.

Sadeghifar, M., Billardon, R., Delagnes, D., Champliaud, H., Tahan, A., & Jahazi, M. (2024). A novel approach for accurate development of the incremental plastic multiplier and consistent tangent operator in thermo-elasto-plastic modeling of materials. *Mechanics of Materials, 199*. DOI: 10.1016/j.mechmat.2024.105184

Sadeghifar, M., Billardon, R., Delagnes, D., Champliaud, H., Tahan, A., & Jahazi, M. (2025). Addressing viscosity-driven singularities: accurate development of thermo-elasto-visco-plastic constitutive models. *Mechanics of Time-Dependent Materials: An International Journal Devoted to the Time-Dependent Behaviour of Materials and Structures*, *29*(4). DOI: 10.1007/s11043-025-09825-5

Salazar, G., Lemyre-Baron, J.-S., Jahazi, M., Champliaud, H., & Tahan, A. (2023). Analysis of Industrial Quenching (Air Transfer + Oil Immersion) and the Cooling Regimes after Immersion. In *Heat Treat 2023: Proceedings of the 32nd ASM Heat Treating Society Conference, October 17–19, 2023 (pp.* 106–113). Detroit, MI, USA. ASM International. DOI: 10.31399/asm.cp.ht2023p0106

Salazar, G., Lemyre-Baron, J.-S., Jahazi, M., Champliaud, H., & Tahan, A. (2024). Identification of Thermal Boundary Conditions during Industrial Quenching (Air Transfer + Mineralized Oil Immersion) of a Hollow Cylinder. In *IFHTSE 2024: Proceedings of the 29th International Federation for Heat Treatment and Surface Engineering World Congress September, Sep 30–Oct 3, 2024* (pp. 152–159). Cleveland, OH, USA. ASM International. DOI: 10.31399/asm.cp.ifhtse2024p0152

Samadi, F., Woodbury, K. A., & Beck, J. V. (2018). Evaluation of Generalized Polynomial Function Specification Methods. *International Journal of Heat and Mass Transfer, 122*, 1116–1127. DOI: 10.1016/j.ijheatmasstransfer.2018.02.018

Samadi, F., Woodbury, K., & Kowsary, F. (2021). Optimal Combinations of Tikhonov Regularization Orders for IHCPs. *International Journal of Thermal Sciences, 161,* 106697. DOI: 10.1016/j.ijthermalsci.2020.106697

Samuel, A., Nayak, U. V., Rao, K. M. P., & Prabhu, K. N. (2023). Estimation of Heat Flux Transient During Quench Hardening of Varying Diameter Steel Probes Using IHCP-Phase Transformation Coupled Model. In *Heat Treat 2023: Proceedings from the 32nd Heat Treating Society Conference and Exposition*, *October 17-19, 2023,* (pp. 88–97). Detroit, Michigan, USA. ASM International. DOI: 10.31399/asm.cp.ht2023p0088

Samuel, A., & Prabhu, K. N. (2022a). Assessment of Heat Transfer Characteristics of Transesterified Waste Sunflower Cooking Oil Blends for Quench Hardening. *Journal of Materials Engineering and Performance, 31(7)*, 5485–5503. DOI: 10.1007/s11665-022-06668-w

Samuel, A., & Prabhu, K. N. (2022b). Residual Stress and Distortion during Quench Hardening of Steels: A Review. *Journal of Materials Engineering and Performance, 31(7),* 5161–5188. DOI: 10.1007/s11665-022-06667-x

Sanchez-Sarmiento, F. B., & Cavaliere, M. A. (2021). Numerical Calculation of the Heat Transfer Coefficients in Multi-Thermocouple Probes by the Reconstruction Temperature Method. *Materials Performance and Characterization, 10*(1), 420–442. DOI: 10.1520/MPC20200144

Schmidt, R. K. (2020). The Design of Aircraft Landing Gear Volumes 1 & 2 [Knovel version]. SAE International. DOI: 10.4271/9780768099430

Simencio Otero, R. L., Viscaino, J. M., Xu, J., Gu, J., Totten, G. E., & Canale, L. C. F. (2018). Quenchant Cooling Curves, Rewetting, and Surface Heat Flux Properties of Vegetable Oils. *Materials Performance and Characterization, 8*(2), 143–169. DOI: 10.1520/MPC20180042

Simsir, C. (2008). *3D Finite Element Simulation of Steel Quenching in Order To Determine the Microstructure and Residual Stresses*. (Doctoral Thesis, Middle East Technical University, Ankara)

Simsir, C. (2014). Modeling and Simulation of Steel Heat Treatment - Prediction of Microstructure, Distortion, Residual Stresses, and Cracking. In J. Dosset & G. E. Totten (Eds.), *ASM Handbook Steel Heat Treating Technologies* (Vol. 4B, pp. 409–466). ASM International. DOI: 10.1520/MPC104479

Simsir, C., & Gur, H. C. (2008). Simulation of Quenching. In C. H. Gur & J. Pan (Eds.), *Handbook of Thermal Process Modeling Steels*. CRC Press.

Srinivasan, V., Moon, K., Greif, D., Wang, D. M., & Kim, M. (2010). Numerical Simulation of Immersion Quenching Process of an Engine Cylinder Head. *Applied Mathematical Modelling, 34*(8), 2111–2128. DOI: 10.1016/j.apm.2009.10.023

Stolz, G. (1960). Numerical Solutions to an Inverse Problem of Heat Conduction for Simple Shapes. *Journal of Heat and Mass Transfer, 82*(1), 20–25. DOI: 10.1115/1.3679871

Sugianto, A., Narazaki, M., Kogawara, M., & Shirayori, A. (2009). A Comparative Study on Determination Method of Heat Transfer Coefficient using Inverse Heat Transfer and Iterative Modification. *Journals of Materials Processing Technology, 209*, 4627–4632. DOI: 10.1016/j.jmatprotec.2008.10.016

Thibault, J. (1978). *Boiling Heat Transfer Around a Horizontal Cylinder and in Tube Bundles*. (Doctoral Thesis, McMaster University, Hamilton, Ontario, Canada).

Tourn, B. A., Alvarez-Hostos, J. C., & Fachinotti, V. D. (2021a). A Modified Sequential Gradient-Based Method for the Inverse Estimation of Transient Heat Transfer Coefficients in Non-Linear One-Dimensional Heat Conduction Problems. *International Communications in Heat and Mass Transfer, 127,* 105488. DOI: 10.1016/j.icheatmasstransfer.2021.105488

Tourn, B. A., Alvarez-Hostos, J. C., & Fachinotti, V. D. (2021b). Implementation of Total Variation Regularization-Based Approaches in the Solution of Linear Inverse Heat Conduction Problems Concerning the Estimation of Surface Heat Fluxes. *International Communications in Heat and Mass Transfer, 125,* 105330. DOI: 10.1016/j.icheatmasstransfer.2021.105330

Tszeng, T. C., & Saraf, V. (2003). A Study of Fin Effects in the Measurement of Temperature Using Surface-Mounted. *Journal of Heat and Mass Transfer, 125*(5). DOI: 10.1115/1.1597622

Unal, C., Daw, V., & Nelson, R. A. (1992). Unifying the Controlling Mechanisms for the Critical Heat Flux and Quenching : The Ability of Liquid to Contact the Hot Surface. *Journal of Heat Transfer, 114*(4), 972-982. DOI: 10.1115/1.2911909

Ungar, E. K., & Eichhorn, R. (1996). Transition Boiling Curves in Saturated Pool Boiling from Horizontal Cylinders. *Journal of Heat Transfer*, *118*(3), 654-661. DOI: 10.1115/1.2822682

Wallis, R. A. (2010). Modeling of Quenching , Residual-Stress Formation, and Quench Cracking. In D. U. Furrer & S. L. Semiatin (Eds.), *ASM Handbook Metal Process Simulation.* (Vol. 22B, pp. 409–466). ASM International. DOI: 10.31399/asm.hb.v22b.a0005530

Wang, L., Li, Y., Zhang, F., Xie, F., & Ma, Y. (2016). Correlations for Calculating Heat Transfer of Hydrogen Pool Boiling. *International Journal of Hydrogen Energy, 41*(38), 17118–17131. DOI: 10.1016/j.ijhydene.2016.06.254

Wells, M. A., & Daun, K. J. (2009). Accurate Determination of Surface Heat Fluxes during Quenching Characterized by Boiling Water Heat Transfer. *Journal of ASTM International, 6*(1), 1–17. DOI: 10.1520/JAI101818

Witte, L. C., & Lienhard, J. H. (1982). On the Existence of Two "Transition" Boiling Curves. *International Journal of Heat and Mass Transfer*, 25(6), 771–779. DOI: 10.1016/0017-9310(82)90089-8

Woodbury, K. A., Najafi, H., de Monte, F., & Beck, J. V. (2023). *Inverse Heat Conduction: Ill-Posed Problems* (2nd ed). John Wiley & Sons Inc.

Xiong, J., Wang, Z., Xiong, P., Lu, T., & Yang, Y. (2020). Experimental Investigation on Transient Boiling Heat Transfer during Quenching of Fuel Cladding Surfaces. *International Journal of Heat and Mass Transfer, 148*, 119131. DOI: 10.1016/j.ijheatmasstransfer.2019.119131

Yamada, T., Toyoda, K., Shigechi, T., Momoki, S., Kanemaru, K., & Tamaguchi, T. (2010). Film Boiling Heat Transfer around a Vertical Finite-Length Cylinder with a Convex Hemispherical Bottom. *Heat Transfer - Asian Research, 39*(3), 166–177. DOI: 10.1002/htj.20289

Yang, S. H., Baek, W.-P., & Chang, S. H. (1997). Pool-Boiling Critical Heat Flux of Water on Small Plates: Effects of Surface Orientation and Size. *Int. Comm. Heat Mass Transfer, 24*(8), 1093–1102. DOI: 10.1016/S0735-1933(97)00103-6

Zabirov, A. R., Yagov, V. V, Kalita, V. I., Radyuk, A. A., Molotova, I. A., & Belyaev, I. A. (2021). Heat Transfer Under Quenching of Cylindrical Bodies in Subcooled Liquids. *Nuclear Engineering and Design, 383* (November), 111380. DOI: 10.1016/j.nucengdes.2021.111380

Zhu, F., Chen, J., & Han, Y. (2022). A Multiple Regression Convolutional Neural Network for Estimating Multi-Parameters Based on Overall Data in the Inverse Heat Transfer Problem. *Journal of Thermal Science and Engineering Applications, 14*(5), 051003. DOI: 10.1115/1.4051841

Zuber, N. (1959). *Hydrodynamics Aspects of Boiling Heat Transfer*. (Doctoral Thesis, University of California, Los Angeles).

Zuber, N., & Tribus, M. (1958). *Further Remarks on the Stability of Boiling Heat Transfer* (Report No. AECU-3631). Los Angeles, California: University of California Department of Engineering.